UNIVERSITY OF SOUTHAMPTON

FACULTY OF ENGINEERING AND THE ENVIRONMENT
Institute of Sound and Vibration Research

Oil-Whirl Instability in an Automotive Turbocharger

by

Punithavathy Kamesh

Thesis for the degree of Doctor of Philosophy

February_2011

UNIVERSITY OF SOUTHAMPTON

ABSTRACT

FACULTY OF ENGINEERING AND THE ENVIRONMENT
INSTITUTE OF SOUND AND VIBRATION RESEARCH

Doctor of Philosophy

OIL-WHIRL INSTABILITY IN AN AUTOMOTIVE TURBOCHARGER

by Punithavathy Kamesh

This thesis is concerned with a theoretical investigation into the nonlinear dynamic behaviour of a turbocharger. Specifically the instabilities due to oil-whirl are examined. These are self-excited vibrations existing in the form of an in-phase whirl mode and a conical whirl mode. Waterfall plots were provided by *Cummins Turbo-Technologies Ltd.,* Huddersfield, UK, based on test data using two different unbalance levels on a turbocharger. The test with the high unbalance indicated that there was shift in the sub-synchronous frequency to synchronous frequency between about 80,000 rpm to 130,000 rpm. The literature suggests that this self-excited vibration can be suppressed using forced excitation. Moreover, it is well known that the existence of limit cycles enables successful operation of a turbocharger. This limit cycle is a periodic motion attributed to the nonlinearity of the oil-film, other than the stable and the unstable equilibrium states predicted by the linear analysis. Hence, a nonlinear analysis is required to analyse the limit cycle and to determine the effect of synchronous excitation on it. In the literature a variety of parameters has been shown to influence the dynamic behaviour of a rotor-bearing system. To avoid over-complicated mathematical modeling, the influence of two such parameters: gyroscopic moment and shaft flexibility are first investigated in this thesis using linear stability theory to determine their significance. Effects of gyroscopic action are investigated using symmetric and asymmetric rigid rotors supported on short journal bearings with full-film using rigid and damped supports. In this thesis, the damper supported journal bearing is used to simulate the floating ring bearings that are commonly used in automotive turbochargers. The outer film of the floating ring bearing is treated as an external damper, since the ring is assumed not to rotate but only wobble giving the damping effect from the squeezing action. A gyroscopic coefficient, which is defined as the ratio of the polar to the transverse moment of inertia of the rotor, is introduced. The threshold value of this coefficient is determined to be $1/2$ for the suppression of the conical whirl instability. The stability of the in-phase whirl mode is unaffected by this parameter. A flexible rotor mounted in floating ring bearings with full-film, is analysed to confirm that it behaves as a rigid body up to a speed of 100,000 rpm. Prior to the unbalance response study, a perfectly balanced rigid rotor supported by rigidly supported bearings is first analysed to determine the nonlinear behaviour of the in-phase whirl. To include the stiffness-like radial restoring force, an oscillating π-film cavitation model for the hydrodynamic bearings is used. The effect of a static load on the rotor is analysed to determine the nonlinear behaviour for a wide range of steady-state eccentricity ratios. A parameter plane separating the region of instability from that of stability is presented using linear analysis to determine the stability threshold at which the oil-whirl is initiated. The onset of oil-whirl phenomenon is shown to be the *Hopf bifurcation*. Particular emphasis is placed on examining the limit cycles (periodic oscillations) around the stability threshold. Reducing the nonlinear equation of motion to Poincaré normal form, the *first Lyapunov coefficients* are evaluated to show the change in the type of bifurcation from sub-critical bifurcation (disappearance of an unstable limit cycle) to super-critical bifurcation (appearance of a stable limit cycle) around the stability threshold. Such bifurcations are demonstrated through plots of orbits using numerical integration by the Runge-Kutta method. With some unbalance added to the rotor-system, waterfall plots are generated to simulate the response characteristics observed in the test data, by running-up the speed. After the Centre Manifold reduction, the equations of motions are averaged for analysis. Using a numerical and an analytical procedure, it is shown that the unbalance is more effective in the transient motion than in the steady-state condition. Unbalance introduces a reduction in the growth rate of whirl amplitude upto a certain optimum unbalance value, above which the effect is reversed. The mechanism behind this behaviour is shown to be the shift in phase caused by the unbalance at the start of whirling, when the dynamic forces are comparable with the unbalance force. This is due to the coupling effect of amplitude and phase in an unbalanced rotor system.

CONTENTS

LIST OF FIGURES

LIST OF TABLES

ACKNOWLEDGEMENTS

First and foremost, it is with immense gratitude that I acknowledge the supervision of Prof. Michael Brennan. I would like to thank him for taking me aboard in the first place. Although I worked off-site, he has made available his support in a number of ways. Without his flexibility and patience in the supervision, this thesis would never have taken shape. I owe my deepest gratitude to Prof. Roy Holmes from the School of Engineering Sciences for his co-supervision and encouragement. His advice paved the foundation of the research presented in this thesis. I am indebted to Prof. Ivana Kovacic of the University of Novi Sad, Serbia and visiting academic in the ISVR, for her co-supervision, support and help, particularly in the area of nonlinear dynamics. She offered the best advice all the time, seeing through my meticulous understanding in each stage. I feel honoured having got the chance to work with all of them.

I would like to thank Mr. Andy Day, Rotor Systems Group Leader, Cummins Turbo Technologies Ltd., Huddersfield, UK for providing a turbocharger, and the required test data that played a vital part of my research. I am grateful to Prof. Neil Ferguson and Dr. Emiliano Rustighi for their kind remarks and suggestions. My eternal gratitude goes to librarian Ms. Sarah Brooks, who went above and beyond in helping me get the required references, permitting me to work remotely. I am indebted to Ms. Maureen Mew, Ms. Joane Hazell and Ms. Heather Smith for their limitless help on every possible level.

I would like to acknowledge the financial support offered by ISVR through the Rayleigh Scholarship award that allowed me pursue this PhD. I would like to thank all the Dynamics group colleagues who extended their help as and when required, during my visits to the University. I would like to acknowledge my ex-mentor Mr. Kent Greenman at Pratt and Whitney, US, for mentoring me in gas turbine rotor dynamics that seeded the interest in my higher education. My hearty thanks to Prof. Maikandan who taught me in my under-graduation, for his constant support to my career.

This thesis would be incomplete without a mention of the support given to me by my beloved husband. I thank you dear, for being there for me always, in the days I was squeezed by the pressure of the research and the parenting of my little angel Jennifer. Without your sacrifices, I could not have completed this. I also thank my parents, my mother-in-law, and my friends, who encouraged me and offered their valuable help and support.

Wisdom is the principle thing;

Therefore get wisdom.

And in all your getting,

get understanding.

Proverbs 4:7, the Holy Bible.

I dedicate this thesis to my dear Lord and Saviour, Jesus Christ; All along the journey, thy hands never let me go!

DEFINITIONS AND ABBREVIATIONS

a_c	linearised cross-coupled coefficient of the full-film bearings $(= a_{rs} = a_{sr})$
a_{rs} , a_{sr}	linearised cross-coupled coefficients
$\tilde{a}$	real part of $c_1(\nu)$
b_d	damping coefficient of the full-film bearings $(= b_{rr} = b_{ss})$
b_{rr} , b_{ss}	linearised direct damping coefficients
b_{xx}, b_{yy}	linearised direct damping coefficients of the cavitated bearing
b_{xy}, b_{yy}	linearised cross-coupled coefficients of the cavitated bearing
$b_{nn}, b_{\phi\phi}$	linearised direct damping coefficients of the cavitated bearing in the polar co-ordinates
$b_{n\phi}, b_{\phi n}$	linearised cross-coupled damping coefficients of the cavitated bearing in the polar co-ordinates
$\tilde{b}$	imaginary part of $c_1(\nu)$
c_1	coefficient of the cubic term in the *Poincaré normal form*
$\hat{d}$	lateral displacement of the nodes of the beam element
e	eccentricity of the journal centre with respect to the housing centre O
e_1, e_2	element numbers of elements 1 and 2 respectively
f	higher order function of $\mathbf{x}$ and ν
$\mathbf{f}$	$= [F_r, F_s]^T$
$\mathbf{f_a}$	$= \left[F_{ra}, F_{sa}\right]^T$
$\mathbf{f_b}$	$= \left[F_{rb}\ , F_{sb}\right]^T$
g_{kl}	coefficients of Taylor's expansion of the higher order function G where $2 \le k + l \le 3$ corresponding to the terms $z^k \bar{z}^l$
$\hat{g}_{kl}$	$= g_{kl}$ for the quadratic terms
$\hat{g}_{21}$	coefficient related to the resonant cubic term
$\mathbf{g_{01}}, \mathbf{g_{10}}$	vector coefficient that couple the terms of the critical eigenspace and the real eigenspace

h	film thickness
h^r, h^θ	functions relating the response phase and the excitation phase
$\mathbf{h_c}$	$=\left[-2\Re\{p_2q_1\}\ \left(1-2\Re\{p_2q_2\}\right)\ -2\Re\{p_2q_3\}\ \left(1-2\Re\{p_2q_4\}\right)\right]^T$
$\mathbf{h_s}$	$=\left[-2\Re\{p_4q_1\}\ -2\Re\{p_4q_2\}\ -2\Re\{p_4q_3\}\ -2\Re\{p_4q_4\}\right]^T$
$\mathbf{h_{kl}}$	complex vectors consisting of the coefficients in the Taylor's expansion of H where $k+l=2$
j	$=\sqrt{-1}$
k	bearing support stiffness from the interference fit $\left(=m\omega_r^{\ 2}\right)$
k_a	arbitrary constant
k_{xx}, k_{yy}	linearised direct stiffness coefficients of the cavitated bearing
k_{xy}, k_{yx}	linearised cross-coupled stiffness coefficients of the cavitated bearing
$k_{nn}, k_{\phi\phi}$	linearised direct stiffness coefficients of the cavitated bearing in the polar co-ordinates
$k_{n\phi}, k_{\phi n}$	linearised cross-coupled stiffness coefficients of the cavitated bearing in the polar co-ordinates
l	distance between the bearings
l_1	*first Lyapunov coefficient*
l_a	distance of the rotor centre of gravity from the turbine bearing centre
l_b	distance of the rotor centre of gravity from the compressor bearing centre
l_c	length of compressor mass from the compressor bearing centre
l_t	length of turbine mass from the turbine bearing centre
m	half mass of the symmetrical rotor
m_a	turbine mass
m_b	compressor mass
m_r	rotor mass $(=2m)$
m_u	rotor mass with unbalance
n	eccentricity ratio (amplitude of whirl) $(=e/C)$
$n_{\max}$	maximum eccentricity ratio (whirl amplitude)

$\dot{n},\ddot{n}$	$=dn/d\tau\,,d^2n/d\tau^2$ respectively
n_s	steady-state eccentricity ratio
n_0	initial eccentricity ratio
$\mathbf{p}$	eigenvector of the Jacobian $\mathbf{A}$ $\left(=\left[p_1\ p_2\ p_3\ p_4\right]^T\right)$
$\overline{\mathbf{p}}$	complex conjugate of $\mathbf{p}$
$\mathbf{q}$	ad-joint eigenvector of the Jacobian $\mathbf{A}$ $\left(=\left[q_1\ q_2\ q_3\ q_4\right]^T\right)$
$\overline{\mathbf{q}}$	complex conjugate of $\mathbf{q}$
r	co-ordinate of the ring centre along the line of centres
$\mathbf{r}$	$=[r,s]^T$
$\hat{\mathbf{r}}$	constraint force vector at the interface of the bearing and its support $=\left[R_r,R_s\right]^T$
r_1	co-ordinate of the journal dynamic centre along the line of centres
r_{1c},s_{1c}	co-ordinates of the rotor centre of gravity along r,s directions respectively
$\mathbf{r}_j$	$=[r_j\ ,\ s_j]^T\ j=1,\ a,\ b,\ 1a,\ 1b,\ 1c,\ ma,\ mb$
$\mathbf{r}_{\mathbf{a}\ ,\ \mathbf{b}}$	co-ordinates of the ring centre in the turbine and the compressor end bearings respectively
$\mathbf{r}_{\mathbf{1a}\ ,\ \mathbf{1b}}$	co-ordinates of the journal dynamic centre in the turbine and the compressor end bearings respectively
$\mathbf{r}_{\mathbf{1c}}$	$=[r_{1c},s_{1c}]^T$
$\mathbf{r}_{\mathbf{ma\,,\,mb}}$	co-ordinates of the turbine and the compressor masses respectively
$\overline{\mathbf{r}}_{\mathbf{ma\,,\,mb}}$	rigid motion of the masses m_a and m_b
$\overline{\overline{\mathbf{r}}}_{\mathbf{ma\,,\,mb}}$	flexible deflection of the masses m_a and m_b
r_p	amplitude of the limit cycle of a perfectly balanced rotor $\left(=\sqrt{-\mu/\sigma}\right)$
r_u	amplitude of the limit cycle of an unbalanced rotor
$\overline{r}_u$	averaged form of r_u
s	co-ordinate of the ring centre perpendicular to the line of centres
$\hat{s}$	root of the characteristic equation for the transverse motion of the turbocharger with a symmetric rotor and full-film bearings $\left(=\lambda/\omega_1\right)$

$\bar{s}$	root of the characteristic equation for the tilt motion of the turbocharger with a symmetric rotor $\left(=\lambda_1/\omega_k\right)$
$\tilde{s}$	$=2\lambda/\omega_1$
$\hat{s}$	root of the characteristic equation for the transverse motion of the general rotor system with cavitated bearings
$\hat{s}_0$	root at the threshold speed $\bar{\omega}_0$ $\left(j\Omega_0\right)$
$\bar{\hat{s}}_0$	conjugate of $\hat{s}_0$ $\left(-j\Omega_0\right)$
s_1	co-ordinate of the journal dynamic centre perpendicular to the line ofcentres
t	time
t_0	start time
u	eccentricity due to unbalance
$\hat{u}$	new complex variable $\left(=z\left(\left\|l_1(\mu)\right\|\right)^{\frac{1}{2}}\right)$
$\mathbf{u}$	real vector on the critical real eigenspace $\mathbf{T^c}$ $\left(=\left[u_1,u_2\right]^T\right)$
u_1,u_2	transformed co-ordinates
$\mathbf{v}$	real vector on the real eigenspace $\mathbf{T^R}$ $\left(=\left[v_1,v_2\right]^T\right)$; all but the critical eigenvalues
v_1,v_2	transformed co-ordinates
w_1	$=\mathbf{g_{10}w_{cs}}$
w_2	$=\mathbf{g_{10}w_{sn}}$
w_{1c}	$=\mathbf{g_{01}w_{cs}}$
w_{2c}	$=\mathbf{g_{01}w_{sn}}$
$\mathbf{w_{kl}}$	vector of coefficients of the Centre Manifold, where $k+l=2$
$\mathbf{w_{sn}}$	vector of coefficients of the sine term in the Centre Manifold equation
$\mathbf{w_{cs}}$	vector of coefficients of the cosine term in the Centre Manifold equation
x_1	state variable $\left(=\bar{X}-\bar{X}_s\right)$
x_2	state variable $\left(\dot{\bar{X}}\right)$
x_3	state variable $\left(=\bar{Y}-\bar{Y}_s\right)$

x_4	state variable $\left(\dot{Y}\right)$
$\mathbf{x}$	state vector $\left(=[x_1, x_2, x_3..x_n]^T\right)$
$\overline{\mathbf{x}}$	co-ordinate vector$\left(=\{u_1, u_2, v_1, v_2\}\right)$
$\underline{\mathbf{x}}$	displacement vector
y_1, y_2	y co-ordinates of the turbine and the compressor masses respectively
y_{1a}, y_{1b}	y co-ordinates of the journal centre at the turbine and the compressor end respectively
y_a, y_b	y co-ordinates of the ring centre at the turbine and the compressor end respectively
$\mathbf{y}$	real vector satisfying the condition $\langle \mathbf{p}, \mathbf{y} \rangle = 0$; $\mathbf{y} \in \Re^4$
z	complex variable in the eigenbasis; $z = u_1 + iu_2$
$\bar{z}$	complex conjugate of z
$\mathbf{A}$	Jacobian determinant of the cavitated rotor-bearing system with perfectly balanced rotor
$\mathbf{A_0}$	2×2 matrix with all the eigenvalues on the imaginary axis
$\mathbf{A^T}$	Transpose of $\mathbf{A}$
$\mathbf{C}$	2×2 matrix with no eigenvalues on the imaginary axis
$\bar{A}$	non-dimensional group related to the bearing properties$\left(\pi \eta_b l_b{}^3 R_b / 2C^3\right)$
A_i	coefficient of the polynomial terms where $i = 0,1,2,3,4$ is the order of the term
$\hat{B}$	$= \beta 2 \hat{\omega} \hat{\alpha} \tilde{s}$
C	clearance between the journal and the bearing
$\mathrm{C_J}$	journal centre
$\mathrm{C_{JS}}$	journal static centre
$\mathrm{C}^a_{\mathrm{JS}}$, $\mathrm{C}^b_{\mathrm{JS}}$	journal static centre at the turbine end and the compressor end respectively
$\mathrm{C_{JD}}$	journal dynamic centre
$\mathrm{C}^a_{\mathrm{JD}}$, $\mathrm{C}^b_{\mathrm{JD}}$	journal dynamic centre at the turbine end and the compressor end respectively
$\mathrm{C_B}$	bearing /floating ring centre

$\mathrm{C}_{\mathrm{B}}^{a}$, $\mathrm{C}_{\mathrm{B}}^{b}$	floating ring centre at the turbine end and the compressor end respectively
C_{M}	mass centre of the journal
CN	conical whirl
$\hat{D}$	determinant of a matrix
F	static load
$\hat{F}$	lateral force acting on the finite element beam model
F_1, F_2	forces applied on the turbine and the compressor masses respectively
F_r	radial force in the full-film bearing along the line of centres
F_s	tangential force in the full-film bearing perpendicular to the line of centres in the direction of rotation
F_{ra}, F_{sa}	film forces along r,s directions respectively in the turbine end bearing of the asymmetric rotor
F_{rb}, F_{sb}	film forces along r,s directions respectively in the compressor end bearing of the asymmetric rotor
F_r^p	radial force in π-film bearing along the line of centres
$\bar{F}_r$	non-dimensional radial force ($= F_r^p / S_m F$)
$\left(\bar{F}_r\right)_s$	non-dimensional radial force at the steady-state
F_s^p	tangential force in π-film bearing perpendicular to the line of centres in the direction of rotation
$\bar{F}_s$	non-dimensional tangential force ($= F_s^p / S_m F$)
$\left(\bar{F}_s\right)_s$	non-dimensional tangential force at the steady-state
F_u	centrifugal force due to unbalance in the rotor
$\bar{F}_X$	force along X direction (vertical) along the direction of the static load
$\bar{F}_Y$	force along Y direction (horizontal) perpendicular to the direction of the static load
G	higher order function related to the critical eigenspace
G^r, G^θ	purely harmonic functions
H	higher order function related to the real eigenspace
I	transverse moment of inertia of the rotor

$\mathbf{I}$	4×4 identity matrix with unities on the main diagonal and zeros elsewhere
IP	in-phase whirl
J	polar moment of inertia of the rotor
$\mathbf{J_t}$	Jacobian determinant of the averaged equations of motion
$\mathbf{J}$	diagonal matrix of the eigenvalues
$\mathbf{K}$	stiffness matrix of the finite element model
$\hat{K}_{11}$	$=-\hat{\alpha}_{11}M_a\hat{s}^2-1$
$\hat{K}_{21}$	$=-\hat{\alpha}_{21}M_a\hat{s}^2$
$\hat{K}_{12}$	$=-\hat{\alpha}_{12}M_b\hat{s}^2$
$\hat{K}_{22}$	$=-\hat{\alpha}_{22}M_b\hat{s}^2-1$
L	finite element beam length
$\mathbf{L_{ab}}$	$=\begin{bmatrix} l_b & 0 \\ 0 & l_a \end{bmatrix}$
$L_{a,b}$	$=l_{a,b}/l$
L_B	bearing length
L_c	$=l_c/l$
L_t	$=l_t/l$
$\hat{M}$	moment on the nodes of the beam element
$M_{a,b}$	$=m_{a,b}/m$
$\hat{M}_a$	$=M_aL_t\hat{s}^2$
$\hat{M}_b$	$=M_bL_c\hat{s}^2$
$\hat{M}_{1a}$	$=M_a\left(1+L_t\right)\hat{s}^2$
$\hat{M}_{1b}$	$=M_b\left(1+L_c\right)\hat{s}^2$
M_r, M_s	moments about r and s respectively
$\mathbf{M}$	mass matrix of the beam element
$\mathbf{M}_1$, $\mathbf{M_2}$	mass matrices of the elements e_1, e_2 respectively
O	housing centre
O	higher order terms

P	oil-film pressure
Q_1^r, Q_1^θ	quadratic terms of harmonic functions related to the amplitude and phase respectively
R_b	bearing radius
R	amplitude of the response along r
R_1	amplitude of the response along r_1
R_r, R_s	constraint forces in the bearing support along r, s directions respectively
S	amplitude of the response along s
S_1	amplitude of the response along s_1
S_m	Sommerfeld number
SE	stable equilibrium
SLC	stable limit cycle
T	time period corresponding to the frequency $\Omega(0)$
$\hat{T}$	trace of a matrix
$\mathbf{T}$	eigenvector basis or eigenbasis
$\mathbf{T}^{\mathrm{C}}$	critical real eigenspace (purely imaginary eigenvalues)
$\mathbf{T}^{\mathrm{R}}$	real eigenspace (all but critical eigenvalues)
U_1	coefficient of the second harmonic cosine term in the averaged equations
$\hat{U}$	$\sqrt{U_1^{\,2} + V_1^2}$
UE	unstable equilibrium
ULC	unstable limit cycle
V	Centre Manifold function
V_1	coefficient of the second harmonic sine term in the averaged equations
$\mathbf{W}_1$	$= \left\{ \mathbf{A}^{-1}\,\mathrm{B}(\mathbf{q}, \bar{\mathbf{q}}) \right\}$
$\mathbf{W}_2$	$= \left\{ \left(2i\Omega_0 \mathbf{I} - \mathbf{A} \right)^{-1} \mathrm{B}(\mathbf{q}, \mathbf{q}) \right\}$
X	co-ordinate of the vertical axis along the direction of the static load
$\bar{X}$	non-dimensional X co-ordinate $\left(X/C\right)$
$\bar{X}_s$	non-dimensional X co-ordinate $\left(X/C\right)$ at the steady-state
Y	co-ordinate of the vertical axis perpendicular the direction of the static load

$\bar{Y}$	non-dimensional Y co-ordinate $\left(Y/C\right)$
$\bar{Y}_s$	non-dimensional Y co-ordinate $\left(Y/C\right)$ at the steady-state
Z	axis along the length of the rotor
α	growth/decay rate of the whirl amplitude $\left(=\Re\left\{\hat{s}\right\}\right)$
$\alpha'(0)$	variation of α with respect to the speed $\left(d\alpha/d\bar{\varpi}\right)_{\bar{\varpi}=\bar{\varpi}_0}$ evaluated at the threshold speed, when $\nu=0$
α_{ij}	influence coefficients of the rotor due to the force F_i acting on the turbine mass ($i=1$) and the compressor mass ($i=2$) and deflection of the turbine mass $\left(j=1\right)$ and the compressor mass ($j=2$)
$\hat{\alpha}_{ij}$	$=\alpha_{ij}m\omega_1^2$
$\hat{\alpha}$	$=\omega_1/\omega_k$
α_0	growth rate at the threshold speed $\left(\alpha(0)\right)$ when $\nu=0$
α_u	$=\alpha'(0)\nu_1$
β	*gyroscopic coefficient* $\left(=J/I\right)$
δ_{ij}	deflection at the turbine mass $\left(j=1\right)$ and the compressor mass $\left(j=2\right)$ due to force F_i applied on either the turbine mass $\left(i=1\right)$ or the compressor mass $\left(i=2\right)$.
$\delta'(0)$	(real part of the left hand side of the Poore's bifurcation algebra) / $\alpha'(0)$
ε	small real parameter introduced for averaging
ϕ	attitude angle of the journal centre
ϕ_s	attitude angle of the journal centre at the steady-state
ϕ_1	angular co-ordinate about r axis
$\bar{\phi}$	angular co-ordinate of the rotor about r_{1c}
$\hat{\phi}$	angular displacement of the nodes of the beam element
φ_u	$=\theta_u-\dfrac{\tau}{2}$
$\bar{\varphi}_u$	averaged form of φ_u
γ	damping coefficient of the external damper

$\hat{\gamma}$	non-dimensional damping coefficient $\left(=\gamma/\bar{A}\right)$
η_b	bearing lubricant viscosity
$\eta'(0)$	part of the imaginary part of the left-hand side of Poore's bifurcation algebra; sign of which implies the time period increase
κ	$=\omega_r/\omega_1$
λ	dimensional response frequency
μ	parameter as a function of ν given by $\alpha(\nu)/\Omega(\nu)$
ν	bifurcation parameter $\left(=\bar{\omega}-\bar{\omega}_0\right)$
ν_c	critical bifurcation parameter
ν_1	scaled bifurcation parameter for averaging $\left(\nu=\varepsilon\nu_1\right)$
θ	angular co-ordinate of the bearing with reference to the line of centres
θ_1	angular co-ordinate about s axis
θ_p	phase angle of the limit cycle of a perfectly balanced rotor
θ_u	phase angle of the limit cycle of an unbalanced rotor
$\bar{\theta}_u$	averaged phase angle of the limit cycle of an unbalanced rotor
$\bar{\theta}$	angular coordinate of the rotor about s_{1c}
$\boldsymbol{\theta}$	$=\left[\theta_1 \quad \phi_1\right]^T$
ρ^2	unbalance eccentricity ratio $\left(=u/C\right)$
${\rho_1}^2$	scaled unbalance eccentricity ratio for averaging $\left(\rho^2=\varepsilon{\rho_1}^2\right)$
σ	sign of the *first Lyapunov coefficient* $l_1(0)$
σ_m	non-dimensional group of the parameters of a rotor system, $S_m/\bar{\omega}$
σ_u	detuning parameter $\left(=\varepsilon\sigma_1\right)$
σ_1	scaled detuning parameter for averaging
τ	non-dimensional time $\left(=\omega t\right)$
$\hat{\tau}$	new non-dimensional time
ω	rotor speed
$\hat{\omega}$	non-dimensional speed related to the transverse motion $\left(=\omega/\omega_1\right)$
$\overset{\frown}{\omega}$	non-dimensional speed related to the tilt motion $\left(=\omega/\omega_k\right)$

$\bar{\varpi}$	non-dimensional speed as a function of the static load $\left(=\left(mC/F\right)^{\frac{1}{2}}\omega\right)$
$\bar{\varpi}_0$	non-dimensional threshold speed (stability threshold)
$\bar{\varpi}_{0u}$	non-dimensional modified threshold speed for the unbalanced rotor
ω_1	characteristic frequency at which the inertial force almost equals the damping force $\left(=2\bar{A}/m\right)$
ω_r	frequency of the rotor mass vibrating on the bearing support stiffness k in the press-fit bearing
ω_k	characteristic frequency at which the inertial moment almost equals the damping moment $\left(=\bar{A}l^2/I\right)$
ω_n	natural frequency
$\boldsymbol{\Psi}$	$=\begin{bmatrix}M_s & M_r\end{bmatrix}^T$
ζ	phase lead in the averaged equations of motion $\left(=\frac{1}{2}\tan^{-1}\left(U_1/V_1\right)\right)$
Φ	amplitude of angular motion corresponding to ϕ_1
$\boldsymbol{\Gamma}$	$\begin{bmatrix}0 & 1\\ -1 & 0\end{bmatrix}$, cross-coupling factor
$\Lambda(t)$	$=[0,\cos\tau,0,\sin\tau]^T$
Θ	amplitude of angular motion corresponding to θ_1
Ω	whirl frequency $\left(=\Im\{\hat{s}\}\right)$
Ω_0	whirl frequency at the threshold speed $(\Omega(0))$
Ω_u	$\left(=\left(\sigma_1+\Omega'(0)\nu_1\right)\right)$
$\Omega'(0)$	change in the $\Omega(0)$ with respect to speed evaluated at $\bar{\varpi}_0$ $\left(d\Omega/d\bar{\varpi}\right)_{\bar{\varpi}=\bar{\varpi}_0}$

CHAPTER 1

INTRODUCTION

1.1 INTRODUCTION

Turbochargers are a special class of turbo-machinery used to improve engine efficiency by utilising the energy in the exhaust gases. These units are typically found on diesel engines. Figure 1.1(a) shows a turbocharger with the compressor and the turbine wheels along with two floating ring bearings. The turbine wheel is made of steel and is integral with the shaft. The aluminium compressor wheel is machined for line to line contact and bolted onto the shaft [2]. This makes the turbine wheel heavier than the compressor wheel and the rotor centre of gravity is generally close to the turbine end. Figure 1.1(b) shows a typical floating ring bearing with oil holes. Figure 1.1(c) demonstrates the working principle of a turbocharger. The exhaust gas energy from the engine is used to drive a turbine. The turbine wheel drives a compressor which is mounted at the opposite end on a common rotor, all enclosed in cast housings. This allows the supply of pre-compressed combustion air into the engine. The engine aspirates the same volume of air, but due to the higher pressure, a greater air mass is supplied into the combustion chamber. Consequently, more fuel can be burnt, so that the engine's power output increases relative to the same speed and swept volume. Automotive turbochargers can operate at very high speeds, in excess of 180,000 rpm [3]. This thesis is concerned with the automotive turbochargers that are characterised by light-weight and high speed. Although various types of oil-film bearings are used, most commercial automotive turbochargers have floating ring bearings due to their low cost [4]. The simplest type is a plain journal bearing, with a film between the rotor and the bearing inner surface. With all types of oil-film bearings, waterfall plots demonstrate the existence of sub-synchronous vibrations along with the unbalance vibrations common in any rotating machinery [3]; waterfall plots are three dimensional plots of response magnitude against its frequency, varying with the rotor speed along the z axis. They are self-excited by the motion of the rotor in the bearing and are caused by a phenomenon called oil-whirl instability [5]. The term sub-synchronous implies that these vibrations are characterised by frequencies that are below the synchronous ones; their frequencies are usually found to be a little less than 50% of the rotor speed. This type of instability can occur whenever oil is trapped in a gap between two concentric cylinders, and one is rotating relative to the other. The oil-whirling within the clearance causes cross-coupling dynamic interaction leading to instability [6]. Oil-film bearings are prone to show one or two sub-synchronous instabilities over extended speed ranges of operation [7]. In a turbocharger, the whirl instability manifests itself in two different forms [2]: in-phase whirl where the two ends of the rotor are in phase and a conical whirl where they are 180^0 out of phase [8]. Figure 1.2 shows a typical waterfall plot of a turbocharger with the two sub-synchronous whirl modes. Figure 1.3(a) shows the schematic representation of the conical whirl and Figure 1.3(b) shows the in-phase whirl mode of a rigid rotor. Figure 1.3(c) shows the in-phase whirl with bending in the case of a flexible rotor.

The self-excited vibration causing the oil-whirl can produce large-amplitude alternating stresses in the rotor, creating fatigue that can result in a shaft crack [9]. They also cause a low frequency rumble and can be of large amplitude at high speeds leading to rotor-stator rub. Oil-whirl instability is a potentially damaging operating condition that must be avoided. Although squeeze-film bearings offer a solution by eliminating the oil rotation at the expense of more complicated designs involving roller bearings, they have no load carrying capacity [6]. This demands external mechanical arrangements [6]. Extensive research activity has been directed to improve the stability of oil-film bearings such as varying the oil supply pressure [10, 11] and supply angle [12], optimising bearing parameters [13], roughening bearing surfaces [14], introducing hybrid features [15], and many others. Nevertheless, a great challenge for turbocharger manufacturers is to suppress these instabilities without great cost, as the market is cost sensitive. One of the main problems in this endeavour is the lack of accurate analytical tools predicting nonlinear rotor dynamic performance of rotors supported in floating ring bearings. This leads to repetitive testing which is costly.

Figure 1.4 shows the test data in the form of waterfall plots obtained from *Cummins Turbo-Technologies Ltd.*, which show the amplitude of vibration varying with frequency and speed. These were produced under two different unbalance levels from the same hardware and conditions. The unbalance levels influence the system behaviour significantly in terms of the response characteristics. These will be referred as the test waterfall plots in this thesis. One of the response frequencies from self-excited vibration does not respond over a specific speed range, where the system responds at a frequency synchronous with the rotor speed. This leaves the speculation that the presence of unbalance in the rotor, could possibly suppress the self-excited vibration, which is an unstable sub-synchronous response. This phenomenon is known as '*quenching*' in the literature, for example [16]; it is the process of increasing the amplitude of the periodic excitation until the free unstable oscillation decays. Although turbochargers exhibit instabilities, sustained operation has been reported to be possible because the vibration is limited by nonlinear effects. Moreover, the literature for example, Gunter [2] suggests that this behaviour, attributed to the nonlinearity of the oil-film in the floating ring bearing, leads to a limit cycle, i.e., periodic oscillation with finite amplitude. Hence, this thesis first aims at investigating the nonlinear behaviour of a turbocharger with a perfectly balanced rotor. And then the effect of unbalance (periodic load excitation) on these sub-synchronous self-excited vibrations is examined.

Prior to investigating the nonlinear dynamic behaviour of a turbocharger, it is necessary to determine the influence of certain parameters on the dynamic stability. There are a number of factors mentioned in the literature that could influence the nonlinear behaviour of turbochargers, such as the shape of the bearing, cavitation, oil grooves, supply pressure, unbalance etc. This will help in deciding if these parameters need to be incorporated into a nonlinear model of a turbocharger to avoid over-complicated mathematical model. Two of these parameters: gyroscopic effects and rotor flexibility effects are investigated using a linear analysis.

1.2 BACKGROUND

A bearing is a machine component that supports or bears a load on a moving interface. Any rotating shaft (rotor) needs to be supported as well as being allowed to rotate, which requires such an interfacing component. In turbochargers, the type of oil-film bearings used is known as hydrodynamic bearings. This name is based on the type of lubrication between the rotor and the bearing. Hydrodynamic bearings get load support by hydrodynamic lift. Figure 1.5 shows the schematic of a journal bearing demonstrating the convergent oil-film between the journal and the bearing. The part of the rotor that is housed inside the bearing is called the journal. The journal rides on a fluid-film; the film is created by the motion of the journal. The pressure exerted by the journal on this film increases and supports the journal. It should be noted that, under static conditions, that is, when the journal is not rotating, the journal rests on the bearing having metal-to-metal contact.

Two types of sub-synchronous instabilities are commonly reported in these hydrodynamic bearings: oil-whirl and oil-whip [3, 8, 17]. Oil-whirl is a phenomenon determined by the properties of the bearing film. It is typically a small amplitude motion with a frequency close to almost half the rotor speed. Oil-whip is a large amplitude motion occurring with a frequency close to that of the first critical speed which is a rotor bending mode. It is commonly encountered when the rotor speed exceeds twice this critical speed. Flexible rotors are analysed for such a phenomenon.

Figure 1.6 shows a waterfall plot of a turbocharger showing the rotor vibration response corresponding to whirl and whip characteristics. The rotor whirls at a frequency about half the rotational speed. After a certain frequency, the rotor vibration shows slightly higher amplitude but the response frequency remains constant with increasing speed, which is due to oil-whip. It is evident that the speed is more than twice the whip frequency. Since a rigid rotor model is used in this thesis for all the analyses except for the study of a flexible rotor, oil-whirl is of primary interest here.

1.2.1 SUB-SYNCHRONOUS OIL-WHIRL AND THE BEARING FORCES

Oil-whirl is self-excited by the motion of the rotor in the journal bearing. With the rotor operating eccentrically relative to the bearing centre, it draws the oil into a wedge to produce a pressurized load-carrying oil-film. As this film is squeezed by a momentary displacement of the journal, the film exerts pressure on the journal. Figure 1.7 shows the pressure profile based on the short-bearing approximation [18, 19]. A short-bearing approximation of the bearing forces, allows lubricant flow along the length of the rotor and around the circumference of the bearing. The derivation of the film force using this approximation is given in Appendix A. The resultant force due to the film pressure is not completely balanced by the rotor weight, specifically in the case of lightly loaded rotors. Figure 1.7 shows that this oil force can be resolved into two components. The radial force component F_r acts along the line of centres, i.e. the line of the bearing centre $\mathrm{C_B}$ and the journal centre $\mathrm{C_J}$; the tangential force F_t acts perpendicular to the line of centres. The tangential component tends to accelerate the rotating journal, so that it performs a secondary orbit in the clearance about the housing centre in the direction of rotation, while F_r tends to restore the journal to its equilibrium state.

1.2.2 OIL-WHIP

As the rotor exhibits oil-whirl, after a certain speed, when the bearings get stiffer related to the shaft, the journal centre describes a closed orbit in the direction of rotation but the path may be of a complex nature [5]. This usually occurs at speeds above the first critical speed of the rotor and with a nearly constant frequency of rotation equal to the first critical speed. In this case, the rotor flexibility is the controlling factor. This phenomenon is called oil-whip. With increasing speed oil-whip approaches asymptotically the natural frequency of the system [3] as shown in Figure 1.6.

1.2.3 SOME TYPES OF OIL-FILM BEARINGS

There are different types of oil-film bearings available for various applications. This thesis discusses three types of bearings such as a plain journal bearing, a floating ring bearing and a press-fit bearing. In a plain journal bearing as shown in Figure 1.5, the journal rotates in a housing of circular cross-section, where the clearance is filled with a bearing fluid. Figure 1.8 shows a floating ring journal bearing which has a thin ring rotating freely between the journal and the housing, forming two hydrodynamic oil-films, the journal-to-ring film and the ring-to-bearing film. In some configurations, the ring is fixed with a pin to the housing [3], where the ring wobbles providing a squeezing action on the film. Figure 1.9 (a) shows a typical floating ring bearing provided with six oil-supply holes, which supply oil from the outer film to the inner film. Press-fit bearings have a fixed bush with tight fit into its housing. Figure 1.9 (b) shows a press-fit bearing with an external groove and six oil holes to pass lubricant to the inner oil-film.

1.2.4 CAVITATION

For small static loads which generate pressures that are small compared to the atmospheric pressure, the clearance may be filled completely with oil. This situation has been shown to be inherently unstable [20, 21], for all the eccentricities and speeds. The rotor does not assume an equilibrium state, but orbits outwards towards the housing. Since a turbocharger is lightly loaded, a full-film bearing model is used in this thesis for the linear analyses investigating the gyroscopic moments and the rotor flexibility. However, for higher loads with super-ambient pressures generated well in excess of atmospheric pressure, the oil-film ruptures close to the position of minimum film thickness $h_{\min}$ shown in Figure 1.7 creating a cavity, or series of cavities, in the divergent section. Work by several authors, for example, [22] has confirmed that the presence of an air cavity stabilises the journal bearing, thus permitting the centre of the rotor to take up an equilibrium position, under certain conditions. The nonlinear investigations in this thesis, concerned with the effect of static and unbalance forces use a cavitated bearing. Figure 1.10 shows an oscillating π-film model, in which the fluid-film remains fixed with respect to the rotor [8, 23]. As the journal rotates in the bearing, the oil-film rotates along with the journal retaining the film extent between $\theta = 0$ (film start) and $\theta = \pi$ (film rupture), where θ is the angular coordinate with reference to the line of centres of the journal and the housing. The dotted line shows position I of the journal giving angular positions corresponding to the film start and rupture at time t_0. The continuous line shows position II of the journal at time $t_0 + t$. As the journal rotates from position I to position II, the film extent remains the same as $\theta = 0$ to π. The journal centre makes an angle of ωt with respect to position I.

1.3 LITERATURE REVIEW

The principle of hydrodynamic lubrication was first established by Beauchamp Tower [24] which motivated Reynolds' [25] to provide the mathematical formulation for the pressure distribution of thin films between two bearing surfaces. This is known today as Reynolds' equation.

Since it is not possible to solve Reynolds' equation directly, Sommerfeld [26] introduced an approximation ignoring the flow in the axial direction known as the "long-bearing approximation," to obtain the film forces. This is more applicable for applications in which the bearing length is large compared with the bearing diameter. Ocvirk [18], along with Dubois [27], introduced another approximation for bearings in which the bearing length is small compared with the bearing diameter, by neglecting the term which has the least effect in narrow bearings. This method was originally proposed by Michell [28] and Cardullo [29]. The resulting solution, which can be applied to bearings having a length-diameter ratio up to about 1, is called the "short-bearing approximation." The pressure-distribution function has been extended to determine expressions giving applied load, attitude angle, location and magnitude of peak film pressure, friction, and required oil flow rate as functions of the eccentricity ratio, including oil flow. However, this short-bearing approximation, assumes that the lubricant is Newtonian, and so any variation in the lubricant viscosity with the shear rate is neglected. To overcome this, Taylor [30] performed an isothermal analysis by including the lubricant shear thinning effect into the short-bearing approximation. Taylor [31] also derived simple expressions for the bearing parameters such as minimum film thickness, maximum pressure and the friction power loss for a highly loaded journal bearing. This effort helped in gaining a clear insight into those parameters in terms of bearing geometrical factors such as radius, length, clearance, and operational factors such as speed and lubricant viscosity.

Newkirk and Taylor [32] first identified the self-induced vibration due to an oil-film. The problem associated with the stability of a high speed rotor-bearing system was not well understood or predictable until the late nineteen sixties and early nineteen seventies. Research has been extended since then to improve stability both experimentally and analytically using various types of fluid-film bearings. Newkirk [32] concluded from experimental observation that short-bearings, large clearances and moderate unit bearing loads increased the range of stable operation. Tondl [33] compared experimentally the stability characteristics of various kinds of journal bearings and reported that the limit of self-excitation was shifted towards much higher speeds when floating bush bearings were used. Floating bush bearings are also known as floating ring bearings as referred in this thesis. A number of other researchers found better stability using floating bush bearings, for example, Dworski [34] and Tanaka et.al. [35]. Various methods have been tried to improve the stability of rotor-bearing systems with plain journal bearings. To cite a few of them, Capone et al. [10] investigated circumferentially fed journal bearings under low load conditions for the influence of supply pressure on the bearing characteristics and the stability threshold. Guo and Kirk [11] showed that the externally pressurised hydrostatic-operating bearing has a good dynamic characteristic because of its linear stiffness and damping coefficients and almost zero cross-coupling terms. These cross-coupling terms are the forces or moments that couple the motions along perpendicular directions. They suggested that if the hydrostatic effect is dominant over the hydrodynamic effect, then the hybrid-operating bearings that include both the effects could play a positive role in a small eccentricity range. San Andres and Childs [12] showed that angled orifice injection had demonstrated improved rotor dynamic performance with virtual elimination of the cross-coupled stiffness coefficients. Their analysis revealed that the fluid momentum exchange at the orifice discharge produces a pressure rise in the hydrostatic recess which retards the shear flow induced by the journal rotation, and thus, reduces the cross-coupling forces.

Another major factor influencing the stability is cavitation. Robertson [36] showed that a full-film short-bearing was completely unstable. He stated that the whirl orbit would grow until it equalled the bearing clearance. Holmes [20] analytically demonstrated whirl orbits in a full-film bearing similar to that shown by Robertson [36]. Poritsky [22] demonstrated that a hydrodynamic bearing can have a threshold stability only if it develops a radial restoring force. Barrett et al. [37] used a π-film model where the film extends from 0 to 180^0 of the clearance while the other half of the clearance is an air cavity. The authors elaborated the effect of unbalance on the stability of a rotor in journal bearings; the effect of radial stiffness-like restoring force in a cavitated model against the damping-like restoring force in the full-film model was discussed. Myers [21] studied a wide-range of cavitation models using linear analyses. He determined that a rotor-bearing system with a static film was much more stable than that with an oscillating film. In a static film, the film extent remained fixed with respect to the housing. This modified the start of the film extent as a function of the journal attitude angle. The oscillating film extent is fixed with respect to the rotor as shown in Figure 1.10. Holmes [38] demonstrated a better correlation of the experimental journal orbits of a rotor system to that predicted by the oscillating π-film cavitation model using the short-bearing approximation.

Rotors with high inertia, particularly in high speed applications experience the gyroscopic effect due to the angular momentum. In general, the gyroscopic effect has not been widely investigated from the point of view of stability in rotor-journal bearing systems. For the angular motion of a simple rigid rotor-bearing system, Tondl [39] analysed the effect of gyroscopic action on the amplitude of the response as the function of speed. He showed that it is considerable in both the narrowing of the speed interval of occurrence of self-excited vibration and the reduction of the resulting amplitudes. Moreover, Tondl showed that, a fairly large coefficient of the gyroscopic moment may even suppress self-excited vibration. Li and Shin [40] reported the splitting of the first resonant frequency into an increasing and another decreasing frequency with rotational speed due to the gyroscopic effect. Angantyr [41] showed that the gyroscopic effect in a gas turbine had a stiffening effect and lead to an increase in the forward whirl frequencies with speed. Gunter and Chen [2] examined the experimental data and three dimensional finite element compressor wheel analysis, with centrifugal forces. They suggested a 20% reduction in the polar moment of inertia of the compressor wheel to produce accurate moment calculations. This was due to the flexibility of the compressor wheel and the lack of a solid connection between the aluminium wheel and the steel turbocharger rotor at high speeds.

Rotor flexibility has also drawn the attention of researchers. Hagg and Warner [42] determined that the rotor flexibility decreased the region of stable operation. Myers [21] and Gardner [8] studied the destabilising effect of the rotor flexibility. They concluded that, its effect on oil-whirl was relatively small, except in the case of very flexible rotors, where it was likely to be swamped by oil-whip. Gunter and Chen [2] demonstrated in the case of a turbocharger, that, when bearings became relatively rigid at high speeds, the rotor flexibility influenced the system behaviour.

Apart from numerical analysis, which is a common technique in modern day research, various nonlinear analytical techniques have been used to study a limit cycle. The limit cycle is a periodic motion exhibited by the journal with finite amplitude. Demonstrating the effect of a static load to improve the stability, Myers [43] introduced the *Hopf bifurcation* theory to show the existence of a small amplitude limit cycle for a symmetric perfectly balanced rigid rotor with a static load supported in cavitated long journal bearings. Linear stability analysis showed the existence of a neutral curve splitting the stability regions of the parameter space defined by the steady-state eccentricity ratio (ratio of the journal eccentricity to the bearing clearance) of the journal and the speed. Gardner [23] applied the method of multiple scales to analyse a similar rotor system with the short-bearing approximation for the bearing forces. Boyaci et al. [44] studied the effects of the nonlinear bearing forces in a symmetric and perfectly balanced rigid rotor supported by two identical floating ring bearings. The nonlinear bearing forces for both the fluid-films were obtained by applying the π-film short-bearing approximation. Applying the *Hopf bifurcation theory*, they studied the bifurcation behaviour (change in the stability of the steady-state) of the system, focussing on the influences of the bearing design parameters on the stability and on the limit cycle.

Since unbalance is an inherent characteristic of any rotor, its effect on the rotor system stability is an area of investigation. Tondl [39] stated that the effect of unbalance substantially depends on all the nonlinear factors influencing the amplitude of a perfectly balanced rotor. He analysed the unbalance effect on the speed of the onset of self-excited vibration and its amplitude. He concluded that if the amplitude of the steady-state vibration increased with speed, then unbalance could lower such amplitude. However, if the steady-state amplitude corresponds to an unstable equilibrium, then there is a theoretical lowering of the amplitude of forced self-excited vibration; the onset of self-excited vibration occurs at an earlier speed in that case.

Kirk and Gunter [45] numerically analysed both horizontal and vertical rotor bearing systems with unbalance. With a full-film of oil in the bearings, they concluded that the addition of unbalance can greatly reduce the magnitude of the limit cycles encountered with vertical balanced rotors and also keep the forces transmitted to a lower value than that of a perfectly balanced shaft. Unbalance in a horizontal journal is highly undesirable and should always be reduced to the lowest possible value. The vertical journal, however, requires the proper unbalance level to allow the system to operate at a low amplitude limit cycle. Barrett et.al [37] used a rotor-bearing model with π-film cavitation and found it possible to optimize the unbalance to minimize the amplitude of the limit cycle and the force transmitted for the limit cycle operation above the stability threshold speed. Gambaudo [46] carried out a general study of the problem of the perturbation of an autonomous differential system, by a time-periodic forcing close to a *Hopf bifurcation* point. A description of the system dynamics in a three parameter space of the bifurcation parameter, the perturbation amplitude, the excitation frequency was presented. This approach presented the advantage of transforming the global problem of the perturbation of a limit cycle into a local one, which allowed them to use perturbation methods. Following Gambaudo’s method, Shaw and Shaw [47] analysed a rotor system similar to that of Myers [43] with the long-bearing approximation, but with unbalance; they showed an extremely complicated dependence on the system parameters and the rotor speed due to the unbalance effect using a periodically perturbed *Hopf bifurcation*. Brown et al. [48] showed that the conditions for chaos in a dynamic system are satisfied by a rigid journal supported on a hydrodynamic bearing film operating at a high eccentricity. Brown also showed that when the rotating unbalance force exceeds the static load, the bearing is intermittently unloaded and chaos can result. Namachivaya and Ariaratnam [49] studied in detail the influence of small periodic perturbations on systems exhibiting the *Hopf bifurcation*. They obtained explicit results related to the bifurcation, along with the stability of the solution, incorporating the method of averaging. Following the work reported in [49], Chen and Ding [50], Ding et.al [51] investigated the periodically perturbed *Hopf bifurcation* for an imbalanced rotor/seal system, for the sub-harmonic resonance condition, where the vibration frequency was half the excitation frequency. The authors showed that the non-synchronised whirl of the imbalanced rotor can be one of the following two types of behaviour: It could be a quasi-periodic motion which is a form of motion that is regular but never exactly repeating, resulting from a *Hopf bifurcation*; or it could be a half-frequency whirl from the period-doubling bifurcation, where the system switches to a new behaviour with twice the period of the original system; the type of behaviour is determined by the structural parameters and the operating conditions. Li et al. [52] presented the dynamic analysis of a rotor/seal system. They demonstrated that the rotor imbalance can lead to a stable rotor dynamic performance above a certain speed in an otherwise unstable system. They showed that under the periodic excitation of rotor unbalance, the whirling vibration of rotor was synchronous, if the rotation speed was below the stability threshold; the vibration became severe and asynchronous which was defined as unstable, if the rotation speed exceeded the threshold.

Although unbalance was shown to be advantageous by several authors under various conditions, Calvo et al. [53] found out that when a turbocharger was used in passenger cars, the whistling noise due to unbalanced forces could be perceived by the driver, which caused discomfort. This was usually in the frequency range between 800 Hz to 3000 Hz of synchronous order. They suggested a procedure to control the turbocharger whistling noise against unbalanced forces variation, in order to maintain the acoustic comfort of the vehicle. Since achieving perfect balance was very expensive, they arrived at a maximum unbalance level specification limit, in order to manufacture acceptable turbochargers from a whistling noise point of view, at the lowest cost possible.

Research on oil-whirl specific to the turbocharger is quite limited. Holmes [3] correlated the results of the linear analysis of a turbocharger with floating ring and press-fit bearings to the related experimental results using a symmetric rigid rotor. Further to that, Holmes et al. [54] demonstrated the behaviour of two sub-synchronous frequencies and their dominance in the operating range using the linear analysis. Alsaeed [55] performed both linear and nonlinear analysis using the finite element analysis code-DyRoBeS [56]. He investigated several hydrodynamic journal bearings demonstrating the benefit of a linear analysis for the design evaluation and maintenance purposes. His analysis showed that the turbocharger with floating ring bearings has the least unstable whirling operation, wherein the external damping offered by the outer film re-stabilised the whirling modes. San Andres and Kerth [7] performed a thermal analysis coupled with a nonlinear rotor dynamic analysis of an automotive turbocharger supported in floating ring journal bearings. They predicted that the floating ring-to-journal speed ratio decreased as the rotor speed increased, mainly owing to the thermal effects on the film viscosities. Gunter and Chen [2] demonstrated the existence of limit cycles at speeds of 100,000 rpm and higher due to the nonlinear action of the fluid-film floating bush bearings using a nonlinear finite element analysis. Guangchi et al. [57] investigated the effect of foundation excitation on the dynamical behaviour of a turbocharger. With the foundation excitation, the authors showed a more complicated behaviour, and development of a chaotic state at a very low rotational speed. Kirk et al. [58] conducted an experimental test on a turbocharger to demonstrate the two unstable whirling modes typically seen in a turbocharger. The experimental results showed that the onset of both the modes occurring in each of the engine testing conditions: unloaded and fully loaded. They suggested that future testing of different bearing designs could be conducted without the use of the engine dynamometer to load the engine, but the full load condition may be necessary for complete verification of stability. Sterling [59] focussed on the relationship between synchronous and sub-synchronous amplitude levels. Applying a series of unbalance masses to the turbine and compressor wheels, he showed that the addition of unbalance can suppress the appearance of sub-synchronous vibration.

Schweizer [60] examined a medium-sized turbocharger supported on full-floating ring bearings. He discussed about further bifurcations (change in dynamic stability) at higher speeds leading to the existence of a stable limit cycle and the possible collapse of such limit cycles leading to mere forced oscillations. In that process, depending on the system parameters such as rotor mass/inertia, shaft stiffness, bearing parameters, the author suggested further kind of bifurcation that lead the rotor became totally unstable; i.e. dangerous high bearing eccentricities and rotor amplitudes, which in practice often lead to the destruction of the rotor. Referring to this as ‘Total Instability’, he showed that, such phenomenon could physically be explained as synchronization of two limit cycles, namely as synchronization of the inner and outer oil-whirl/whip of the floating ring bearings. Gjika et al. [61] showed the progress on the nonlinear dynamic behaviour modelling of the rotor-bearing system (RBS) incorporating two oil-films in series: a hydrodynamic one with a squeeze-film damper commonly used in turbochargers. Their prediction and measured synchronous response and total motion (synchronous and sub-synchronous) were in good agreement. Both demonstrated the nonlinear character of the RBS behaviour, including several sub-synchronous frequency components over the operating speed range.

This thesis investigates the nonlinear dynamic behaviour of a turbocharger under the action of static and periodic loads (unbalance force) on the rotor. The oscillating π-film cavitated bearings are used in these analyses. The effect of the gyroscopic moment and the rotor flexibility are also investigated using linear analysis of the rotor-bearing system with a full-film bearing model. The following section lists the objectives in detail.

1.4 THESIS OBJECTIVES

The objectives of this thesis are to:

- investigate the effect of the gyroscopic moment on sub-synchronous whirl instabilities of a turbocharger with full-film bearings using linear analysis;
- examine the limit of rotor speed for the turbocharger of interest up to which a rigid-rotor assumption with full-film bearings is reasonable;
- determine the linear stability threshold indicating the onset of oil-whirl, under the influence of a static load, for a general rotor system with a perfectly balanced rotor in cavitated short-bearings with an oscillating π-film;

- determine the change in the nonlinear dynamic behaviour of the general rotor system, as the state (position) of the journal centre across the bearing clearance changes, under the effect of the static load;

- simulate the effect of unbalance in a turbocharger with cavitated bearings, both in the transient and in the steady-state motion, to analyse the behaviour in the test waterfall plots provided by *Cummins Turbo-Technologies Ltd*;

- determine the nonlinear mechanism that controls the whirl amplitude and the phase of an unbalanced rotor in the turbocharger with cavitated bearings.

1.5 NOVEL CONTRIBUTIONS OF THE THESIS

- A gyroscopic coefficient has been introduced to study the effect of gyroscopic moments in a turbocharger with symmetric rotor using a simplified, linearised equation of motion following Holmes [3, 54]; this coefficient is the ratio of the polar moment of inertia to the transverse moment of inertia of the rotor. Its value beyond a threshold of $1/2$, has been shown to completely suppress the conical whirl instability in a turbocharger. This value was shown to be unaffected by the addition of an external damper support and the asymmetry of the rotor.

- A speed limit has been determined for the validity of the assumption of a rigid rotor by analysing a flexible rotor modelled by superimposing the rigid dynamic motion and the flexible static deflections for a specific turbocharger.

- Further to the work of Myers and Gardner [23, 43], in charting the stability threshold between the stable and unstable equilibrium states from the linear equations of motion, the interplay of the oil-film forces with the static load towards the system stability has been determined.

- The nonlinear effect of the oil-film forces based on the short-bearing approximation, leading to periodic vibration of the rotor has been demonstrated; this occurs around the speed at which the equilibrium state of the rotor becomes unstable. When the journal centre crosses about 32% of the bearing clearance with respect to the bearing centre, the nonlinear dynamic behaviour of the rotor-bearing system with an oscillating π-film cavitation, has been shown to change significantly.

- Unbalance has been shown to reduce the growth of the whirl amplitude in the transient motion. The advantageous effect of unbalance has been shown to prevail only up to a certain level (optimum value). The nonlinear mechanism behind the sub-synchronous response characteristics due to synchronous excitation has been determined.

1.6 THESIS OUTLINE

This thesis consists of 7 Chapters. A brief outline of the contents of these Chapters is presented here.

Chapter 1 gives the introduction to the oil-whirl in a turbocharger. The test waterfall plots provided by *Cummins Turbo-Technologies Ltd.* based on the data collected from the unbalance tests on a turbocharger are introduced; they are utilised in setting the thesis objectives. A brief literature survey is provided. The novel contributions of this thesis are articulated.

Prior to investigating the nonlinear behaviour of the turbocharger, in **Chapter 2** the effect of gyroscopic moment is analysed using the linearised equation of motion. The first part of Chapter 2 reviews the linear analysis of a turbocharger using a symmetric rotor with three different types of support conditions of the bearing. A simplified approach is presented to study the stability behaviour of the turbocharger with full-film bearings. Later, the effect of the gyroscopic moments due to the inertia of the rotor is investigated on the conical whirl instability of the turbocharger. Both the rigidly supported and the externally damped bearing conditions are investigated to represent the plain journal bearings and the floating film journal bearings respectively. Finally, the effects are verified with a more realistic asymmetric rotor model considering both the in-phase and the conical whirl instabilities.

Similar to Chapter 2, the rotor flexibility effect is analysed in **Chapter 3**; a flexible rotor is investigated for its effect on the stability of the turbocharger. The flexible static deflections of the rotor in terms of its influence coefficients are superimposed onto the rigid dynamic motion of the rotor in full-film bearings discussed in Chapter 2. Using a simple finite element model of two-dimensional beams, the influence coefficients of the rotor are determined. This Chapter is mainly aimed at verifying the validity of the assumption of a rigid rotor made in all the other Chapters. A speed limit is predicted for the turbocharger under investigation for the rigid behaviour of the rotor.

Since turbochargers are lightly loaded, the effect of static load has been ignored in the previous Chapters. **Chapter 4** gives the linear analysis of a general rotor-bearing system under the effect of the static load. In order to effectively capture the physical behaviour, a cavitated bearing model is used in this Chapter to allow for the stiffness-like radial restoring force in the bearings. Note that a full-film bearing is used in Chapters 2 and 3. The bearings are assumed to have an oscillating π-film cavitation. From the Jacobian determinant of the linearised equations of motion, the stability threshold that separates the stable and the unstable equilibrium states of the journal is determined; this is represented in a parameter plane of the rotor speed and the steady-state eccentricity ratio. The analysis also presents the inter-play of the bearing forces and the static load in the system, rendering a physical insight into the stabilising characteristic of the static load.

Chapter 5 discusses the nonlinear analysis of the general rotor system given in Chapter 4. This Chapter aims at investigating the periodic vibration (limit cycle) of the journal motion in the neighbourhood of the stability threshold attributed to the nonlinearity of the oil-film. Using analytical techniques, such as the *Hopf bifurcation* theory and the normal form theory [62, 63], the rotor-bearing system is analysed for the disappearance of an unstable limit cycle (sub-critical bifurcation) and the appearance of a stable limit cycle (super-critical bifurcation) close to the stability threshold. The Chapter advances the discussion on the Central Manifold reduction and the *first Lyapunov coefficients* [63] calculation to determine the type of bifurcation. These observations are also compared with the numerical analysis using the orbit plots. With the help of the operating curve corresponding to a turbocharger, its nonlinear behaviour based on the type of bifurcation is analysed.

In **Chapter 6**, based on the operating curve chosen to represent a turbocharger, the test waterfall plots are simulated numerically by adding unbalance to the rotor system used in Chapter 4. The change in the whirl amplitude and its phase angle in the transient motion and in the steady-state, with increase in the unbalance, is investigated. A detailed analysis of the rate of change of amplitude and phase is presented aiming at the determination of the mechanism behind the unbalance effect. Particular emphasis is placed on analysing the behaviour at the start of whirling, when the unbalance force is comparable with that of the hydrodynamic forces in the bearings. Using the method of averaging, the equations of motion are simplified to show the coupled nature of the response amplitude and the phase due to the unbalance in the system, which is observed in the numerical analysis.

Chapter 7 gives the major conclusions of the thesis on the investigation into the nonlinear behaviour of an automotive turbocharger; these are related to the effect of the gyroscopic moments, the rotor flexibility, a static load and the unbalance force on the instability of the turbocharger. A brief overview of the thesis is presented. Some recommendations for future work are given.

FIGURES

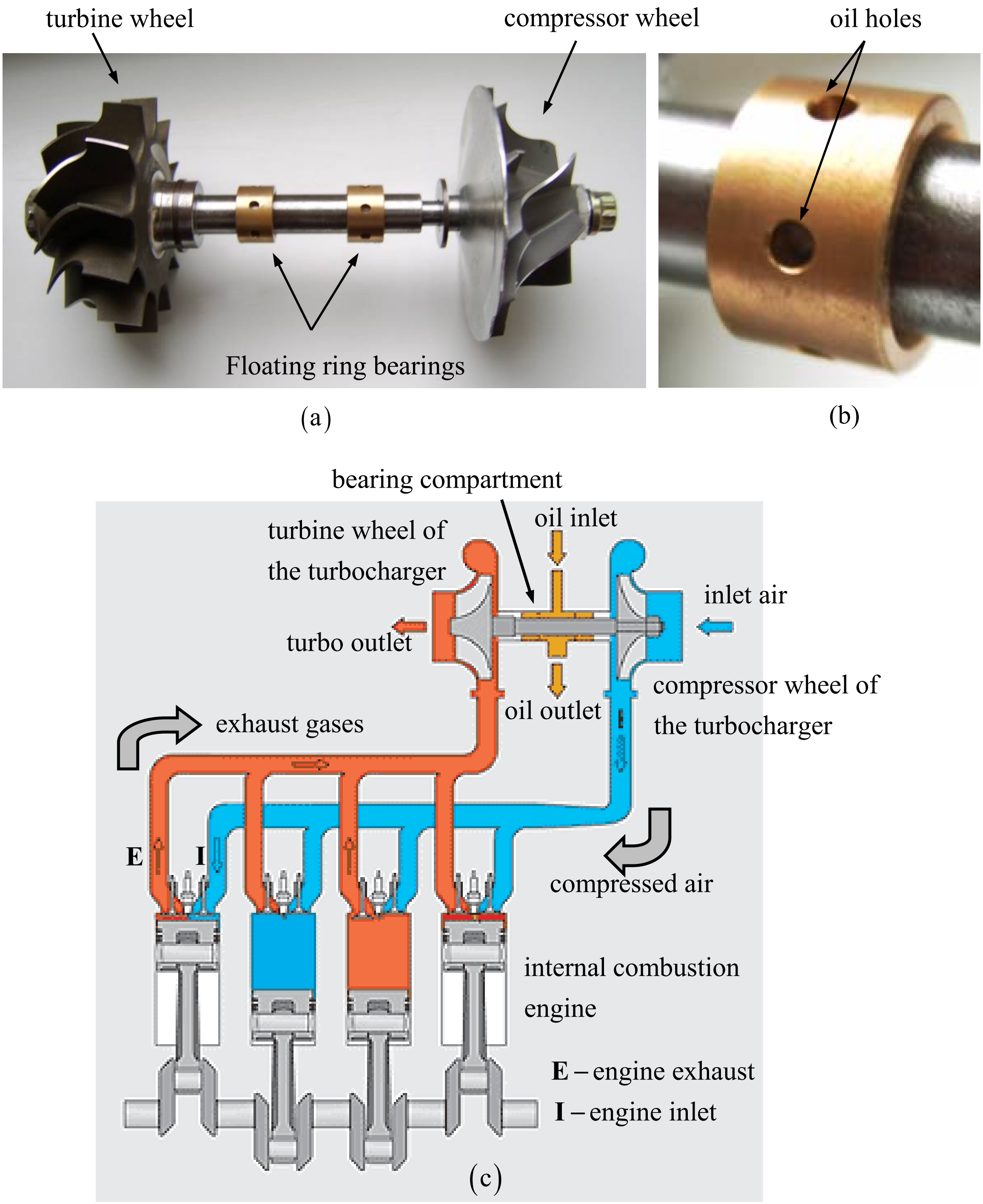

Figure 1.1 (a) A typical turbocharger (from *Cummins Turbo-Technologies Ltd.)* which is the assembly of compressor wheel, turbine wheel and two identical floating ring bearings (b) A typical floating ring bearing (c) Schematic representation of the working principle of a turbocharger driven by the exhaust gases of a 4 cylinder engine (adapted from the website: http://www.turbocompressori.net/new_turbochargers.htm)

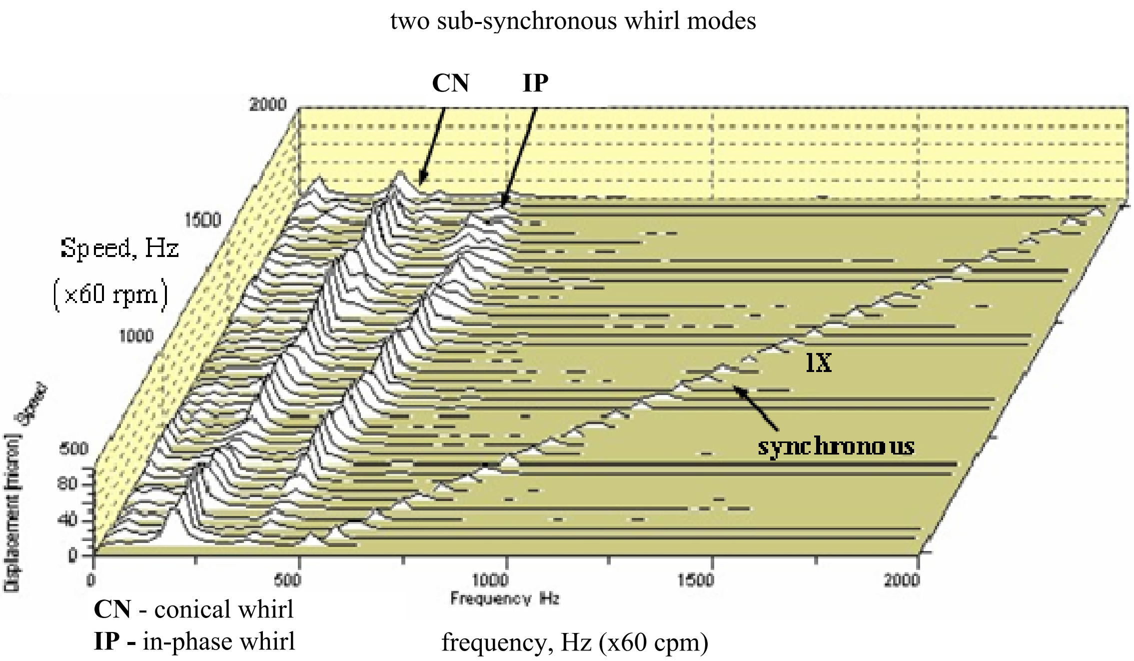

Figure 1.2 A typical waterfall plot of a turbocharger showing the two sub-synchronous whirl modes. Adapted from the waterfall plot provided by *Cummins Turbo-Technologies Ltd.*

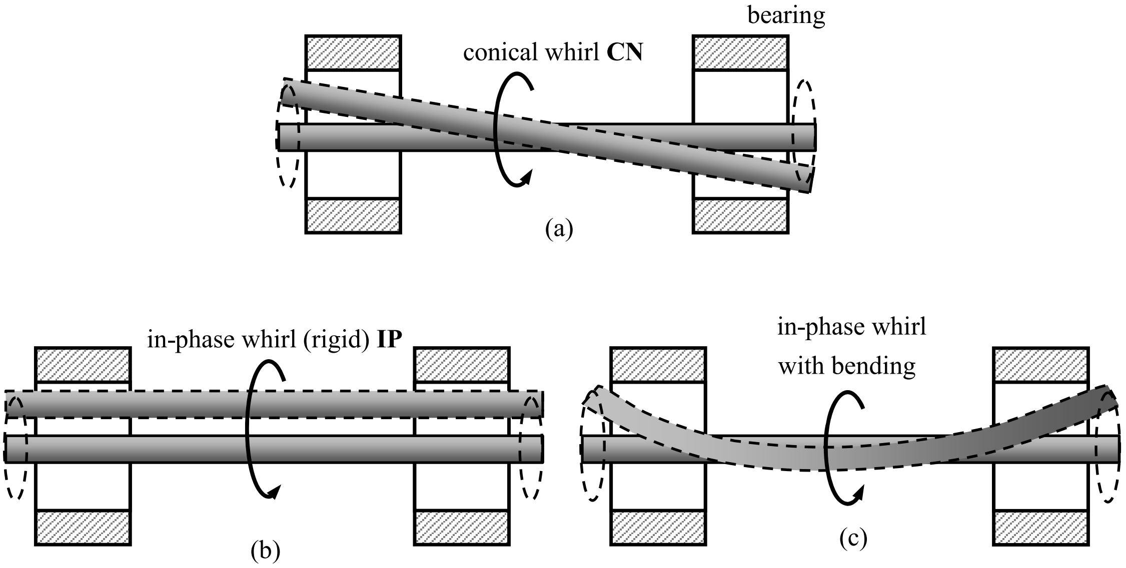

Figure 1.3 Schematic representation of the whirl modes in a turbocharger; (a) conical whirl (b) in-phase whirl in a rigid rotor (c) in-phase whirl showing bending in a flexible rotor [8, 9]. The turbine wheel and the compressor wheel are not shown here.

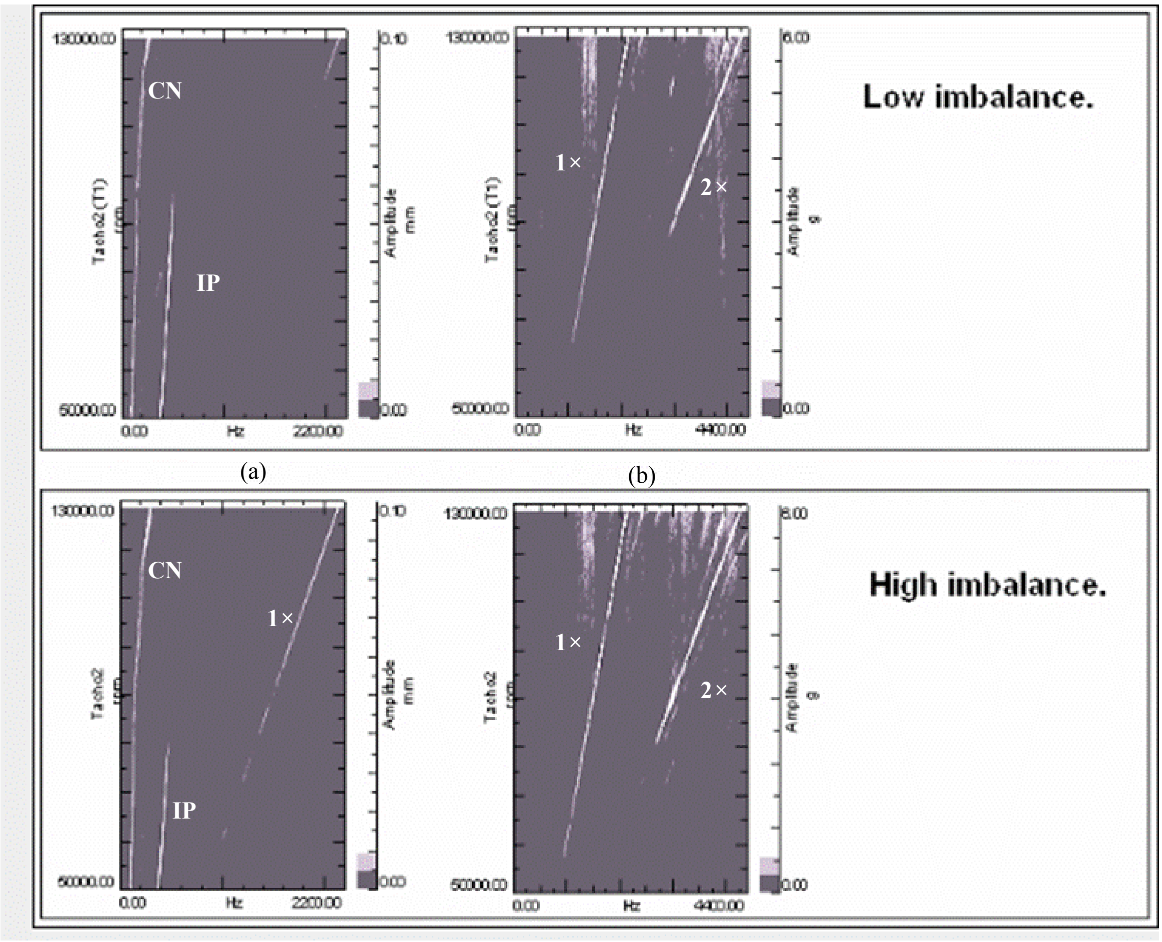

(a) (b)

SHAFT MOTION **ACCELERATION**

(c) (d)

CN - CONICAL WHIRL

IP - IN-PHASE WHIRL

1× - SYNCHRNOUS WHIRL FIRST HARMONIC

2× - SYNCHRNOUS WHIRL SECOND HARMONIC

Figure 1.4 Adapted from the comparative test waterfall plots provided by *Cummins Turbo-Technologies Ltd.* based on the data was collected from the same hardware/conditions but with different unbalance levels: (a) shaft motion with low unbalance (b) acceleration with low unbalance (c) shaft motion with high unbalance (d) acceleration with high unbalance.

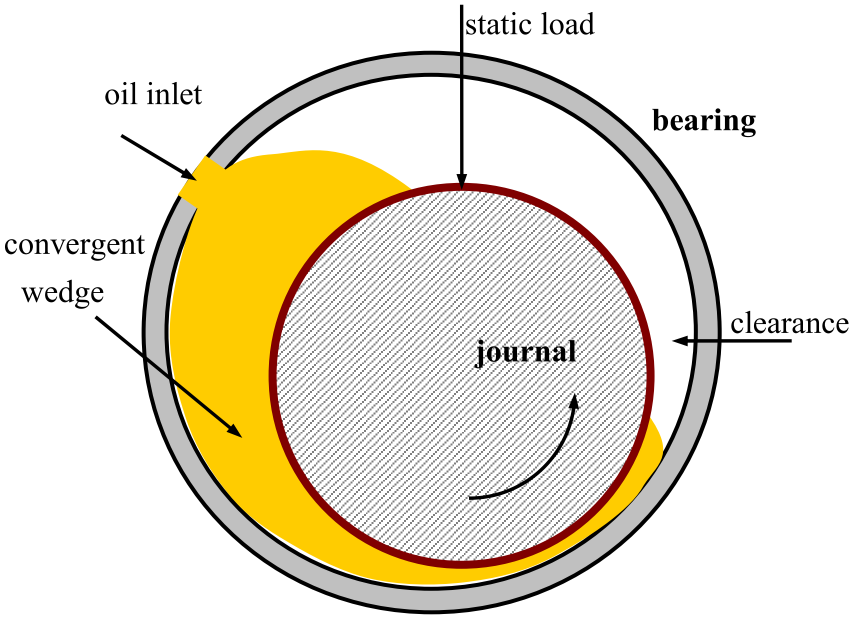

Figure 1.5 Schematic of a journal bearing demonstrating the hydrodynamic lift produced by the squeezing action of the oil-film creating a converging wedge [64].

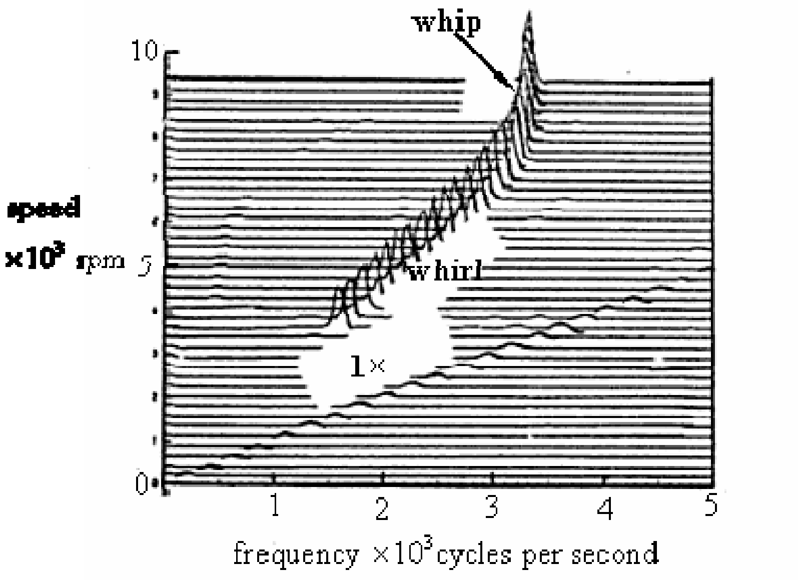

Figure 1.6 Waterfall plot of a turbocharger showing whirl and whip vibration characteristics. Adapted from Holmes [3].

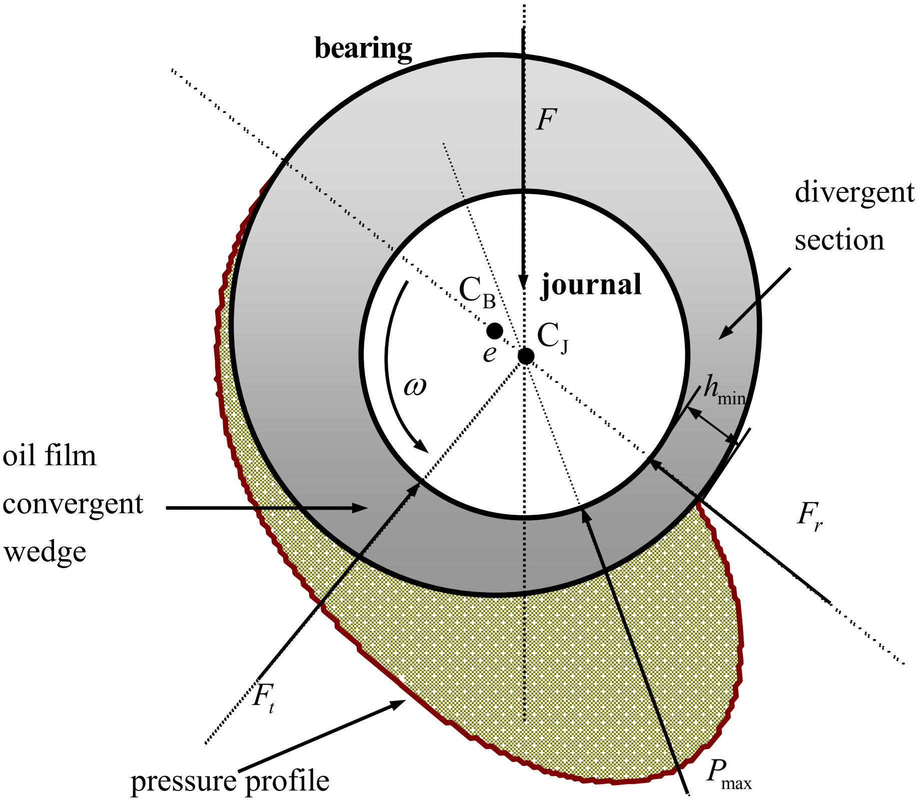

Figure 1.7 Schematic of a journal in a bearing with oil-film in the clearance; F_r is the radial force acting along the line of centres and F_t is the tangential oil-film force tending to cause the whirling of a lightly loaded journal, spinning at speed ω, in a journal bearing [5]; C_B is the bearing centre, C_J is the journal centre, e is the eccentricity of the journal centre, P_{max} is the maximum pressure, F is the static load, h_{min} is the minimum film thickness.

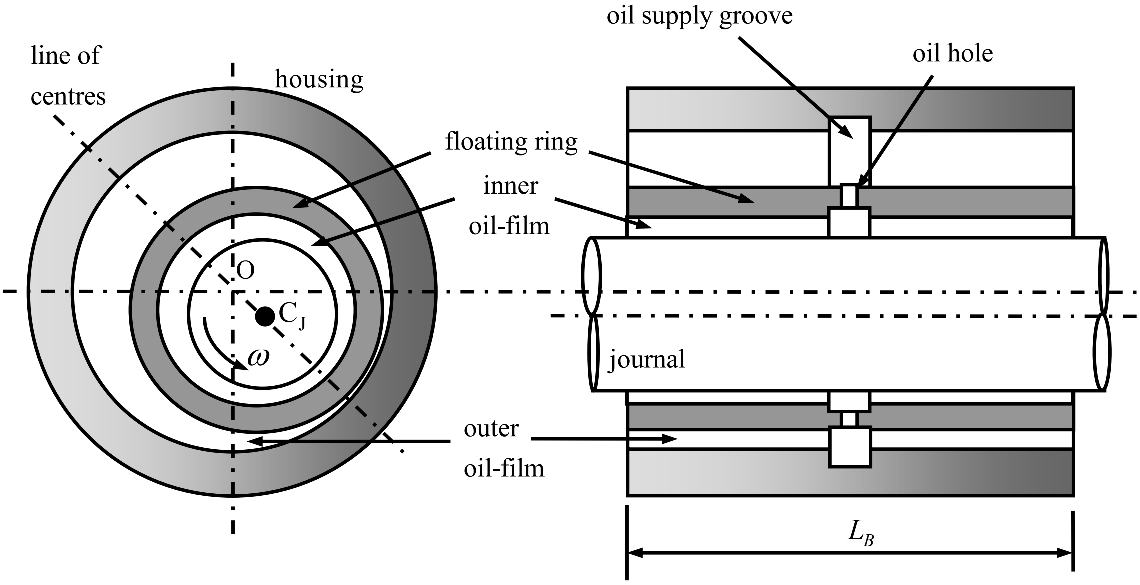

Figure 1.8 Schematic diagram of a floating ring bearing [65]; $\mathrm{C_J}$ is the dynamic journal centre and O is the centre of the stationary housing, L_B is the bearing length; ω is the journal speed; the floating ring is assumed to wobble and not to rotate in this thesis. The squeezing action of the outer film is treated as an external damper.

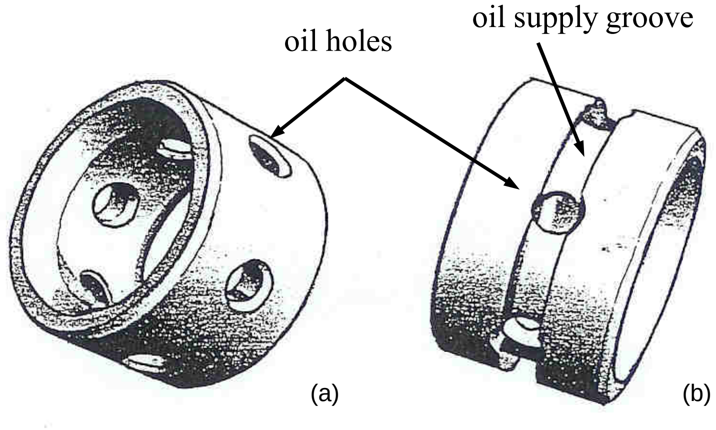

Figure 1.9 Typical turbocharger bearings (a) floating ring bearing provided with six oil-supply holes, which supply oil from the outer film to the inner film. (b) press-fit bearing with a tight fit into its housing and provided with an external groove and six oil-supply holes to pass lubricant to the inner oil-film; from Holmes [54].

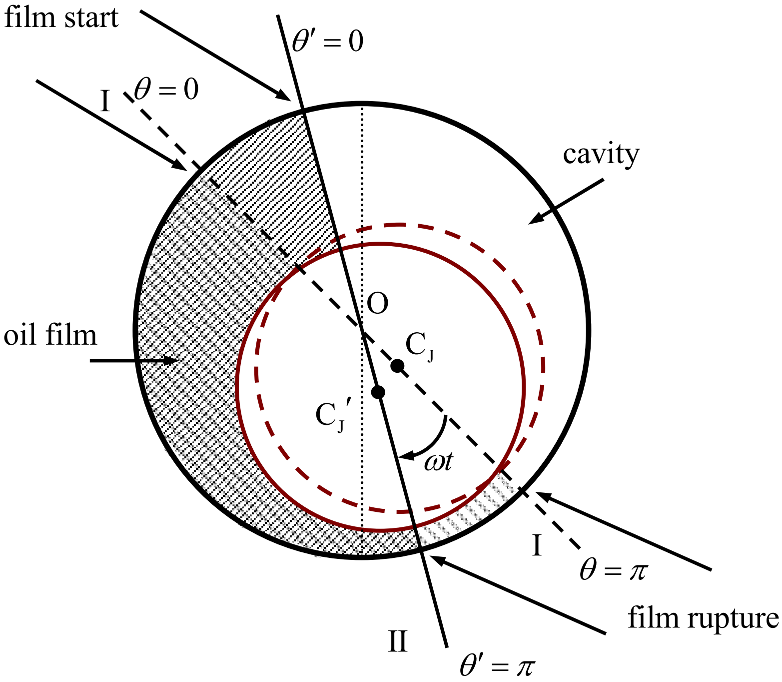

Figure 1.10 Schematic diagram of a journal in a plain bearing with an oscillating π-film cavitation which rotates along with the rotor. The film boundaries $(0, \pi)$ remain the same as the journal centre C_J corresponding to position I shown in dashed lines, changes to C_J' corresponding to position II shown in continuous lines due to the journal rotation at a speed ω; reproduced from Gardner [8].

CHAPTER 2

THE EFFECT OF GYROSCOPIC MOMENTS ON THE STABILITY OF A TURBOCHARGER

2.1 INTRODUCTION

The gyroscopic effect caused by rotation and the polar moment of inertia of the rotating body can be an important dynamic effect in a rotor system. Since turbochargers are high speed applications exhibiting oil-whirl instability, it is important to investigate their behaviour including the gyroscopic moments. Holmes [3] studied the effect of various bearing types like floating ring, press-fit bearings. He showed a good qualitative correlation of waterfall plots to the results of a linear analysis for transverse motion. Holmes et al. [54] demonstrated the manifestation of two oil-whirl frequencies in turbochargers. The work reported by Gunter and Chen in [2] suggests that the two frequencies correspond to an in-phase whirl from the transverse motion and a conical whirl from the tilt motion. The details of these modes have been discussed in Chapter 1. This Chapter aims to investigate the tilt motion of a similar symmetric rigid rotor to determine the effect of gyroscopic moments on the conical whirl. A brief review of the transverse motion of the turbocharger with various types of support such as rigid, flexible and damper is presented first. A plain journal bearing which is rigidly supported, and the bearing clearance is fully filled with oil without rupture of the film (no cavitation), is first considered for the analysis based on the fluid-film forces derived by Holmes [20]. Then the effect of gyroscopic moments in the presence of an outer film, which is treated as an external damper, is investigated in order to simulate a floating ring bearing described in Chapter 1. The ring is assumed not to rotate but only wobble. Since the turbine is much heavier than the compressor in a turbocharger, the effect of rotor asymmetry on the influence of gyroscopic moments is also investigated using an asymmetric rotor with floating ring bearings for both transverse and tilt motion. Since turbochargers are lightly loaded, static eccentricity due to the gravity load of the rotor is neglected in this Chapter.

2.2 SYMMETRIC ROTOR - TRANSVERSE MOTION: A BRIEF REVIEW OF PREVIOUS WORK

2.2.1 INTRODUCTION

This Section reviews the dynamic analysis of a turbocharger presented by Holmes [3]. The equations of motion are derived for a rigid rotor mounted in three types of bearings detailed in Chapter 1: plain, press-fit and floating ring bearings for the transverse motion of the rotor. The effects of various support characteristics of these bearings are investigated to determine their role in the stability of the in-phase whirl.

2.2.2 RIGID SUPPORT (PLAIN JOURNAL BEARINGS)

This Sub-Section presents the analysis of the turbocharger with rigidly support bearings. Figure 2.1(a) shows a schematic diagram of a turbocharger rotor with plain journal bearings, where $\mathrm{C_B}$ is the bearing centre, $\mathrm{C_{JS}}$ is the static journal centre, $\mathrm{C_{JD}}$ is the dynamic journal centre and O is the centre of the stationary casing. Plain journal bearings are journal bearings with their outer ring (race) fixed, which offers a rigid support to the bearing. Figure 2.1(b) shows the schematic of a symmetric rotor of mass $2m$ mounted in rigidly supported bearings. Assuming a full oil-film [20] (no cavitation), the oil-film forces acting on each journal of the turbocharger with rigid supports are given by [3]:

$$F_r = b_{rr}\dot{r}_1 + a_{rs}s_1 , \tag{2.1}$$

$$F_s = b_{ss}\dot{s}_1 - a_{sr}r_1 , \tag{2.2}$$

where r_1 and s_1 are the co-ordinates of the journal dynamic centre $\mathrm{C_{JD}}$; r_1 is along the line of centres of the journal and the housing, s_1 is perpendicular to the line of centres in the direction of rotation; b_{rr}, b_{ss} are the linearised direct damping coefficients of the oil-film; a_{rs}, a_{sr} are the linearised cross-coupled stiffness coefficients. It can be seen from the Eqs. (2.1) and (2.2), that the coefficients a_{rs}, a_{sr} cross couple the two forces. This means that a displacement s_1 produces a force along r_1 due to the coefficient a_{rs} and likewise r_1 produces a force along s_1 due to the coefficient a_{sr}. These coefficients are obtained by linearising the film forces derived from the Reynolds' equation for thin films applying full-film boundary condition [20]. Some details of the derivation are given in Appendix A. Since the gravity load is negligible compared to the dynamic loads from the bearing in a turbocharger, the steady-state eccentricity of the journal is assumed to be negligible leading to equal coefficients along r_1 and s_1 directions giving [3],

$$a_{rs} = a_{sr} = a_c = \overline{A}\omega , \tag{2.3}$$

$$b_{rr} = b_{ss} = b_d = 2\overline{A} , \tag{2.4}$$

where $(\cdot)_d$ denotes direct and $(\cdot)_c$ denotes cross-coupled; $\overline{A} = \pi\eta_B L_B{}^3 R_B / (2C^3)$ in which η_B is the viscosity of the bearing oil, L_B is the bearing length, R_B is the radius of the bearing, C is the clearance between the journal and the fixed housing. Eqs. (2.1) and (2.2) can be now be simplified as:

$$\mathbf{f} = b_d\dot{\mathbf{r}}_1 + a_c\boldsymbol{\Gamma}\mathbf{r}_1 , \tag{2.5}$$

where $\mathbf{r}_1 = [r_1, s_1]^T, \mathbf{f} = [F_r, F_s]^T$; $\mathbf{\Gamma} = \begin{bmatrix} 0 & 1 \\ -1 & 0 \end{bmatrix}$ is a cross coupling factor that couples the two equations in Eq. (2.5), giving $\mathbf{\Gamma}\mathbf{r}_1 = [s_1, -r_1]^T$ which will be applied for cross coupling hereafter. Using Newton's second law of motion, the equations of motion of the turbocharger with a symmetric rigid rotor of mass $2m$ mounted in two identical plain journal bearings as shown in Figure 2.1(b) is given by:

$$m\ddot{\mathbf{r}}_1 + \mathbf{f} = 0\,. \tag{2.6}$$

Assuming solutions, $r_1 = R_1 e^{\lambda t}$ and $s_1 = S_1 e^{\lambda t}$ to Eq. (2.6) and using the non-dimensional groups $\omega_1 = 2\overline{A}/m$ and $\hat{s} = \lambda/\omega_1$, Eq. (2.6) becomes

$$\begin{bmatrix} \hat{s}^2 + \hat{s} & \hat{\omega}/2 \\ -\hat{\omega}/2 & \hat{s}^2 + \hat{s} \end{bmatrix} \begin{Bmatrix} R_1 \\ S_1 \end{Bmatrix} = 0\,, \tag{2.7}$$

where $\hat{\omega} = \omega/\omega_1$ in which ω_1 is a characteristic frequency of the turbocharger with rigid support, at which the inertial force is approximately equal to the damping force. Using the complex form of the co-ordinates $r_1 + js_1$, Eq. (2.7) gives the characteristic equation,

$$\hat{s}^2 + \hat{s} - j\left(\hat{\omega}/2\right) = 0\,, \tag{2.8}$$

which is a quadratic Eq. with three forces: $\hat{s}^2$ - inertial force, $\hat{s}$ - damping force and $-j\left(\hat{\omega}/2\right)$ - cross-coupled stiffness force. The two roots of Eq. (2.8) are,

$$\hat{s}_{1,2} = \frac{-1 \pm \sqrt{1 + j2\hat{\omega}}}{2}\,. \tag{2.9}$$

The root with a positive real part is unstable, signifying the growth of the whirl amplitude while that with a negative real part is stable indicating the decay of the whirl amplitude. The imaginary part of the roots gives the corresponding whirl frequencies. Figure 2.2 shows the real parts plotted against the rotational speed ($\hat{\omega}$) of the turbocharger, where $\hat{s}_1$ is a stable root and $\hat{s}_2$ is an unstable root. For low speeds, when $\hat{\omega} << 1$ i.e. $\omega << \omega_1$,

$$\hat{s}_1 \approx -1-\left(j\hat{\omega}/2\right), \tag{2.10}$$

$$\hat{s}_2 \approx j\hat{\omega}/2, \tag{2.11}$$

where $\hat{s}_1$ is a stable root with negative real part and $\hat{s}_2$ is purely imaginary (on the verge of instability). For high speeds, when $\hat{\omega} >> 1$ i.e. $\omega >> \omega_1$,

$$\hat{s}_1 \approx \left(-1-\sqrt{\hat{\omega}}-j\sqrt{\hat{\omega}}\right)\Big/2, \tag{2.12}$$

$$\hat{s}_2 \approx \sqrt{\hat{\omega}}+j\sqrt{\hat{\omega}}/2. \tag{2.13}$$

Equation (2.11) suggests that the whirl frequency is $\hat{\omega}/2$ or of order 0.5 at low speeds, and at high speeds, the whirl frequency is given by Eq. (2.13), i.e., $\sqrt{\hat{\omega}}/2$, which is less than 0.5. Figure 2.3 shows the plot of the whirl frequency of the unstable root. Figure 2.4 shows a waterfall plot from a commercial turbocharger with press-fit bearings, exhibiting a sub-synchronous vibration of order 0.5 for a much greater speed range. The response departs relatively slowly from 0.5 as speed increases. This behaviour also occurs in a press-fit bearing with relatively high housing stiffness, since they would behave like plain journal bearings until the oil-film forces become sufficiently high for the housing stiffness to affect the dynamic behaviour. These are discussed in the following Sub-Section.

2.2.3 FLEXIBLE SUPPORT (PRESS-FIT BEARINGS)

This Sub-Section presents the analysis of the turbocharger with its rotor mounted in bearings with flexible supports. Figure 2.5 shows a schematic diagram of a turbocharger, assuming the support flexibility due to the interference of the bearing and the housing acts as a spring in series with the oil-film. The stiffness of the flexible support is denoted by k. Figure 2.6 shows the co-ordinate system with film forces - F_r, F_s and the constraint forces at the interference - R_r , R_s. The fluid-film forces in each bearing are given by [3]:

$$\mathbf{f} = b_d\left(\dot{\mathbf{r}}_1 - \dot{\mathbf{r}}\right) + a_c\boldsymbol{\Gamma}\left(\mathbf{r}_1 \text{-} \mathbf{r}\right), \tag{2.14}$$

where $\mathbf{r} = [r, s]^T$; r, s are the co-ordinates of the bearing centre with reference to the housing centre O. Coefficients, a_c, b_d are given by Eqs. (2.3) and (2.4). The oil-film forces are transmitted to the housing through the interference fit, that is the spring that connects the bearing and the housing. Hence the constraint forces (reactions) at the interface are given by [3]:

$$\mathbf{f} = \hat{\mathbf{r}} = k\mathbf{r}, \tag{2.15}$$

where $\hat{\mathbf{r}} = \left[R_r, R_s\right]^T$, $k = \omega_r{}^2 m$, ω_r being the frequency of mass m vibrating on the spring (interference fit) of stiffness k. The resulting equation is,

$$m\ddot{\mathbf{r}}_1 + \omega_r{}^2 m\mathbf{r} = 0. \tag{2.16}$$

Assuming solutions of the form, $r = Re^{\hat{s}t}$ for all the responses r, s, r_1, s_1 and combining Eq. (2.16) with Eq. (2.6), the equation of transverse motion of a rigid rotor in press-fit bearings is given by

$$\begin{bmatrix} -\hat{s} & -\hat{\omega}/2 & \hat{s}^2 + \hat{s} & \hat{\omega}/2 \\ \hat{\omega}/2 & -\hat{s} & -\hat{\omega}/2 & \hat{s}^2 + \hat{s} \\ \kappa^2 & 0 & \hat{s}^2 & 0 \\ 0 & \kappa^2 & 0 & \hat{s}^2 \end{bmatrix} \begin{Bmatrix} R \\ S \\ R_1 \\ S_1 \end{Bmatrix} = 0, \tag{2.17}$$

where $\kappa = \omega_r/\omega_1$. Co-ordinates r, s and r_1, s_1 can be related respectively from the 3rd and 4th rows in Eq. (2.17) condensing it into a 2×2 matrix,

$$\begin{bmatrix} \left(\hat{s}^3/\kappa^2\right)+\hat{s}^2+\hat{s} & \hat{\omega}/2\left[1+\hat{s}^2/\kappa^2\right] \\ -\hat{\omega}/2\left[1+\hat{s}^2/\kappa^2\right] & \left(\hat{s}^3/\kappa^2\right)+\hat{s}^2+\hat{s} \end{bmatrix} \begin{Bmatrix} R_1 \\ S_1 \end{Bmatrix} = 0\,, \tag{2.18}$$

which, by using the complex form of the co-ordinates $r_1 + js_1$, gives the characteristic equation,

$$\left(1/\kappa^2\right)\hat{s}^3 + \left[1 - j\left(\hat{\omega}/2\kappa^2\right)\right]\hat{s}^2 + \hat{s} - j(\hat{\omega}/2) = 0\,. \tag{2.19}$$

The cubic Eq. (2.19) has a third root when compared to that of the turbocharger with a rigid support due to the support stiffness k. There are two stable roots and, one unstable root. Figure 2.7 shows the plot of the imaginary part of the unstable root for $\kappa = 0.5$, 1. At low speeds, the slope of the curve is of the order 0.5 indicating oil-whirl of frequency equivalent to half-rotational speed. As speed increases, the curve asymptotes to a frequency ratio of $\kappa\,(= \omega_r/\omega_1)$, indicating the effectiveness of constant support stiffness. For very high κ, i.e. $\kappa >> 1$, the curve behaves like that of a rigid support as shown in Figure 2.3, since the condition suggests a very high support stiffness. Figure 2.8 gives an interesting overall picture of all the roots of the equations of motion in the complex plane for the turbocharger with press-fit bearings. The unstable root starts from zero speed. After a certain speed, the real part reduces while the imaginary part remains constant. The physical reasoning for this behaviour could be the following:

At low speeds, since the oil-film stiffness is relatively low, most of the vibration is that of the rotor in its bearings. As the oil-film forces are functions of speed, the whirl frequency keeps increasing. But, for higher speeds, as the bearing becomes relatively rigid, the support stiffness influences the natural frequency. Hence, it remains constant for very low κ, for example, 0.1. Interestingly, the stable roots start from the natural frequency of the rotor mass interacting with the support flexibility, as the cross-coupled stiffness is zero at zero speed. Figure 2.9 shows the plot of the real and the imaginary parts of the three roots showing the growth/decay rate of the sub-synchronous whirl amplitude and the whirl frequency respectively, when $\kappa = 1$. As in the case of the bearing with rigid support, the stable root (A) moves towards the negative real axis indicating an increase in damping and by the effect of support stiffness, asymptotes to a constant frequency at higher speeds. The second stable root (B), which is mostly from the support stiffness, has a constant imaginary part (frequency), that increases for higher κ, i.e. $\omega_r \geq \omega_1$ as shown in Figure 2.9. The real part approaches zero with increasing speed implying negligible damping.

Although press-fit bearings are one of the types of fluid-film bearings in use, most commercial automotive turbochargers use floating ring bearings, which is investigated in the following Sub-Section.

2.2.4 DAMPER SUPPORT (FLOATING RING BEARINGS)

This Sub-Section presents the analysis of the turbocharger with externally damped bearings. Figure 2.10 shows a schematic diagram of a turbocharger with floating ring bearings. The floating ring bearing configuration differs from the press-fit bearing in the way in which the bearing is constrained. The former is backed by an external damper of damping coefficient γ which represents the outer film while the latter has a flexible support representing the interference fit between the ring and the housing. Considering only the squeezing action of the outer film, assuming that the ring that separates the inner film and the outer film is fixed, the floating ring bearing is represented as an external damper in series with the inner film which is a journal bearing. This suggests that the equations of motion will only differ in terms of the constraint forces which are given by [3, 54]:

$$\hat{\mathbf{r}} = \gamma \dot{\mathbf{r}} . \tag{2.20}$$

A similar treatment given in the case of the press-fit bearings discussed in Section 2.2.3, gives the matrix equation of the turbocharger with a damper support as:

$$\begin{bmatrix} \hat{s}^2\left(1+\frac{2}{\hat{\gamma}}\right)+\hat{s} & \hat{\omega}\left(\frac{1}{2}+\frac{\hat{s}}{\hat{\gamma}}\right) \\ -\hat{\omega}\left(\frac{1}{2}+\frac{\hat{s}}{\hat{\gamma}}\right) & \hat{s}^2\left(1+\frac{2}{\hat{\gamma}}\right)+\hat{s} \end{bmatrix}\begin{Bmatrix} r_1 \\ s_1 \end{Bmatrix}=0, \tag{2.21}$$

where $\hat{\gamma}=\gamma/\overline{A}$. Using the complex form of the co-ordinate r_1+js_1, Eq. (2.21) gives the characteristic equation:

$$\left(1+\frac{2}{\hat{\gamma}}\right)\hat{s}^2+\left(1-\frac{j\hat{\omega}}{\hat{\gamma}}\right)\hat{s}-\frac{j\hat{\omega}}{2}=0, \tag{2.22}$$

which has roots,

$$\hat{s}_{1,2}=-\left[\left(1-j\frac{\hat{\omega}}{\hat{\gamma}}\right)\pm\sqrt{1-\frac{\hat{\omega}^2}{\hat{\gamma}^2}+2j\hat{\omega}\left[1+\frac{1}{\hat{\gamma}}\right]}\right]\Bigg/\left[2\left(1+\frac{2}{\hat{\gamma}}\right)\right]. \tag{2.23}$$

Choosing a value of $\hat{\gamma}=\gamma/\overline{A}=10$ based on [3], Figure 2.11 shows the imaginary part of the unstable root plotted against the non-dimensional speed. Its order of 0.5 at low speeds indicates oil-whirl of frequency equivalent to half-rotational speed. At higher speeds, the order asymptotically approaches a value of about 0.08. From a physical viewpoint, the order of 0.5 would be expected at low speeds, where the oil-film forces are low in relation to the external damping force, and most of the vibration takes place between the rotor and the floating ring. For higher speeds, the oil-film forces become higher and the relatively lower external damping helps to influence the vibration frequency.

For low speeds, when $\hat{\omega}<<1$ i.e. $\omega<<\omega_1$, $\hat{s}_1\approx j\hat{\omega}/2$ is on the verge of instability. $\hat{s}_2\approx-1$ as $\hat{\omega}\to 0$ is a stable root. For sufficiently high speeds, when $\hat{\omega}>>1$ i.e. $\omega>>\omega_n$, $\hat{s}_1\approx j\hat{\omega}/(2+\hat{\gamma})$, where $\hat{s}_1$ is on the verge of instability with a frequency of sub-harmonic order of $1/(2+\hat{\gamma})$ and $\hat{s}_2\approx-1/2(1+2/\hat{\gamma})$ is a stable root. Thus, for $\hat{\gamma}=10$, it is 0.083. A typical waterfall plot from a turbocharger with floating ring bearings is shown in Figure 2.12, where $1/(2+\hat{\gamma}) \approx 0.1$, and so $\hat{\gamma} = \gamma/\bar{A} = \gamma/(b/2) = 8$. This gives $\gamma/b = 4$ i.e. the external damping is about four times the inner oil-film damping. As most of the relative vibration would take place between the ring and the housing at higher speeds, proportionately higher damping will be induced in the outer film. Hence a factor of four is not unreasonable.

However, the effect of an external damper on the sub-synchronous vibration of the turbocharger in floating ring bearings is unlikely to be significant. Figure 2.13 shows the real part of the roots plotted against their corresponding imaginary part. A corresponding plot for the rigid support is shown for comparison. The behaviour of the roots is very similar to that in the case of a rigid support. However, the stable root shows a considerable reduction in frequencies. When compared with that of the rigid support which is shown in dotted line, the plots show some difference at higher speeds, while they behave very much alike at lower speeds when the vibration is between the rotor and the ring. This suggests that the added damping in the outer film is unlikely to eliminate such sub-harmonic vibration.

2.2.5 CONCLUSIONS

A simple linear model was used to analyse the turbocharger with symmetric rotor-bearing system with full-film short-bearings. The system was analysed for three different bearing supports, such as rigid, flexible and damped supports.

The simple model gives results qualitatively consistent with observations of commercial turbocharger sub-synchronous unstable vibration. Added damping in the outer film is unlikely to be productive in controlling self-excited sub-synchronous vibration. However, altering the stiffness of the support as in the case of a press-fit bearing may be worthy of investigation.

2.3 EFFECT OF GYROSCOPIC ACTION

2.3.1 INTRODUCTION

This Section investigates the behaviour of a turbocharger considering the gyroscopic effect. Since the gyroscopic action introduces moments in the system, tilt motion is analysed similar to the transverse motion in the previous Section (2.2), for its effect on the stability of the conical whirl. Equation of tilt motion is derived for the turbocharger with rigid support. The effect of gyroscopic moments is investigated by comparing the results with a model of a turbocharger without such moments.

2.3.2 EQUATION OF TILT MOTION

2.3.2.1 WITHOUT THE GYROSCOPIC MOMENTS

The equation of tilt motion of the turbocharger with rigid support is derived in this Sub-Section without considering the gyroscopic moments. Figure 2.14 shows a schematic diagram of a turbocharger with symmetric rotor supported on two identical plain journal bearings for tilt motion; θ_1, ϕ_1 are the angular co-ordinates about s and r axes respectively and l is the distance between the bearings. For a rigid symmetric rotor with transverse moment of inertia I about its centre of gravity supported on rigidly housed uncavitated bearings, the equation of motion ignoring gyroscopic moments is given by:

$$I\ddot{\boldsymbol{\theta}} + \boldsymbol{\psi} = 0\,, \tag{2.24}$$

where $\boldsymbol{\theta} = \begin{bmatrix}\theta_1 & \phi_1\end{bmatrix}^T$, $\boldsymbol{\psi} = \begin{bmatrix}M_s & M_r\end{bmatrix}^T$, $M_r = -F_s l$ and $M_s = -F_r l$ are the moments about r and s axes respectively due to the oil-film forces F_r, F_s. For small displacements, the angular co-ordinates θ_1, ϕ_1 can be written in terms of the linear co-ordinates r, s as:

$$l\boldsymbol{\theta}/2 = \begin{bmatrix} -r_1 & -s_1 \end{bmatrix}^T . \tag{2.25}$$

Substituting for $F_{r,s}$ from Eqs. (2.1) and (2.2) in terms of r and s co-ordinates, and using the transformation in Eqs. (2.25) and their corresponding derivatives, Eqs. (2.24) becomes:

$$I\ddot{\boldsymbol{\theta}} + \bar{A}l^2\dot{\boldsymbol{\theta}} + \frac{\bar{A}l^2\omega}{2}\boldsymbol{\Gamma\theta} = 0 . \tag{2.26}$$

Assuming solutions, $\theta_1 = \Theta e^{\lambda t}$, $\phi_1 = \Phi e^{\lambda t}$ to Eq. (2.26) gives the equation of motion in matrix form as:

$$\begin{bmatrix} \bar{s}^2 + \bar{s} & \bar{\omega}/2 \\ -\bar{\omega}/2 & \bar{s}^2 + \bar{s} \end{bmatrix} \begin{Bmatrix} \theta_1 \\ \phi_1 \end{Bmatrix} = 0 , \tag{2.27}$$

where $\bar{s} = \lambda/\omega_k$; $\bar{\omega} = \omega/\omega_k$ is the non-dimensional speed, $\omega_k = \bar{A}l^2/I$ is a characteristic frequency of the turbocharger, when the inertial moment is almost equal to the damping moment. Note that this non-dimensional speed is different from $\hat{\omega}$ defined in the previous Section, since this one depends on ω_k which is a function of the moment of inertia and the distance between the bearing centres. Since the aim is to investigate the gyroscopic effect, the gyroscopic moments are included in the equation of motion in the following Sub-Section.

2.3.2.2 WITH THE GYROSCOPIC MOMENTS

When the spinning rotor tilts about one of the transverse axes, the rotor experiences a moment, which results in a gyroscopic moment about the other transverse axis. The effect of these moments about the two transverse axes shown in Figure 2.14 is included in the equation of tilt motion in this Sub-Section. Considering the gyroscopic moments, $J\omega\dot{\phi}_1, J\omega\dot{\theta}_1$ [66] where $J\omega$ is the angular moment of the rotor, J is the polar moment of inertia of the rotor as shown in Figure 2.14, the equation of tilt motion of the turbocharger with rigid support is given by:

$$I\ddot{\boldsymbol{\theta}} + \boldsymbol{\psi} + J\omega\,\boldsymbol{\Gamma}\dot{\boldsymbol{\theta}} = 0, \tag{2.28}$$

where the gyroscopic moment is present along with the other moments given in Eq. (2.24). A similar treatment described as in the case without the gyroscopic moments gives Eq. (2.28) in the form:

$$\begin{bmatrix} \bar{s}^2 + \bar{s} & \widehat{\omega}(1/2 + \beta\bar{s}) \\ -\widehat{\omega}(1/2 + \beta\bar{s}) & \bar{s}^2 + \bar{s} \end{bmatrix} \begin{Bmatrix} \theta_1 \\ \phi_1 \end{Bmatrix} = 0, \tag{2.29}$$

where $\beta = J/I$. β is the ratio of the polar to the transverse moment of inertia, which is referred as the *gyroscopic coefficient* hereafter. Applying Routh's stability criterion ($A_2 > \left(A_1A_4/A_3\right) + \left(A_3A_0/A_1\right)$) [20] to the characteristic equation,

$$\bar{s}^4 + 2\bar{s}^3 + (1 + \widehat{\omega}^2\beta^2)\bar{s}^2 + \widehat{\omega}^2\beta\bar{s} + \frac{\widehat{\omega}^2}{4} = 0, \tag{2.30}$$

where A_i is the coefficient of the term $\bar{s}^i$, gives the condition, that the *gyroscopic coefficient* β must be greater than $1/2$ for a stable conical whirl. This implies that the threshold value of β for the stability of the conical whirl is $1/2$. It is evident from Eq. (2.29) and the coefficients in Eqs. (2.3) and (2.4) that this ratio relates to the ratio of the cross-coupled stiffness coefficient to the damping coefficient of the bearing. This implies that the threshold value of the coefficient plays a significant role in the effect of the gyroscopic moments on the stability of the conical whirl mode of the rotor, which will be discussed in detail in Section 2.3.4.

2.3.3 ANALYSIS: TILT MOTION WITHOUT THE GYROSCOPIC EFFECT

This Sub-Section presents the analysis of the dynamic behaviour of the turbocharger rotor system with rigid support ignoring the gyroscopic effect, using the equation of motion derived in Section 2.3.2.1. Using the complex form $\theta_1 + j\phi_1$ of the angular co-ordinates, Eq. (2.27) becomes:

$$\bar{s}^2 + \bar{s} - j\left(\hat{\omega}/2\right) = 0, \tag{2.31}$$

which is a quadratic equation with three moments, $\bar{s}^2$- inertial moment, $\bar{s}$- damping moment and $-j\left(\hat{\omega}/2\right)$- cross-coupled stiffness moment. The roots of the characteristic equation are given by:

$$\bar{s}_{1,2} = \left(-1 \pm \sqrt{1 + j2\hat{\omega}}\right)\Big/2. \tag{2.32}$$

For low speeds, when $\hat{\omega} << 1$,

$$\bar{s}_1 \approx -1 - (j\hat{\omega}/2), \tag{2.33}$$

$$\bar{s}_2 \approx j\hat{\omega}/2, \tag{2.34}$$

where $\bar{s}_1$ is a stable root with a negative real part and $\bar{s}_2$ being purely imaginary is on the verge of instability. For high speeds, when $\hat{\omega} >> 1$,

$$\bar{s}_1 \approx \left(-1 - \sqrt{\hat{\omega}} - j\sqrt{\hat{\omega}}\right)\Big/2, \tag{2.35}$$

$$\bar{s}_2 \approx \left(\sqrt{\hat{\omega}} + j\sqrt{\hat{\omega}}\right)\Big/2, \tag{2.36}$$

where $\bar{s}_1$ is a stable root with negative real part and $\bar{s}_2$ is an unstable root with a positive real part. Substituting the unstable root $\bar{s}_2 \approx j\hat{\omega}/2$ into Eq. (2.31) for low speeds gives:

$$\underbrace{-\frac{\hat{\omega}^2}{4}}_{\text{inertial moment}} + \underbrace{\frac{j\hat{\omega}}{2}}_{\text{damping moment}} \underbrace{-\frac{j\hat{\omega}}{2}}_{\substack{\text{cross-coupled}\\ \text{stiffness moment}}} = 0\,. \tag{2.37}$$

The term $-\hat{\omega}^2/4$ is negligible, since $\hat{\omega} << 1$. Hence, in this speed range, the system is whirling at a frequency, where the damping moment and the cross-coupled stiffness moments balance each other. Similarly for the high speed range, substituting the unstable root $\bar{s}_2 \approx \dfrac{\sqrt{\hat{\omega}} + j\sqrt{\hat{\omega}}}{2}$ gives:

$$\underbrace{\frac{j\hat{\omega}}{2}}_{\text{inertia moment}} + \underbrace{\frac{\sqrt{\hat{\omega}}(1+j)}{2}}_{\text{damping moment}} \underbrace{-\frac{j\hat{\omega}}{2}}_{\substack{\text{cross-coupled}\\ \text{stiffness moment}}} = 0\,. \tag{2.38}$$

The damping moment $\sqrt{\hat{\omega}}(1+j)/2$ is small compared to the terms containing $\hat{\omega}$, since $\hat{\omega} >> 1$. Hence, in this speed range, the system is whirling at a frequency, where the inertia moment and the cross-coupled stiffness moments balance each other. Having examined the asymptotes, to help understand the overall behaviour of the moments over the speed range, the unstable root from Eq. (2.32) is substituted into Eq. (2.31) and the moments are plotted in the argand plane, in Figure 2.15. This shows that the damping moment has a positive real part, while the inertial moment has a negative real part. Similarly, moments related to the stable root, give damping with a negative real part and an inertial moment with a positive real part as shown in Figure 2.16. The cross-coupled stiffness moment is purely imaginary (negative) acting like a reference axis. This implies that the damping moment with a negative real part relates to the negative real part of the root of the equation indicating stable whirl.

2.3.4 ANALYSIS: TILT MOTION WITH THE GYROSCOPIC EFFECT

This Sub-Section presents the analysis of the equation of tilt motion derived in Section 2.3.2.2, considering the gyroscopic effect on the dynamic behaviour of the turbocharger with rigid support. From Eq. (2.29), the characteristic equation of tilt motion including gyroscopic moments is given by:

$$\bar{s}^2+\bar{s}-j\beta\hat{\omega}\bar{s}-j\frac{\hat{\omega}}{2}=0, \tag{2.39}$$

which has $-j\beta\hat{\omega}\bar{s}$ -gyroscopic moment in addition to the three moments in Eq. (2.31). The solution to the quadratic Eq. (2.39) is

$$\bar{s}_{1,2}=\frac{-1+j\beta\hat{\omega}\pm\sqrt{1-\beta^2\hat{\omega}^2+2j\hat{\omega}(1-\beta)}}{2}. \tag{2.40}$$

For low speeds, when $\hat{\omega}<<1$, $\bar{s}_1\approx-1+j\beta\hat{\omega}-\frac{j\hat{\omega}}{2}$ is a stable root and $\bar{s}_2\approx\frac{j\hat{\omega}}{2}$ is on the verge of instability (purely imaginary).

For high speeds, when $\hat{\omega}>>1$, $\bar{s}_1\approx\frac{-1}{2}$ is a purely real root and $\bar{s}_2\approx\frac{-1+j\beta\hat{\omega}+\sqrt{-\beta^2\hat{\omega}^2}}{2}\approx j\beta\hat{\omega}$ is on the verge of instability. Substituting the root $\bar{s}_2\approx\frac{j\hat{\omega}}{2}$ into Eq. (2.39) for low speeds gives:

$$\underbrace{-\frac{\hat{\omega}^2}{4}}_{\substack{\text{inertial}\\ \text{moment}}}+\underbrace{\frac{j\hat{\omega}}{2}}_{\substack{\text{damping}\\ \text{moment}}}+\underbrace{\frac{\beta\hat{\omega}^2}{2}}_{\substack{\text{gyroscopic}\\ \text{moment}}}\underbrace{-\frac{j\hat{\omega}}{2}}_{\substack{\text{cross-coupled}\\ \text{stiffness moment}}}=0. \tag{2.41}$$

Equation (2.41) shows that the damping moment and the cross-coupled moment balance each other, while the gyroscopic moment is trying to balance the inertial moment. For

$\beta = 1/2$, they are perfectly balanced. Now, substituting the root $\bar{s}_2 \approx j\beta\,\hat{\omega}$ into Eq. (2.39) for high speeds gives,

$$\underbrace{-\beta^2\hat{\omega}^2}_{\substack{\text{inertial}\\\text{moment}}} + \underbrace{j\beta\hat{\omega}}_{\substack{\text{damping}\\\text{moment}}} + \underbrace{\beta^2\hat{\omega}^2}_{\substack{\text{gyroscopic}\\\text{moment}}} \underbrace{-\frac{j\hat{\omega}}{2}}_{\substack{\text{cross-coupled}\\\text{stiffness moment}}} = 0, \tag{2.42}$$

where the inertial moment balances the cross-coupled stiffness moment, while the damping moment is counteracting the cross-coupled stiffness moment. Similar to the low speed range, here the damping moment perfectly balances the cross-coupled stiffness moment for $\beta = 1/2$. Now considering $\bar{s}_{1,2}$ from Eq. (2.40), it is clear that for $\beta = 1/2$, the roots factorise easily into:

$$\bar{s} = \frac{-1 + j\beta\hat{\omega} \pm \sqrt{\left(1 + j\beta\hat{\omega}\right)^2}}{2}, \tag{2.43}$$

giving $\bar{s}_1 = -1$, $\bar{s}_2 = j\hat{\omega}/2$ which are purely real and purely imaginary solutions. Thus $\beta = 1/2$ is the threshold value of the *gyroscopic coefficient* where the unstable root with positive real part becomes purely imaginary. Physically this means that the turbocharger is whirling in its perturbed position without any further growth of amplitude.

As in the case of tilt motion without the gyroscopic effect given in Section 2.3.3, plotting each of the moments in Eq. (2.39) for the unstable root in Eq. (2.40), Figure 2.17 shows that the damping moment has positive real part for $\beta = 0.1$. As β is increased to 0.25, Figure 2.18 shows that except for the cross-coupled stiffness moment, all the other moments are affected by the change, where the real part of the damping moment is reduced and its imaginary part increases. Added to that, the gyroscopic and inertial moments tend to become more real and less imaginary.

Figure 2.19 is the plot of the real and the imaginary parts of the moments from the unstable root of the equation of tilt motion, when $\beta = 1/2$. It shows an interesting balance between the moments where, the damping moment is purely imaginary like the cross-coupled moment and counteracts it. Likewise the gyroscopic moment is purely real counteracting the purely real inertial moment. From Eq. (2.42), it is evident that the gyroscopic term influences all the moments except the cross-coupled stiffness moment. This observation signifies the effect of gyroscopic moment in changing the direction of these moments with an increase in β, and thereby making the system damping effective to counteract the de-stabilising effect of cross-coupled stiffness. Figure 2.20 shows the plot of the real and imaginary parts of the moments from the unstable root of the equation of tilt motion of the turbocharger with rigid support with the gyroscopic effect, when $\beta = 0.75$. It can be seen in Figure 2.20 that the further increase in β to 0.75, makes the real part of the damping moment negative and stabilises the conical whirl. This finding agrees with that of Tondl [39], which states that the gyroscopic action reduces the amplitude of self-excited vibration and for a fairy large coefficient of the gyroscopic term, it may even suppress it completely. Other than the effect on the amplitude, gyroscopic moments have been shown in the literature to influence the direction of whirl which is discussed in the following Sub-Section.

2.3.5 GYROSCOPIC EFFECT ON WHIRL FREQUENCIES

Angantyr [41] and Li [40] reported in their studies that gyroscopic effect splits the natural frequencies into a forward and a backward whirl. A forward whirl occurs when the rotor whirls in the direction of spin and a backward whirl occurs if the whirl is opposite to the direction of spin. The gyroscopic moments increase the effective stiffness of the system for a forward whirl and hence increase the frequency. However, the effective stiffness of the system reduces for a backward whirl and hence the frequency reduces with speed [66, 67]. This Sub-Section presents the discussion of the gyroscopic effect on the variation of the stable and unstable sub-synchronous frequencies with increasing speed in the turbocharger under investigation.

Figure 2.21 shows the plot of the sub-synchronous conical whirl frequencies varying with the rotational speed of the turbocharger with rigid support, for various values of $1/2 \le \beta < 1$. The stabilised frequency keeps increasing with speed implying a forward whirl. But, the stable frequency increases upto certain speed and then starts decreasing with increasing speed implying a backward whirl. This behaviour can be verified from Eq. (2.40) by looking at the asymptotes of the stable root for low and high speeds which are $\overline{s}_{1L} \approx -1 + j\left(\beta\widehat{\omega} - \widehat{\omega}/2\right)$ and $\overline{s}_{1H} \approx -1/2 + j0$ respectively. This shows that the stable frequency increases with the speed at low speeds while it becomes zero at high speeds. This implies that the stable whirl changes direction at a certain speed depending on β. The split nature of the frequencies due to the gyroscopic moments is clearly observed when β =1, where, both the unstable and the stable frequencies are equal (both forward), till they split into a forward and a backward whirl at a certain speed. Substituting $\beta = 1$ in Eq. (2.40) and considering the asymptotes, gives the frequency $\widehat{\omega}/2$ for low speeds for both the modes. For high speeds, the stabilised frequency is $\widehat{\omega}$ and the stable frequency is 0 signifying forward and backward whirl modes respectively. Figure 2.22 shows a similar plot of the conical whirl frequencies for various values of $\beta \geq 1$. The two frequencies exhibit similar behaviour of a forward and a backward whirl for all the cases.

2.3.6 CONCLUSIONS

A simple linear model of a turbocharger with a rigid rotor mounted in rigidly supported short-bearings with full-film was analysed for the stability of the tilt motion of the rotor. The effect of the gyroscopic moment on the stability of the conical whirl was investigated.

The stability of the conical mode of a turbocharger with rigid support is controlled by the *gyroscopic coefficient* β, which is the ratio of the polar to the transverse moment of inertia of the rotor. The threshold value of the *gyroscopic coefficient* is $\beta = 1/2$ for the conical whirl stability, when the turbocharger is on the verge of instability. The conical whirl instability seems to be completely suppressed for $\beta > 1/2$. This threshold ratio relates to the ratio of cross-coupled stiffness to the damping coefficient of an uncavitated bearing. The gyroscopic moment increases the imaginary part of the damping moment and helps in balancing the cross-coupled stiffness moment. With an increase in β, the gyroscopic effect changes the relative direction of the inertial and damping moments, which helps in stabilising the conical whirl. The gyroscopic effect seems to change the direction of whirl corresponding to the conical whirl frequencies; the unstable frequency increases with the speed exhibiting a forward whirl albeit becoming stable for $\beta > 1/2$ and the stable frequency decreases with the increasing speed exhibiting a backward whirl.

The threshold value of the *gyroscopic coefficient* has been evaluated considering a rigid support. In order to evaluate this value for the system with floating ring bearings, external dampers have to be included similar to Section 2.2.4. This is presented in the following Section.

2.4 INFLUENCE OF EXTERNAL DAMPING ON THE STABILISING GYROSCOPIC MOMENT

2.4.1 INTRODUCTION

It has been shown in Section 2.3 that the gyroscopic moment controls the stability of the conical whirl for the turbocharger with rigid support. From the ratio of the polar and the transverse moment of inertia of the rotor, the g*yroscopic coefficient* β has been determined as the controlling parameter whose threshold value is found to be $1/2$. Since floating ring bearings are mostly used in turbochargers due to their low cost as discussed in Chapter 1, this Section analyses the influence of the outer film on the way in which the g*yroscopic coefficient* controls the stability. The outer film of the floating ring is treated as an external damper in series with the inner film which is the bearing, similar to Section 2.2.4.

2.4.2 EQUATIONS OF TILT MOTION WITH GYROSCOPIC MOMENT

Similar to the equations derived in Section 2.2.4, considering the fluid-film forces for the floating ring bearing from Eqs. (2.14), and including the gyroscopic moments similar to Section 2.3, applying a linear transformation as in Eqs. (2.25), the equations of tilt motion of the turbocharger with damper support, considering gyroscopic effect is given by:

$$I\frac{2\ddot{\mathbf{r}}_1}{l} + 2\bar{A}(\dot{\mathbf{r}}_1 - \dot{\mathbf{r}})l + \bar{A}\omega\mathbf{\Gamma}(\mathbf{r}_1 - \mathbf{r})l + J\omega\mathbf{\Gamma}\frac{2\dot{\mathbf{r}}_1}{l} = 0\,, \qquad (2.44)$$

$$\left[I\frac{2\ddot{\mathbf{r}}_1}{l^2} + J\omega\mathbf{\Gamma}\frac{2\dot{\mathbf{r}}_1}{l^2}\right] + \gamma\dot{\mathbf{r}} = 0\,. \qquad (2.45)$$

Applying a similar treatment to Eqs. (2.44) and (2.45) as described in the Section 2.3, the characteristic equation of the system is given by

$$\underbrace{\left(1+\frac{2}{\hat{\gamma}}\right)\bar{s}^2}_{\text{inertial moment}} + \underbrace{\left[1-j\frac{\widehat{\omega}}{\hat{\gamma}}\right]\bar{s}}_{\text{damping moment}} \underbrace{-\frac{\beta\widehat{\omega}^2}{\hat{\gamma}} - j\beta\widehat{\omega}\left(1+\frac{2}{\hat{\gamma}}\right)\bar{s}}_{\text{gyroscopic moment}} \underbrace{-j\frac{\widehat{\omega}}{2}}_{\text{cross-coupled moment}} = 0\,. \quad (2.46)$$

Setting $\beta = 0$, gives the characteristic equation without the gyroscopic moment as

$$\underbrace{\left(1+\frac{2}{\hat{\gamma}}\right)\bar{s}^2}_{\text{inertial moment}} + \underbrace{\left(1-j\frac{\widehat{\omega}}{\hat{\gamma}}\right)\bar{s}}_{\text{damping moment}} \underbrace{-j\frac{\widehat{\omega}}{2}}_{\text{cross-coupled moment}} = 0\,, \qquad (2.47)$$

with two roots $\bar{s}_{1,2} = \left[-\left(1-j\frac{\widehat{\omega}}{\hat{\gamma}}\right) \pm \sqrt{1-\frac{\widehat{\omega}^2}{\hat{\gamma}^2}+2j\widehat{\omega}\left[1+\frac{1}{\hat{\gamma}}\right]}\right]\Big/ 2\left(1+\frac{2}{\hat{\gamma}}\right)$, where $\bar{s}_1$ is an unstable root and $\bar{s}_2$ is a stable root. Figure 2.23 shows the plot of the real part of these roots against the rotor speed, for $\hat{\gamma} = 10$. Figure 2.24 shows the plot of the moments in Eq. (2.47) related to the unstable root, for $\hat{\gamma} = 10$. Plots of the moments corresponding to the rigid support discussed in Section 2.2.4, are given for comparison. The real part of the damping moment increases due to the external damping, which reduces its effect in balancing the destabilising cross-coupled stiffness moment relative to the rigid support.

Now, considering the gyroscopic effect, Eq. of tilt motion (2.46) has an unstable root $\bar{s}_1$ and a stable root $\bar{s}_2$ which are:

$$\bar{s}_{1,2} = \frac{-\left[1-j\left[\frac{\hat{\omega}}{\hat{\gamma}}+\beta\hat{\omega}\left(1+\frac{2}{\hat{\gamma}}\right)\right]\right] \pm \sqrt{\left[1-j\left[\frac{\hat{\omega}}{\hat{\gamma}}+\beta\hat{\omega}\left(1+\frac{2}{\hat{\gamma}}\right)\right]\right]^2 + 2\hat{\omega}\left(1+\frac{2}{\hat{\gamma}}\right)\left(\frac{\beta\hat{\omega}}{\hat{\gamma}}+j\right)}}{2\left(1+\frac{2}{\hat{\gamma}}\right)} \tag{2.48}$$

Unlike the case of the rigid support, where the gyroscopic moment is damping-like, with damper support, the gyroscopic moment of the rotor also has a stiffness-like term, $\beta\hat{\omega}^2/\hat{\gamma}$. Figure 2.25 shows the plot of the real and the imaginary parts of the moments for $\beta = 0.25$. The stiffness-like term in combination with the damping moment seem to offer a restoring moment in the system, whose physical significance needs further investigation. Increasing β to 0.5 shows a perfect balance in the moments similar to turbocharger with the rigid support as shown in Figure 2.26, when the cross-coupled stiffness moment is balanced by the restoring moment, i.e. the damping moment + the stiffness-like gyroscopic moment. The inertial moment is balanced by the damping-like gyroscopic moment. In this case, the restoring moment is purely real. Further increase of β continues to change the relative direction of the moments as shown in Figure 2.27, keeping the real part of the restoring moment negative, giving a stable whirl. The real parts of the unstable root for three different values of β as a function of speed are shown in Figure 2.28, which verifies the threshold value of the *gyroscopic coefficient*, $\beta = 1/2$, for the stability of the conical whirl. The threshold value remains unaltered by the presence of an external damper.

Figure 2.29 and Figure 2.30 show the plots of the conical whirl frequencies varying with the speed for $\beta < 1$ and $\beta > 1$ respectively. For the low speed range, the unstable and the stable conical whirl frequencies exhibit very similar behaviour of the split into forward and backward whirl motions as with the rigid support shown in Figure 2.21 and Figure 2.22, However for high speeds, the stable conical whirl becomes forward again by increasing with speed due to the presence of the external damper. This could be due to the relatively higher damping of the external damper suppressing the gyroscopic effect, since most of the motion is between the ring and the damper as discussed in Section 2.2.4.

2.4.3 CONCLUSIONS

A turbocharger with a symmetric rigid rotor mounted in full-film bearings with externally damped support was analysed for the stability of the conical whirl i.e. the tilt motion of the rotor. The external dampers were used to simulate the outer-film of the floating ring bearings.

The external dampers are unlikely to improve the stability of the turbocharger. The threshold value of the *gyroscopic coefficient* $\beta = 1/2$, for a stable conical whirl, remains unaltered by the addition of an external damper to each of the journal bearings. The gyroscopic moment means a stiffness-like moment is added to the damping-like gyroscopic moment seen with the rigid support. The gyroscopic moment along with the damping moment counteracts the de-stabilising cross-coupled stiffness moment, effectively stabilising the conical whirl for $\beta > 1/2$. However, the physical significance of this combination needs further investigation. The gyroscopic moments produces similar behaviour of a forward and a backward whirl corresponding to the two frequencies as observed in the turbocharger with rigid support. But for high speeds, the addition of an external damper seems to change the backward whirl corresponding to the stable frequency a forward whirl again.

So far, the turbocharger rotor has been assumed to have a symmetric rotor. However, as discussed in Chapter 1, the turbine wheel is heavier than the compressor wheel. Hence, the rotor is asymmetric with respect to the centre of gravity. This is considered in the following Section.

2.5 ASYMMETRIC MODEL – TRANSVERSE AND TILT MOTION WITH THE GYROSCOPIC EFFECT

2.5.1 INTRODUCTION

In the previous Sections, a turbocharger with a symmetric rotor was analysed, considering the transverse and the tilt motion separately. However in practice, the turbine is much heavier than the compressor of a turbocharger. So the centre of gravity of the turbocharger is nearer to the turbine bearing centre. Hence, this Section investigates a turbocharger with an asymmetric rotor mounted in floating ring bearings under the influence of the gyroscopic moments. Both the transverse and the tilt motion are considered in this Section to analyse the conical and the in-phase whirl modes under the influence of the gyroscopic effect.

2.5.2 EQUATION OF MOTION

Figure 2.31 shows a schematic diagram of an asymmetric rotor of a turbocharger with floating ring bearings and the forces acting on the rotor due to both the transverse and the tilt motion discussed in previous Sections; l_a, l_b are the distances of the centre of gravity of the rotor from the turbine and the compressor bearing centres respectively. Assuming a rigid rotor of mass m_r mounted in two identical bearings with full-film, the equations of transverse motion of the turbocharger in the inner film of the bearing is given as [54]:

$$\mathbf{f_a} + \mathbf{f_b} = -m_r \ddot{\mathbf{r}}_{\mathbf{1c}}, \tag{2.49}$$

where $\mathbf{r_{1c}} = [r_{1c}, s_{1c}]^T$, r_{1c}, s_{1c} are the co-ordinates of the centre of gravity of the rotor. $\mathbf{f_a} = \left[F_{ra}, F_{sa}\right]^T$ are the film forces on the rotor in the turbine end bearing and $\mathbf{f_b} = \left[F_{rb}\ , F_{sb}\right]^T$ are the film forces in the compressor end bearing. Using the film forces for the bearings with the damper support given in Eq. (2.14), the forces in the bearings are given by:

$$\mathbf{f_a} = 2\bar{A}(\dot{\mathbf{r}}_{\mathbf{1a}} - \dot{\mathbf{r}}_{\mathbf{a}}) + \bar{A}\omega\mathbf{\Gamma}(\mathbf{r_{1a}} - \mathbf{r_a}), \tag{2.50}$$

$$\mathbf{f_b} = 2\bar{A}(\dot{\mathbf{r}}_{\mathbf{1b}} - \dot{\mathbf{r}}_{\mathbf{b}}) + \bar{A}\omega\mathbf{\Gamma}(\mathbf{r_{1b}} - \mathbf{r_b}), \tag{2.51}$$

where $\mathbf{r}_j = [r_j\ , s_j]^T$, $j = a,\ b,\ 1a,\ 1b$; $\mathbf{r_{a\ ,\ b}}$ are the co-ordinates of the ring centre $\mathrm{C_B}$ in the turbine and compressor end bearings; $\mathbf{r_{1\ a\ ,\ 1\ b}}$ are the corresponding co-ordinates of the journal dynamic centre $\mathrm{C_D}$. The equations of tilt motion with the gyroscopic effect as seen in Figure 2.31 are given by:

$$\mathbf{f_b}^T\mathbf{L_{ab}} - \mathbf{f_a}^T\mathbf{L_{ab}} + J\omega\mathbf{\Gamma}\dot{\boldsymbol{\theta}} = -I\ddot{\boldsymbol{\theta}}, \tag{2.52}$$

where $\mathbf{L_{ab}} = \begin{bmatrix} l_b & 0 \\ 0 & l_a \end{bmatrix}$, l_a and l_b are the distances of the rotor centre of gravity from the turbine bearing centre and compressor bearing centre respectively as shown in Figure 2.31; θ_1, ϕ_1 are the angular displacements of the rotor about s_{1c}, r_{1c} respectively. From the slope of the rotor, the linear co-ordinate transformation can be done through:

$$\mathbf{r_{1c}} = \mathbf{r_{1b}} + \frac{\mathbf{L_{ab}}}{l}\left(\mathbf{r_{1a}} - \mathbf{r_{1b}}\right), \tag{2.53}$$

$$\boldsymbol{\theta} = \frac{\left(\mathbf{r_{1b}} - \mathbf{r_{1a}}\right)}{l}, \tag{2.54}$$

where the derivatives of $\boldsymbol{\theta}$ are given by the corresponding derivatives of the right hand side of Eq. (2.54). Substituting for the forces from Eqs. (2.50) and (2.51), and using the transformation in Eqs. (2.53) and (2.54), the equations of motion are given by :

$$\begin{aligned} m_r\left[\ddot{\mathbf{r}}_{\mathbf{1b}}\left(1-\frac{l_b}{l}\right)+\ddot{\mathbf{r}}_{\mathbf{1a}}\frac{l_b}{l}\right] &+ 2\bar{A}(\dot{\mathbf{r}}_{\mathbf{1a}} - \dot{\mathbf{r}}_{\mathbf{a}}) + \bar{A}\omega\mathbf{\Gamma}(\mathbf{r_{1a}} - \mathbf{r_a}) \\ &+ 2\bar{A}(\dot{\mathbf{r}}_{\mathbf{1b}} - \dot{\mathbf{r}}_{\mathbf{b}}) + \bar{A}\omega\mathbf{\Gamma}(\mathbf{r_{1b}} - \mathbf{r_b}) = 0 \end{aligned}, \tag{2.55}$$

$$\begin{aligned} I\left(\frac{\ddot{\mathbf{r}}_{\mathbf{1b}} - \ddot{\mathbf{r}}_{\mathbf{1a}}}{l}\right) &+ l_b[2\bar{A}(\dot{\mathbf{r}}_{\mathbf{1b}} - \dot{\mathbf{r}}_{\mathbf{b}}) + \bar{A}\omega\mathbf{\Gamma}(\mathbf{r_{1b}} - \mathbf{r_b})] \\ &- l_a[2\bar{A}(\dot{\mathbf{r}}_{\mathbf{1a}} - \dot{\mathbf{r}}_{\mathbf{a}}) + \bar{A}\omega\mathbf{\Gamma}(\mathbf{r_{1a}} - \mathbf{r_a})] + \frac{J\omega}{l}\mathbf{\Gamma}\left(\dot{\mathbf{r}}_{\mathbf{1b}} - \dot{\mathbf{r}}_{\mathbf{1a}}\right) = 0 \end{aligned}. \tag{2.56}$$

Applying Eq. (2.15), at the interface between the ring and the external damper (outer film) and substituting for the forces from Eqs. (2.50), (2.51), the equations of motion in the outer film are given by

$$\gamma\dot{\mathbf{r}}_{\mathbf{a}} - 2\bar{A}(\dot{\mathbf{r}}_{\mathbf{1a}} - \dot{\mathbf{r}}_{\mathbf{a}}) - \bar{A}\omega\mathbf{\Gamma}(\mathbf{r_{1a}} - \mathbf{r_a}) = 0, \tag{2.57}$$

$$\gamma\dot{\mathbf{r}}_{\mathbf{b}} - 2\bar{A}(\dot{\mathbf{r}}_{\mathbf{1b}} - \dot{\mathbf{r}}_{\mathbf{b}}) - \bar{A}\omega\mathbf{\Gamma}(\mathbf{r_{1b}} - \mathbf{r_b}) = 0. \tag{2.58}$$

Combining Eqs. of motion (2.55) through (2.58) and assuming solutions of the form $r = Re^{\lambda t}$, gives the matrix form in terms of non-dimensional groups as:

$$\begin{bmatrix} \frac{\hat{\gamma}}{2}\tilde{s}+\tilde{s} & \hat{\omega} & 0 & 0 & -\tilde{s} & -\hat{\omega} & 0 & 0 \\ -\hat{\omega} & \frac{\hat{\gamma}}{2}\tilde{s}+\tilde{s} & 0 & 0 & \hat{\omega} & -\tilde{s} & 0 & 0 \\ 0 & 0 & \frac{\hat{\gamma}}{2}\tilde{s}+\tilde{s} & \hat{\omega} & 0 & 0 & -\tilde{s} & -\hat{\omega} \\ 0 & 0 & -\hat{\omega} & \frac{\hat{\gamma}}{2}\tilde{s}+\tilde{s} & 0 & 0 & \hat{\omega} & -\tilde{s} \\ -\tilde{s} & -\hat{\omega} & -\tilde{s} & -\hat{\omega} & \tilde{s}+\left(\tilde{s}^2 L_b/2\right) & \hat{\omega} & \tilde{s}+\left(\tilde{s}^2\left(1-L_b\right)/2\right) & \hat{\omega} \\ \hat{\omega} & -\tilde{s} & \hat{\omega} & -\tilde{s} & -\hat{\omega} & \tilde{s}+\left(\tilde{s}^2 L_b/2\right) & -\hat{\omega} & \tilde{s}+\left(\tilde{s}^2\left(1-L_b\right)/2\right) \\ 2L_a\tilde{s} & 2\hat{\omega}L_a & -2L_b\tilde{s} & -2\hat{\omega}L_b & -2L_a\tilde{s}-\hat{\alpha}\tilde{s}^2 & \left(-2\hat{\omega}L_a-\hat{B}\right) & 2L_b\tilde{s}+\hat{\alpha}\tilde{s}^2 & \left(2\hat{\omega}L_b+\hat{B}\right) \\ -2\hat{\omega}L_a & 2L_a\tilde{s} & 2\hat{\omega}L_b & -2L_b\tilde{s} & \left(2\hat{\omega}L_a+\hat{B}\right) & -2L_a\tilde{s}-\hat{\alpha}\tilde{s}^2 & \left(-2\hat{\omega}L_b-\hat{B}\right) & \left(2L_b\tilde{s}+\hat{\alpha}\tilde{s}^2\right) \end{bmatrix} \begin{Bmatrix} R_a \\ S_a \\ R_b \\ S_b \\ R_{1a} \\ S_{1a} \\ R_{1b} \\ S_{1b} \end{Bmatrix} = 0, \tag{2.59}$$

where, $L_{a,b} = l_{a,b}/l$, $\hat{\alpha} = \omega_1/\omega_k$, $\tilde{s} = 2\lambda/\omega_1$, $\hat{B} = \beta 2\hat{\omega}\hat{\alpha}\tilde{s}$. Note that $m_r = 2m$, where m is the half-symmetrical rotor mass used for the symmetrical rotor in the preceding Sections.

The characteristic equation of motion (2.59) is an eighth order polynomial having 4 pairs of conjugate roots. Figure 2.32 shows the plot of the roots of the equation of motion given in Eq. (2.59), indicating the growth/decay of the whirl amplitude, as a function of the rotational speed. There are two unstable roots with positive real parts and two stable roots with negative real parts for $\beta = 0.25$ and $\hat{\alpha} = 2$ (for a typical turbocharger). Figure 2.33 shows their corresponding imaginary parts, i.e. the frequencies of the sub-synchronous whirl modes along side the synchronous line in comparison with that of the case without the gyroscopic effect ($\beta = 0$).

When $\beta = 0$, i.e. without considering the gyroscopic effect, Figure 2.34 shows the plot of the real parts of the unstable root. The real parts cross each other at a certain speed, indicating a switch in the dominant root [54]. Figure 2.35 shows the plots of their corresponding frequencies. This behaviour agrees with a typical waterfall diagram from a turbocharger shown in Figure 2.36, where the mode switches after a certain speed. The modeshape of mode-1 is shown in Figure 2.37. This is the low frequency conical whirl that is dominant in the low speeds. Figure 2.38 shows the modeshape of mode-2 which is the relatively high frequency in-phase whirl is dominant in the high speed range.

Figure 2.39 shows the plots of the real parts of the roots varying with the speed, considering the gyroscopic moment, when $\beta = 0.25$. Adding gyroscopic moment to the system, which increases β to 0.25, shows a reduction in the speed at which the modes switch as seen in Figure 2.39. This could be due to the reduction in the conical whirl frequencies due to the gyroscopic effect as given in Figure 2.33. Figure 2.40 shows the plot of the imaginary part of the roots varying with speed. The plot shows a purely imaginary root for the conical mode when $\beta = 1/2$ as observed with the turbocharger with a symmetric rotor. For $\beta > 0.5$, the system has a stable conical whirl.

2.5.3 CONCLUSIONS

A turbocharger with an asymmetric rotor model with full-film floating ring bearings was analysed for stability using linear analysis. The outer-film of the bearing was modelled as an external damper. Both the translation and the tilt motion of the rotor were considered to analysed the in-phase and the conical whirl respectively.

The turbocharger exhibits two unstable modes: a conical mode and an in-phase whirl mode. The conical mode is dominant in the low speed range, while the in-phase whirl mode is dominant in the high speed range. The gyroscopic moment reduces the speed at which the switch in mode occurs. Similar to the symmetric rotor, the conical whirl of the asymmetric rotor stabilises for $\beta \geq 1/2$. This suggests that the threshold value of the *gyroscopic coefficient* $\beta = 1/2$ for a stable conical whirl, remains unaffected by the asymmetry of the rotor.

2.6 SUMMARY AND CONCLUSIONS

A simple linear model of a turbocharger with a symmetric rigid rotor and two identical full-film journal bearings was analysed. The transverse motion of the rotor was reviewed, under the effect of various support conditions. The effect of gyroscopic moment was investigated for the tilt motion of the turbocharger, with rigid and damped support. An asymmetric model of the turbocharger was also analysed for the effect of gyroscopic moment for both the type of motions.

The conical whirl instability which is self-excited by a tilt motion of the turbocharger with rigid support is controlled by the *gyroscopic coefficient* β. This coefficient is given by the ratio of the polar to the transverse moment of inertia of the rotor. With an increase in β, the gyroscopic moment changes the relative direction of the inertial and damping moments, which helps in stabilising the conical whirl. The threshold value of β for a stable conical whirl is found to be $1/2$, when the turbocharger is on the verge of instability. The instability is completely suppressed for $\beta > 1/2$. The threshold ratio does not seem to be affected by adding an external damper to the bearing and the asymmetry of the rotor. A turbocharger exhibits the whirl instability in the form of a conical whirl and an in-phase whirl. The conical whirl is dominant in the low speed range, while the in-phase whirl is dominant in the high speed range. The gyroscopic moment seems to reduce the speed at which the switch in the dominant mode occurs. The gyroscopic effect changes the directions of the conical whirl, wherein, the rotor experiences a forward whirl with an unstable frequency, and a backward whirl with a stable frequency. This effect is unaffected by the change in the stability of the unstable conical whirl for $\beta > 1/2$. However, the presence of the external damper seems to change the backward whirl into a forward whirl at high speeds.

The gyroscopic effect being controlled by the tilt motion affects only the conical whirl. Hence it may be ignored for the nonlinear analysis of the in-phase whirl. However, the rigid assumption of the rotor needs an investigation before proceeding to the nonlinear analysis. Hence a flexible shaft is investigated in the following Chapter.

FIGURES

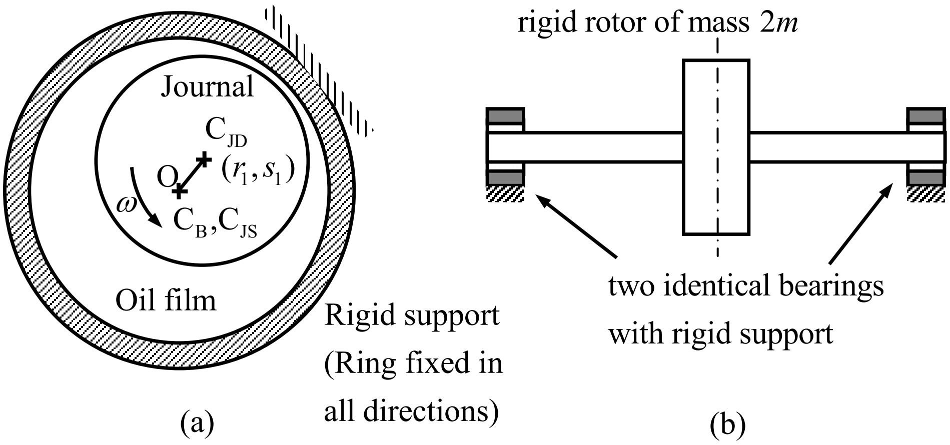

Figure 2.1 (a) Schematic diagram of a turbocharger with plain uncavitated journal bearings (equivalent to a system with floating ring bearing with the ring fixed in all directions) $\mathrm{C_B}$ is the bearing centre, $\mathrm{C_{JS}}$ is the static journal centre, $\mathrm{C_{JD}}$ is the dynamic journal centre and O is the centre of the stationary casing; r_1, s_1 are the co-ordinates of the journal centre (b) Schematic diagram of a symmetric rotor supported on two identical bearings with rigid support [54].

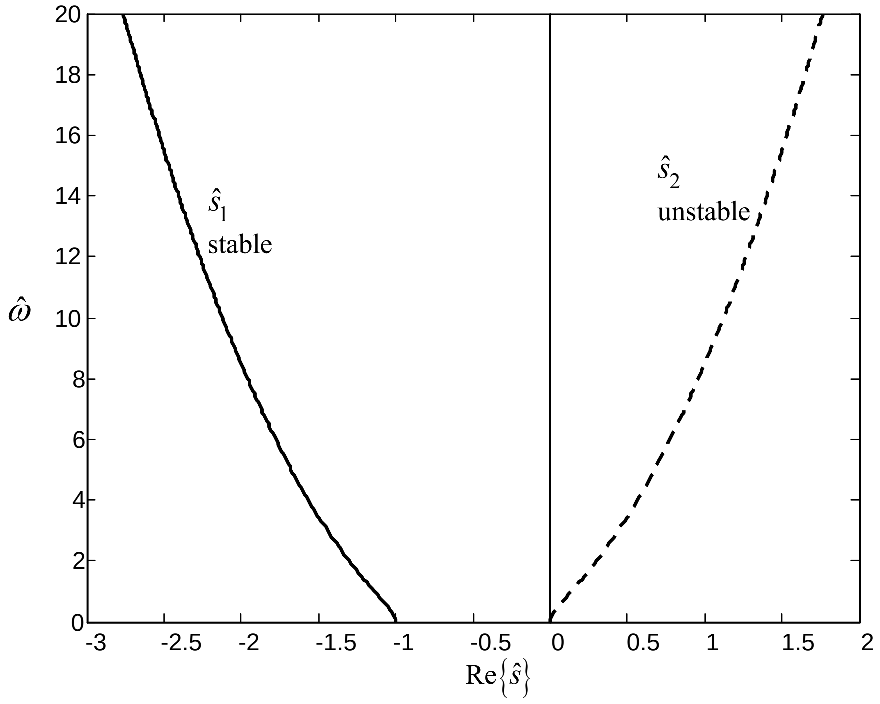

Figure 2.2 Plot of the real parts of the roots $\hat{s}$ showing the growth/decay rate of the sub-synchronous whirl amplitude against the rotational speed $\hat{\omega}$, for the transverse motion of the turbocharger with rigid support.

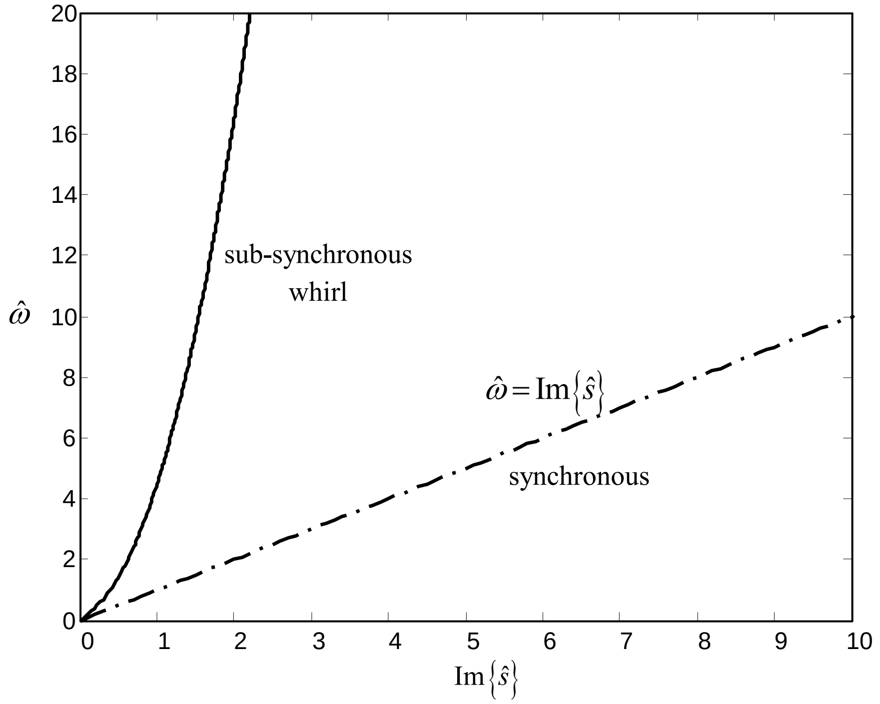

Figure 2.3 Plot of the sub-synchronous whirl frequency varying with the rotating speed of the turbocharger with rigid support, for the transverse motion. Synchronous frequency is shown for comparison as a function of speed.

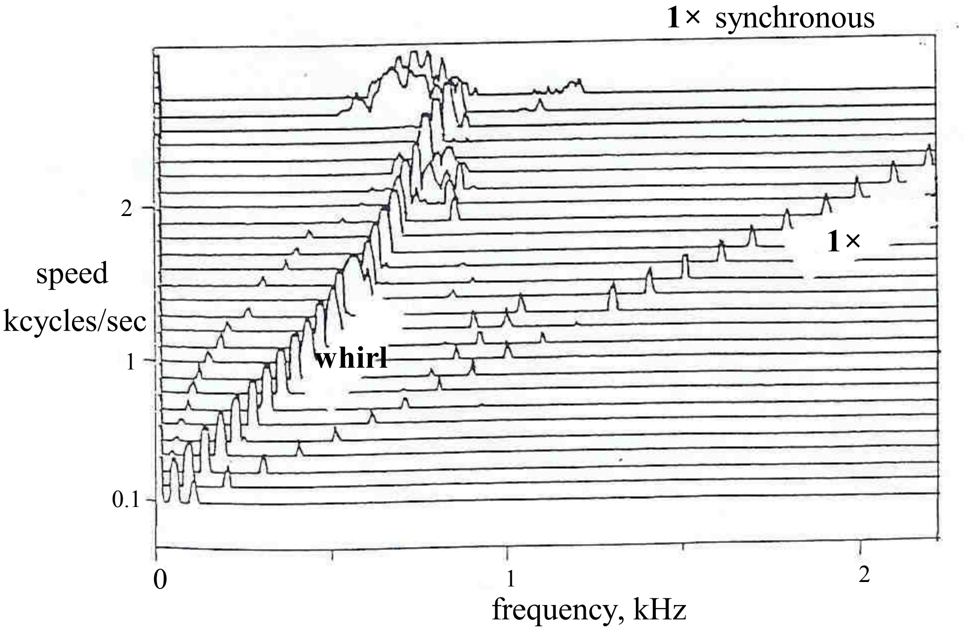

Figure 2.4 Waterfall diagram for a commercial turbocharger fitted with press-fit bearings; adapted from Holmes [3].

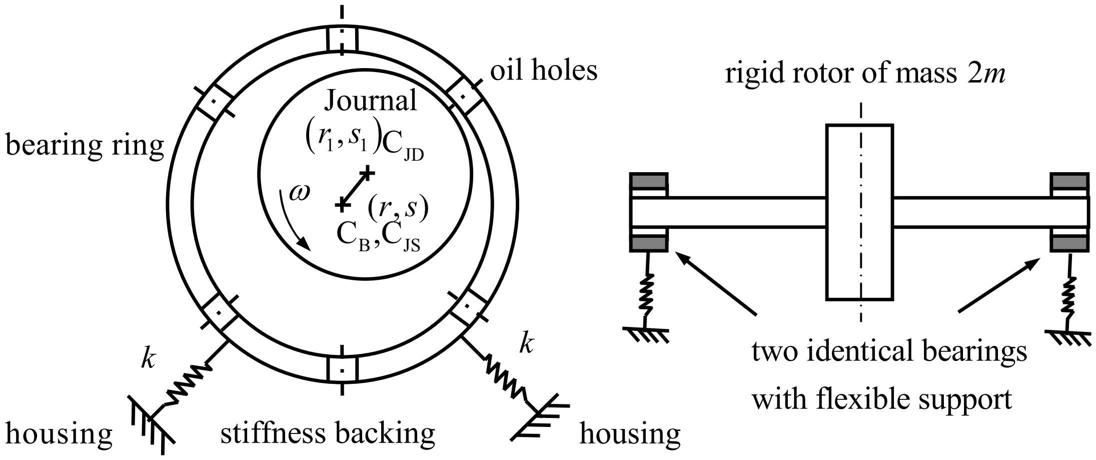

Figure 2.5 Schematic diagram of a turbocharger with press-fit bearings (flexible support). The interference fit between the ring and the housing of the bearings is treated as a spring giving flexible support to the bearing. C_B is the bearing centre, C_{JS} is the static journal centre, C_{JD} is the dynamic journal centre, k is the stiffness of the flexible support [54].

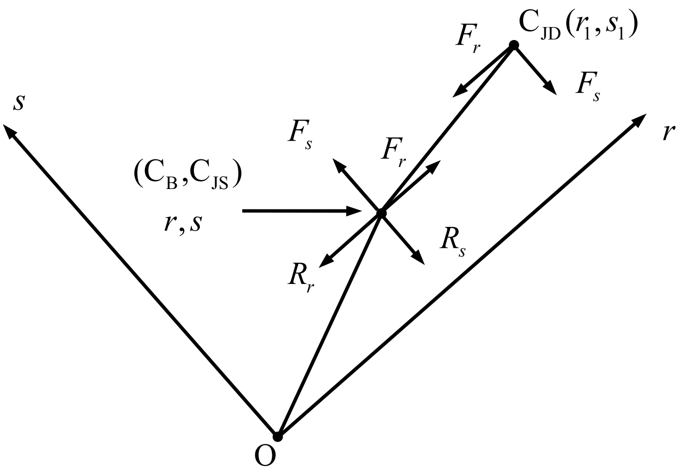

Figure 2.6 Co-ordinate system and dynamic forces in a symmetric rotor – uncavitated floating ring bearing system, C_B is the bearing centre, C_{JS} is the static journal centre, C_{JD} is the dynamic journal centre and O is the centre of the stationary casing.

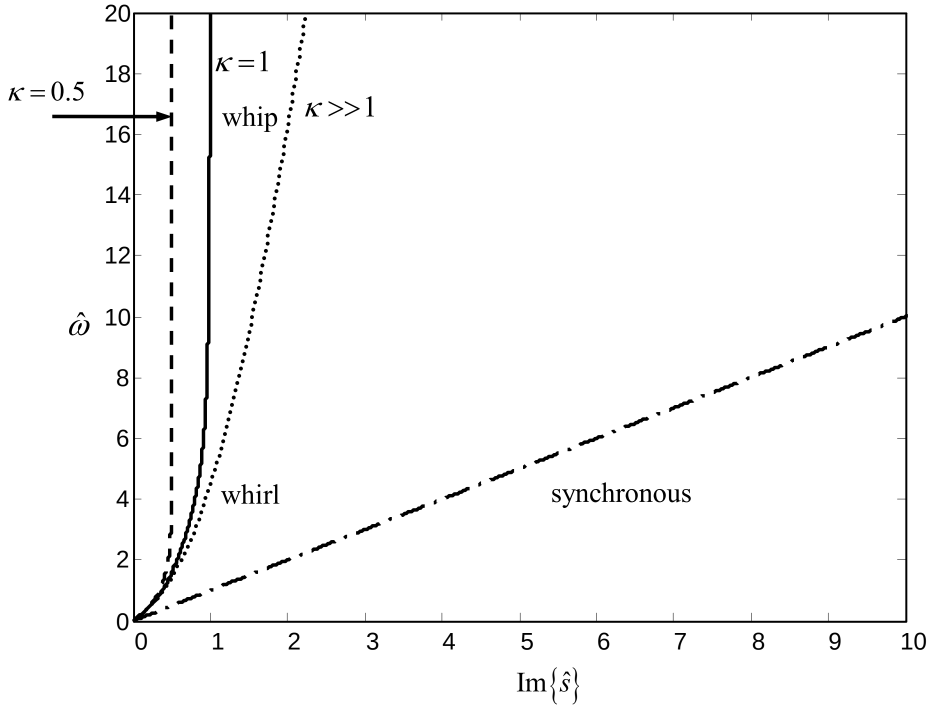

Figure 2.7 Plot of the sub-synchronous whirl frequency varying with the rotating speed of the turbocharger with flexible support; synchronous frequency is shown for comparison as a function of speed; κ is the non-dimensional stiffness coefficient of the support.

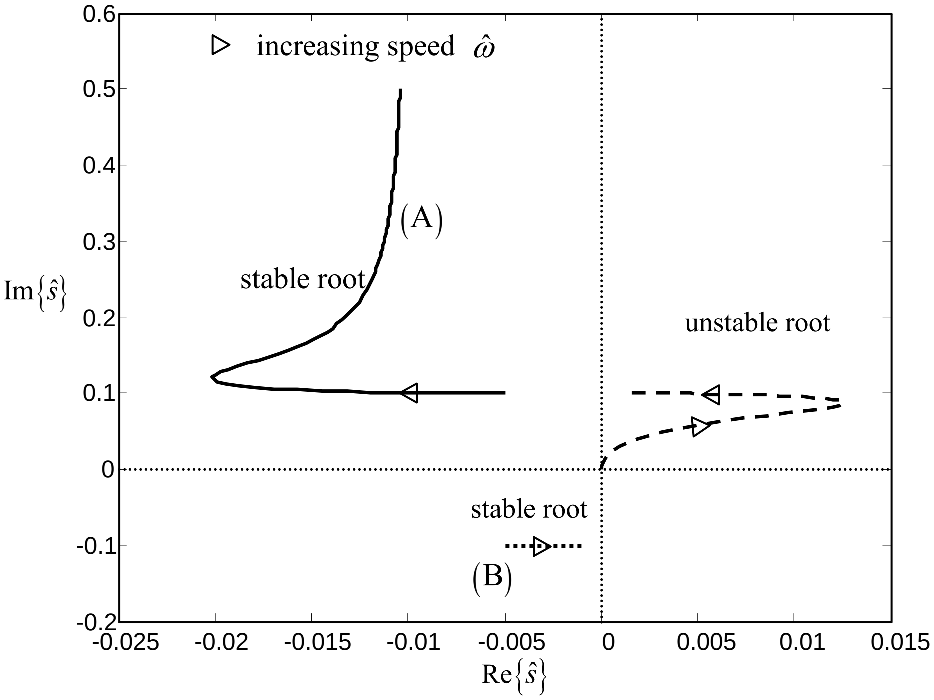

Figure 2.8 Plot of the real and the imaginary parts of the roots showing the growth/decay rate of the sub-synchronous whirl amplitude and the whirl frequency respectively, for the transverse motion of the turbocharger with flexible support, when $\kappa = 0.1$.

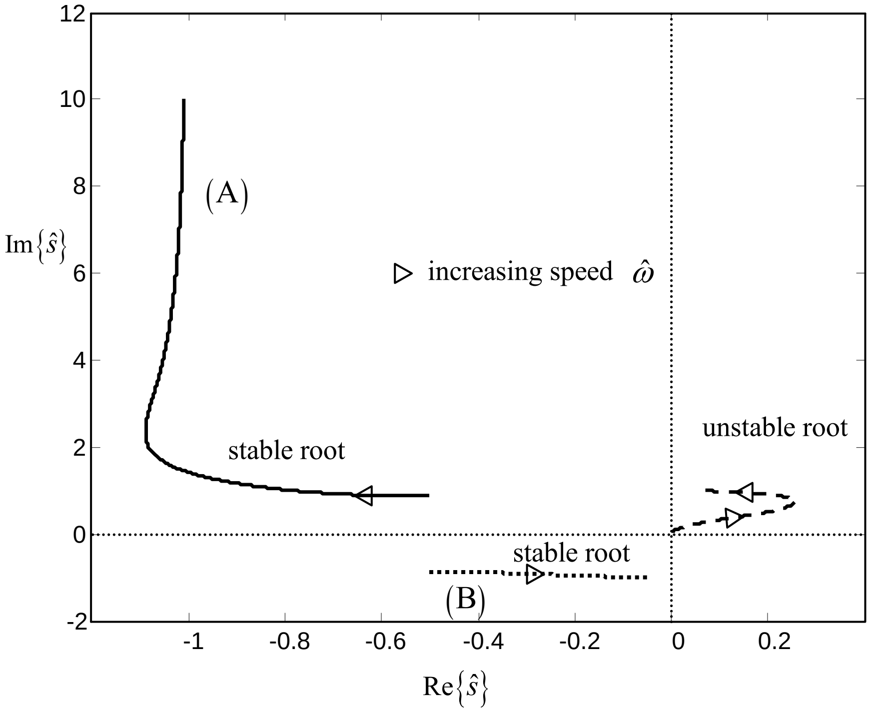

Figure 2.9 Plot of the real and the imaginary parts of the roots showing the growth/decay rate of the sub-synchronous whirl amplitude and the whirl frequency respectively, for the transverse motion of the turbocharger with flexible support, when $\kappa = 1$.

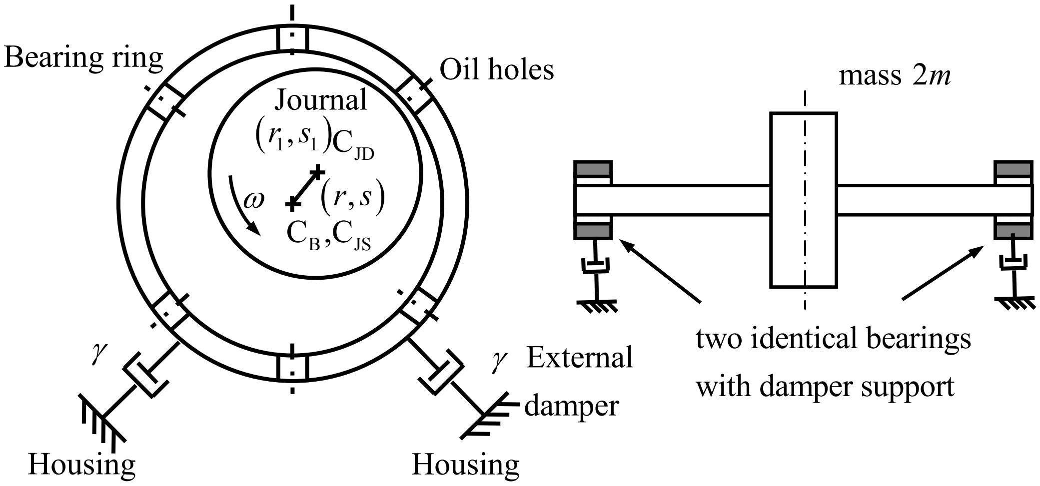

Figure 2.10 Schematic of a turbocharger with uncavitated floating ring bearings with the outer film treated as an external damper; C_{B} is the bearing centre, C_{JS} is the static journal centre, C_{JD} is the dynamic journal centre. γ is the damping coefficient of the external damper. Oil holes in the ring allow the flow of oil from the outer clearance between the housing and the ring to the inner clearance between the ring and the journal [54].

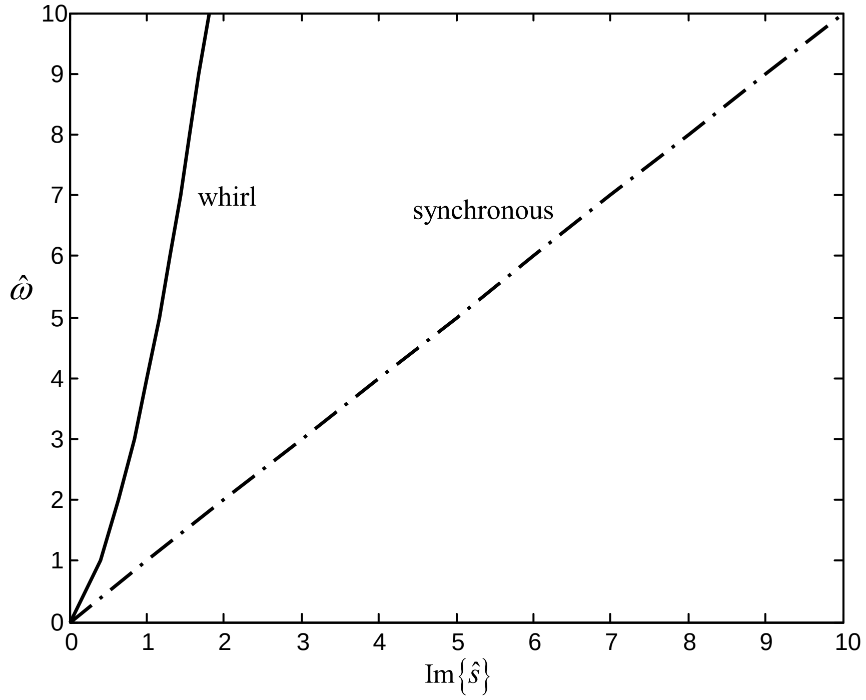

Figure 2.11 Plot of the sub-synchronous whirl frequency varying with the rotating speed of the turbocharger with damper support; synchronous frequency is shown for comparison as a function of speed.

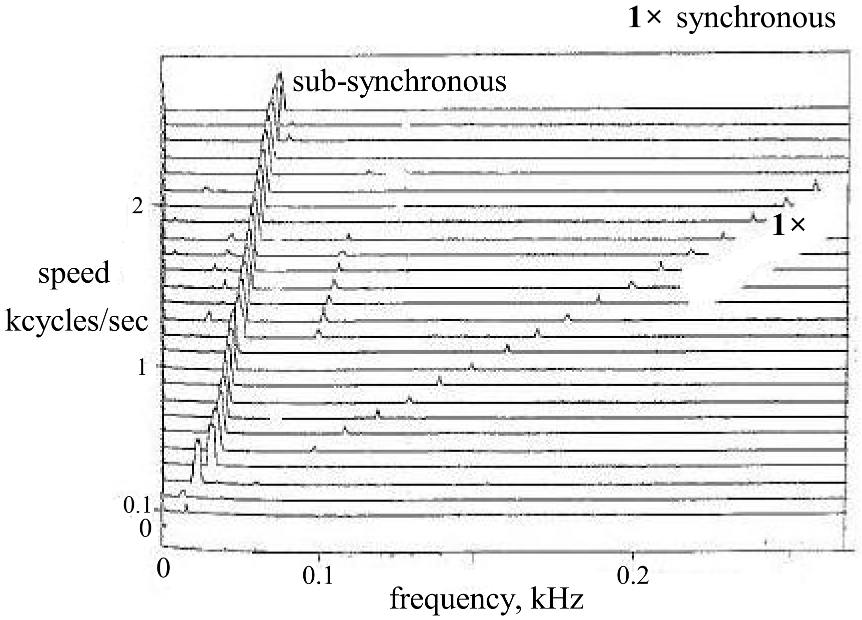

Figure 2.12 Water fall diagram from a commercial turbocharger with floating ring bearings; adapted from Holmes [3].

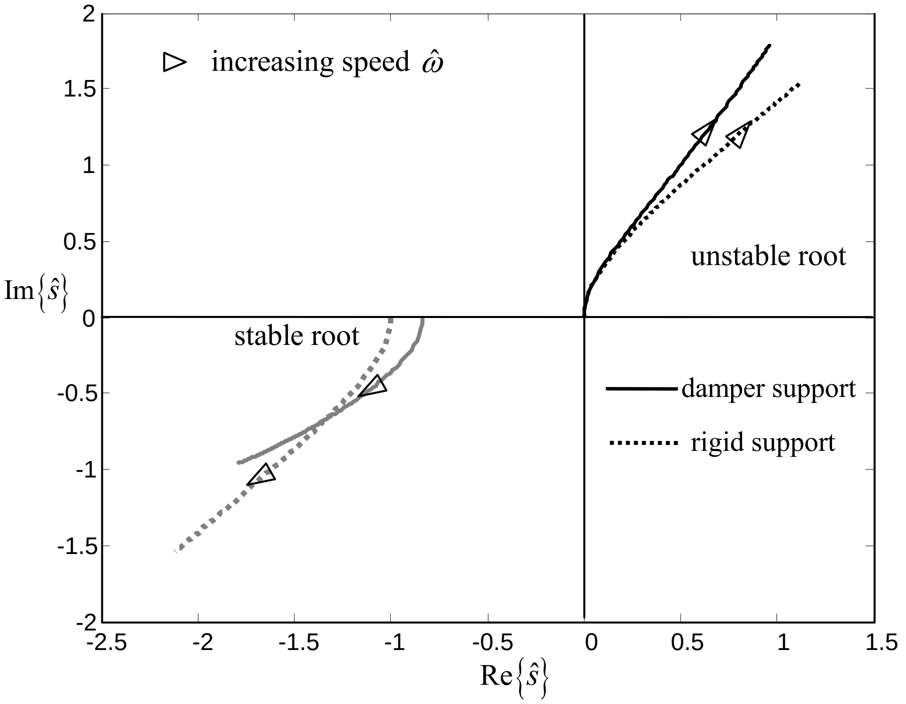

Figure 2.13 Plot of the real and the imaginary parts of the roots comparing the growth/decay rate of the sub-synchronous whirl amplitude and the whirl frequency for the transverse motion of the turbocharger with damper support with that of the rigid support. The curves corresponding to the rigid support are shown in dotted lines.

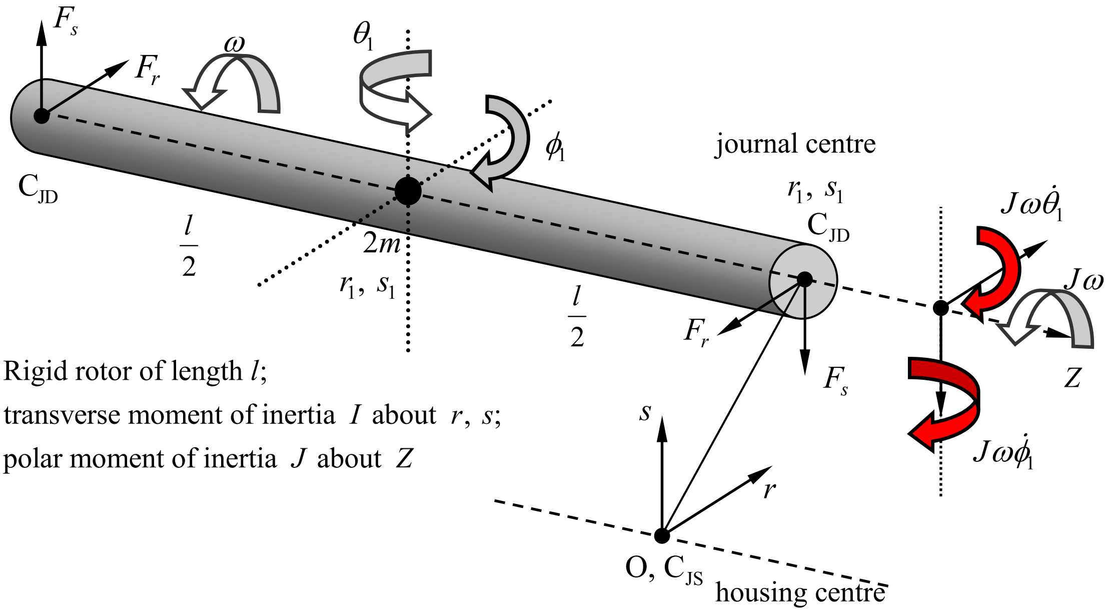

Figure 2.14 Co-ordinate system of the symmetric rotor model of the turbocharger with two identical plain journal bearings for tilt motion with gyroscopic moments; O is the centre of the stationary housing, $\mathrm{C_{JS}}$ is the static journal centre, $\mathrm{C_{JD}}$ is the dynamic journal centre; θ_1 and ϕ_1 are the tilt co-ordinates about s and r axes respectively; $J\omega$ is the angular momentum of the rotor about its spin axis Z; l is the distance between the bearings; r_1, s_1 are the co-ordinates of the journal centre. Compressor and turbine wheels are not shown here.

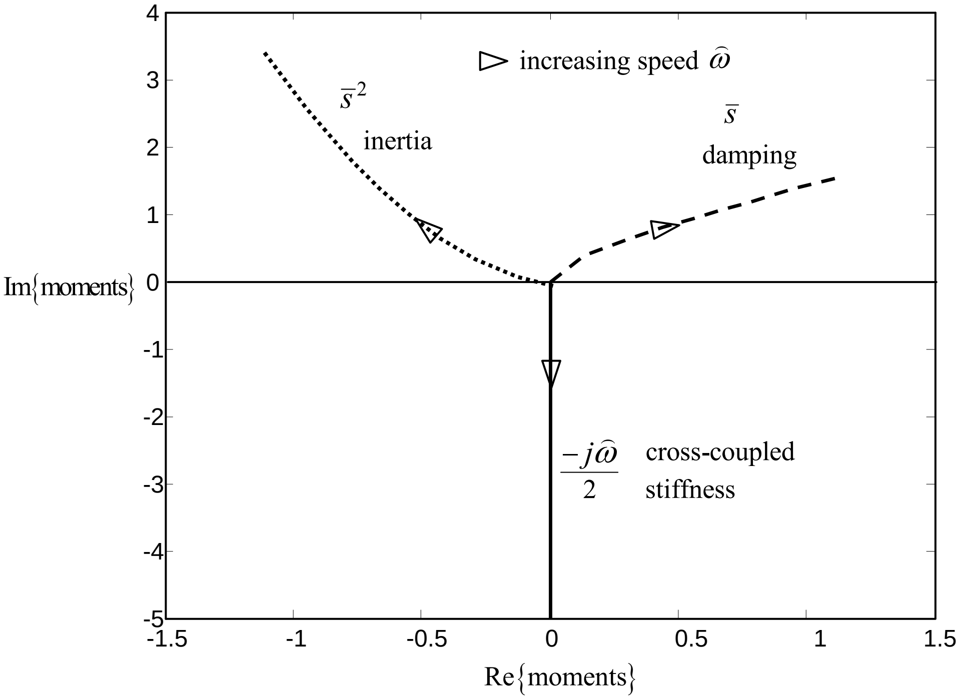

Figure 2.15 Plot of the real and imaginary parts of the moments from the unstable root of the equation of tilt motion of the turbocharger with rigid support without the gyroscopic effect.

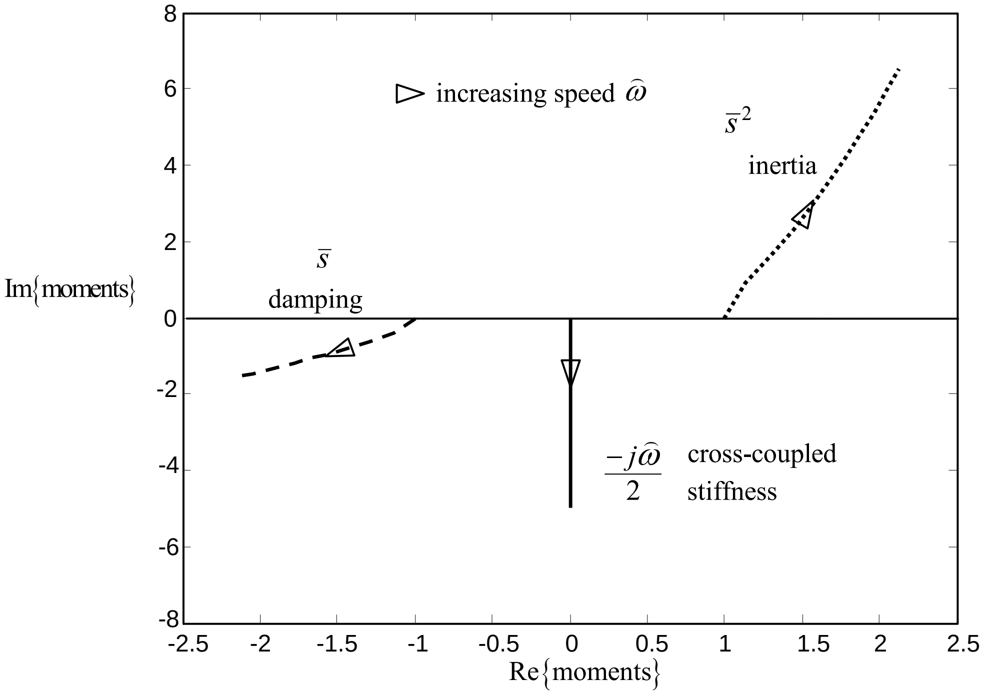

Figure 2.16 Plot of the real and imaginary parts of the moments from the stable root of the equation of tilt motion of the turbocharger with rigid support without the gyroscopic effect.

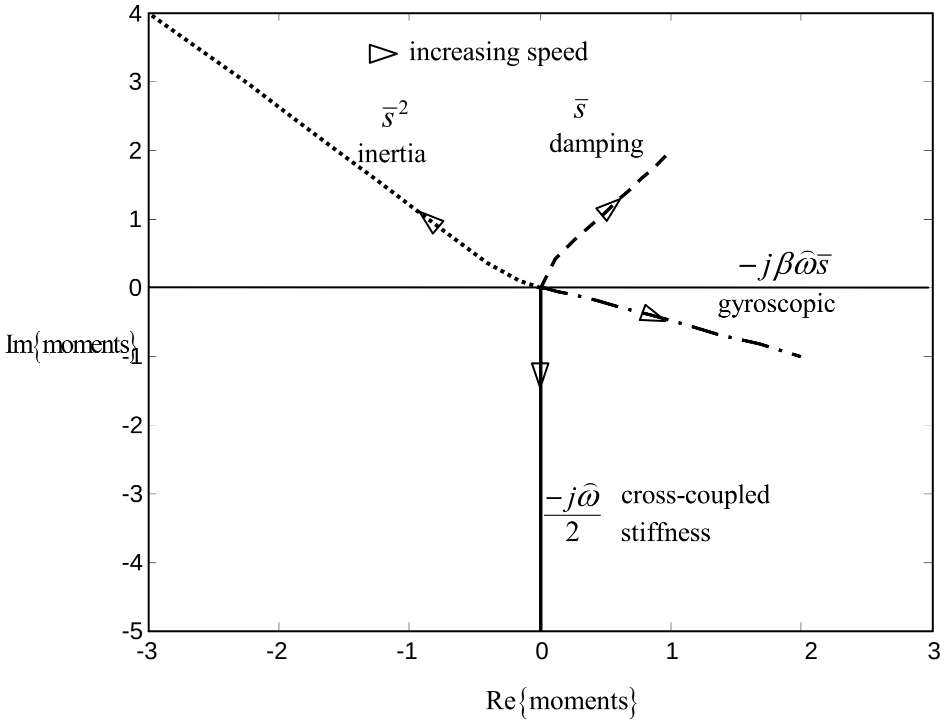

Figure 2.17 Plot of the real and imaginary parts of the moments from the unstable root of Eq. (2.39) of the turbocharger with rigid support with the gyroscopic effect when $\beta = 0.1$ (unstable)

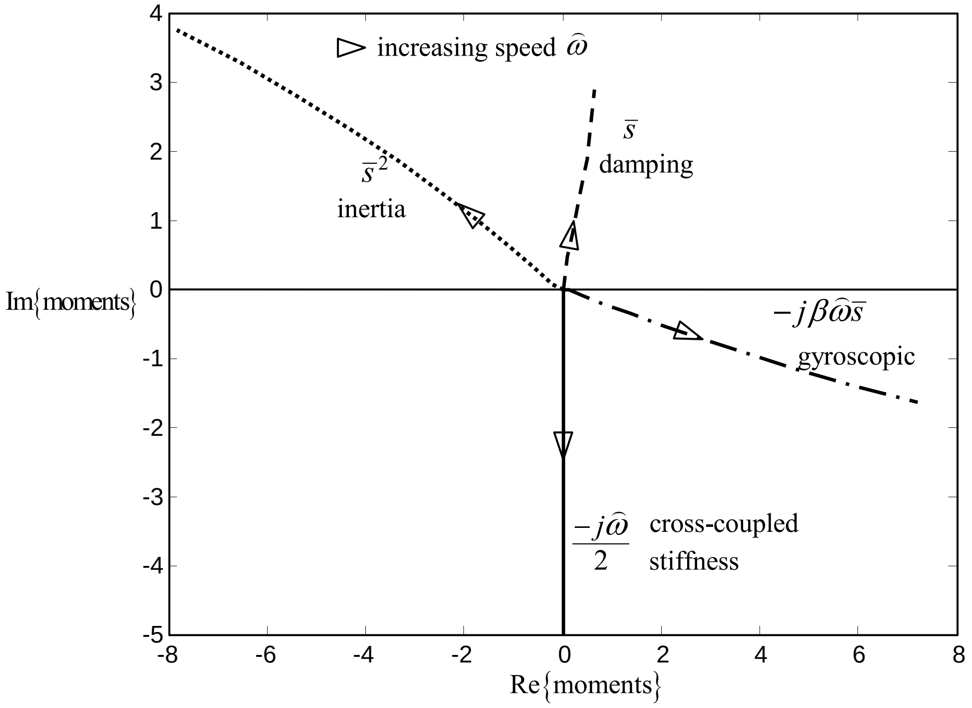

Figure 2.18 Plot of the real and imaginary parts of the moments from the unstable root of Eq. (2.39) of the turbocharger with rigid support with the gyroscopic effect when $\beta = 0.25$ (unstable).

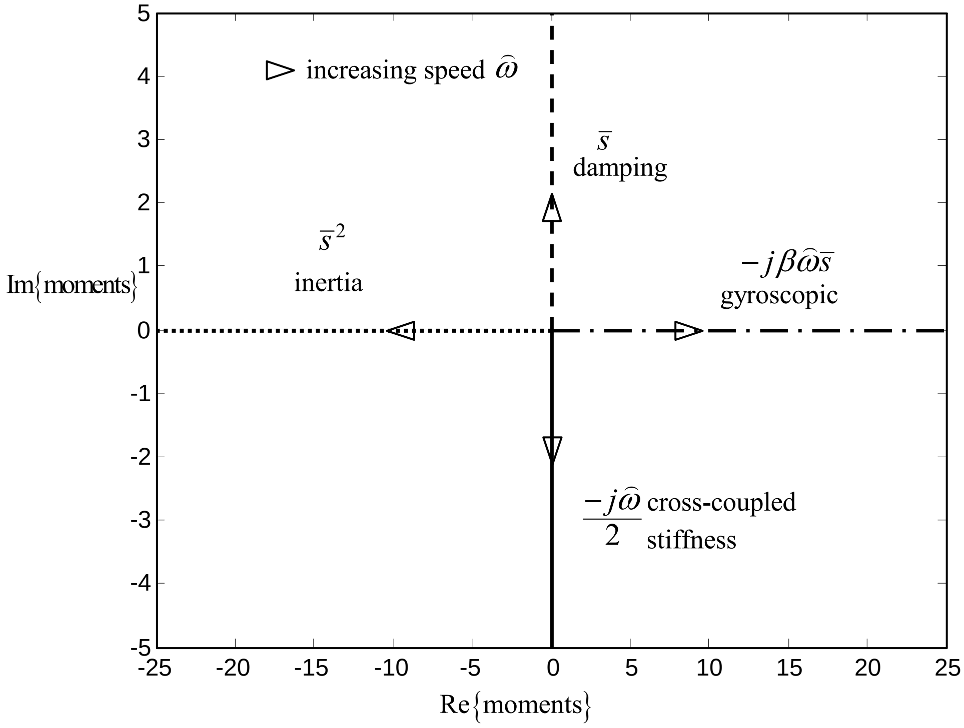

Figure 2.19 Plot of the real and imaginary parts of the moments from the unstable root of Eq. (2.39) of the turbocharger with rigid support with the gyroscopic effect when $\beta = 1/2$ (threshold).

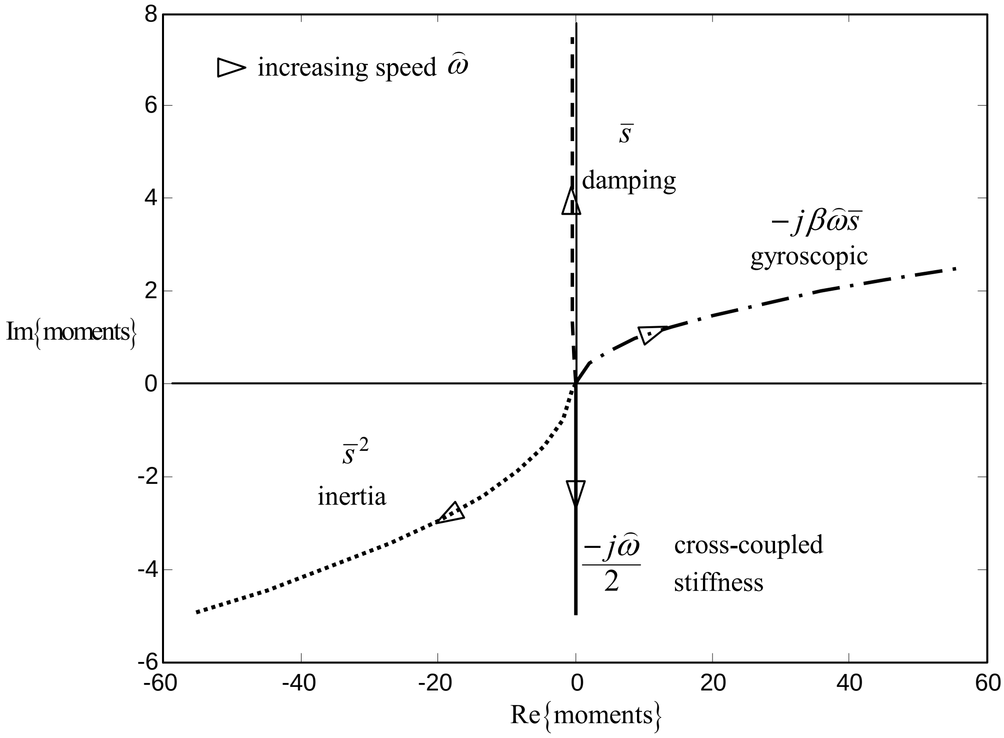

Figure 2.20 Plot of the real and imaginary parts of the moments from the unstable root of Eq. (2.39) of the turbocharger with rigid support with the gyroscopic effect when $\beta = 0.75$ (stable).

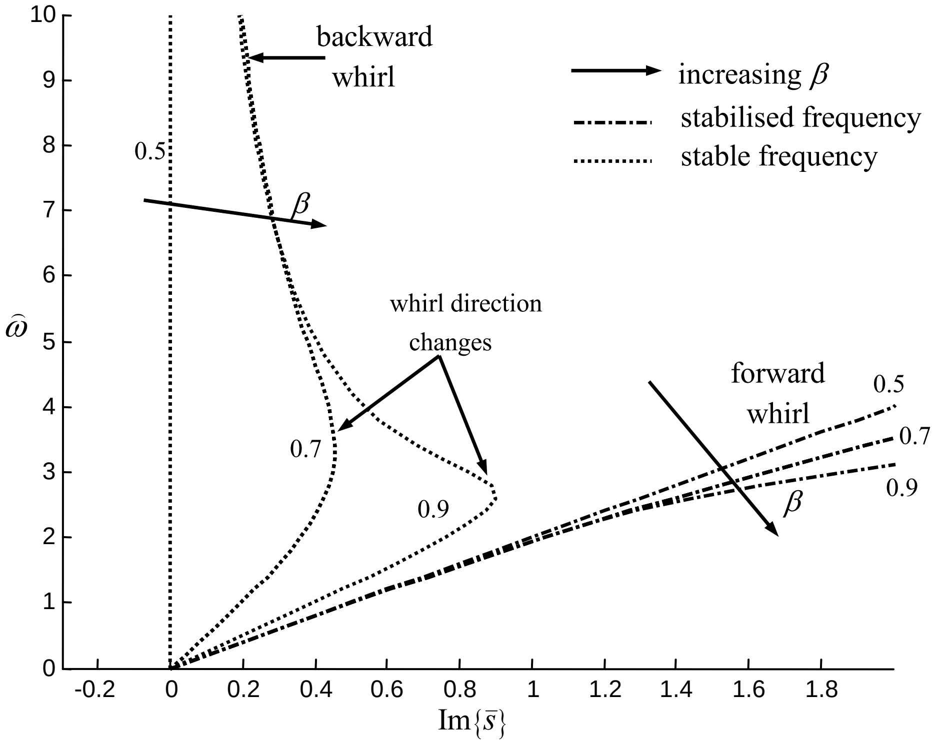

Figure 2.21 Plot of the sub-synchronous conical whirl frequencies varying with the rotational speed of the turbocharger with rigid support, for various values of $1/2 \le \beta < 1$. The stable frequencies show a change in the whirl direction after a certain speed by decreasing with speed.

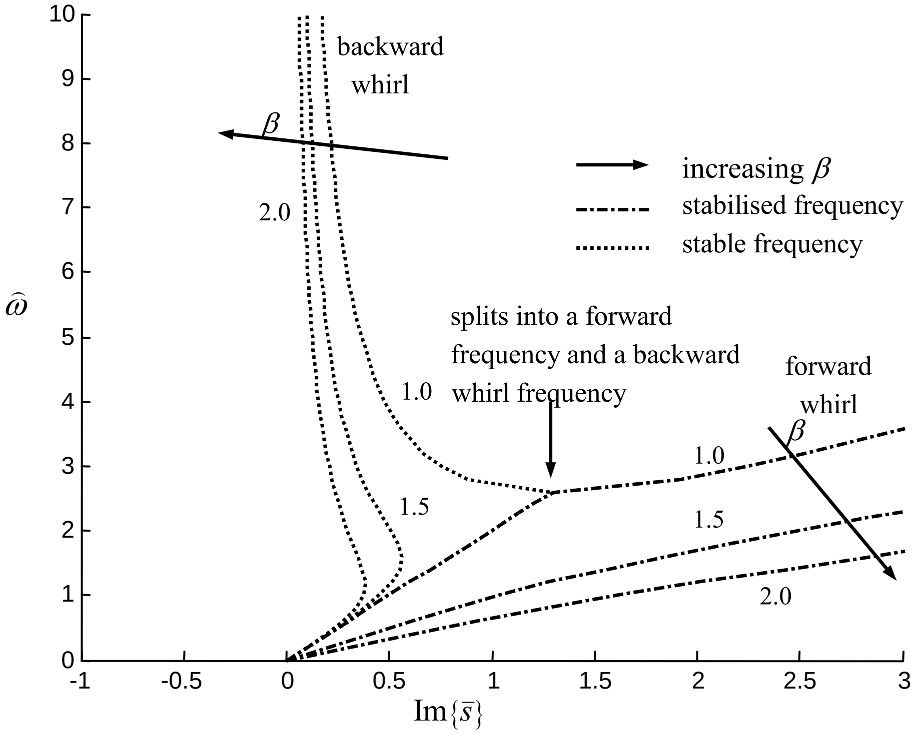

Figure 2.22 Plot of the sub-synchronous conical whirl frequencies varying with the rotational speed of the turbocharger with rigid support, for various values of $1 \le \beta < 2$. The stable frequencies show a change in the whirl direction after a certain speed by decreasing with speed.

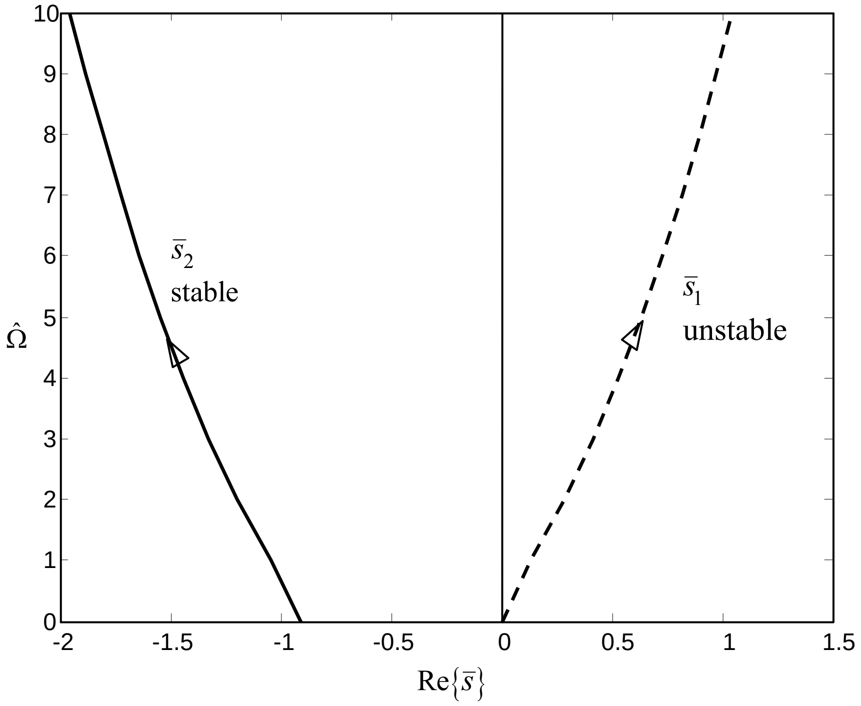

Figure 2.23 Plot of the real part of the roots of the equation of tilt motion of the turbocharger with damper support against the rotor speed without the gyroscopic effect, when $\gamma = 10$.

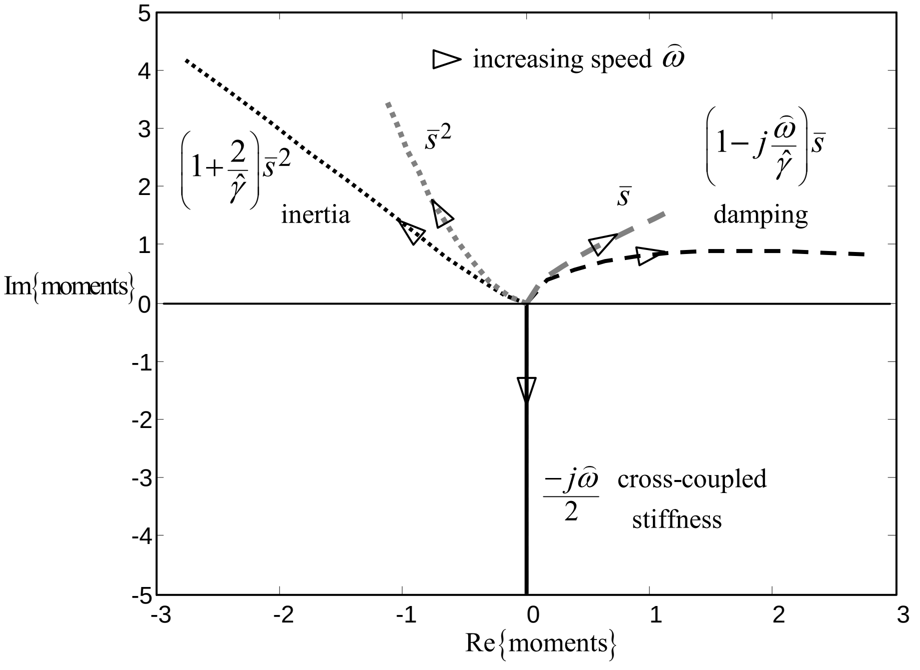

Figure 2.24 Plot of the real and the imaginary parts of the moments from the unstable root of Eq. (2.46) of the turbocharger with damper support without the gyroscopic effect when $\hat{\gamma} = 10$. The corresponding plots from the rigidly supported turbocharger are shown in grey lines for comparison. The cross-coupled stiffness moment is purely imaginary for both rigid and damper supported turbochargers.

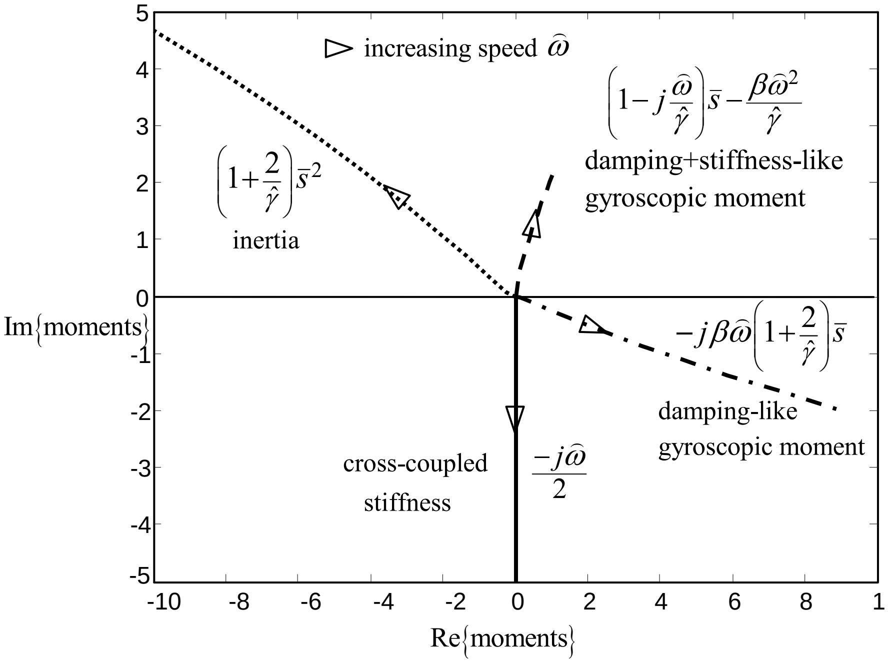

Figure 2.25 Plot of the real and the imaginary parts of the moments from the unstable root of Eq. (2.46) of the turbocharger with damper support with the gyroscopic effect, when $\hat{\gamma}=10$ and $\beta=0.25$.

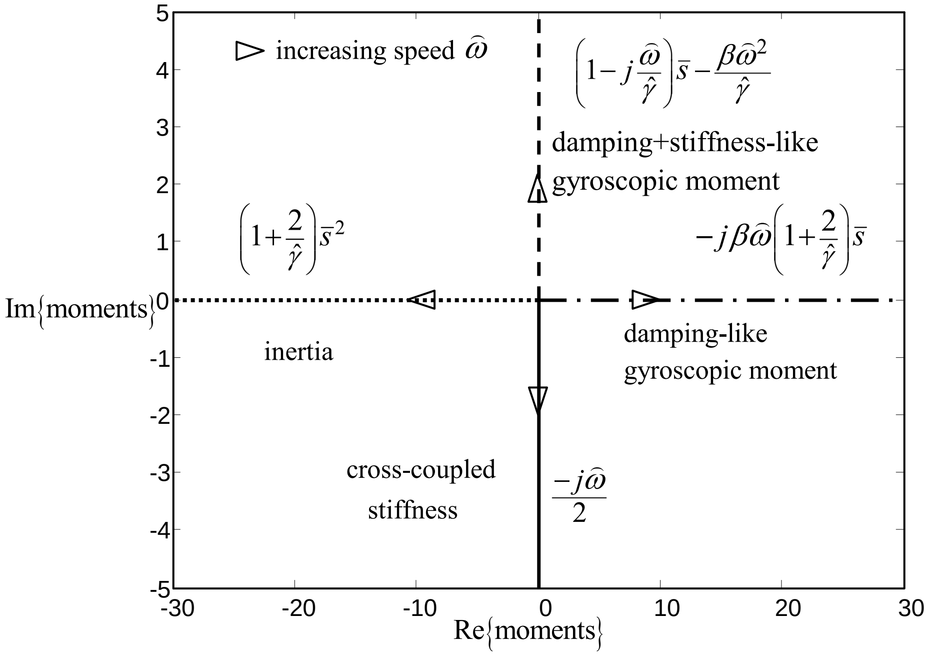

Figure 2.26 Plot of the real and the imaginary parts of the moments from the unstable root of Eq. (2.46) of the turbocharger with damper support with the gyroscopic effect, when $\hat{\gamma}=10, \beta=1/2$.

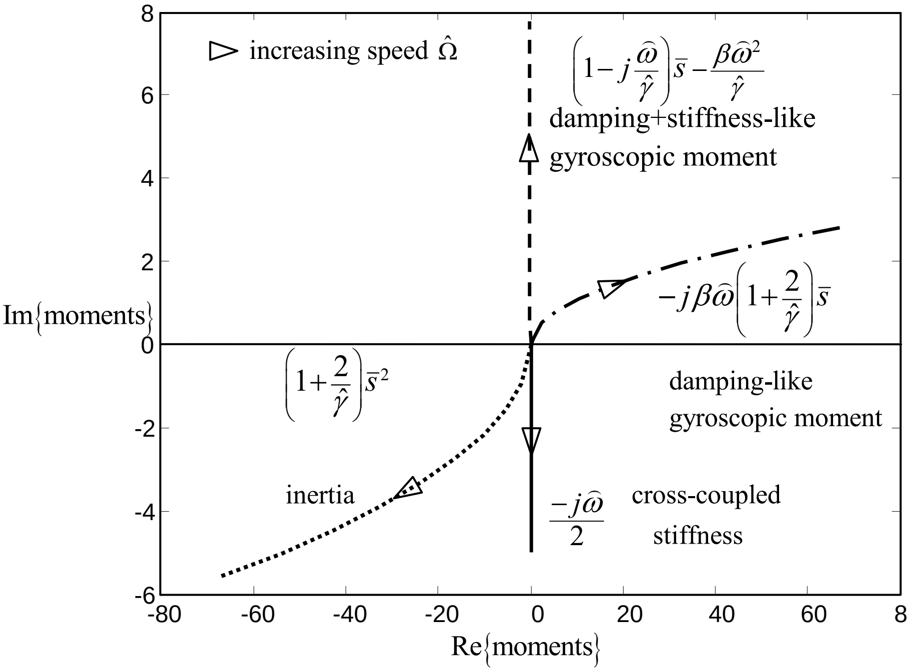

Figure 2.27 Plot of the real and the imaginary parts of the moments from the unstable root of Eq. (2.46) of the turbocharger with damper support with the gyroscopic effect, when $\hat{\gamma}=10, \beta=0.75$.

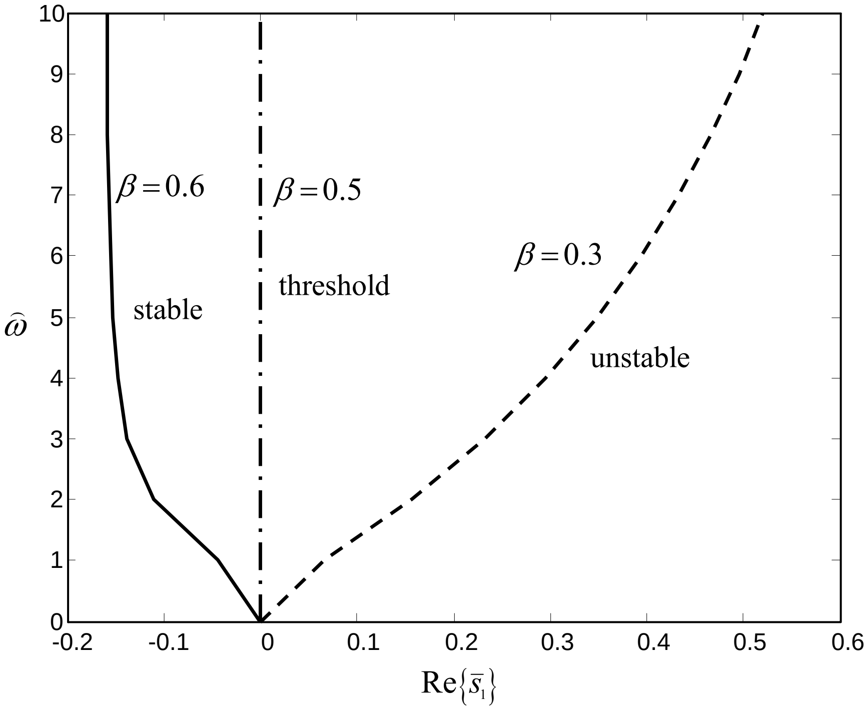

Figure 2.28 Plot showing the change of stability of the conical whirl of the turbocharger with damper support, due to change in the ratio β from the gyroscopic effect.

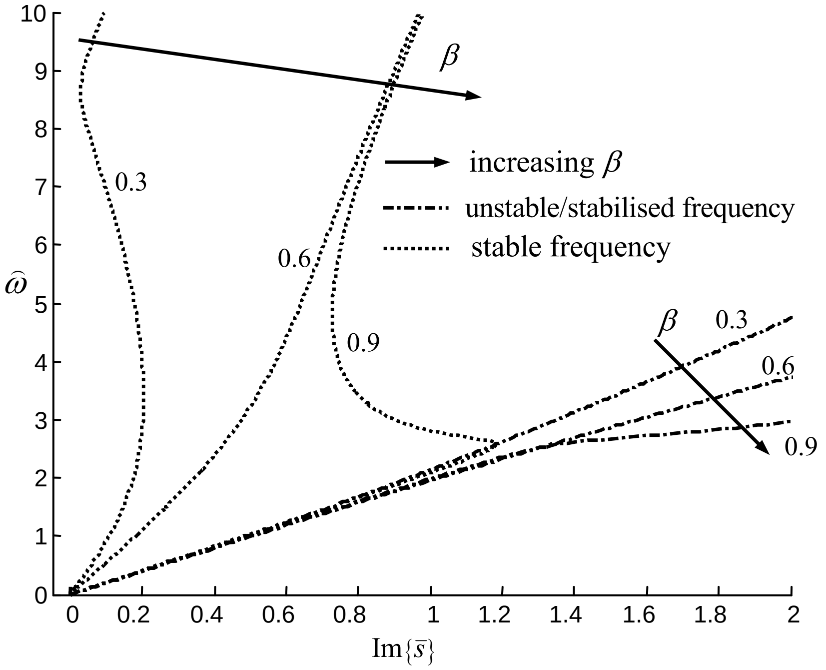

Figure 2.29 Plot of the sub-synchronous conical whirl frequencies varying with the rotational speed of the turbocharger with damper support, for various values of $\beta < 1$. The stable frequencies changes from backward to forward whirl again at high speeds.

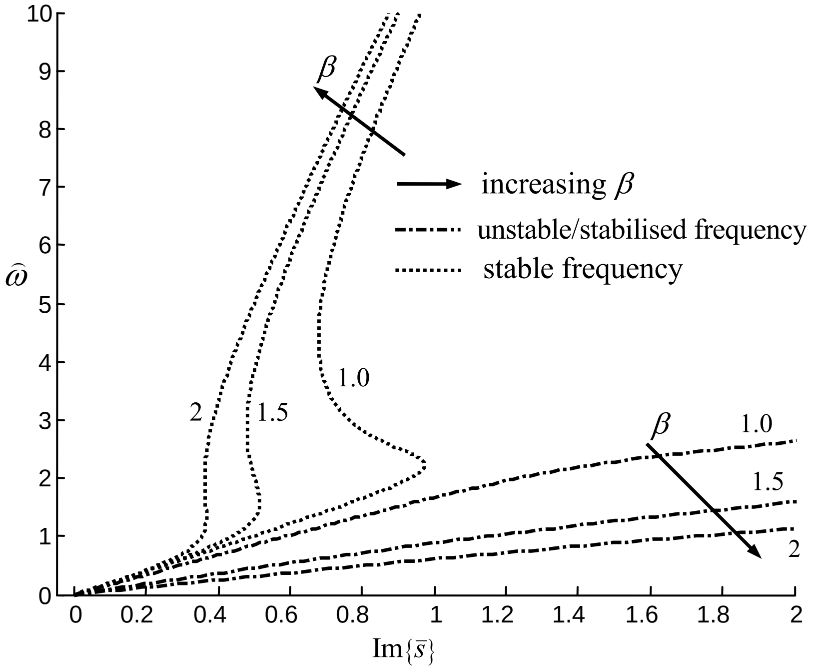

Figure 2.30 Plot of the sub-synchronous conical whirl frequencies varying with the rotational speed of the turbocharger with damper support, for various values of $\beta > 1$. The stable frequencies changes from backward to forward whirl again at high speeds.

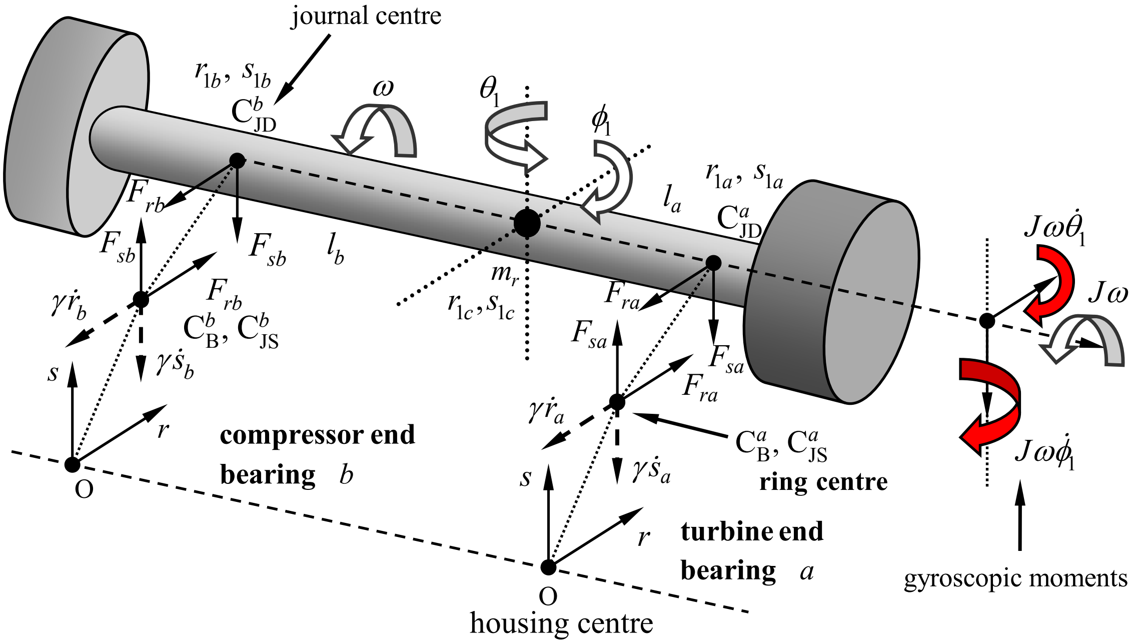

Figure 2.31 Co-ordinate system and forces acting on the rigid rotor model of a turbocharger with floating ring bearings - linear and tilt motion including gyroscopic moments; l_a and l_b are the distances between the bearing centres and the rotor centre of gravity; $J\omega$ is the angular moment of the rotor about the spin axis Z, where ω is the spin speed and J is the polar moment of inertia of the rotor; m_r is the full rotor mass. The external damping forces are shown in dashed lines.

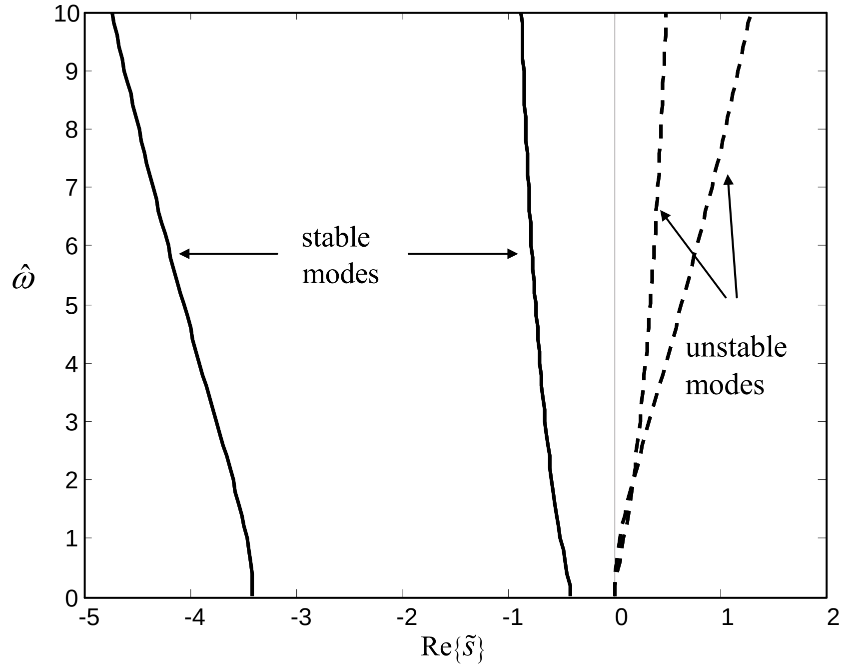

Figure 2.32 Plot of the growth/decay rates of sub-synchronous whirl amplitude varying with the rotational speed of the turbocharger with an asymmetric rotor in floating ring bearings, when $\hat{\gamma} = 10,\ L_a = 0.3,\ L_b = 0.7,\ \alpha = 2, \beta = 0.25$.

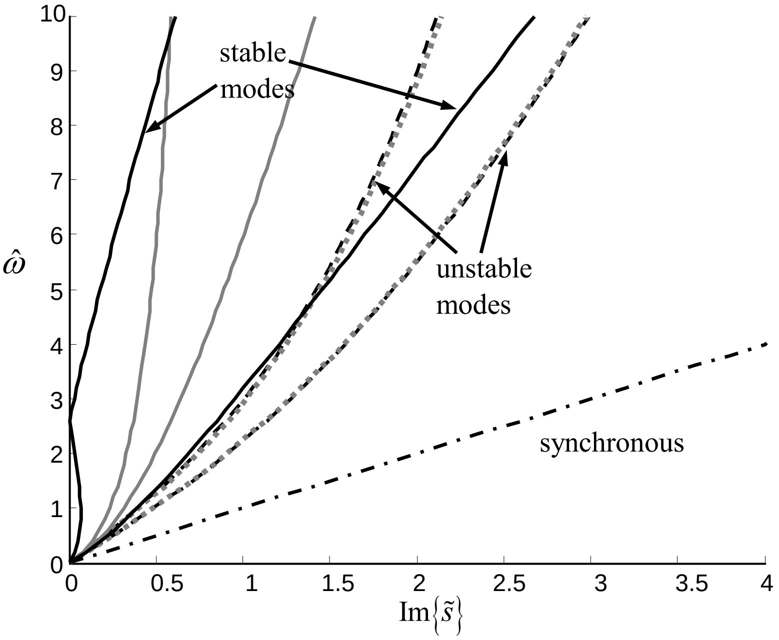

Figure 2.33 Plot of the sub-synchronous whirl frequencies (imaginary part of the roots) and the rotor speed of the turbocharger with asymmetric rotor in floating ring bearings ($\hat{\gamma}=10, L_a=0.3, L_b=0.7, \alpha=2, \beta=0.25$). Corresponding whirl frequencies for $\beta=0$ are shown in grey lines for comparison. Synchronous vibration is shown for comparison as a function of speed

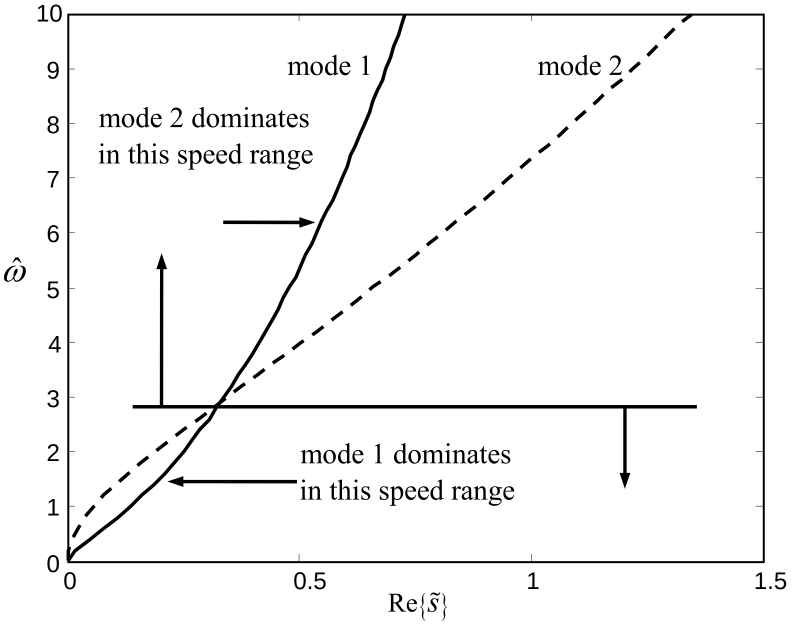

Figure 2.34 Plot of the real part of the unstable roots of Eq. (2.59) of the turbocharger with asymmetric rotor in floating ring bearings and the rotor speed when $\hat{\gamma}=10,\ L_a=0.3,\ L_b=0.7,\ \alpha=2,\ \beta=0$.

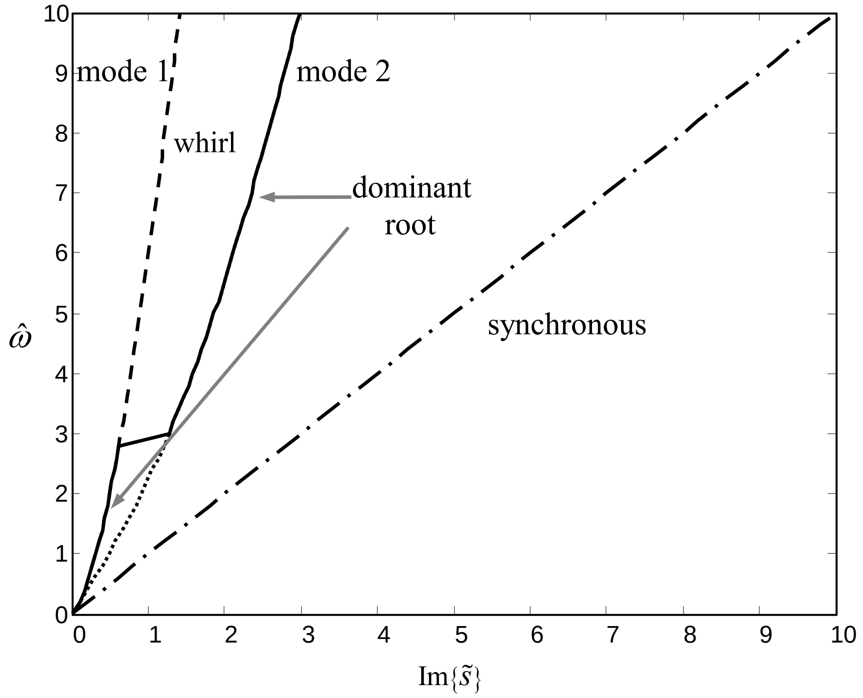

Figure 2.35 Plot of the imaginary part of the roots of Eq. (2.46) showing the sub-synchronous whirl frequencies varying with the rotational speed of the turbocharger with floating ring bearings when $\hat{\gamma}=10,\ L_a=0.3,\ L_b=0.7,\ \alpha=2,\ \beta=0$. The synchronous frequency is shown for comparison as a function of the speed.

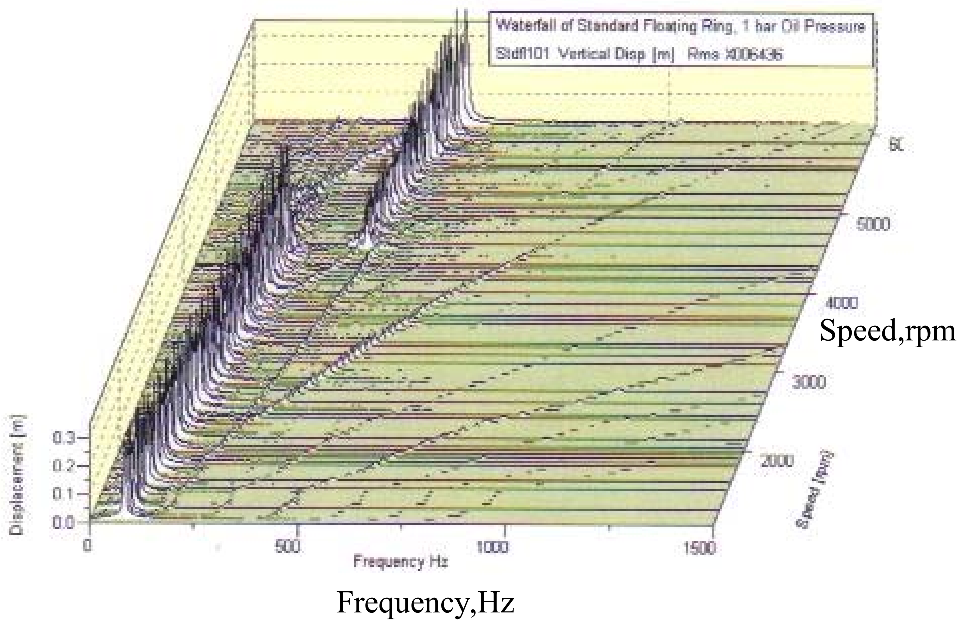

Figure 2.36 Waterfall diagram for a turbocharger with floating ring bearings (speed axis is engine speed $\cong 1/12$ x turbocharger speed [54].

Mode - 1

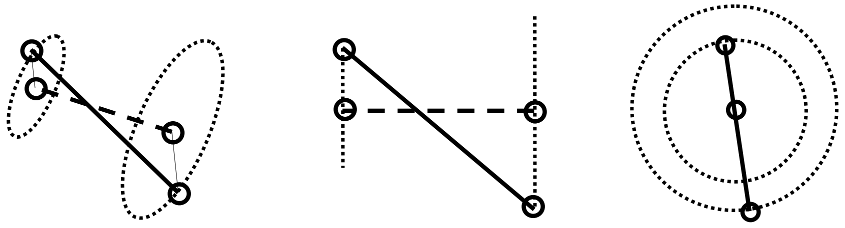

Figure 2.37 Mode shape of the rotor corresponding to mode-1 (conical mode), which is dominant in the lower speed range as shown in Figure 2.34 and Figure 2.35.

Mode - 2

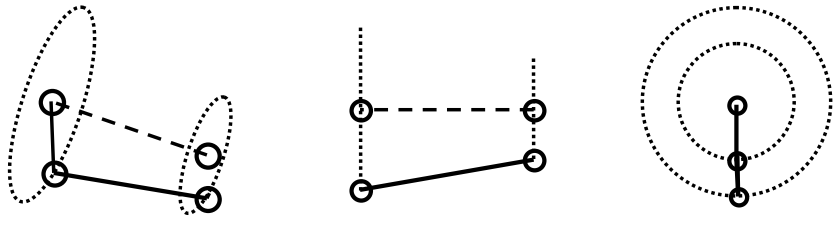

Figure 2.38 Mode shape of the rotor corresponding to mode-2 (in-phase whirl mode), which is dominant in the higher speed range as shown in Figure 2.34 and Figure 2.35.

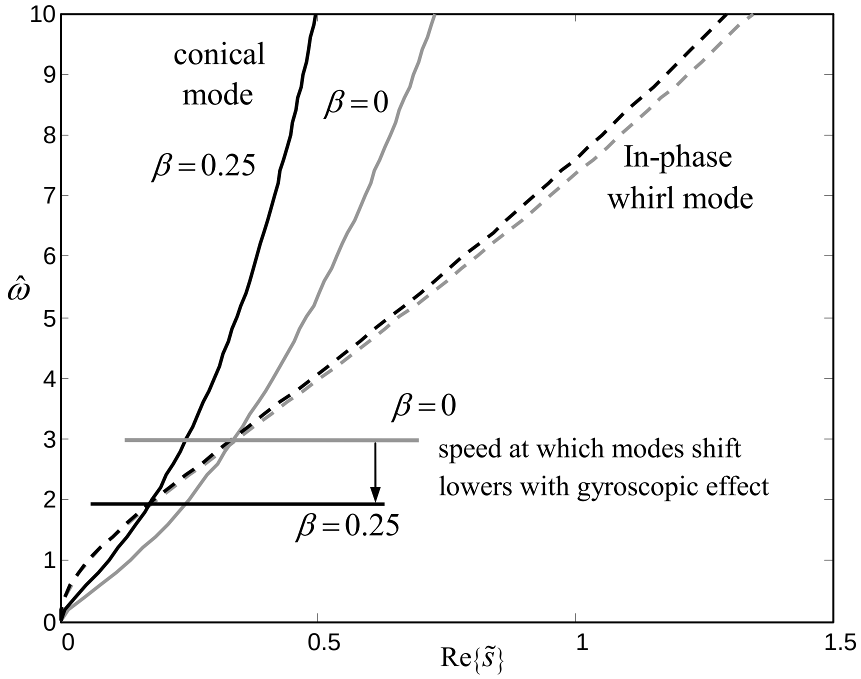

Figure 2.39 Plot showing the effect of gyroscopic moment on the speed at which the dominant mode shifts from the conical to the in-phase whirl, when $\hat{\gamma} = 10,\ L_a = 0.3,\ L_b = 0.7,\ \alpha = 2$. The corresponding plot without the gyroscopic effect is shown in grey lines for comparison.

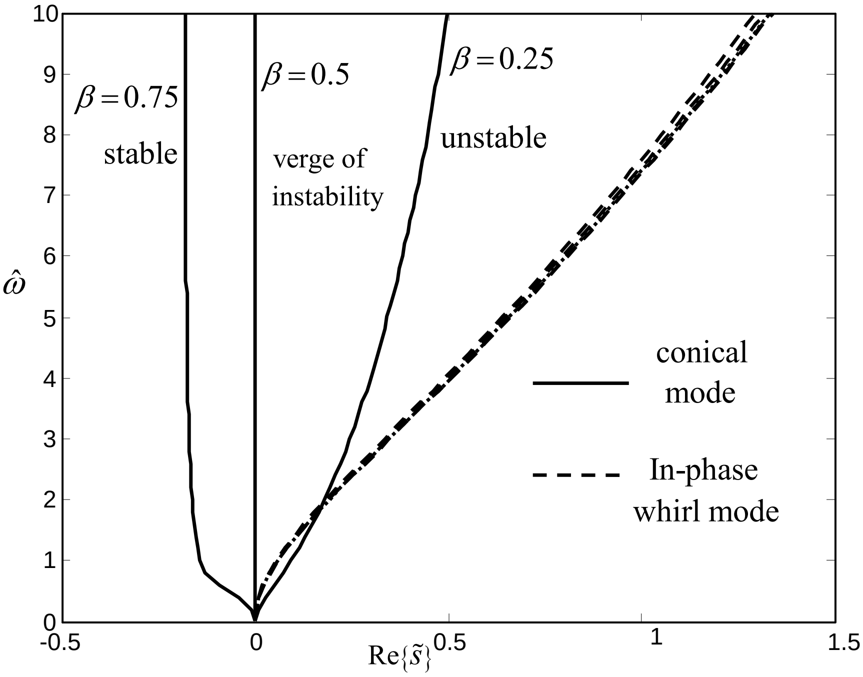

Figure 2.40 Plot of the real part of the roots of the turbocharger with floating ring bearings, when plotted against the rotational speed. Change in the stability of the conical whirl mode with change in the gyroscopic coefficient β is shown, when $\hat{\gamma} = 10,\ L_a = 0.3,\ L_b = 0.7,\ \alpha = 2$.

CHAPTER 3

INFLUENCE OF ROTOR FLEXIBILITY ON THE DYNAMIC BEHAVIOUR OF A TURBOCHARGER

3.1 INTRODUCTION

In the previous chapter, using a rigid rotor, the gyroscopic effect was analysed for its significance in the oil-whirl instability. Gunter and Chen [2] predicted that the in-phase whirl mode is a bending mode for a typical turbocharger. It was seen in Chapter 2 that in the case of a rigid rotor, the natural oil-whirl frequency changes with speed. In the case of flexible rotor, the rotor flexibility is in series with the bearing stiffness. Since the rotor flexibility does not change, the rotor whirls at a constant frequency, when the rotor bending frequency occurs at the rotor speed. This phenomenon is defined as oil whip [68]. Since the turbocharger rotor is a relatively rigid structure supported by flexible bearings, it is convenient to assume the rotor to be rigid. However, most automotive turbochargers operate at very high speeds in excess of 180,000 rpm, and the bearings become relatively stiff compared to the rotor at these speeds. This means that rotor flexibility can be important with respect to oil-whirl as shown by Gunter and Chen [2]. Hence it is important to determine whether the rotor flexibility significantly affects the dynamic behaviour at high speeds for a turbocharger. The aim of this chapter, therefore, is to analyse the stability of a turbocharger with a flexible rotor supported by two identical floating ring bearings. The outer film of the bearing is treated as an external damper in series to the inner film as discussed in Chapter 2 and the ring is assumed not to rotate but only wobble. The effect of flexibility is investigated by superimposing the rigid motion of the rotor and the static deflection of the rotor.

3.2 EQUATIONS OF MOTION

3.2.1 INTRODUCTION

The aim of this section is to derive the equations of motion of a turbocharger with a flexible rotor supported by floating ring bearings similar to that with the rigid rotor in Section 2.5. The outer ring is modelled as an external damper as discussed in Chapter 2. The bearings have a full oil-film without cavitation [20]. The method involves the technique of superimposing the rigid motion of the rotor and its static deflection to capture the flexible rotor dynamics. The treatment does not allow for the transverse moment of inertia of the turbine and the compressor discs. The equation of rigid motion and flexible deflection are derived first and then the system of equations for the journal motion in the inner and the outer film of the floating ring bearings are combined into a single matrix equation.

3.2.2 EQUATION OF RIGID MOTION

In this Sub-Section, the rigid motion of the turbocharger rotor supported in externally damped bearings is considered to derive the equation of rigid motion alone. Figure 3.1 shows a typical turbocharger with dimensions used for the investigation in this chapter. Figure 3.2 shows the co-ordinate system of a turbocharger with flexible rotor supported in two identical floating ring bearings. The turbine and compressor masses are m_a and m_b respectively; $\mathrm{C}_{\mathrm{JD}}^{a}$, $\mathrm{C}_{\mathrm{JD}}^{b}$ are the bearing centres of the turbine end bearing and the compressor end bearing; $\mathrm{C}_{\mathrm{JS}}^{a}$, $\mathrm{C}_{\mathrm{JS}}^{b}$ are the corresponding journal static centres which are the same as the ring centres $\mathrm{C}_{\mathrm{B}}^{a}$, $\mathrm{C}_{\mathrm{B}}^{b}$, since the static load is ignored due to the light weight of the turbocharger. The distance between the two bearing centres is l, the distance between the compressor bearing centre and the compressor centre of gravity is l_c, and the distance between the turbine bearing centre and the turbine centre of gravity is l_t. Note that the ring is treated as fixed and the outer film between the ring and the housing is treated as a damped support, which is discussed in detail in Chapter 1. The co-ordinates of the turbine and the compressor mass centres of masses m_a and m_b are r_{ma}, s_{ma} and r_{mb}, s_{mb} respectively; r_{1a}, s_{1a} and r_{1b}, s_{1b} are the co-ordinates of the corresponding journal centres, $r_{a,b}$ and $s_{a,b}$ are the co-ordinates of the corresponding ring centres. The whirl orbit was assumed to be circular about the bearing centre, since the static load is negligible and the static centre is same as the bearing centre. Assuming a full oil-film [20], the oil-film forces between the rotor and the ring $\mathbf{f_a}$, $\mathbf{f_b}$ are given in Eqs. (2.50) and (2.51) in Chapter 2. It has been shown in Chapter 2 that a turbocharger has self-excited sub-harmonic vibration in the form of an in-phase whirl mode and a conical whirl mode. Hence the equations of motion in terms of both the forces and the corresponding moments need to be considered as given in section 2.5 of Chapter 2. The equations of translation motion describing the in-phase whirl of the turbocharger rotor of masses m_a and m_b in the damper supported bearings are given by:

$$-\mathbf{f_a} - \mathbf{f_b} = m_a \ddot{\mathbf{r}}_{\mathbf{ma}} + m_b \ddot{\mathbf{r}}_{\mathbf{mb}}\,, \tag{3.1}$$

where $\mathbf{r_i} = \left[r_i, s_i\right],\ i = ma,\ mb$ and the oil-film forces $\mathbf{f_a}$, $\mathbf{f_b}$ are given by Eqs. (2.50) and (2.51) in Chapter 2. Now, for the conical whirl, the equations of tilt motion described by the moments about the two bearing centres have to be defined separately. In the case of the symmetric rigid rotor in Chapter 2, the moment of inertia of the rotor is used for the acceleration term of the equations of tilt motion. But in this chapter, the present treatment does not allow for the consideration of the inertia directly, since rotor bending is allowed and the masses are away from the bearing centres unlike the asymmetric rotor in section 2.5. Hence, the moment equation is derived using the inertia forces due to the acceleration of the masses C_B^a, C_B^b, which in the rZ and sZ planes shown in Figure 3.2 are given by:

$$\mathbf{f_b}(l) - m_a \ddot{\mathbf{r}}_{\mathbf{ma}}(l_t) + m_b \ddot{\mathbf{r}}_{\mathbf{mb}}(l_c + l) = 0\,, \tag{3.2}$$

$$-\mathbf{f_a}(l) - m_a \ddot{\mathbf{r}}_{\mathbf{ma}}(l_t + l) + m_b \ddot{\mathbf{r}}_{\mathbf{mb}}(l_c) = 0\,. \tag{3.3}$$

Figure 3.3 shows the net deflection of the turbine mass considering the rigid motion and the flexible deflection at the turbine end, which is the similar to that of the compressor mass. Note that the rigid motion is defined by the dynamics of the rotor, while the flexible deflection is evaluated under static conditions. From the rigid motion of the rotor, the co-ordinates of the masses can be determined from the co-ordinates of the journal in the bearings as shown in Figure 3.2 such as:

$$\bar{\mathbf{r}}_{\mathbf{ma}} = \mathbf{r}_{\mathbf{1a}} - \left(\left(\mathbf{r}_{\mathbf{1b}} - \mathbf{r}_{\mathbf{1a}} \right) l_t / l \right), \tag{3.4}$$

$$\bar{\mathbf{r}}_{\mathbf{mb}} = \mathbf{r}_{\mathbf{1a}} + \left(\left(\mathbf{r}_{\mathbf{1b}} - \mathbf{r}_{\mathbf{1a}} \right) (l_c + l) / l \right), \tag{3.5}$$

where $\left(\mathbf{r}_{\mathbf{1b}} - \mathbf{r}_{\mathbf{1a}} \right) / l$ gives the slope of the rotor along r and s directions. As mentioned in the introduction of this Chapter, in order to analyse the flexible rotor, the treatment requires both the rigid dynamic motion and the flexible deflection of the rotor. Hence the flexible deflection under the static load is determined in the following Sub-Section.

3.2.3 FLEXIBLE DEFLECTION OF THE ROTOR

Under the action of the turbine and compressor weight, the rotor undergoes bending. In this Sub-Section, this bending effect is included into the equations of motion in the form of certain coefficients known as the influence coefficients. The influence coefficient is defined as the deflection of the rotor under the action of a unit force. The influence coefficients α_{ij} define the bending strength of the rotor in terms of the dimensions of the rotor and its material properties such as density and Young's modulus. The flexible deflection is superimposed onto the rigid motion by considering the net deflection of the masses as shown in Figure 3.3. The flexible deflection $\bar{\bar{\mathbf{r}}}_{\mathbf{ma}}$ of the turbine mass m_a due to the inertial forces of the masses m_a and m_b is given by:

$$-\bar{\bar{\mathbf{r}}}_{\mathbf{ma}} = -\alpha_{11} (m_a \ddot{\mathbf{r}}_{\mathbf{ma}}) - \alpha_{12} (m_b \ddot{\mathbf{r}}_{\mathbf{mb}}), \tag{3.6}$$

$$-\bar{\bar{\mathbf{r}}}_{\mathbf{mb}} = -\alpha_{21}(m_a\ddot{\mathbf{r}}_{\mathbf{ma}}) - \alpha_{22}(m_b\ddot{\mathbf{r}}_{\mathbf{mb}}), \tag{3.7}$$

where $\bar{\bar{\mathbf{r}}}_i = \left[\bar{\bar{r}}_i, \bar{\bar{s}}_i\right]$, $i = ma,\ mb$, α_{ij} is the influence coefficient of the rotor given by the deflection of masses m_a, m_b due to the force F_i acting on one of the masses; F_1 and F_2 are the respective forces acting on m_a and m_b respectively. Figure 3.4 shows the schematic of the deflections and the forces to calculate the influence coefficients. Figure 3.1 shows a typical turbocharger with the dimensions. Since the rotor is a stepped type, a simple finite element model [69] is used to determine the influence coefficients. Some details of the finite element model used for this evaluation is provided in Appendix B. Assuming the rotor to be pin-pinned, i.e., the translation is fixed at the bearing centre but rotation allowed, the coefficients are obtained by applying a force at the turbine mass centre and the compressor mass centre separately. Figure 3.4 shows the application of the force for determining the deflection δ_i under the action of a force F_j. The influence coefficients $\alpha_{ij} = \delta_i / F_j$, $\forall \quad i, j = 1,2$, are determined from the deflections of m_a and m_b. For a typical turbocharger shown in Figure 3.1 these coefficients are calculated to be $\begin{bmatrix} \alpha_{11} & \alpha_{12} \\ \alpha_{21} & \alpha_{22} \end{bmatrix} = 10^{-8} \times \begin{bmatrix} 7.199 & 1.312 \\ 1.312 & 4.392 \end{bmatrix}$. The net deflections along r and s directions as shown in Figure 3.3 are given by:

$$\mathbf{r}_{\mathbf{ma}} = \bar{\mathbf{r}}_{\mathbf{ma}} - \bar{\bar{\mathbf{r}}}_{\mathbf{ma}}, \tag{3.8}$$

$$\mathbf{r}_{\mathbf{mb}} = \bar{\mathbf{r}}_{\mathbf{mb}} - \bar{\bar{\mathbf{r}}}_{\mathbf{mb}}, \tag{3.9}$$

where $\bar{\mathbf{r}}_{\mathbf{ma}}$, $\bar{\bar{\mathbf{r}}}_{\mathbf{ma}}$ and $\bar{\mathbf{r}}_{\mathbf{mb}}$, $\bar{\bar{\mathbf{r}}}_{\mathbf{mb}}$ are given by Eqs. (3.4) and (3.6). These coordinates of the masses are used in determining the moments in Eqs. (3.2) and (3.3).

As discussed in Chapter 2, treating the outer film of the floating ring bearing as an external damper, at the interface between the ring and the stationary housing as shown in Figure 3.2 , the forces are given by [54]:

$$\mathbf{f}_{\mathbf{a}} = \gamma\dot{\mathbf{r}}_{\mathbf{a}}, \tag{3.10}$$

$$\mathbf{f_b} = \gamma \dot{\mathbf{r}}_\mathbf{b}, \tag{3.11}$$

where $\mathbf{f_a}$, $\mathbf{f_b}$ are given by Eqs. (2.50) and (2.51) in Chapter 2; γ is the damping coefficient of the outer film (external damper). Now, the equation of translation motion given in Eq. (3.1), the equations of tilt motion given in Eqs. (3.2) and (3.3), the equations of translation in the outer film given in Eqs. (3.10) and (3.11) together describe the equations of motion of the turbocharger with flexible rotor in the floating ring bearings. Substituting for the forces from Eqs. (2.50) and (2.51) into Eqs. (3.1) and assuming a solution of the form $[r,s]=\left[R,S\right]e^{\lambda t}$ gives:

$$-b_d(\lambda R_{1a}-R_a)-a_c(\lambda S_{1a}-S_a)-b_d(\lambda R_{1b}-R_b)-a_c(\lambda S_{1b}-S_b)-m_a\lambda^2 R_1-m_b\lambda^2 R_2=0\,, \tag{3.12}$$

$$-b_d(\lambda S_{1a}-S_a)+a_c(\lambda R_{1a}-R_a)-b_d(\lambda S_{1b}-S_b)+a_c(\lambda R_{1b}-R_b)-m_a\lambda^2 S_1-m_b\lambda^2 S_2=0\,. \tag{3.13}$$

Likewise, substituting into Eqs. of tilt motion (3.2) , (3.3), and the Eqs. of translation in the outer film (3.10), (3.11) results in a set of twelve equations. These twelve equations are related to the twelve degrees of freedom of the system. Four of them are related to the ring co-ordinates, while the rest eight of them are related to the journal coordinates in the two bearings. These can be written in the matrix form, which after non-dimensionalising gives the equations of motion of a turbocharger with a flexible rotor in the floating ring bearings as:

$$\begin{bmatrix}
0 & 0 & -\hat{s} & -\frac{\hat{\omega}}{2} & 0 & 0 & \hat{s} & \frac{\hat{\omega}}{2} & -\hat{M}_a & 0 & \hat{M}_{1b} & 0 \\
-\hat{s} & -\frac{\hat{\omega}}{2} & 0 & 0 & \hat{s} & \frac{\hat{\omega}}{2} & 0 & 0 & \hat{M}_{1a} & 0 & -\hat{M}_b & 0 \\
0 & 0 & \frac{\hat{\omega}}{2} & -\hat{s} & 0 & 0 & -\frac{\hat{\omega}}{2} & \hat{s} & 0 & -\hat{M}_a & 0 & \hat{M}_{1b} \\
\frac{\hat{\omega}}{2} & -\hat{s} & 0 & 0 & -\frac{\hat{\omega}}{2} & \hat{s} & 0 & 0 & 0 & \hat{M}_{1a} & 0 & -\hat{M}_b \\
0 & 0 & 0 & 0 & 1+L_t & 0 & -L_t & 0 & \hat{K}_{11} & 0 & \hat{K}_{12} & 0 \\
0 & 0 & 0 & 0 & -L_c & 0 & 1+L_c & 0 & \hat{K}_{21} & 0 & \hat{K}_{22} & 0 \\
0 & 0 & 0 & 0 & 0 & 1+L_t & 0 & -L_t & 0 & \hat{K}_{11} & 0 & \hat{K}_{21} \\
0 & 0 & 0 & 0 & 0 & -L_c & 0 & 1+L_c & 0 & \hat{K}_{21} & 0 & \hat{K}_{22} \\
\left(\frac{\hat{\gamma}}{2}+1\right)\hat{s} & \frac{\hat{\omega}}{2} & 0 & 0 & -\hat{s} & -\frac{\hat{\omega}}{2} & 0 & 0 & 0 & 0 & 0 & 0 \\
-\frac{\hat{\omega}}{2} & \left(\frac{\hat{\gamma}}{2}+1\right)\hat{s} & 0 & 0 & \frac{\hat{\omega}}{2} & -\hat{s} & 0 & 0 & 0 & 0 & 0 & 0 \\
0 & 0 & \left(\frac{\hat{\gamma}}{2}+1\right)\hat{s} & \frac{\hat{\omega}}{2} & 0 & 0 & -\hat{s} & -\frac{\hat{\omega}}{2} & 0 & 0 & 0 & 0 \\
0 & 0 & -\frac{\hat{\omega}}{2} & \left(\frac{\hat{\gamma}}{2}+1\right)\hat{s} & 0 & 0 & \frac{\hat{\omega}}{2} & -\hat{s} & 0 & 0 & 0 & 0
\end{bmatrix}
\begin{Bmatrix} R_a \\ S_a \\ R_b \\ S_b \\ R_{1a} \\ S_{1a} \\ R_{1b} \\ S_{1b} \\ R_1 \\ S_1 \\ R_2 \\ S_2 \end{Bmatrix} = 0, \tag{3.14}$$

where $2m = m_a + m_b$; $\hat{M}_a = M_a L_t \hat{s}^2$, $\hat{M}_{1a} = M_a\left(1+L_t\right)\hat{s}^2$, $\hat{M}_{1b} = M_b\left(1+L_c\right)\hat{s}^2$, $\hat{M}_b = M_b L_c \hat{s}^2$, $\hat{K}_{11} = -\hat{\alpha}_{11} M_a \hat{s}^2 - 1$, $\hat{K}_{21} = -\hat{\alpha}_{21} M_a \hat{s}^2$, $\hat{K}_{12} = -\hat{\alpha}_{12} M_b \hat{s}^2$, $\hat{K}_{22} = -\hat{\alpha}_{22} M_b \hat{s}^2 - 1$, $\hat{\alpha}_{ij} = \alpha_{ij} m \omega_1^2$, $M_{a,b} = m_{a,b}/m$, $L_t = \left(l_t/l\right)$, $L_c = \left(l_c/l\right)$ are the non-dimensional groups. $\hat{\gamma} = \gamma/A$, $\hat{s} = \lambda/\omega_1$, $\omega_1 = 2\bar{A}/m$, $\hat{\omega} = \omega/\omega_1$, $\bar{A} = \frac{\pi \mu_B L_B{}^3 R_B}{C^3}$ are the same as defined in Chapter 2. This equation is solved and the stability of the roots are analysed in the following Section.

3.3 ANALYSIS: ROTOR BENDING AND SUB-SYNCHRONOUS WHIRL

In this Section, the stability of the roots of the characteristic equation and the related modeshapes of the turbocharger with flexible rotor and floating ring bearings are analysed. The characteristic equation of the determinant given in Eq. (3.14) is solved for the turbocharger shown in Figure 3.1 using the values α_{11}= 7.199e-8 $\sec^2/kg$, α_{12}= 1.312e-8 $\sec^2/kg$, α_{21}= 1.312e-8 $\sec^2/kg$, α_{22}= 4.392e-8 $\sec^2/kg$. m_a= 0.2513 kg, m_b= 0.0676 kg, l_c=33.13 mm, l=38.7 mm, l_t=35.02 mm, $\bar{A} = 1297$, $\hat{\gamma} = 10$. Note that the calculation of the influence coefficients is described in section 3.2.3. The solution gives 6 pairs of complex conjugate roots, of which two pairs are unstable roots with positive real parts similar to Chapter 2. The real parts of the roots are plotted in Figure 3.5 and Figure 3.6. The real parts of the roots give the damping in the system while the imaginary parts give the whirl frequency. The positive real parts imply that the whirl amplitude grows with time, where the journal centre keeps whirling outward. The negative real parts imply that the whirl amplitude reduces with time regaining the journal centre's original position. Figure 3.7 shows the imaginary parts of the roots, which are the whirl frequencies of the turbocharger rotor in the floating ring bearings as a function of non-dimensional speed. It was seen in Chapter 2 that the whirling frequencies are functions of the rotor speed. However, Figure 3.7 shows that the two frequencies corresponding to modes 4 and 6, have a natural frequency at zero speed. Since the stiffness of the bearings is speed dependent, the stiffness is negligible at zero speed. The flexible model has rotor stiffness in series with the bearing stiffness and damping. Hence, these two modes must be due to the vibration of the compressor and the turbine masses on the rotor spring under free-free condition. Moreover, Mode 4 remains almost at a constant frequency for all the speeds, which indicates that this frequency is mainly determined by the rotor stiffness. Mode 6 increases with increasing speed, which indicates that this frequency is determined by the effective stiffness of the rotor and the bearings.

Similar to the rigid rotor behaviour discussed [54], Figure 3.6 shows the real parts of the two unstable modes 2 and 4 crossing at a certain speed. This behaviour indicates a shift of the dominant mode, with mode 2 dominant in the low speed range and mode 3 dominant in the high speed range. Compared to the models used in Chapter 2 where the displacements of the journals in the two bearings were considered alone, the present treatment allows the relative displacements of the masses and the journals in the bearings to be observed. The modeshapes are effectively governed by the in-phase and out-of-phase movements of these 4 locations on the rotor. Figure 3.8 shows the modeshape of mode 1 which is a stable conical mode. Figure 3.9 shows the modeshape of mode 4 which is the next stable mode. This mode is a result of journal displacements in the bearings being out of phase with each other appearing like a second bending mode of the rotor. This mode has little or no displacement of the masses but has high amplitudes at the bearing centres. Figure 3.10 and Figure 3.11 are the mode-shapes of mode 5 and 6 respectively. They are more like bending modes driven mostly by the compressor mass.

The unstable mode 2 that is dominant in the low speed range is the conical mode which is shown in Figure 3.12(a), (b) at low speeds and Figure 3.12(c), (d) at high speeds respectively. This mode is essentially a rigid body mode and is little affected by the rotor flexibility. Figure 3.13(a) and (b) show the modeshapes of mode 3 that is dominant in the high speed range which is an in-phase whirl mode. At low speed of about 7771 rpm, the mode shows almost no bending in the rotor as shown in Figure 3.13(a), (b). But at high speeds, above about 101,030 rpm, i.e. around a whirl frequency of 22,581 rpm, the rotor starts to show a little bending as shown in Figure 3.13(c), (d). Figure 3.14 shows a comparison of this mode for various speeds, where the rotor shows bending and a very little change in the modeshape after about 100,000 rpm.

Figure 3.7 shows that the whirl frequency of the rotor is about 50% of the rotor speed at low speeds. However the ratio of the frequency to the speed reduces with increasing speed. This implies that the rotor’s whirling frequency is about the first bending frequency only at a very high speed for the turbocharger under investigation. A simple eigenvalue analysis is done using the finite element model created for the influence coefficients determination in section 3.2.3, with added mass matrix. The beam model is pinned at the two bearing locations. It showed that the first bending frequency under pin-pin condition is about 100,000 rpm. This implies that the rotor must be whirling at this frequency only at a speed above 200,000 rpm considering a 0.5 frequency ratio. The details of the mass matrix and the eigenvalue calculation are given in Appendix B.

3.4 CONCLUSIONS

A turbocharger linear model with a flexible rotor was developed by super-imposing the rigid motion and the flexible deflection. The flexibility of the rotor was incorporated into the model in the form of influence coefficients. The rotor-bearing system had full-film floating ring bearings, with the outer-film modelled as an external damper. The system was analysed for the stability of the whirling motion.

Similar to the rigid rotor model in Chapter 2, the flexible rotor model exhibits the conical and the in-phase unstable whirl modes. For the turbocharger investigated, the conical mode is almost a rigid body mode at high speeds while the in-phase whirl mode stays fairly rigid up to a speed of about 100,000 rpm and then starts showing little bending. Based on the analysis, it seems that assuming the rotor to be rigid is reasonable upto a speed of 100,000 rpm.

Although turbochargers have unstable modes, literature suggests their successful operation due to the nonlinearity of the oil-film. Hence a nonlinear analysis is essential to investigate the instabilities in greater detail. This is performed in the next chapter considering the effect of a static load which has been ignored in Chapter 2 and 3.

FIGURES

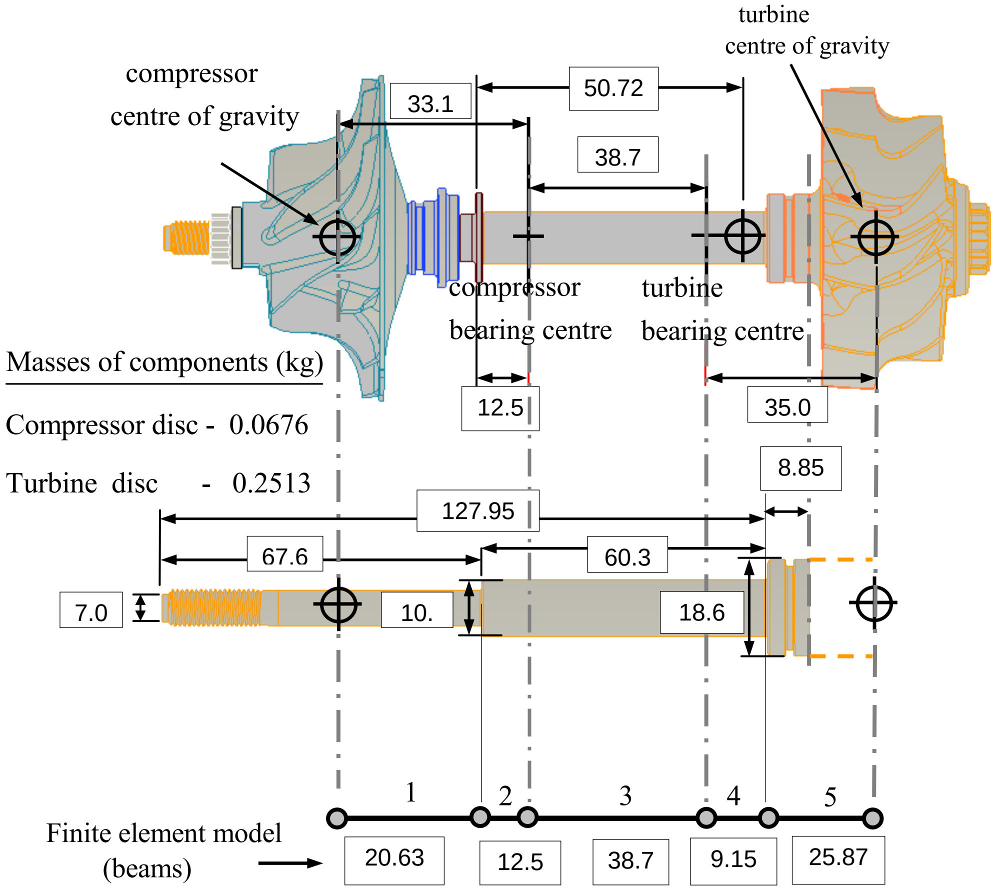

Figure 3.1 A typical automotive turbocharger used in the investigation of the effect of the rotor flexibility in the stability of the turbocharger. The finite element beam model used to calculate the influence coefficients of the rotor detailed in section 3.2.3 is also shown. All dimensions are in mm. (Adapted from the drawing given by *Cummins Turbo-Technologies Ltd)*

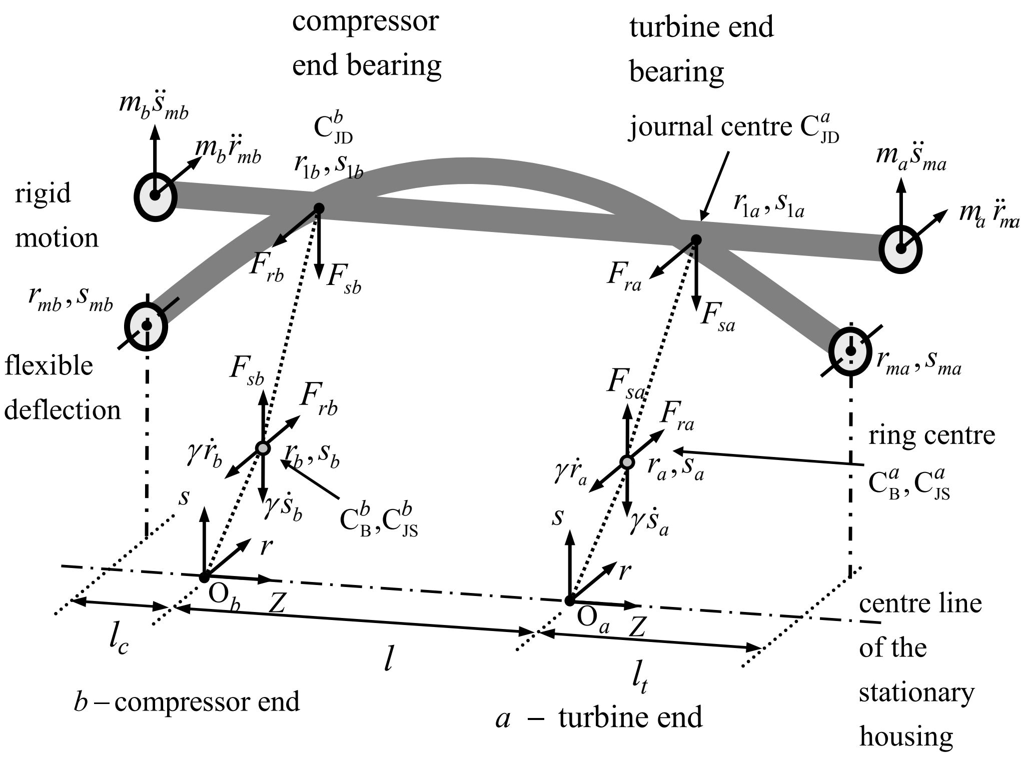

Figure 3.2 Co-ordinate system of a turbocharger with a flexible rotor and two identical floating ring bearings. Both the flexible deflection of the rotor and the rigid motion are superimposed; $(\cdot)_a$ represents the turbine end and $(\cdot)_b$ represents the compressor end; m_a, m_b are the turbine and the compressor masses respectively; C^a_B, C^b_B are the ring centres and and C^a_{JS}, C^b_{JS} are the corresponding journal static centres; l is the distance between the bearings; l_c is the distance between the compressor bearing centre and the compressor centre of gravity, and l_t is the distance between the turbine bearing centre and turbine centre of gravity; γ is the damping coefficient of the outer film; r is the axis along the line of centres of the journal and the bearing; s is the axis perpendicular to the line of centres in the plane of the bearing; Z is the axis along the length of the bearing; $r_{a,b}$, $s_{a,b}$ are the co-ordinates of the ring centre; $r_{1a,1b}$, $s_{1a,1b}$ are the co-ordinates of the journal dynamic centre; r_{ma}, s_{ma} and r_{mb}, s_{mb} are the co-ordinates of the turbine and the compressor mass centres respectively.

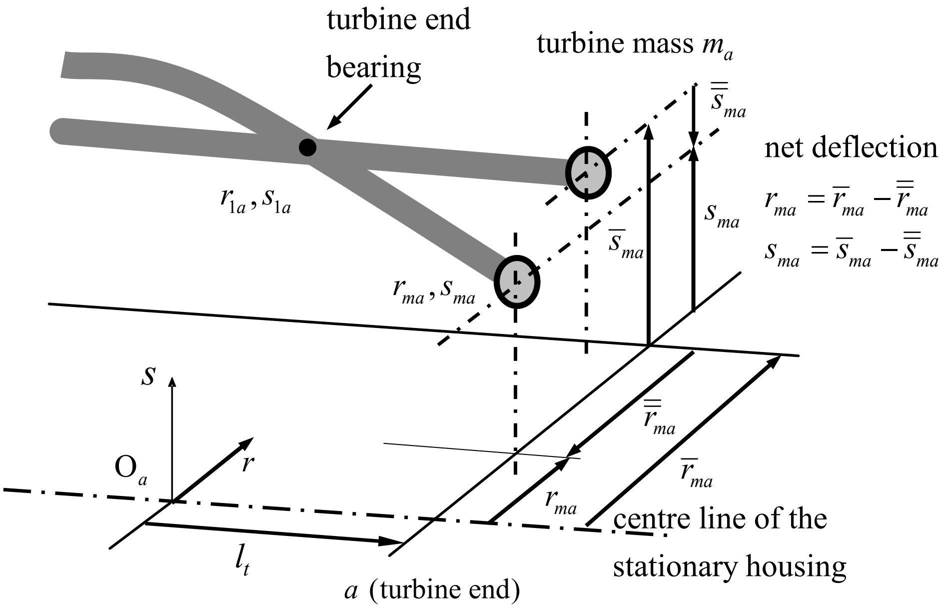

Figure 3.3 Net deflection of the turbine mass from both the rigid motion and the flexible deflection; r_{ma}, s_{ma} are the co-ordinates of the turbine mass with respect to the origin which is the centre of the stationary housing O_a; $\bar{r}_{ma}, \bar{s}_{ma}$ are the co-ordinates of the mass from the rigid motion alone. $-\bar{\bar{r}}_{ma}, -\bar{\bar{s}}_{ma}$ are the flexible deflections from position $\bar{r}_{ma}, \bar{s}_{ma}$ along r, s directions; r_{mb}, s_{mb} are determined likewise at the compressor end, where all the corresponding subscripts are replaced by mb.

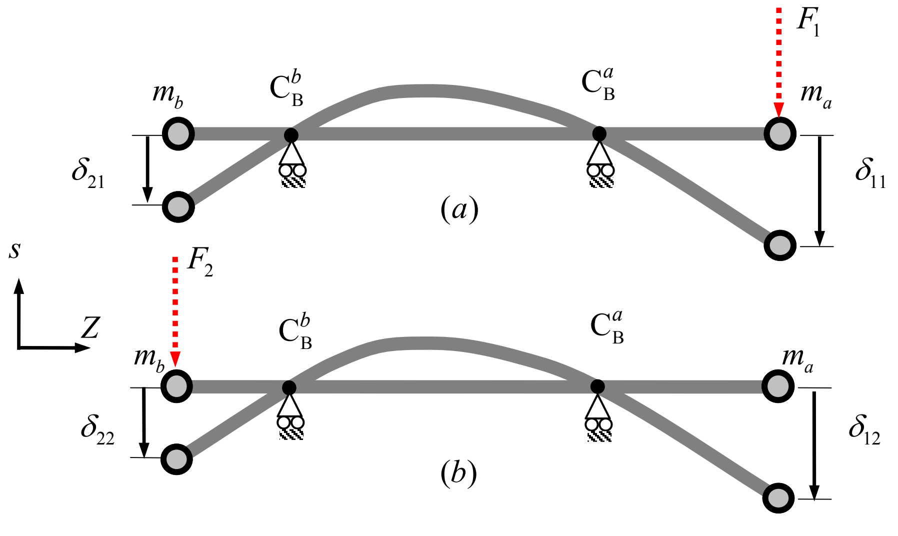

Figure 3.4 a) Rotor deflections at the turbine and the compressor mass centres under a static force F_1 applied at m_a; δ_{11}, δ_{21} are the corresponding displacements of m_a and m_b. b) Rotor deflections at the turbine and compressor mass centres under a static force F_2 applied at m_b; δ_{22}, δ_{12} are the corresponding displacements of m_b and m_a. The bearing centres are pinned allowing only rotation about the r axis; all other relative motions are constrained.

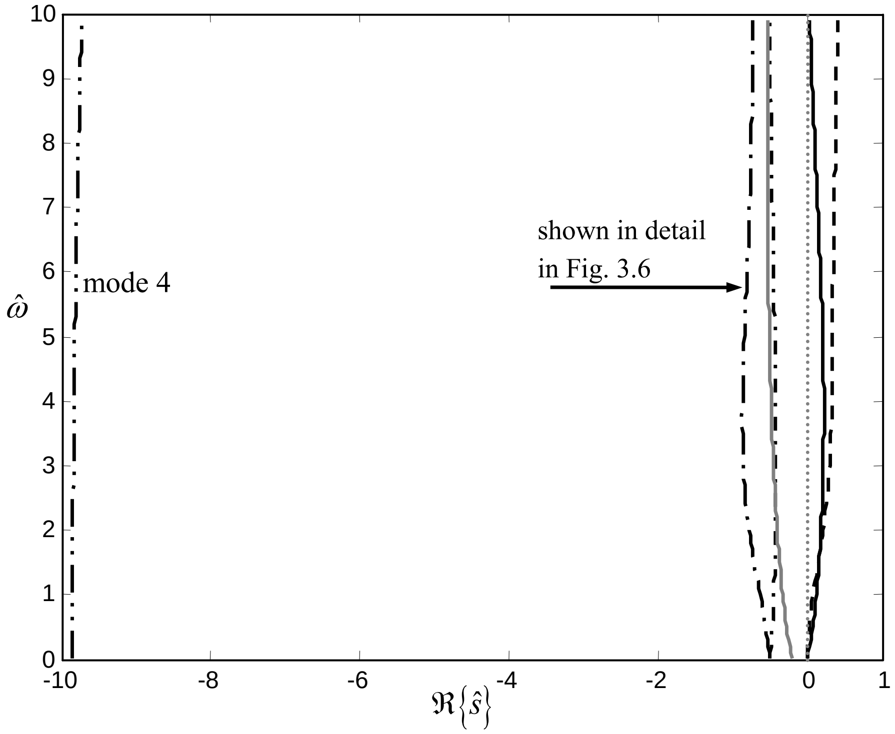

Figure 3.5 Plot of the real parts of the roots of the determinant of the matrix given in Eq. (3.14) giving the growth rate of the whirl amplitude of the turbocharger rotor shown in Figure 3.1 in floating ring bearings, when $\overline{A} = 1297$, $\overline{\gamma} = 10$.

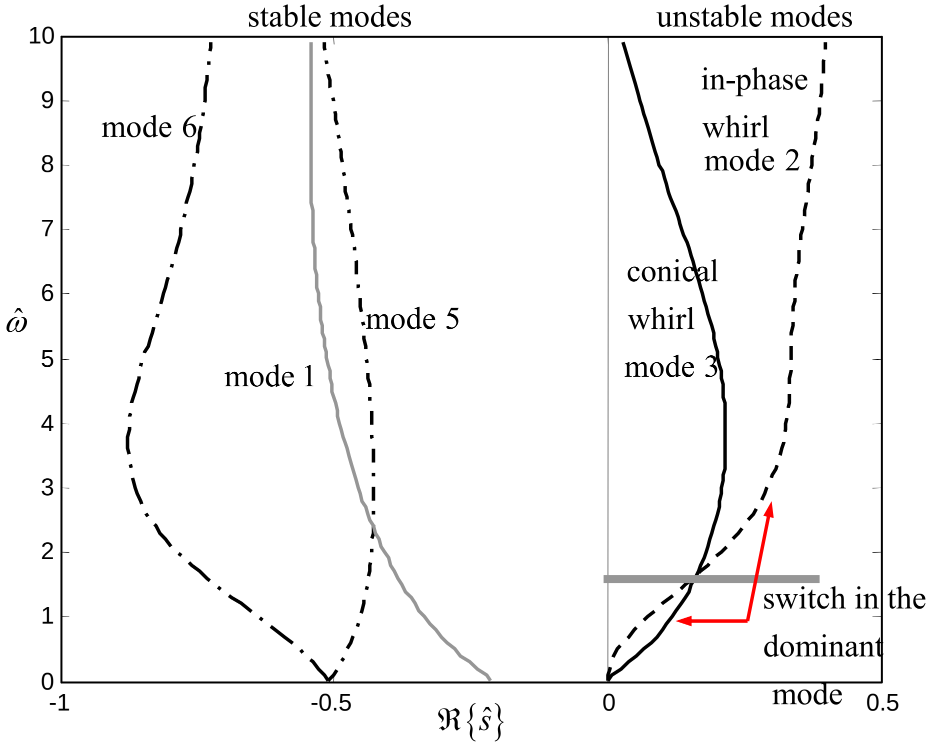

Figure 3.6 Plot of the real parts of the roots of the determinant of the matrix given in Eq. (3.14) giving the growth rate of the whirl amplitude of the turbocharger rotor shown in Figure 3.1 in floating ring bearings, when $\overline{A} = 1297$, $\hat{\gamma} = 10$. Mode 4 is not shown here for clarity.

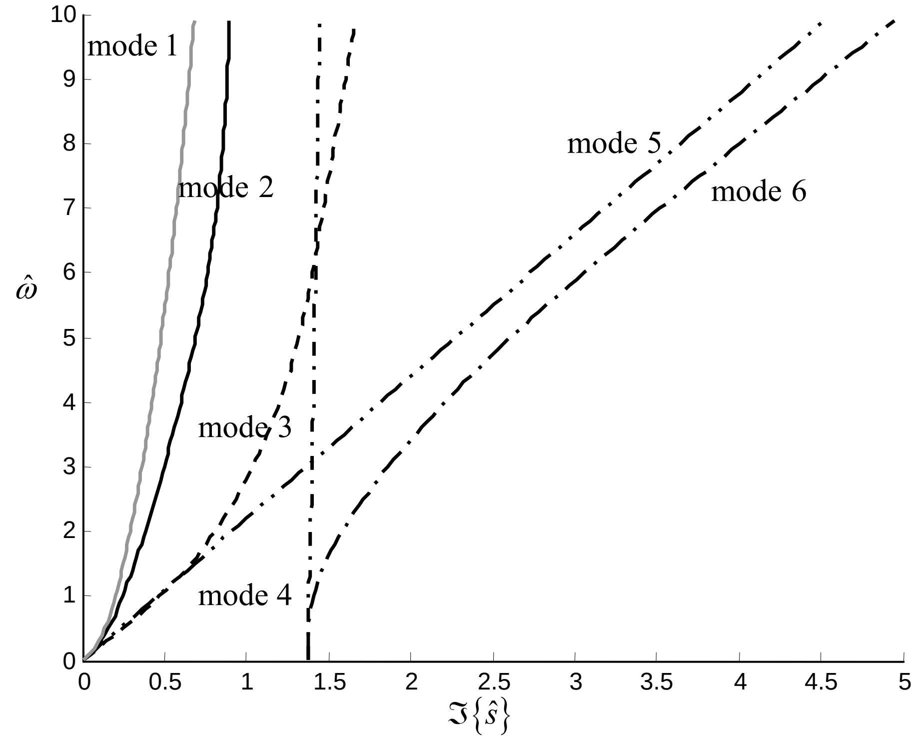

Figure 3.7 Plot of the imaginary parts of the roots of the determinant of the matrix given in Eq. (3.14) giving the whirl frequency of the turbocharger rotor shown in Figure 3.1 in floating ring bearings, when $\overline{A} = 1297$, $\hat{\gamma} = 10$. Mode 2 and mode 3 are the two unstable frequencies.

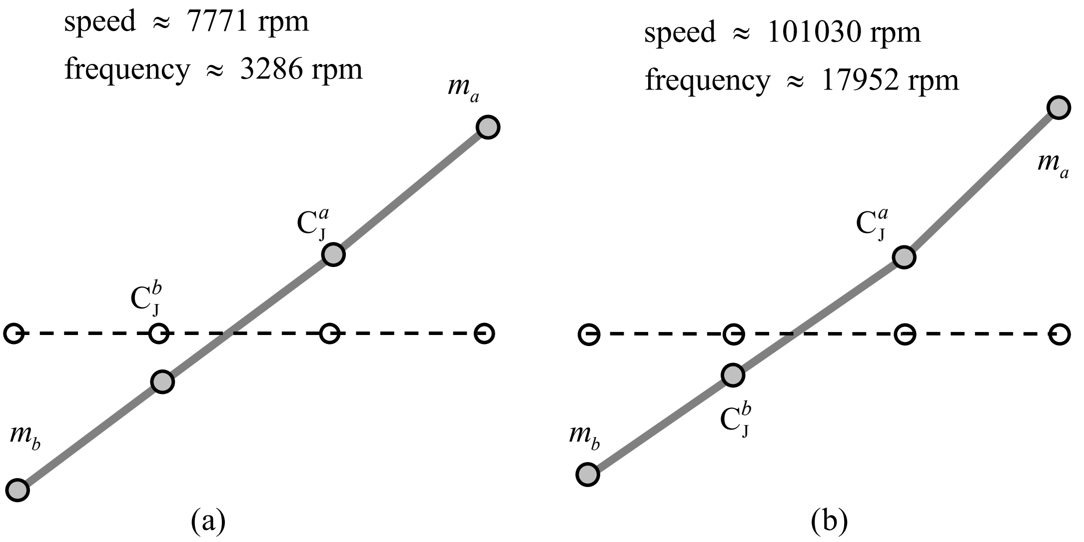

Figure 3.8 Mode shape of mode 1 which is a stable mode. (a) At a low speed $\hat{\omega} = 0.1$ (b) At a high speed $\hat{\omega} = 1.3$

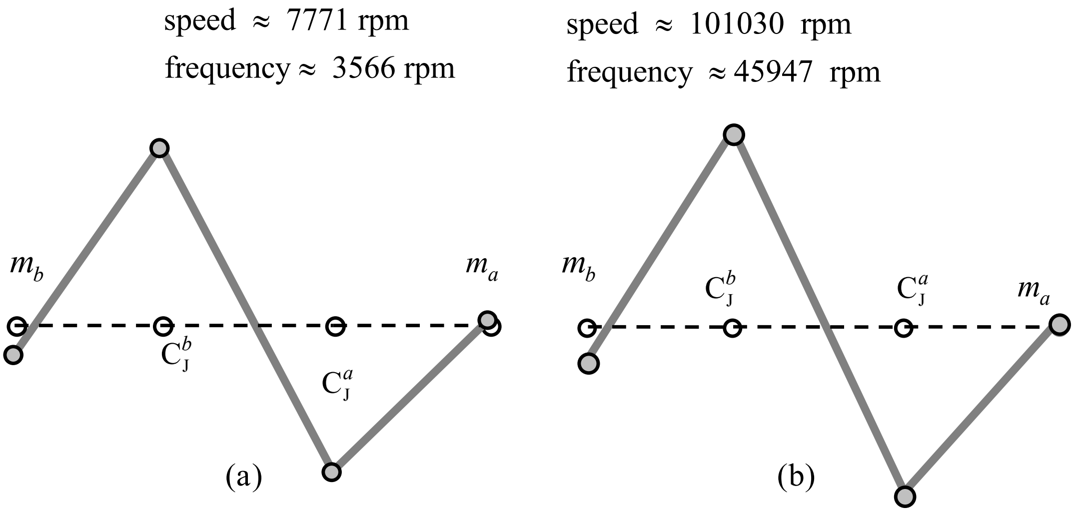

Figure 3.9 Mode shape of mode 4 which is a stable mode. (a) At a low speed $\hat{\omega} = 0.1$ (b) At a high speed $\hat{\omega} = 1.3$

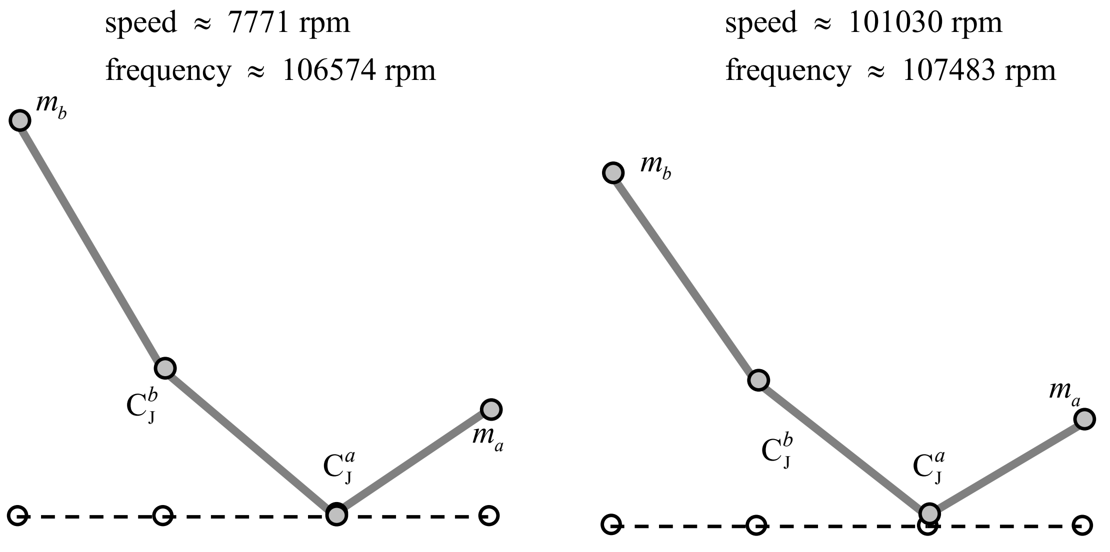

(a) (b)

Figure 3.10 Mode shape of mode 5 which is a stable mode. (a) At a low speed $\hat{\omega} = 0.1$ (b) At a high speed $\hat{\omega} = 1.3$

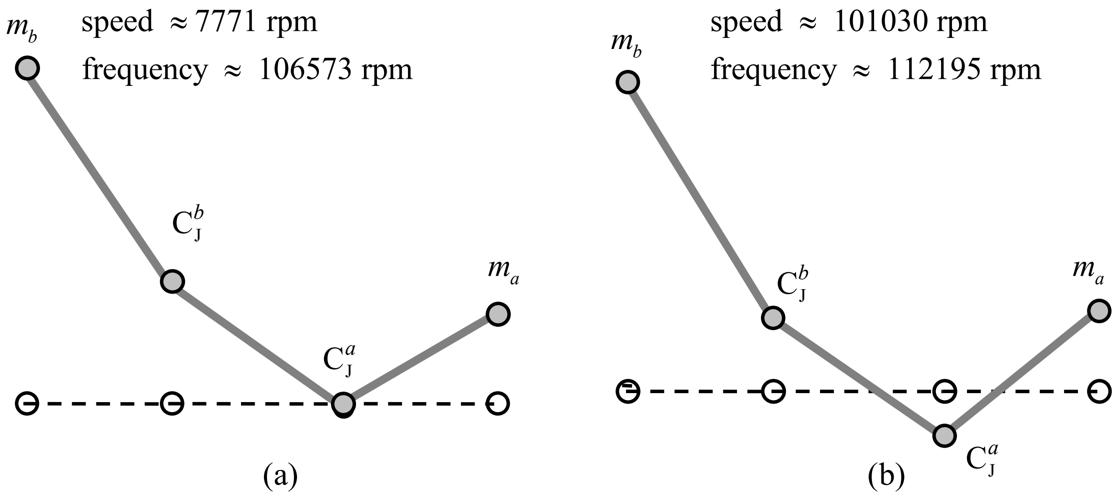

(a) (b)

Figure 3.11 Mode shape of mode 6 which is a stable mode. (a) At a low speed $\hat{\omega} = 0.1$ (b) At a high speed $\hat{\omega} = 1.3$

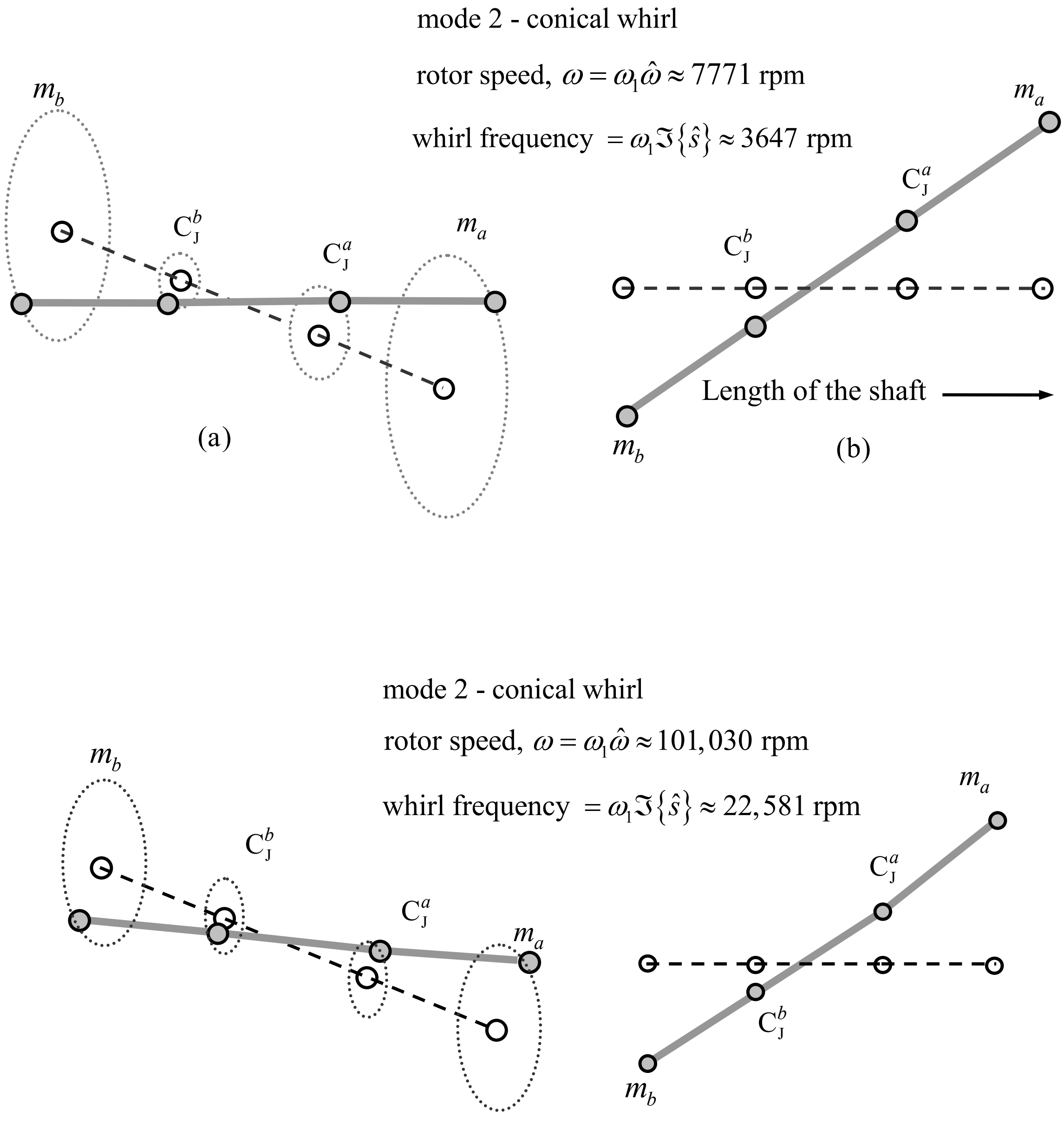

Figure 3.12 (a) 3 dimensional view of the mode shape of the conical whirl mode (b) Front view of the mode shape at a low speed of about 7771 rpm, at a whirl frequency of about 3647 rpm, when $\hat{\omega} = 0.1$, $\Im\{\hat{s}\} = 0.051$. (c) 3 dimensional view of the mode shape (d) Front view of the mode shape at a high speed of about 101,030 rpm, at a whirl frequency of about 22,581 rpm, when $\hat{\omega} = 0.1$, $\Im\{\hat{s}\} = 0.051$. The path of the compressor and the turbine centre of gravities and the journal motion in the bearings are shown in dotted lines.

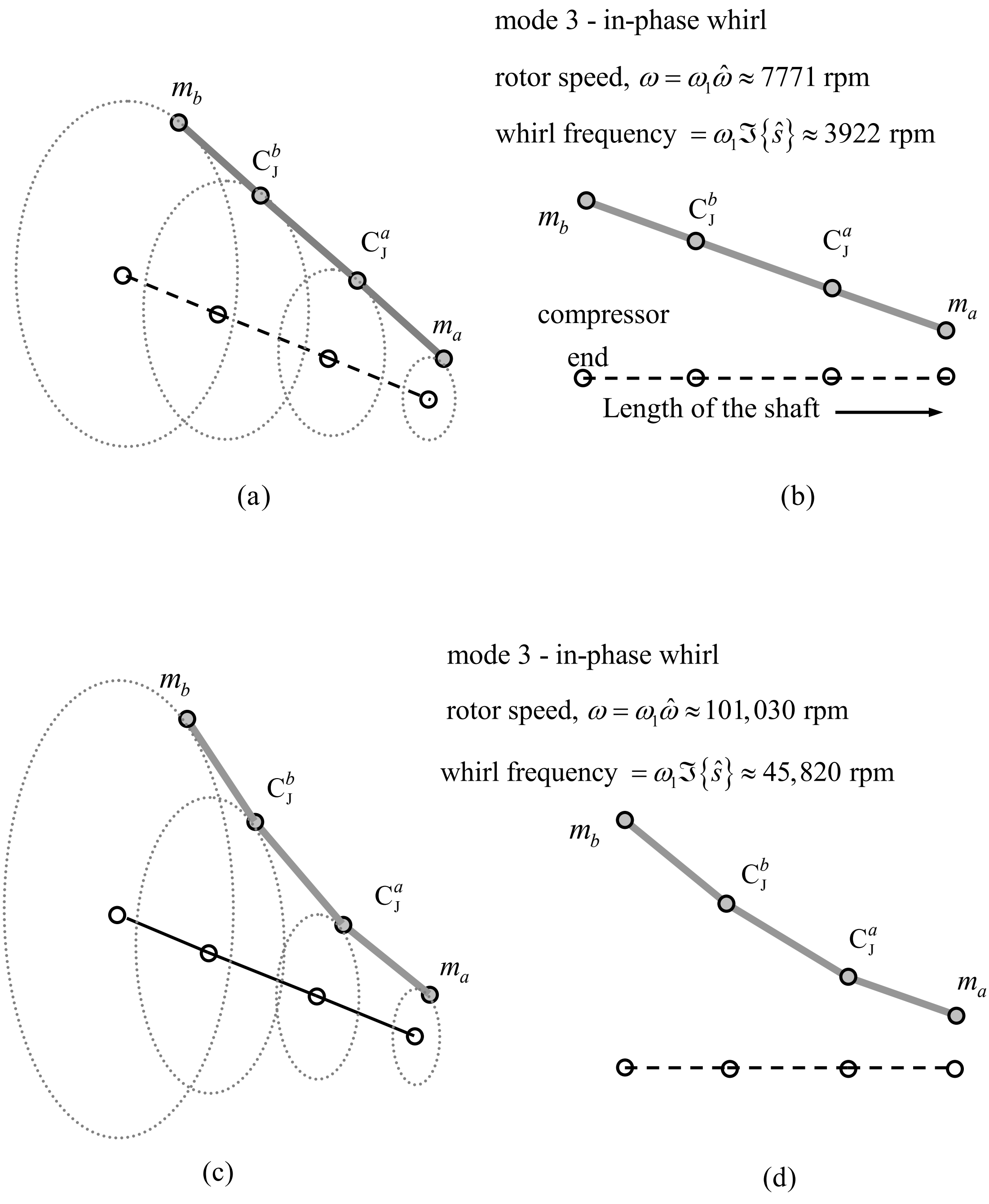

Figure 3.13 (a) 3 dimensional view of the mode shape of the in-phase whirl mode (b) Front view of the mode shape at a low speed of about 7771 rpm, at a whirl frequency of about 3922 rpm, when $\hat{\omega} = 0.1$, $\Im\{\hat{s}\} = 0.051$. The modeshape shows a rigid motion of the rotor. (c) 3 dimensional view of the mode shape (d) Front view of the mode shape at a high speed of about 101,030 rpm, at a whirl frequency of about 45,820 rpm, when $\hat{\omega} = 0.1$, $\Im\{\hat{s}\} = 0.051$. The modeshape shows bending of the rotor. The path of the compressor and the turbine centre of gravities and the journal motion in the bearings are shown in dotted lines.

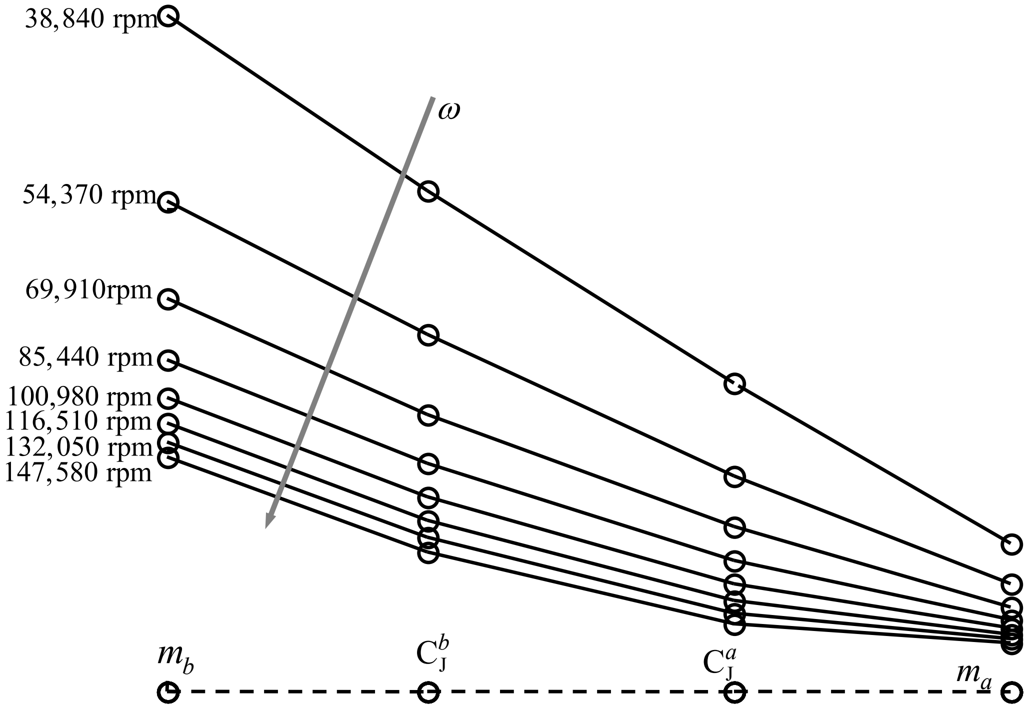

Figure 3.14 Mode shape of the in-phase whirl mode showing bending as the rotor speed is increased. Bending effect is relatively significant for speeds greater than about 69,910 rpm.

CHAPTER 4

THE EFFECT OF STATIC LOAD ON OIL-WHIRL IN A PERFECTLY BALANCED ROTOR-BEARING SYSTEM: LINEAR ANALYSIS

4.1 INTRODUCTION

In the previous Chapter, since the weight of the turbocharger rotor is negligible compared to the dynamic loads acting on the rotor, the static eccentricity ratio due to the gravity load has been neglected. Myers [43] has demonstrated the effect of a static load on the dynamics of a rotor-bearing system with rigid supports using the long-bearing approximation of the bearing forces. He used an oscillating π-film cavitation model which is detailed in Chapter 1. Myers presented a linear analysis to determine the stability threshold. His work includes a nonlinear analysis using the *Hopf bifurcation* method [70] applying *Poore's bifurcation formula* [71] to analyse the stability of the limit cycles. The long-bearing approximation gives the whirl frequency to speed ratio around unity; however, the oil-whirl occurs at a frequency ratio of 0.5 as shown in Chapter 2. To overcome this, Gardner [23] used the short-bearing approximation of the bearing forces and performed a similar exercise to analyse the linear and nonlinear influences of the static load on a similar rotor-bearing system using the static π-film cavitation model [8]. Nevertheless, Holmes [38] demonstrated a better correlation of the experimental journal orbits of a rotor system to that predicted by the oscillating π-film cavitation model using the short-bearing approximation [18]. This Chapter aims at analysing the influence of a static load using the short-bearing approximation [18] of the hydrodynamic bearings with an oscillating π-film cavitation model, to combine the benefits of the two in simulating oil-whirl. Although the difference between the static and the oscillating π-film models does not affect the linear steady-state analysis [8, 21], this model is used for its nonlinear effect which is presented in the next Chapter.

Myers and Gardner [23, 43] detailed a linear analysis to determine the threshold speed in the parameter plane of steady-state eccentricity ratio and the speed of the rotor. Further to that, with the help of the asymptotic analysis, this Chapter presents the case when the steady-state eccentricity ratio tends to zero. The significance of the radial restoring force in terms of various system parameters is discussed. The onset of oil-whirl at the stability threshold is reviewed to be a *Hopf bifurcation* [70] by analysing the eigenvalues of the Jacobian determinant of the linearised system, about the steady-state solution.

The gyroscopic effect is not considered in this Chapter, since the interest is in the in-phase whirl which is not affected by the gyroscopic moments as discussed in Chapter 2. The rotor is assumed to be rigid based on the work in Chapter 3, which showed that the flexibility of a typical turbocharger rotor could be insignificant up to about 100,000 rpm.

4.2 STABILITY THRESHOLD

4.2.1 INTRODUCTION

The aim of this Section is to determine the stability threshold of the bearing equilibrium state and to define the corresponding stable and unstable regions in terms of the steady-state eccentricity ratio and the rotational speed of the rotor. This is achieved by analysing the linearized equations of motion of a perfectly balanced rigid rotor mounted in journal bearings with a rigid support. An oscillating π-film cavitation model which is detailed in Chapter 1 is used as boundary conditions for the short-bearing approximation [18] of the Reynolds' equation in deriving the oil-film forces.

The details of boundary conditions in the derivation of the oil-film forces are discussed in Appendix A. The influence of the static load on the radial restoring force of the oil-film is studied. The case when the eccentricity ratio tends to zero is also considered.

4.2.2 EQUATIONS OF MOTION

4.2.2.1 CARTESIAN COORDINATES

The rotor-bearing system considered in this Chapter consists of a symmetric rigid rotor of mass $2m$ supported in two identical rigidly supported journal bearings similar to the configuration given in Chapter 1, Section 2.2.2. Figure 4.1 shows a schematic diagram of the rotor in the bearing, where e is the eccentricity of the journal centre with respect to the housing centre O in the clearance C; ϕ is the attitude angle of the line of journal centre $\mathrm{C_J}$ and the bearing centre $\mathrm{C_B}$ with the vertical direction. Note that, from this Chapter onwards, the journal centre is not distinguished as the static and dynamic centres $(\mathrm{C_{JS}},\mathrm{C_{JD}})$ separately as done in the previous Chapters. This is because, the treatment is focussed on the static load effect in terms of its steady-state position defined by n_s, ϕ_s; the suffix s denotes the steady-state; X,Y are the coordinates of the journal centre along the vertical and the horizontal axes respectively; F is the static load along X; ω is the rotational speed of the rotor; F_r^p, F_r^p are the radial and the tangential forces along r,s respectively, acting on the rotor, due to the pressure in the oil-film caused by the rotation of the rotor; $(\cdot)^p$ denotes the presence of an oscillating π-film cavitation in the bearings. For an oscillating π-film, the extent of fluid-film is from $\theta = 0$ to π radians, while the air cavity extends from $\theta = \pi$ to 2π radians of the clearance as discussed in Chapter 1. The other commonly used π film cavitation model is the static π-film model [8]. The static film model has the film extent fixed with respect to the housing where the boundary conditions are functions of the derivatives of the eccentricity ratio and the attitude angle. In the case considered in this chapter, the film extent is governed by the dynamics of the rotor. Holmes [38] demonstrated a better correlation of the experimental journal centre orbits of a rotor system with that predicted by the oscillating π-film cavity model compared to the static π-film cavitation model. The radial force F_r^p, and the tangential force F_s^p are non-dimensionalised as $\bar{F}_r = F_r^p / S_m F$, $\bar{F}_s = F_r^p / S_m F$; S_m is the modified Sommerfeld number for short-bearings and is given by [23]:

$$S_m = \frac{L_B{}^3 R_B \eta_B \omega}{C^2 F}, \tag{4.1}$$

which is a non-dimensional group defined by the bearing radius R and length L, the clearance C, the viscosity of oil-film μ_c, the speed ω and the static load F. It can be seen from Eq. (4.6) in comparison with Eq. (4.4), that the non-dimensional load capacity (static load) $\bar{F}$ is given by the inverse of the Sommerfeld number $1/S_m$. $\bar{F}_r$ and $\bar{F}_s$ are obtained by integrating the short-bearing approximation of the Reynolds' equation for thin films and applying the boundary condition of an oscillating π-film. The film forces are given by [19, 23] :

$$\bar{F}_r = -\left\{ \frac{n^2(1-2\dot{\phi})}{\left(1-n^2\right)^2} + \frac{\pi \dot{n}\left(1+2n^2\right)}{2\left(1-n^2\right)^{5/2}} \right\}, \tag{4.2}$$

$$\bar{F}_s = \left\{ \frac{\pi n(1-2\dot{\phi})}{4\left(1-n^2\right)^{\frac{3}{2}}} + \frac{2n\dot{n}}{\left(1-n^2\right)^2} \right\}, \tag{4.3}$$

where n is the eccentricity ratio given by the ratio of the eccentricity e to the clearance C. The derivation of these hydrodynamic forces is given in Appendix A. The radial restoring force $\bar{F}_r$ helps the stability of the rotor, while the tangential force $\bar{F}_s$ causes the rotor to whirl as seen in Chapter 1. From Eq. (4.2), it can be seen that $\bar{F}_r$ is stiffness-like in nature due to the presence of the spring force term $\left[n^2(1-2\dot{\phi}) / \left(1-n^2\right)^2 \right]$. The radial force in a full-film [20] is entirely damping-like in nature and is given by $\overline{F}_r = \left[\pi\dot{n}\left(1+2n^2\right)\Big/2\left(1-n^2\right)^{5/2}\right]$. Under the action of the film forces given by Eqs. (4.2) and (4.3) in each bearing, the equations of motion of the symmetric rotor supported in two such identical journal bearings with rigid support, along X and Y are given by:

$$m\frac{d^2X}{dt^2} = F + F_r^p \cos\phi - F_s^p \sin\phi \quad = F_X\,, \tag{4.4}$$

$$m\frac{d^2Y}{dt^2} = F_r^p \sin\phi + F_s^p \cos\phi \quad = F_Y\,. \tag{4.5}$$

From Figure 4.1, it is seen that the static load is given by $F = \sqrt{\left(F_r^p\right)^2 + \left(F_s^p\right)^2}$. The non-dimensional form of Eqs. (4.4) and (4.5) are given as:

$$\frac{\overline{\omega}^2\ddot{\overline{X}}}{S_m} = \frac{1}{S_m} + \overline{F}_r \cos\phi - \overline{F}_s \sin\phi\,, \tag{4.6}$$

$$\frac{\overline{\omega}^2\ddot{\overline{Y}}}{S_m} = \overline{F}_r \sin\phi + \overline{F}_s \cos\phi\,, \tag{4.7}$$

where: $\overline{X} = X/C$, $\overline{Y} = Y/C$, $\overline{\omega} = \left(mC/F\right)^{\frac{1}{2}}\omega$, $\tau = \omega t$, ω is the rotor speed; the over-dots denote the derivative with respect to τ; Note that $\overline{\omega}$ is non-dimensionalised using the static load, since the influence of the static load is the subject of interest in this Chapter. Hence it is different to the non-dimensional speed $\hat{\omega}$ used in the previous Chapters. Equations (4.6) and (4.7) can be represented as the functions of co-ordinates in the form:

$$\ddot{\overline{X}} = \frac{S_m}{\overline{\omega}^2}\overline{F}_X(\overline{X},\overline{Y},\dot{\overline{X}},\dot{\overline{Y}},S_m)\,, \tag{4.8}$$

$$\ddot{Y} = \frac{S_m}{\bar{\omega}^2}\bar{F}_Y(\bar{X},\bar{Y},\dot{\bar{X}},\dot{\bar{Y}},S_m). \tag{4.9}$$

4.2.2.2 POLAR CO-ORDINATES

The Cartesian system is mostly used in this thesis which is convenient for analytical purposes. Some of the advantages of this form are listed by Barrett [37]. However, it is found to be convenient to use the polar form in MATLAB programming as well as for the asymptotic analysis in Section 4.3.1.

Using the equations $X = n\cos\phi$ and $Y = n\sin\phi$, the equations of motion in n,ϕ coordinates are given by:

$$mC\left[\frac{d^2n}{dt^2} - n\left(\frac{d\phi}{dt}\right)^2\right] = F\cos\phi + F_r^{\,p}, \tag{4.10}$$

$$mC\left[n\frac{d^2\phi}{dt^2} + 2\frac{dn}{dt}\frac{d\phi}{dt}\right] = F_s^{\,p} - F\sin\phi. \tag{4.11}$$

The non-dimensional form of Eqs. (4.10) and (4.11) are given by:

$$\frac{\bar{\omega}^2}{S_m}(\ddot{n} - n\dot{\phi}^2) = \frac{1}{S_m}\cos\phi + \bar{F}_r, \tag{4.12}$$

$$\frac{\bar{\omega}^2}{S_m}(n\ddot{\phi} + 2\dot{n}\dot{\phi}) = \bar{F}_s - \frac{1}{S_m}\sin\phi, \tag{4.13}$$

where $\bar{F}_r$ and $\bar{F}_s$ are given by Eqs. (4.2) and (4.3).

4.2.2.3 STEADY-STATE CONDITION

In this Chapter, the main interest is to analyse the steady-state of the system using the linear analysis. In this Sub-Section, certain useful relations in terms of the system parameters and the steady-state variables are derived. When the journal motion reaches the steady-state, the dynamic behaviour does not change with time. Hence, in the steady-state, the solution to Eqs. (4.8) and (4.9) gives the equilibrium state X_s, Y_s, where, $X_s = n_s \cos(\phi_s)$, $Y_s = n_s \sin(\phi_s)$; n_s is the steady-state eccentricity ratio and ϕ_s is the steady-state attitude angle, which are the solutions to Eqs. (4.6) and (4.7) obtained by setting the time derivatives to zero. Under the steady-state condition, from Figure 4.1, the component of the resulting force along Y is given by:

$$\left(\overline{F}_r\right)_s \sin\phi_s + \left(\overline{F}_s\right)_s \cos\phi_s = 0\,, \tag{4.14}$$

which gives,

$$\tan\phi_s = -\left(\frac{\overline{F}_s}{\overline{F}_r}\right)_s, \tag{4.15}$$

where the subscript s denotes the steady-state condition. Substituting for $\overline{F}_r$, $\overline{F}_s$ from Eqs. (4.2) and (4.3) gives,

$$\tan\phi_s = \frac{\pi\left(1-n_s^2\right)^{\frac{1}{2}}}{4n_s}. \tag{4.16}$$

Now, the inverse of the non-dimensional load capacity is given by the Sommerfeld number as:

$$S_m(n_s) = \frac{1}{\sqrt{\left(\overline{F}_r\right)_s^2 + \left(\overline{F}_s\right)_s^2}} = \frac{4\left(1-n_s^2\right)^2}{n_s\left[\pi^2\left(1-n_s^2\right)+16n_s^2\right]^{\frac{1}{2}}}. \tag{4.17}$$

A change in the speed affects the Sommerfeld number as seen in Eq. (4.1) which in turn affects the steady-state equilibrium state. Lund [72] introduced a system parameter σ_m which is independent of the rotor speed. It is constant for any rotor system subject to a constant load, using a lubricant of constant viscosity and is defined by:

$$\sigma_m = \frac{S_m}{\bar{\omega}} = \left(\frac{L_B{}^3 R_B \eta_B}{\left(mCF\right)^{\frac{1}{2}} C^2} \right). \tag{4.18}$$

Note that the speed is non-dimensional. Figure 4.2 shows the locus of the equilibrium states defined by the parameters n_s, ϕ_s and is plotted using Eq. (4.16). Under the action of the static load, the journal centre assumes the steady-state which is defined by the locus shown in Figure 4.2. When the radial force is negligible $\left(F_r\right)_s \to 0$, Eq. (4.15) shows that $\phi_s \to 90^0$, i.e., the journal centre moves horizontally due to the tangential force which acts like a damping force as in the case of the full-film bearings [20]. When the tangential force is negligible, $\left(F_s\right)_s \to 0$, $\phi_s \to 0^0$, the journal centre moves vertically down towards the housing like a mass on a spring. As these forces vary, the journal centre traces the path shown in Figure 4.2. It can be seen from Eqs. (4.2) and (4.3) that the ratio $\left(\bar{F}_t / \bar{F}_r\right)_s$ is independent of the speed. The relationship between these forces with the static load is discussed in the following Section.

4.3 ANALYSIS OF THE LINEARIZED EQUATIONS OF MOTION

In this section, the equations of motion are linearised and analysed to determine the stability threshold between the stable and the unstable equilibrium states of the journal centre. The equilibrium states are defined in a parameter plane of the steady-state eccentricity ratio of the journal centre and the rotor speed. The whirl frequency of the rotor system is verified at this stability threshold. The equations of motion given in

Eqs. (4.8) and (4.9) are defined in the form of a first order system in terms of the state variables, $x_1 = X - X_s$, $x_2 = \dot{X}$, $x_3 = Y - Y_s$, $x_4 = \dot{Y}$ as:

$$\begin{cases} \dot{x}_1 = x_2, \\ \dot{x}_2 = \dfrac{S_m}{\overline{\omega}^2} \overline{F}_X(x_1, x_2, x_3, x_4, S_m), \\ \dot{x}_3 = x_4, \\ \dot{x}_4 = \dfrac{S_m}{\overline{\omega}^2} \overline{F}_Y(x_1, x_2, x_3, x_4, S_m). \end{cases} \tag{4.19}$$

The Jacobian determinant $D\,\mathrm{f}(x)$ of the system (4.19), which is of the form $\dot{x} = \mathrm{f}(x)$, is given by:

$$\mathbf{A} = \frac{\partial(\dot{x}_1, \dot{x}_2, \dot{x}_3, \dot{x}_4)}{\partial(\overline{X}, \dot{\overline{X}}, \overline{Y}, \dot{\overline{Y}})} = \begin{vmatrix} 0 & 1 & 0 & 0 \\ -\dfrac{k_{xx}}{\overline{\omega}^2} & -\dfrac{b_{xx}}{\overline{\omega}^2} & -\dfrac{k_{xy}}{\overline{\omega}^2} & -\dfrac{b_{xy}}{\overline{\omega}^2} \\ 0 & 0 & 0 & 1 \\ -\dfrac{k_{yx}}{\overline{\omega}^2} & -\dfrac{b_{yx}}{\overline{\omega}^2} & -\dfrac{k_{yy}}{\overline{\omega}^2} & -\dfrac{b_{yy}}{\overline{\omega}^2} \end{vmatrix}, \tag{4.20}$$

where:

$$\begin{aligned} k_{xx} &= -S_m \left(\frac{\partial \overline{F}_X}{\partial \overline{X}} \right)_s, k_{xy} = -S_m \left(\frac{\partial \overline{F}_X}{\partial \overline{Y}} \right)_s, b_{xx} = -S_m \left(\frac{\partial \overline{F}_X}{\partial \dot{\overline{X}}} \right)_s, b_{xy} = -S_m \left(\frac{\partial \overline{F}_X}{\partial \dot{\overline{Y}}} \right)_s, \\ k_{yx} &= -S_m \left(\frac{\partial \overline{F}_Y}{\partial \overline{X}} \right)_s, k_{yy} = -S_m \left(\frac{\partial \overline{F}_Y}{\partial \overline{Y}} \right)_s, b_{yx} = -S_m \left(\frac{\partial \overline{F}_Y}{\partial \dot{\overline{X}}} \right)_s, b_{yy} = -S_m \left(\frac{\partial \overline{F}_Y}{\partial \dot{\overline{Y}}} \right)_s. \end{aligned} \tag{4.21}$$

To compute the eigenvalues $\hat{s}$ of $\mathbf{A}$, the characteristic equation is given by:

$$\left| \mathbf{A} - \hat{s}\mathbf{I} \right| = 0, \tag{4.22}$$

where $\mathbf{I}$ is a 4×4 identity matrix. The determinant in Eq. (4.22) expands into,

$$\begin{aligned}&\bar{\omega}^4\hat{s}^4+\left(b_{xx}+b_{yy}\right)\bar{\omega}^2\hat{s}^3+\left(\left(k_{xx}+k_{yy}\right)\bar{\omega}^2+b_{xx}b_{yy}-b_{xy}b_{yx}\right)\hat{s}^2\\&+\left(b_{xx}k_{yy}+b_{yy}k_{xx}-b_{xy}k_{yx}-b_{yx}k_{xy}\right)\hat{s}+\left(k_{xx}k_{yy}-k_{xy}k_{yx}\right)=0\end{aligned}. \tag{4.23}$$

In the stable region, the eigenvalues of the characteristic equation given in Eq. (4.23) are two complex conjugate pairs with negative real parts implying the existence of decaying amplitude. One of them crosses the imaginary axis at the threshold speed. At this speed, one of the pairs of eigenvalues is purely imaginary and this pair becomes unstable with a positive real part, which corresponds to growing amplitude, above the threshold speed. Using Routh's stability criterion, $A_2>(A_1A_4/A_3)+(A_3A_0/A_1)$, where A_p, $p=0,1,2,3,4$ are the coefficients of terms $\hat{s}^p$; p denotes the order of the term, a threshold speed $\bar{\omega}_0$ that divides the stable and the unstable equilibrium states is determined, which is given by [23]:

$$\bar{\omega}_0{}^2=\frac{B_{xx}B_{yy}-B_{xy}B_{yx}}{\left(\dfrac{\left(B_{xx}+B_{yy}\right)\left(K_{xx}K_{yy}-K_{xy}K_{yx}\right)}{\left(B_{xx}K_{yy}+B_{yy}K_{xx}-B_{xy}K_{yx}-B_{yx}K_{xy}\right)}-\dfrac{\left(B_{xx}K_{xx}+B_{yy}K_{yy}+B_{xy}K_{yx}+B_{yx}K_{xy}\right)}{\left(B_{xx}+B_{yy}\right)}\right)}. \tag{4.24}$$

Figure 4.3 is a plot of $\bar{\omega}_0$ from Eq. (4.24) as a function of n_s, which separates the stable and the unstable equilibrium states defined in terms of the steady-state eccentricity ratio and the rotational speed. If the speed is less than the threshold speed, the journal centre, when perturbed, spirals inwards to a stable equilibrium state. On the other hand, if the speed is greater than the threshold speed ($\bar{\omega}>\bar{\omega}_0$), the journal centre reaches an unstable equilibrium state. Any small displacement from this state, takes the journal centre on to an orbit which leads it to spiral out towards the housing away from the equilibrium state. The threshold curve asymptotes vertically for an eccentricity ratio of $n_s\approx 0.76$. This implies that all the equilibrium states corresponding to the steady-state eccentricity ratios above about 0.76 are stable. When $n_s\rightarrow 0$, the threshold speed is $\bar{\omega}_0=2.76$. Two operating curves that represent two types of rotor systems are shown for $\sigma_m=0.1$ and 10. For a certain combination of the system parameters defined in Eq.

(4.18) i.e. for a specific rotor system, these curves show at what eccentricity ratio and speed their equilibrium state changes stability. When $\sigma_m >> 1$, the system becomes unstable at a low eccentricity ratio ($n_s \approx 0.05$) as the speed is increased. When $\sigma_m << 1$, the system becomes unstable at a much higher eccentricity ratio ($n_s \approx 0.7$).

Figure 4.4(a) shows the real parts of the unstable eigenvalues crossing the imaginary axis and Figure 4.4(b) shows the imaginary parts crossing 0.5 which indicates oil-whirl at a frequency of the order of the half-rotational speed. The frequency lines corresponding to each eccentricity ratio crosses 0.5 at different speeds, which relates to the variation in the threshold speed with the eccentricity ratio. The whirling frequency reduces from a higher value which is fairly synchronous with the speed to about 0.5 at the threshold speed indicating the onset of oil-whirl. Above $\bar{\omega}_0$, it reduces further with the increasing speed. From Eq. (4.23), the whirl frequency at the threshold speed is given by [23]:

$$\Omega_0 = \left(\frac{\left(B_{xx}K_{yy} + B_{yy}K_{xx} - B_{xy}K_{yx} - B_{yx}K_{xy} \right)}{\left(B_{xx} + B_{yy} \right)} \right)^{\frac{1}{2}} \frac{1}{\bar{\omega}_0}. \tag{4.25}$$

Figure 4.5 shows the plot of Eq. (4.25) where the whirl frequency at the threshold speed is 0.5. This is referred as the half-frequency whirl in the literature. However, the whirl frequency reduces as the steady-state eccentricity ratio increases. It reaches zero, when $n_s \approx 0.76$, where the threshold speed asymptotes vertically indicating the disappearance of oil-whirl. In order to get a physical insight into the behaviour of the static load with increase in the steady-state eccentricity ratio, the following section analyses the role of the bearing forces.

4.3.1 THE EFFECT OF STATIC LOAD IN THE BEARINGS WITH π-FILM CAVITATION

Figure 4.3 shows that the threshold speed asymptotes to infinity at an eccentricity ratio about 0.76, implying the existence of stable equilibrium states for all speeds when $n_s > 0.76$. It can be seen in Figure 4.2 that, increasing the static load increases the eccentricity of the rotor in the bearing clearance by virtue of the film stiffness and damping characteristics. This seems to increase the film forces which balance the static load in order to achieve an equilibrium state. To this end, it is necessary to understand the role of the film forces in achieving a stable operation. This is done in this section by starting with the analysis of the horizontal asymptote of the threshold curve when $n_s \to 0$.

As it has already been mentioned, Figure 4.3 shows a threshold value of $\bar{\omega}_0 = 2.76$ when $n_s \approx 0$. In order to evaluate this value analytically, let $n_s^2 << 1$ then $1 \pm n_s^2 \approx 1$, and Eqs. (4.16) and (4.17) can be simplified to:

$$\phi_s(n_s) \approx \tan^{-1}\left(\frac{\pi}{4n_s}\right), \tag{4.26}$$

$$S_m(n_s) = \frac{1}{\bar{F}} = \frac{1}{n_s\left[\left(\frac{\pi}{4}\right)^2 + n_s^2\right]^{\frac{1}{2}}}. \tag{4.27}$$

Equation (4.26) and (4.27) define the oil-film forces and the static load as functions of the steady-state eccentricity ratio. The occurrence of a factor $\pi/4$ can be seen in Equations (4.26) and (4.27). Hence, considering the case when $n_s^2 << \pi^2/16$, Eq. (4.27) gives the approximation of Sommerfeld number as:

$$S_m = \frac{4}{n_s \pi}. \tag{4.28}$$

Since the coefficients are directly defined in terms of the steady-state eccentricity ratio, for this asymptote analysis, the polar form of the equations of motion given in Eqs.

(4.12) and (4.13) are considered in this Section. For $n_s^{\,2} << \pi^2/16$, using Eq. (4.28), the linear coefficients of the characteristic equation given in Eq. (4.23) can be simplified as:

$$K_{nn} \approx \left(\frac{2n_s}{\pi}\right),\ K_{n\phi} \approx \left(\frac{n_s}{4}\right),\ K_{\phi n} \approx -\frac{1}{4n_s},\ K_{\phi\phi} \approx \frac{n_s}{\pi}, \tag{4.29}$$

$$B_{nn} \approx \left(\frac{1}{2}\right),\ B_{n\phi} \approx -\left(\frac{2n_s^{\,2}}{\pi}\right),\ B_{\phi n} \approx -\left(\frac{2}{\pi}\right),\ B_{\phi\phi} \approx \left(\frac{1}{2}\right). \tag{4.30}$$

Similar to Eq. (4.24), using the polar coefficients given in Eqs. (4.29) and (4.30), the threshold speed can be written in the form,

$$\bar{\omega}_0 = \sqrt{\frac{\widehat{A}}{\widehat{B}-\widehat{C}}}, \tag{4.31}$$

where:

$$\widehat{A} = \left(B_{nn}B_{\phi\phi} - B_{\phi n}B_{\phi n}\right)S_m\pi,$$

$$\widehat{B} = \frac{\left(B_{nn}+B_{\phi\phi}\right)\left(K_{nn}K_{\phi\phi}-K_{n\phi}K_{\phi n}\right)}{\left(B_{nn}K_{\phi\phi}+B_{\phi\phi}K_{nn}-B_{n\phi}K_{\phi n}-B_{\phi n}K_{n\phi}\right)},$$

$$\widehat{C} = \frac{\left(B_{nn}K_{nn}+B_{\phi\phi}K_{\phi\phi}+B_{n\phi}K_{\phi n}+B_{\phi n}K_{n\phi}\right)}{\left(B_{nn}+B_{\phi\phi}\right)}.$$

These are the functions of the coefficients in the polar co-ordinates equivalent to that of Eq. (4.21). Using the Sommerfeld number in Eq. (4.28), the threshold speed is approximately determined from Eq. (4.31) using ,

$$\widehat{A} \approx \frac{16}{n_s\pi^2}\left(\frac{\pi^2}{16}-n_s^2\right),\ \widehat{B} \approx \left(\frac{\pi}{24n_s}\right), \widehat{C} \approx \left(\frac{3n_s}{2\pi}\right), \tag{4.32}$$

Thus,

$$\bar{\omega}_0^2 \approx \frac{24\pi}{\left(\pi^2 - 36n_s^2\right)} = \frac{24}{\pi}, \tag{4.33}$$

i.e.

$$\bar{\omega}_0 \approx \sqrt{\frac{24}{\pi}} \approx 2.764, \tag{4.34}$$

which can be seen in Figure 4.3 for $n_s \approx 0$. From Eq. (4.31), it can be seen that, when $A < 0$, $\bar{\omega}_0{}^2$ becomes negative as $\widehat{B} > \widehat{C}$ ($\bar{\omega}_0$ is imaginary). From Eq. (4.32), it is seen that this occurs when $n_s{}^2 > \pi^2/16$. For $n_s{}^2 < \pi^2/16$, $\bar{\omega}_0{}^2$ is positive. This suggests that $\bar{\omega}_0{}^2$ changes its sign when $n_s = +\pi/4 \approx +0.79$. This is a reasonably good approximation of the vertical asymptote at $n_s \approx 0.76$, although it stems from the assumption $n_s^2 << 1$. This suggests that there is physical significance of the eccentricity ratio, $n_s = +\pi/4$. Using Eq. (4.26), considering $n_s = \pi/4$, the approximate tangent of the steady-state attitude angle is given by:

$$\tan\phi_s = -\left(\frac{\bar{F}_s}{\bar{F}_r}\right)_s \approx \left(\frac{\pi}{4n_s}\right) = 1, \tag{4.35}$$

which makes $\phi_s = 45^\circ$ and,

$$\bar{F}_s = -\bar{F}_r. \tag{4.36}$$

Substituting for $\bar{F}_s$ from Eq. (4.36) into Eq. (4.14) gives,

$$\left(\bar{F}_r\right)_s \sin\phi_s - \left(\bar{F}_r\right)_s \cos\phi_s = \frac{1}{S_m} = \bar{F}, \tag{4.37}$$

i.e.,

$$\frac{1}{S_m} = \bar{F} = \sqrt{2}\left(\bar{F}_r\right)_s \text{ or } \left(\frac{\bar{F}_r}{\bar{F}}\right)_s = \frac{1}{\sqrt{2}} = 0.707\,. \tag{4.38}$$

As discussed in Section 4.2.2.3, the eccentricity increases as the static load increases. Figure 4.6 shows a reduction in the attitude angle with the increase in the static load. Figure 4.7(a) shows the plot showing the behaviour of the film forces and the tangent of the attitude angle in the parameter plane shown in Figure 4.3. Figure 4.7(b) shows the plot of the modified Sommerfeld number in the parameter plane. It can be seen in Figure 4.7(a), that the stability threshold increases rapidly when ϕ_s reaches 45°, $n_s \approx 0.62$. The following characteristics can be observed from Figure 4.7(a) and (b):

- when $0 < n_s < 0.62$, $90^\circ < \phi_s < 45^\circ$, the tangential force that causes the whirling is greater than the radial restoring force;

- when $n_s \approx 0.5$, $\phi_s \approx 55^0$, the eccentricity of the journal is about midway of the total clearance. The static load ($1/S_m$) is equal to the ratio of the radial force to the tangential force which is about $1/\sqrt{2}$ as shown in Figure 4.7(b);

$$S_m = \tan(\phi_s) \approx \sqrt{2} \text{ or } \bar{F} = \frac{\bar{F}_r}{\bar{F}_s} = \frac{1}{\sqrt{2}}; \tag{4.39}$$

- when $n_s = 0.62$, $\phi_s = 45^\circ$, from Eqs. (4.36) and (4.38), it is evident that the radial and tangential forces are equal and the radial restoring force balances about 70% of the static load. Figure 4.8 shows the stiffness coefficients in polar coordinates plotted under the steady-state conditions, where the negative destabilising cross-coupled stiffness $K_{\phi n}$ [73] changes its sign at this eccentricity ratio;

- when $n_s > 0.62$, $\phi_s > 45^\circ$, the radial force is dominant and the tangential force reduces. Hence the system stability improves rapidly for $0.62 < n_s < 0.76$ while the threshold speed asymptotes to infinity. $K_{\phi n}$ is positive but of a relatively low value for $0.62 \le n_s \le 0.76$;

- as $n_s \to 1$, $\phi_s \to 0$, $\cos(\phi_s) \to 1$, Eq. (4.37) gives $\left(\bar{F}_r\right)_s = -\bar{F}$, i.e., the radial force balances the static load. Hence, for $n_s > 0.76$, the system is stable. $K_{\phi n}$ is positive yielding a stable system. Figure 4.5 shows the absence of oil-whirl frequency for $n_s > 0.76$.

4.4 CONCLUSIONS

The linear analysis of the rotor system with a rigid rotor supported in short journal bearings with oscillating π-film cavitation has been presented. From the characteristic equation of the Jacobian determinant of the system, the stability threshold that separates the stable and the unstable equilibrium states was determined; this was plotted in a parameter plane of the steady-state eccentricity ratio and the rotor speed. A steady-state analysis considering the case that eccentricity ratio approaches zero was presented to analyse the interplay of the film forces in the presence of a static load.

The threshold speed indicates the onset of oil-whirl in the rotor bearing system with π-film cavity at a frequency of the order 0.5 which is equivalent to half-rotational speed. When the steady-state eccentricity ratio is about 0.62 and the attitude angle of the journal centre is about 45°, the radial force equals the tangential force, where the stability threshold starts increasing rapidly. The presence of the static load provides a higher eccentricity to the journal which helps in completely suppressing oil-whirl for $n_s > 0.76$. This is achieved by an increase in the radial restoring force, and reduction in the tangential force. The radial force almost balances the static load bringing the journal centre to a stable equilibrium state, which is otherwise unstable.

Since turbochargers are lightly loaded, the non-dimensional stability threshold speed is around 2.76, above which the rotor whirls outwards to the housing. However, experiments and the literature suggest the existence of a limit cycle leading to their successful operation. The occurrence of a limit cycle is related to a nonlinear system, and, thus, the nonlinearity should be taken into consideration. This is discussed in the next Chapter.

FIGURES

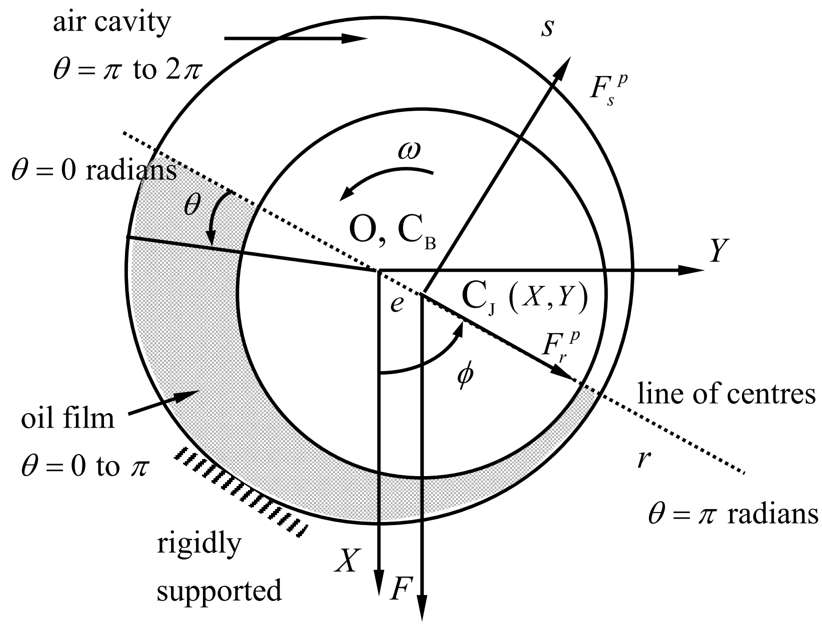

Figure 4.1 Co-ordinate system of a rotor-bearing system with a rigid rotor in rigidly supported bearing with oscillating π-film cavitation; e is the eccentricity of the journal centre from the bearing centre C_B. The bearing is rigidly supported to the housing making C_B coincide with the housing centre O; $n = e/C$ is the eccentricity ratio where C is the clearance; ϕ is the attitude angle of the line of centres of the journal C_J and the bearing centre C_B; with respect to the vertical axis; r is the along the line of centres and s is the axis perpendicular to the line of centres respectively; F_r^p, F_s^p are the radial and tangential forces acting along r and s respectively; F is the static load; ω is the spin speed; X, Y are the co-ordinates of the journal centre along the axes X, Y whose origin is at the housing centre.

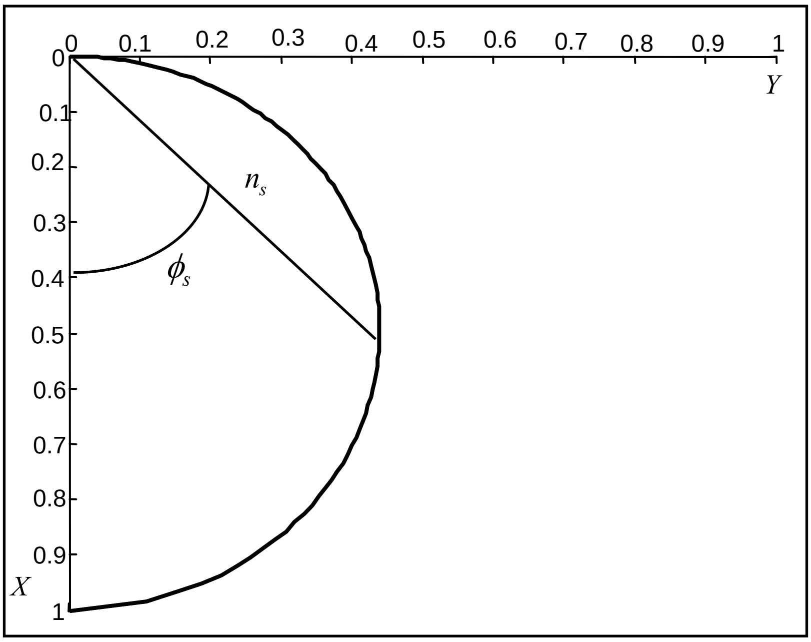

Figure 4.2 Locus of the equilibrium states (n_s, ϕ_s) of the rotor system plotted using Eq. (4.16).

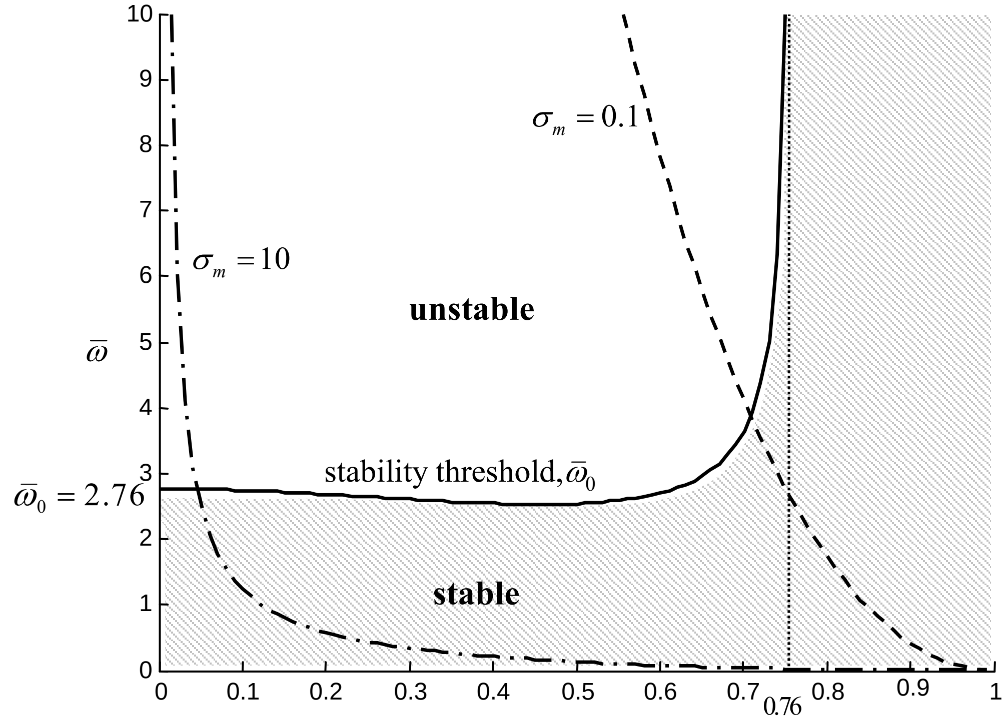

Figure 4.3 Parametric plane with the threshold speed $\bar{\omega}_0$, separating the stable and the unstable equilibrium states under the influence of the static load on the rotor system. Two operating curves illustrating two different rotor systems for $\sigma_m = 0.1$, $\sigma_m = 10$ are also plotted alongside.

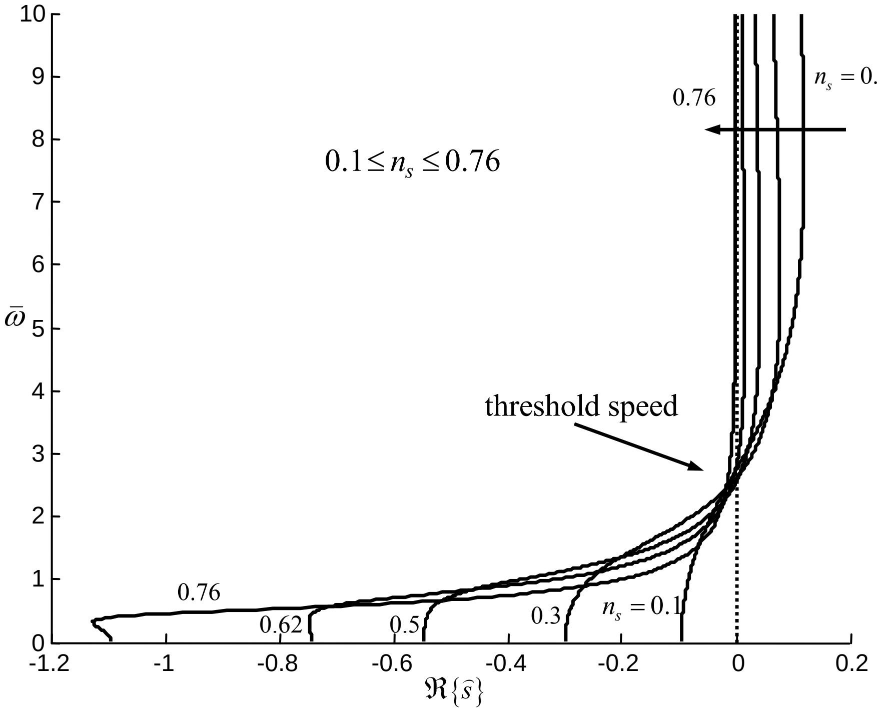

(a)

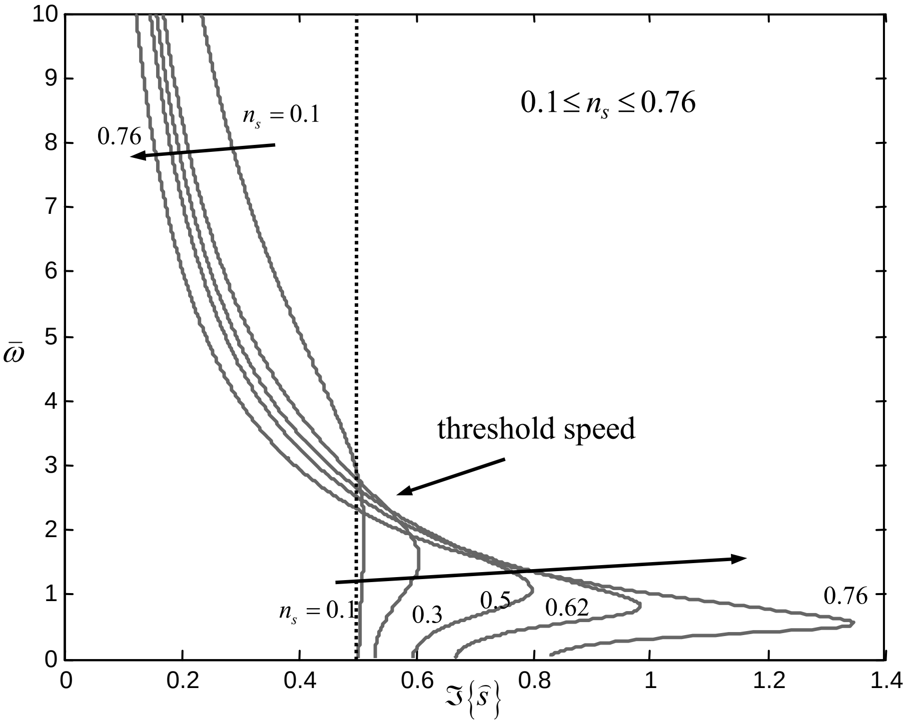

(b)

Figure 4.4 (a) Plot of the real part showing the change in stability (bifurcation) in the dynamic behaviour of the rotor system of the equilibrium state (b) the imaginary part of the unstable eigenvalues of the rotor-bearing system under the effect of a static load. It can be seen that the frequency ratio (imaginary part), of the unstable eigenvalue is 0.5, at the threshold speed indicating the half speed oil-whirl.

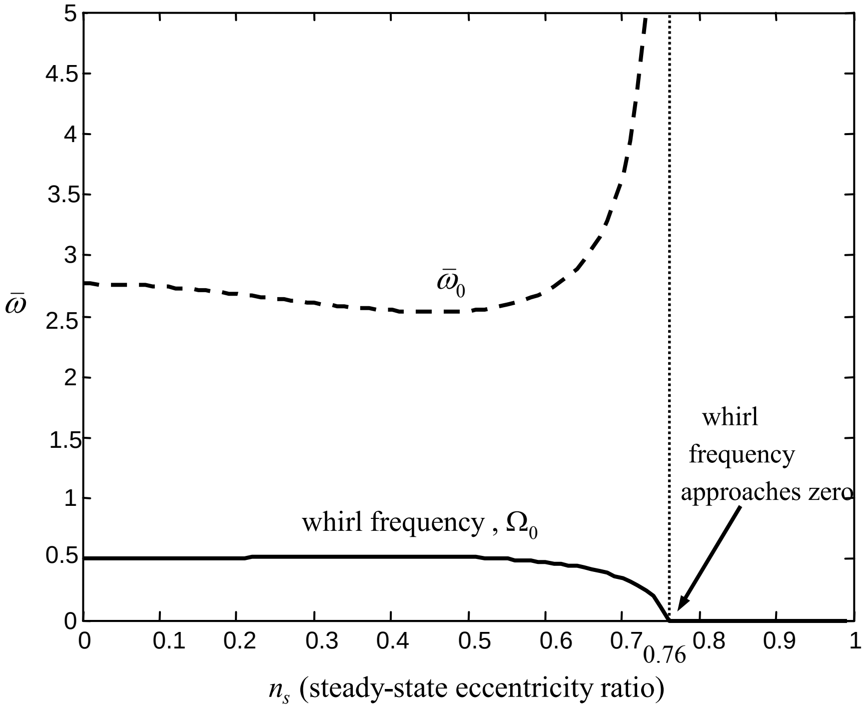

Figure 4.5 Plot showing the reduction of oil-whirl frequency ratio Ω_0 corresponding to the threshold speed given by Eq. (4.25) from 0.5 to 0 with increase in the steady-state eccentricity ratio n_s, as the threshold speed $\bar{\omega}_0$ approaches infinity.

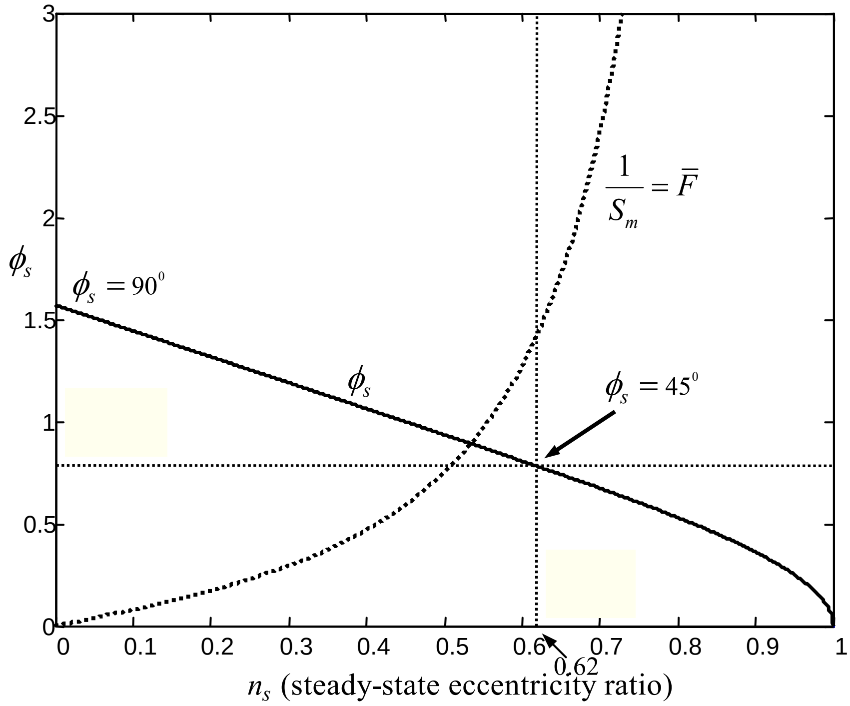

Figure 4.6 Plot illustrating the decreasing steady-state attitude angle ϕ_s with the increasing non-dimensional static load $1/S_m$ against the steady-state eccentricity ratio n_s (assuming fixed speed and bearing geometry).

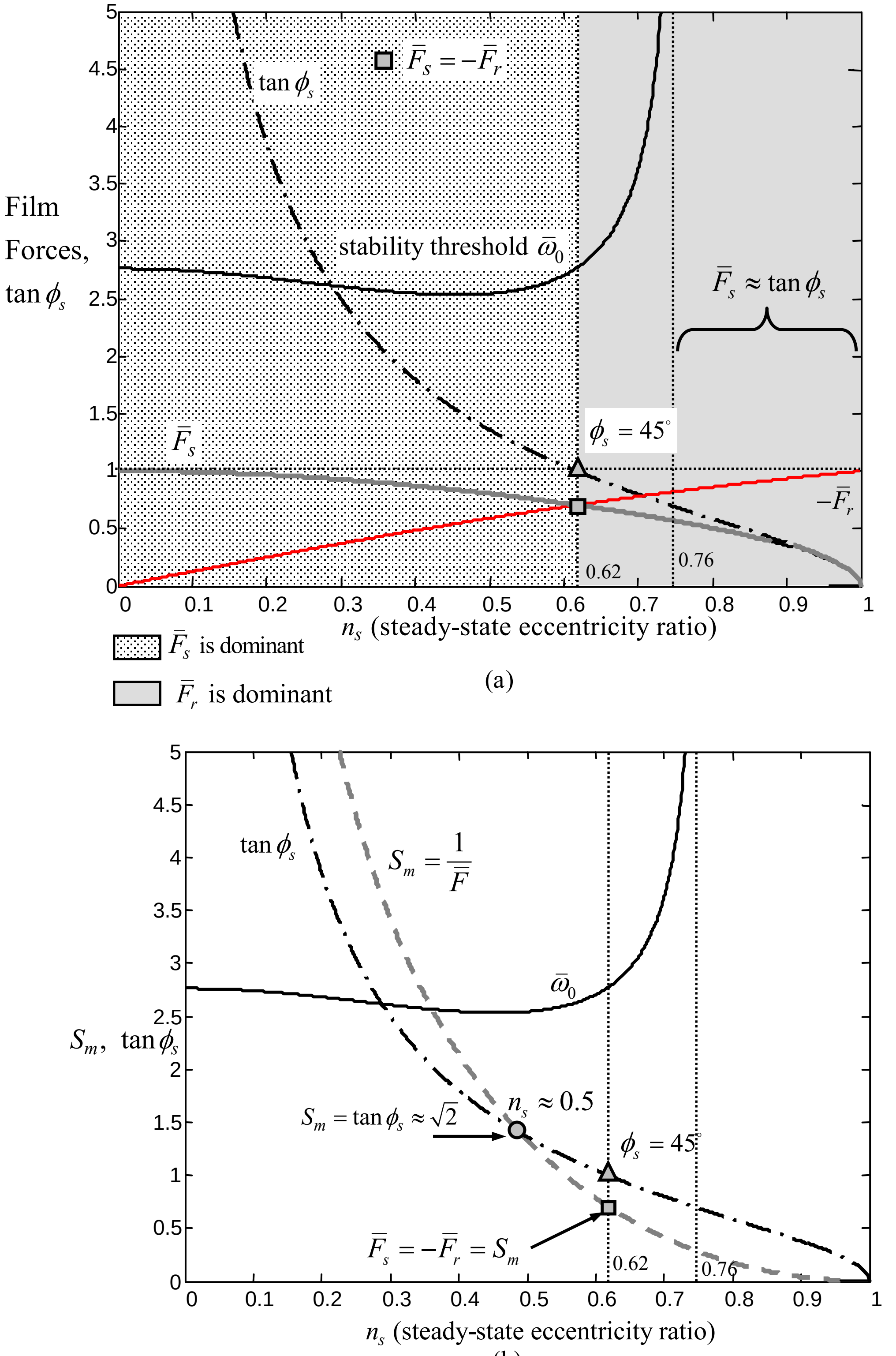

Figure 4.7(a) Plot illustrating the variation of the linearised non-dimensional radial and the tangential film forces $\bar{F}_{r,s}$ in the bearing, alongside the stability threshold $\bar{\omega}_0$, tangent of the steady-state attitude angle $\tan\phi_s$ with the increase in the steady-state eccentricity ratio. (b) Plot of the modified Sommerfeld number S_m varying with the steady-state eccentricity ratio along with the tangent of the steady-state attitude angle $\tan\phi_s$.

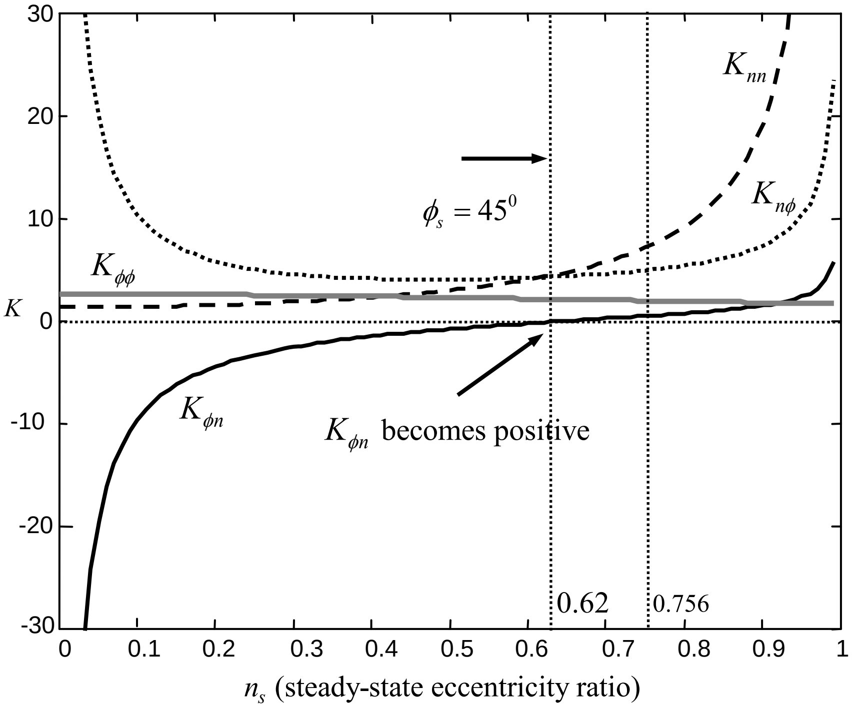

Figure 4.8 Plots showing the variation of linearised stiffness coefficients with steady-state eccentricity ratio in polar coordinates. The negative cross-coupled stiffness term $K_{\phi n}$ becomes positive at $n_s = 0.62$ when $\phi_s = 45^{\circ}$ and remains relatively low as the threshold speed asymptotes to infinity which is shown in Figure 4.7.

CHAPTER 5

THE EFFECT OF STATIC LOAD ON OIL-WHIRL IN A PERFECTLY BALANCED ROTOR-BEARING SYSTEM: NONLINEAR ANALYSIS

5.1 INTRODUCTION

In the previous Chapter, the linearised equations of motion of a general rotor-bearing system with perfectly balanced rotor in short journal bearings with the oscillating π-film cavitation model were investigated. However, in order to analyse the nonlinear behaviour such as the limit cycle of the journal motion, it is necessary to perform a nonlinear analysis. This Chapter presents a nonlinear analysis of the general rotor-bearing system used in Chapter 4, to determine the conditions yielding the occurrence of a limit cycle and to examine its characteristics. As mentioned in the previous Chapter, combining the benefit of the oscillating π-film cavitation model used by Myers [43] and the short-bearing approximation applied by Gardner [8], the rotor-bearing system under investigation has short-bearings with oscillating π-film cavitation. It has already been shown in the literature that the onset of oil-whirl is the *Hopf bifurcation* [21, 23]. Applying the *Hopf bifurcation* theory, Gardner [8] and Myers [21, 43] determined the nature of the bifurcation using *Poore's bifurcation algebra* [43, 71] to analyse the nonlinear characteristics of rotor systems. In this Chapter, the nature of the bifurcation for the rotor system under investigation is determined by evaluating the *first Lyapunov coefficients* [62, 63] of the equations of motion in the normal form, using the Centre Manifold Theorem [63]. They are also verified with *Poore's bifurcation algebra* following Myers and Gardner [8, 21]. The occurrence of sub-critical (disappearance of an unstable limit cycle) and super-critical (appearance of a stable limit cycle) bifurcations [70] is shown numerically by using the Runge-Kutta integration method, with the help of orbit plots. Based on the analytical and the numerical methods, the nonlinear behaviour of the in-phase whirl motion of the general rotor-system with a perfectly balanced rigid rotor mounted in rigidly-supported bearings is analysed first, and then the applicability of the analysis to a turbocharger is discussed.

5.2 HOPF BIFURCATION

In the previous Chapter, it was shown that the stable and the unstable equilibrium states of the journal are separated by the stability threshold which is a function of the steady-state eccentricity ratio, which in turn is a function of the static load of the rotor. It has been shown analytically, numerically, and experimentally in the literature that, the equilibrium state can bifurcate into a periodic orbit with a non-trivial amplitude [74], which is known as the limit cycle. In order to analyse the stability of the limit cycle in the neighbourhood of the threshold curve, several authors such as Myers [43], Gardner [23] , Ding [51], Wang [70] have applied the *Hopf bifurcation* theorem. In order to apply the theorem, it is necessary to first verify the occurrence of the *Hopf bifurcation* at the stability threshold, which physically signifies the onset of oil-whirl instability in the rotor system. This is presented in this Section following an introduction to the *Hopf bifurcation* theorem.

Consider a dynamic system whose behaviour is described by the first order ordinary differential equation:

$$\dot{\mathbf{x}} = \frac{d\mathbf{x}}{dt} = \mathrm{f}(\mathbf{x}, v)\,, \tag{5.1}$$

where: $\mathbf{x} \in \Re^n$, $\mathbf{x} = [x_1, x_2, x_3..x_n]^T$ is a real n dimensional vector. As the system parameter ν changes, the *Hopf bifurcation* occurs when a single complex conjugate pair of eigenvalues of the linearized system of equations become purely imaginary in the process of crossing the imaginary axis to the right hand side. The value of the bifurcation parameter at which this occurs is the critical (bifurcation) value ν_c. More precisely, the *Hopf bifurcation* occurs when the following four conditions are satisfied [63]:

1) Equation $\dot{\mathbf{x}} = \mathrm{f}(\mathbf{x}, \nu)$ has an equilibrium state $\mathbf{x} = \mathbf{x}_\mathrm{s}(\nu)$;

2) The Jacobian matrix $\mathbf{A} = \mathrm{f}'(\mathbf{x}_\mathrm{s}, \nu)_{\nu=\nu_c}$ has exactly a pair of complex conjugate eigenvalues $\hat{s} = \alpha(\nu) \pm j\Omega(\nu)$, such that when $\nu = \nu_c$, then $\alpha(\nu_c) = 0$ and $\Omega(\nu_c) \neq 0$, and no other eigenvalues exist with zero real part;

3) $\mathrm{f}(x, \nu)$ is continuously differentiable k times (C^k) in the neighbourhood of $(x, \nu) = (x_s, \nu_c)$, $k \geq 3$ (second and third order derivatives should exist);

4) $\left(\dfrac{d\alpha(\nu)}{d\nu}\right)_{\nu_c} \neq 0$, where $\alpha(\nu)$ is the real part of the eigenvalue which is continuous at ν_c.

Conditions 2) and 4) indicate that the linear stability of the equilibrium state is lost as the system parameter ν crosses the critical value ν_c. Under these conditions, the equilibrium state bifurcates leading to the birth of the periodic solution which is known as a limit cycle. The limit cycle, by definition, is a unique isolated closed trajectory (orbit). It has the property that, at least one other neighbouring trajectory spirals either towards or away from the limit cycle. In the neighbourhood of which, there is no other isolated closed trajectory for such a continuous dynamic system [63].

In general, excluding the special case where bifurcation occurs for $\nu = \nu_c$,

- the existence of a periodic solution in the case of $\nu > \nu_c$ is called a super-critical bifurcation;
- the existence of a periodic solution in the case of $\nu < \nu_c$ is called a sub-critical bifurcation.

In sub-critical bifurcation, an unstable limit cycle exists below the critical bifurcation value along with the stable equilibrium. The neighbouring trajectories are repelled from the unstable limit cycle. Any perturbation to a position within the limit cycle moves the system to a stable equilibrium state as shown in Figure 5.1(a). If perturbed to a position outside of the limit cycle, the system moves to a completely unstable behavior where the system moves far away from the stable equilibrium [8]. In super-critical bifurcation, there exists a stable limit cycle above the critical bifurcation value along with the unstable equilibrium. The stable limit cycle attracts all the neighbouring trajectories as shown in Figure 5.1(b). Any small perturbation from the closed trajectory causes to return to the limit cycle, making the system stick to the limit cycle. A system with a stable limit cycle can exhibit self-sustained oscillations. The occurrence of the *Hopf bifurcation* is shown in the following Sub-Section in the rotor system under investigation.

5.2.1 OIL-WHIRL: HOPF BIFURCATION

The aim of this Sub-Section is to show the occurrence of the *Hopf bifurcation* in the rotor system under investigation. Considering the rotor system defined by the equations of motion given in Eq. (4.19), it was shown in Chapter 4 that the equilibrium states are the functions of the speed and the qualitative behaviour of the rotor dynamic system changes as the speed is varied at the stability threshold. The threshold curve splits the equilibrium states of the system into stable and unstable equilibrium states as illustrated in Figure 4.3. Choosing the bifurcation parameter to be:

$$\nu = \bar{\varpi} - \bar{\varpi}_0 , \tag{5.2}$$

allows the critical value $\nu_c = 0$ at the stability threshold. Condition 2) is verified from the eigenvalues of the Jacobian determinant discussed in Chapter 4. The characteristic equation of the Jacobian matrix $\mathbf{A}$ given in Eq. (4.19) gives a pair of the complex conjugates of purely imaginary eigenvalues and another pair of conjugates of eigenvalues with negative real parts at the threshold speed as shown in Figure 5.2. The function $\mathrm{f}(\mathbf{x}, \nu)$ given in Eq. (5.1), is basically a function of the forces as seen in Eq. (4.19). These forces are related to the film forces given in Eqs. 4.2 and 4.3, which have non-zero second and third order derivatives and thus condition 3) is satisfied.

The last condition for a *Hopf bifurcation* is the continuity of the real part of the conjugate pair of the eigenvalues that cross the imaginary axis as the function of the bifurcation parameter ν. This condition is verified as follows using the characteristic equation given in Eq. (4.23) [8], which can be re-written in the form:

$$\hat{s}^4 + A'\frac{1}{\overline{\omega}^2}\hat{s}^3 + \frac{1}{\overline{\omega}^2}\left(B' + \frac{1}{\overline{\omega}^2}C'\right)\hat{s}^2 + \frac{1}{\overline{\omega}^4}D'\hat{s} + \frac{1}{\overline{\omega}^4}E' = 0\,. \tag{5.3}$$

First consider a small increment in the speed $\delta\omega$ with respect to the threshold speed as:

$$\overline{\omega} = \overline{\omega}_0 + \delta\overline{\omega}\,, \tag{5.4}$$

and a corresponding increment in the eigenvalues of the Jacobian matrix $\mathbf{A}$ as:

$$\hat{s} = \hat{s}_0 + \delta\hat{s}\,, \tag{5.5}$$

where $\hat{s}_0 = j\Omega_0$ is purely imaginary at $\overline{\omega}_0$. In order to verify the continuity of the real part of the eigenvalue, the variation of the eigenvalues $\hat{s} = \alpha + j\Omega$, as the speed changes from $\overline{\omega}_0$ to $\delta\overline{\omega}$ can be written as:

$$\frac{\delta\hat{s}}{\delta\overline{\omega}} = \left(\frac{d\alpha}{d\overline{\omega}}\right)\Bigg|_{\overline{\omega}_0}^{\delta\overline{\omega}} + \left(\frac{d\Omega}{d\overline{\omega}}\right)\Bigg|_{\overline{\omega}_0}^{\delta\overline{\omega}}\,. \tag{5.6}$$

Using Eqs. (5.4) and (5.5), the characteristic equation in Eq. (5.3) is expanded in $\hat{s}$ about $\hat{s}_0$ using Taylor's series upto the first order, which after re-arranging gives,

$$\frac{\delta\widehat{s}}{\delta\overline{\varpi}}=-\frac{\left\{\begin{array}{l}-j\left[\dfrac{1}{\overline{\varpi}_0^{\,2}}\left(\dfrac{dA'}{d\overline{\varpi}}\right)-\dfrac{A'2}{\overline{\varpi}_0^{\,3}}\right]I_0^{\,3}-\left(\begin{array}{l}+\left[\left(\dfrac{1}{\overline{\varpi}_0^{\,2}}\right)\left(\dfrac{dB'}{d\overline{\varpi}}\right)-\dfrac{2B'}{\overline{\varpi}_0^{\,3}}\right]\\+\left[\left(\dfrac{1}{\overline{\varpi}_0^{\,4}}\right)\left(\dfrac{dC'}{d\overline{\varpi}}\right)-\dfrac{4C'}{\overline{\varpi}_0^{\,5}}\right]\end{array}\right)I_0^{\,2}\\+j\left[\left(\dfrac{1}{\overline{\varpi}_0^{\,4}}\left(\dfrac{dD'}{d\overline{\varpi}}\right)-\left(\dfrac{4D'}{\overline{\varpi}_0^{\,5}}\right)\right)\right]I_0+\left[\left(\dfrac{1}{\overline{\varpi}_0^{\,4}}\right)\left(\dfrac{dE'}{d\overline{\varpi}}\right)-\left(\dfrac{4E'}{\overline{\varpi}_0^{\,5}}\right)\right]\end{array}\right\}}{\left\{\left(-j4I_0^{\,3}\right)-\dfrac{A'}{\overline{\varpi}_0^{\,2}}\left(3\left(I_0\right)^2\right)+jI_0\dfrac{2}{\overline{\varpi}_0^{\,2}}\left[B'+\dfrac{C'}{\overline{\varpi}_0^{\,2}}\right]+\dfrac{D'}{\overline{\varpi}_0^{\,4}}\right\}}. \tag{5.7}$$

Thus, the derivative α' is obtained by separating the real part of Eq. (5.7) as:

$$\alpha'=\frac{d\alpha}{d\overline{\varpi}}=-\left(\frac{\widehat{a}\widehat{c}-\widehat{b}\widehat{d}}{\widehat{c}^2+\widehat{d}^2}\right), \tag{5.8}$$

where:

$$\widehat{a}=\left[\frac{1}{\overline{\varpi}_0^{\,2}}\frac{dE'}{d\overline{\varpi}}-\frac{4E'}{\overline{\varpi}_0^{\,3}}\right]-\left[\frac{dB'}{d\overline{\varpi}}-\frac{2B'}{\overline{\varpi}_0}+\frac{1}{\overline{\varpi}_0^{\,2}}\frac{dC'}{d\overline{\varpi}}-\frac{4C'}{\overline{\varpi}_0^{\,3}}\right]\Omega_0^{\,2},\ \widehat{c}=\left\{\frac{D'}{\overline{\varpi}_0^{\,2}}-3A'\Omega_0^{\,2}\right\}$$

$$\widehat{b}=\Omega_0\left\{\left[\frac{1}{\overline{\varpi}_0^{\,2}}\frac{dD'}{d\overline{\varpi}}-\frac{4D'}{\overline{\varpi}_0^{\,3}}\right]-\left[\frac{dA'}{d\overline{\varpi}}-\frac{2A'}{\overline{\varpi}_0}\right]\Omega_0^{\,2}\right\},\ \widehat{d}=\Omega_0\left\{2B'+\frac{2C'}{\overline{\varpi}_0^{\,2}}-4\Omega_0^{\,2}\overline{\varpi}_0^{\,2}\right\};$$

$\dfrac{d(\cdot)}{d\overline{\varpi}}=\dfrac{d(\cdot)}{dn_s}\dfrac{dn_s}{d\overline{\varpi}}$; $\dfrac{d\overline{\varpi}}{dn_s}=\dfrac{1}{\sigma_m}\dfrac{dS_m}{dn_s}$. The derivatives of the coefficients A',B',C',D',E' are evaluated at $\overline{\varpi}=\overline{\varpi}_0$ to calculate $\left(\alpha'\right)_{\nu_c}$. Figure 5.3 shows that $\alpha'>0$ and continuous at $\nu_c=0$. Table 5.1 lists the values of the derivative α' for a given set of eccentricities in the range $0<n_s\le 0.75$. Thus, all the four conditions are satisfied by the rotor system under investigation at the stability boundary, which shows that the onset of the oil-whirl is a Hopf bifurcation. Since the aim is to investigate the nonlinear behaviour of the system leading to the evolution of the limit cycle, the type of bifurcation is analysed in the following Sub-Section to determine the stability of the limit cycle.

5.3 STABILITY OF THE LIMIT CYCLE

According to the *Hopf bifurcation* theorem, the occurrence of a *Hopf bifurcation* leads to a significant change in the stability of a dynamic system and implies the birth of the limit cycle. In order to understand the behaviour of the limit cycle, the type of bifurcation (also referred as the direction of bifurcation) needs to be determined, i.e., whether it is a sub-critical or a super-critical bifurcation as discussed in Section 5.2. Since the bifurcation parameter is the speed, which is a function of the steady-state eccentricity ratio, the bifurcation direction ought to change with the steady-state eccentricity ratio. The aim of this Section is to determine the steady-state eccentricity ratio at which the bifurcation direction changes from sub-critical to super-critical. This is done by first reducing the 4-dimensional system given in Eq. (4.19) to a 2-dimensional system, essentially in a single equation in complex co-ordinates using Centre Manifold Reduction theorem [63]. Following that, the equation is reduced to the normal form in order to evaluate the *first Lyapunov coefficients* [62, 63]. The reduction and the associated derivations, closely follow the procedure given in the text book by Kuznetsov [63]. The Centre Manifold reduction is discussed in detail in order to extend the theory in the next Chapter, when the effect of unbalance is added as a periodic excitation.

5.3.1 CENTRE MANIFOLD REDUCTION

In this Sub-Section, the Centre Manifold theorem is applied to the 4-dimensional equation of motion of the rotor-bearing system under investigation, to reduce it to a 2-dimensional system. This simplification helps in focussing on the local behaviour of the system considering only the critical eigenvalues at ν_c. Let $\mathbf{x}-\mathbf{x}_s$ be denoted as $\mathbf{x}(\nu)$, so that the equations of motion given in Eq. (4.19) can be expressed in the form of Eq. (5.1), i.e.:

$$\dot{\mathbf{x}} = \mathbf{A}\mathbf{x} + \mathrm{F}(\mathbf{x},\nu)\,, \tag{5.9}$$

where: $\mathbf{x} \in \Re^4$; $\mathbf{x} = [x_1, x_2, x_3, x_4]^T$ is a 4-dimensional real vector; $\mathrm{F}(\mathbf{x},\nu)$ denotes the function of higher order terms with Taylor expansions in $\mathbf{x}$, $\mathbf{A}$ is the Jacobian $\mathrm{f}'(0,0)$,

$\dot{\mathbf{x}}$ is the time derivative with respect to τ; Note that the Jacobian determinant is evaluated at the threshold speed, i.e. when $\nu = 0$ for the equilibrium position $\mathbf{x} = 0$; it is because of the assumption $\mathbf{x} = \mathbf{x} - \mathbf{x_s}$. This implies that the equilibrium state $\mathbf{x_s}$ is shifted to the origin $\mathbf{x} = 0$ by the Implicit Function Theorem [63] for sufficiently small $|\nu|$. The eigenvalues of $\mathbf{A}$ are $\hat{s}_i$, $i = 1, 2...4$; $\hat{s}_{1,2}$ are a pair of complex conjugate eigenvalues $\hat{s}(\nu) = \alpha(\nu) \pm j\Omega(\nu)$, such that when $\nu = 0$, then $\alpha(0) = \alpha_0 = 0$ and $\Omega(0) = \Omega_0 > 0$ and the other 2 eigenvalues $\hat{s}_{3,4} = -\alpha_1 \pm j\Omega_1$ have purely negative real parts. Since the aim of this section is to reduce the 4-dimensional system given in Eq. (5.9) to a 2-dimensional system, it is essential to split the system into two equations of 2-dimensions. This is done using the eigenvalue (modal) decomposition of the matrix $\mathbf{A}$ in such a way that $\mathbf{J} = \mathbf{TAT}^{-1}$ where $[\mathbf{T}]_{4\times4}$ is the eigenbasis (eigenvector basis) which is an invertible matrix, consisting of the 4 eigenvectors corresponding to the 4 eigenvalues of $\mathbf{A}$. $\mathbf{J}$ is the resulting diagonal matrix whose diagonal elements are the corresponding eigenvalues. Introducing a linear invertible change of variables (co-ordinate transformation), such as [51, 63]:

$$\bar{\mathbf{x}} = \mathbf{Tx}, \tag{5.10}$$

where $\bar{\mathbf{x}} = \{u_1, u_2, v_1, v_2\}$ are the transformed co-ordinates. Now, system (5.9) in its eigenbasis [63] that is in the new co-ordinates is defined as:

$$\dot{\mathbf{u}} = \mathbf{A_0 u} + \mathrm{G}(\mathbf{u}, \mathbf{v}), \qquad \mathbf{u} = [u_1, u_2]^T \in \Re^2, \tag{5.11}$$

$$\dot{\mathbf{v}} = \mathbf{Cv} + \mathrm{H}(\mathbf{u}, \mathbf{v}), \qquad \mathbf{v} = [v_1, v_2] \in \Re^2, \tag{5.12}$$

where $\Re^2$ denotes a real 2-dimensional vector, $\mathbf{u} = [u_1, u_2]^T$ is a real vector on the critical real eigenspace $\mathbf{T^C}$ with the eigenvectors corresponding to only the purely imaginary eigenvalues $\hat{s}_{1,2}$ (critical eigenvalues). Since any multiple of an eigenvector is also an eigenvector corresponding to an eigenvalue, all such vectors form the corresponding eigenspace. $\mathbf{v}$ is on the real eigenspace $\mathbf{T^R}$ which is spanned with the eigenvectors corresponding to $\hat{s}_{3,4}$ (all but the critical eigenvalues). $\mathbf{A_0}$ is a 2×2 real matrix corresponding to the critical eigenvalues at $\nu = 0$ i.e. $\hat{s}_{1,2} = \pm j\Omega_0$; the complex eigenvalues are in the Jordan canonical form where the complex conjugates of eigenvalues $\hat{s}$ and $\overline{\hat{s}}$ are written as $\begin{bmatrix} \Re\{\hat{s}\} & -\Im\{\hat{s}\} \\ \Im\{\hat{s}\} & \Re\{\hat{s}\} \end{bmatrix}$. Thus, $\mathbf{A_0} = \begin{bmatrix} 0 & -\Omega_0 \\ \Omega_0 & 0 \end{bmatrix}$ and likewise $\mathbf{C} = \begin{bmatrix} \alpha_1 & -\Omega_1 \\ \Omega_1 & \alpha_1 \end{bmatrix}$; G, H are the higher order functions. It is convenient to rewrite this system in the complex form by introducing a complex variable $z = u_1 + ju_2$ and its conjugate $\bar{z}$, which gives,

$$\dot{z} = \hat{s}_1 z + \mathrm{G}(z, \bar{z}, \mathbf{v}), \tag{5.13}$$

$$\dot{\mathbf{v}} = \mathbf{C}\mathbf{v} + \mathrm{H}(z, \bar{z}, \mathbf{v}). \tag{5.14}$$

Equation corresponding to $\dot{\bar{z}}$ is ignored because it is just the conjugate of Eq. (5.13). Note that the focus is on $\nu = 0$, which is the reason for not including ν as a variable in the functions G, H. In order to simplify the Centre Manifold computation by avoiding the coordinate transformation and the associated calculations, there is a useful method known as the projection method; this uses only the eigenvectors corresponding to the critical eigenvalues of the Jacobian matrix $\mathbf{A}$ and its transpose $\mathbf{A}^T$. To apply this method, let $\mathbf{q} = [q_1, q_2, q_3, q_4]^T$ be the 4-dimensional complex eigenvector corresponding to the eigenvalue $\hat{s}_1(0) = j\Omega_0$, and $\mathbf{p} = [p_1, p_2, p_3, p_4]^T$ be the ad-joint complex eigenvector. Then:

$$\mathbf{A}\mathbf{q} = j\Omega_0\mathbf{q};\ \mathbf{A}\bar{\mathbf{q}} = -j\Omega_0\bar{\mathbf{q}}, \tag{5.15}$$

$$\mathbf{A^T}\mathbf{p} = -j\Omega_0\mathbf{p};\ \mathbf{A^T}\bar{\mathbf{p}} = j\Omega_0\bar{\mathbf{p}}, \tag{5.16}$$

where the over-bar denotes the complex conjugate; $\mathbf{p}$ and $\mathbf{q}$ are normal with their standard scalar product represented as $\langle \mathbf{p},\mathbf{q} \rangle = \sum_{i=1}^{n} \bar{\mathbf{p}}_\mathbf{i} \mathbf{q}_\mathbf{i} = 1$. In order to use a 4-dimensional real vector $\mathbf{y}$ instead of the 2-dimensional real vector $\mathbf{v}$, condition $\langle \mathbf{p},\mathbf{y} \rangle = 0$ must be satisfied. Since $\mathbf{p}$ is complex and $\mathbf{y}$ is real, this sets two real constraints on $\mathbf{y}$ where the real and the imaginary parts of $\langle \mathbf{p},\mathbf{y} \rangle$ must vanish, in effect giving only 2-dimensions. The application of this method needs the definition of the vector $\mathbf{x}$ from Eq. (5.9) in terms of the complex variable z and the vector $\mathbf{y}$, which is given by [63]:

$$\mathbf{x} = z\mathbf{q} + \bar{z}\bar{\mathbf{q}} + \mathbf{y}\,. \tag{5.17}$$

Performing a scalar multiplication of $\mathbf{p}$ on both the sides of Eq. (5.17) results in,

$$z = \langle \mathbf{p},\mathbf{x} \rangle, \tag{5.18}$$

using the conditions $\langle \mathbf{p},\mathbf{y} \rangle = 0$, $\langle \mathbf{p},\mathbf{q} \rangle = 1$ and $\langle \mathbf{p},\bar{\mathbf{q}} \rangle = 0$. Details of the proof for the condition $\langle \mathbf{p},\bar{\mathbf{q}} \rangle = 0$ is given in Kuznetsov [63]. Substituting Eq. (5.18) for z in Eq. (5.17) gives the expression of $\mathbf{y}$ as:

$$\mathbf{y} = \mathbf{x} - \langle \mathbf{p},\mathbf{x} \rangle \mathbf{q} - \langle \bar{\mathbf{p}},\mathbf{x} \rangle \bar{\mathbf{q}}\,, \tag{5.19}$$

where $\mathbf{y}$ satisfies $\langle \mathbf{p},\mathbf{y} \rangle = 0$, since $\langle \mathbf{p},\bar{\mathbf{q}} \rangle = 0$. Substituting Eq. (5.17) into Eq. (5.9), the system is written as:

$$\dot{z}\mathbf{q} + \dot{\bar{z}}\bar{\mathbf{q}} + \dot{\mathbf{y}} = \mathbf{A}\left(z\mathbf{q} + \bar{z}\bar{\mathbf{q}} + \mathbf{y}\right) + \mathrm{F}\left(\left(z\mathbf{q} + \bar{z}\bar{\mathbf{q}} + \mathbf{y}\right), \nu\right). \tag{5.20}$$

From Eq. (5.20), the $\dot{z}$ and $\dot{\mathbf{y}}$ terms can be separated directly except for the higher order function F. Hence, it is necessary to split the higher order function $\mathrm{F}(\mathbf{x},\nu)$ into $\mathrm{F}(z,\nu)$, $\mathrm{F}(\mathbf{y},\nu)$ respectively using Eqs. (5.18) and (5.19). Using the scalar product of $\mathbf{p}$

on both the sides of Eq. (5.20) and separating the terms related to co-ordinate z, the equation of motion in the complex co-ordinate z is given by:

$$\dot{z} = \hat{s}_1 z + \left\langle \mathbf{p}, \mathrm{F}\left(z\mathbf{q} + \overline{z}\overline{\mathbf{q}} + \mathbf{y}, \nu\right)\right\rangle . \tag{5.21}$$

Note that $\mathbf{A}\left(z\mathbf{q}\right) = j\Omega_0 z\mathbf{q}$ from Eq. (5.15). Similarly, separating the terms corresponding to $\mathbf{y}$ from Eq. (5.20) and using Eq. (5.19), the equation of motion in $\mathbf{y}$ is given by:

$$\dot{\mathbf{y}} = \left.\begin{array}{l} \mathbf{A}\mathbf{y} + \mathrm{F}(z\mathbf{q} + \overline{z}\overline{\mathbf{q}} + \mathbf{y}, \nu) \\ \qquad -\left\langle \mathbf{p}, \mathrm{F}(z\mathbf{q} + \overline{z}\overline{\mathbf{q}} + \mathbf{y}, \nu)\right\rangle \mathbf{q} \\ \qquad -\left\langle \overline{\mathbf{p}}, \mathrm{F}(z\mathbf{q} + \overline{z}\overline{\mathbf{q}} + \mathbf{y}, \nu)\right\rangle \overline{\mathbf{q}}, \end{array}\right\} . \tag{5.22}$$

Now, the system given in Eqs. (5.13) and (5.14) can be equivalently expressed using Eqs. (5.21) and (5.22) as:

$$\dot{z} = \hat{s}_1 z + \mathrm{G}(z, \overline{z}, \mathbf{y}) , \tag{5.23}$$

$$\dot{\mathbf{y}} = \mathbf{A}\mathbf{y} + \mathrm{H}(z, \overline{z}, \mathbf{y}), \tag{5.24}$$

where the functions G and H, using Taylor’s expansion, are written as [63]:

$$\begin{aligned} \mathrm{G}(z, \overline{z}, \mathbf{y}) = {} & \frac{1}{2} g_{20} z^2 + g_{11} z\overline{z} + \frac{1}{2} g_{02} \overline{z}^2 + \frac{1}{6} g_{30} z^3 \\ & + \frac{1}{2} g_{21} z^2 \overline{z} + \frac{1}{2} g_{12} z\overline{z}^2 + \frac{1}{6} g_{03} \overline{z}^3 + \left\langle \mathbf{g_{10}}, \mathbf{y}\right\rangle z + \left\langle \mathbf{g_{01}}, \mathbf{y}\right\rangle \overline{z} + \ldots \end{aligned} ;$$

$$\mathrm{H}(z, \overline{z}, \mathbf{y}) = \frac{1}{2} \mathbf{h_{20}} z^2 + \mathbf{h_{11}} z\overline{z} + \frac{1}{2} \mathbf{h_{02}} \overline{z}^2 + \ldots ;$$

$g_{20}, g_{02}, g_{30}, g_{21}, g_{12}, g_{03}$ are complex numbers; $\mathbf{g_{10}}, \mathbf{g_{01}}, \mathbf{h_{ij}}$ are 2-dimensional complex vectors. The calculation of these coefficients is discussed in detail in Section 5.3.2. It can be seen that Eqs. (5.23) and (5.24) are coupled in $\mathbf{y}$ and z. In order to uncouple them, the Center Manifold Theorem is applied. Details of the theorem can be found in the text books on bifurcation theory, for example [63]. According to this theorem, there exists a local smooth 2-dimensional invariant manifold (function) W^{C} tangent to $\mathbf{T}^{\mathbf{C}}$ at the equilibrium state $z = 0$ of the form:

$$\mathbf{y} = \mathrm{V}(z,\bar{z}) = \frac{1}{2}\mathbf{w}_{\mathbf{20}}z^2 + \mathbf{w}_{\mathbf{11}}z\bar{z} + \frac{1}{2}\mathbf{w}_{\mathbf{02}}\bar{z}^2, \tag{5.25}$$

where $\langle \mathbf{p}, \mathbf{w}_{\mathbf{ij}} \rangle = 0$; $\mathbf{w}_{\mathbf{ij}}$ is a 4-dimensional complex vector. Since V must be real [63], $\mathbf{w}_{\mathbf{11}}$ is real and $\mathbf{w}_{\mathbf{20}} = \bar{\mathbf{w}}_{\mathbf{02}}$. The Centre Manifold must be at least quadratic due to the tangent property. It can be seen that $\mathbf{y}$ is defined as a function of z and $\bar{z}$ variables. Substituting for $\mathbf{y}$ in Eq. (5.23) decouples it from Eq. (5.24). To this end, $\mathbf{w}_{\mathbf{ij}}$ needs to be determined. This is done by differentiating Eq. (5.25) with respect to τ, and equating the right hand side to that of Eq. (5.24) using,

$$\dot{\mathbf{y}} = \frac{\partial \mathrm{V}(z,\bar{z})}{\partial z}\dot{z} + \frac{\partial \mathrm{V}(z,\bar{z})}{\partial \bar{z}}\dot{\bar{z}}, \tag{5.26}$$

gives,

$$\begin{aligned}&\mathbf{w}_{20}z\dot{z} + \mathbf{w}_{11}\left(z\dot{\bar{z}} + \bar{z}\dot{z}\right) + \mathbf{w}_{02}\bar{z}\dot{\bar{z}}\\ &= \mathbf{A}\left(\frac{1}{2}\mathbf{w}_{20}z^2 + \mathbf{w}_{11}z\bar{z} + \frac{1}{2}\mathbf{w}_{02}\bar{z}^2\right) + \frac{1}{2}\mathbf{h}_{\mathbf{20}}z^2 + \mathbf{h}_{\mathbf{11}}z\bar{z} + \frac{1}{2}\mathbf{h}_{\mathbf{02}}\bar{z}^2\end{aligned}. \tag{5.27}$$

Substituting for $\dot{z}$ and $\dot{\bar{z}}$ from Eq. (5.23), and equating the coefficients of the like-terms in $z, \bar{z}$ in Eq. (5.27) upto quadratic level gives:

$$\begin{cases} z^2: & \left(2\mathbf{I}\Omega_0 - \mathbf{A}\right)\mathbf{w}_{\mathbf{20}} = \mathbf{h}_{\mathbf{20}}, \\ z\bar{z}: & \left(2\mathbf{I}\Omega_0 - \mathbf{A}\right)\mathbf{w}_{\mathbf{11}} = \mathbf{h}_{\mathbf{11}}, \\ \bar{z}^2: & \left(-2\mathbf{I}\Omega_0 - \mathbf{A}\right)\mathbf{w}_{\mathbf{02}} = \mathbf{h}_{\mathbf{02}}. \end{cases} \tag{5.28}$$

Note that Eq. (5.27) does not have any linear term. Using Eq. (5.28), $\mathbf{w}_{\mathbf{ij}}$ can be determined in terms of $\mathbf{h}_{\mathbf{ij}}$. Now, substituting for $\mathbf{y}$ in Eq. (5.23) from Eq. (5.25) allows the restriction of Eqs. (5.23) and (5.24) to the Centre Manifold according to the reduction principle [63] of the Centre Manifold Theorem as given by:

$$\begin{aligned}\dot{z} &= \hat{s}_1 z + \frac{1}{2} g_{20} z^2 + g_{11} z\bar{z} + \frac{1}{2} g_{02} \bar{z}^2 + \frac{1}{6}\left(g_{30} + 6\left\langle \mathbf{g_{10}}, \left(2\Omega_0 \mathbf{I} - \mathbf{A}\right)^{-1} \mathbf{h_{20}} \right\rangle \right) z^3 \\ &+ \frac{1}{2}\left(g_{21} - 2\left\langle \mathbf{g_{10}}, \mathbf{A}^{-1}\mathbf{h_{11}} \right\rangle + \left\langle \mathbf{g_{01}}, \left(2\Omega_0 \mathbf{I} - \mathbf{A}\right)^{-1} \mathbf{h_{20}} \right\rangle \right) z^2 \bar{z} + \dots\end{aligned} \quad . \qquad (5.29)$$

The dynamics of the unstable system defined by Eq. (5.23) and (5.24) is essentially determined by the expression of $\dot{z}$ given in Eq. (5.29). This is in agreement with Shoshitaishvili's theorem [75], which states that all the essential events near the bifurcation parameter value occur on the invariant manifold; they are captured by the n_0-dimensional system, where n_0 is the dimension of the Centre Manifold. Simplifying the coefficients of the cubic terms in Eq. (5.29) gives,

$$\dot{z} = \hat{s}_1 z + \frac{1}{2} \hat{g}_{20} z^2 + \hat{g}_{11} z\bar{z} + \frac{1}{2} \hat{g}_{02} \bar{z}^2 + \frac{1}{6} \hat{g}_{30} z^3 + \frac{1}{2} \hat{g}_{21} z^2 \bar{z} + \dots, \qquad (5.30)$$

where $\hat{g}_{21} = g_{21} - 2\left\langle \mathbf{g_{10}} . \mathbf{A}^{-1}\mathbf{h_{11}} \right\rangle + \left\langle \mathbf{g_{01}} . \left(2\Omega_0 \mathbf{I} - \mathbf{A}\right)^{-1} \mathbf{h_{20}} \right\rangle$;

$\hat{g}_{30} = \left(g_{30} + 6\left\langle \mathbf{g_{10}}, \left(2\Omega_0 \mathbf{I} - \mathbf{A}\right)^{-1} \mathbf{h_{20}} \right\rangle \right)$ and so on, while for the quadratic terms i.e., $i + j = 2$, $\hat{g}_{ij} = g_{ij}$. It can be seen that the first order system given in Eq. (5.9) is now reduced to a single equation in complex co-ordinates $z, \bar{z}$, which can be transformed to the normal form which is presented in the following Sub-Section.

5.3.2 NORMAL FORM – FIRST LYAPUNOV COEFFICIENT

This Sub-Section aims to calculate the *first Lyapunov coefficient* in order to determine the nature (type) of bifurcation in the rotor system under investigation. To this end, Eq. (5.30) needs to be transformed to its normal form. A normal form is a simplified form of a mathematical system obtained by applying a transformation (often a change of co-ordinates) that is considered to preserve the essential features of the original system [76]. The purpose is to obtain an approximation to the (unknown) solution of the original system that is valid over an extended range in time.

The Centre Manifold restriction given in Eq. (5.30) has a linear term and higher order terms upto cubic level. This equation which is of the form:

$$\dot{z} = \widehat{s}z + \sum_{2\le k+l\le 3} \frac{1}{k!l!}\hat{g}_{kl} z^k \overline{z}^l, \tag{5.31}$$

where $2 \le k+l \le 3$ denotes the quadratic and the cubic terms; $k+l=2$ such as 20, 02 and 11 denote the quadratic terms $z^2, \overline{z}^2, z\overline{z}$ and $k+l=3$ such as 30, 03, 21, 12 denote the cubic terms $z^3, \overline{z}^3, z^2\overline{z}, z\overline{z}^2$; $\widehat{s} = \widehat{s}(\nu) = \alpha(\nu) + j\Omega(\nu)$, $\alpha(0)=0$, $\Omega(0)=\Omega_0 > 0$, and $\hat{g}_{ij} = \hat{g}_{ij}(\nu)$ can be transformed using an inverse parameter-dependent change of complex coordinate [63], smoothly depending on the parameter, such as:

$$z = z + h(z,\overline{z})z^k\overline{z}^l, \tag{5.32}$$

where $h(z,\overline{z}) = \sum_{2\le k+l\le 3} \frac{1}{k!l!} h_{kl} z^k \overline{z}^l$ for all sufficiently small $|\nu|$, into an equation with only the resonant cubic term:

$$\dot{z} = \widehat{s}(\nu)z + c_1(\nu)z^2\overline{z}\,, \tag{5.33}$$

which is the *Poincaré normal form* for the *Hopf bifurcation*. Note that Eqs. (5.31) and (5.33) are in their general forms consisting of functions of ν and not specific to $\nu = 0$. According to the theorem, if the 2-dimensional system has 2 pure imaginary eigenvalues, $\widehat{s}_{1,2} = \pm j\Omega_0$, then the first equation of the normalised system has only the term (monomial) $z^k\overline{z}^l$ satisfying,

$$k\widehat{s}_1 + l\widehat{s}_2 - \widehat{s}_1 = 0\,, \tag{5.34}$$

which gives $k - (l+1) = 0$. Thus Eq. (5.34) suggests that $k = l+1$; for a cubic term $k+l=3$, hence the irremovable term is $z^2\overline{z}$. This irremovable nonlinear term in the normal form is referred as the resonant term [62, 77]. The proof for the above Lemma can be found in [63]. The normal form reduction procedure using Eq. (5.32), gives $c_1(\nu)$ in terms of the $\hat{g}_{kl}$ coefficients which is given by [63]:

$$c_1(\nu) = \frac{\hat{g}_{20}\hat{g}_{11}(2\hat{s}_1 + \hat{s}_2)}{2|\hat{s}_1|^2} + \frac{|\hat{g}_{11}|^2}{\hat{s}_1} + \frac{|\hat{g}_{02}|^2}{2(2\hat{s}_2 - \hat{s}_1)} + \frac{\hat{g}_{21}}{2}. \tag{5.35}$$

When $\nu = 0,\ \hat{s}_1 = j\Omega_0,\ \hat{s}_2 = -j\Omega_0,$ the coefficient c_1 is given as:

$$c_1(0) = \frac{j}{2\Omega_0}\left(\hat{g}_{20}\hat{g}_{11} + 2|\hat{g}_{11}|^2 + \frac{1}{3}|\hat{g}_{02}|^2\right) + \frac{\hat{g}_{21}}{2}. \tag{5.36}$$

A limit cycle is a nonlinear phenomenon and c_1 is the coefficient of the higher order term defining the nonlinearity of the system in Eq. (5.33). Hence, the determination of c_1 is the only requirement to investigate the nonlinear behaviour of the system based on the *Poincaré normal form.* This is done by using the higher order function of the original system in Eq. (5.9), since c_1 depends on the coefficients g_{ij}. When $\nu = 0$, using Taylor's expansion, the function $\mathrm{F}(\mathbf{x}, 0)$ in Eq. (5.9) can be written in terms of second and third order terms as:

$$\mathrm{F}(\mathbf{x}, 0) = \frac{1}{2}\mathrm{B}(\mathbf{x}, \mathbf{x}^1) + \frac{1}{6}\mathrm{C}(\mathbf{x}, \mathbf{x}^1, \mathbf{x}^2), \tag{5.37}$$

where B and C represent the second and the third derivative terms of the expansion respectively. The vector variables $\mathbf{x}^1, \mathbf{x}^2$ indicate that B and C are multilinear functions. Note that these are 4-dimensional vector functions since $\mathbf{x} = [x_1, x_2, x_3, x_4]^T$. They are defined as [63]:

$$\mathrm{B}_i(\mathbf{x}, \mathbf{x}^1) = \sum_{j,k=1}^{4} \frac{\partial^2 F_i(\mathbf{x}, 0)}{\partial x_j \partial x_k} \mathbf{x}_j \mathbf{x}_k^1;\ i = 1, 2, 3, 4, \tag{5.38}$$

$$\mathrm{C}_i(\mathbf{x},\mathbf{x}^1,\mathbf{x}^2)=\sum_{j,k,l=1}^{4}\frac{\partial^3 F_i(\mathbf{x},0)}{\partial x_j\partial x_k\partial x_l}\mathbf{x}_j\mathbf{x}_k^1\mathbf{x}_l^2;\ i=1,2,3,4. \tag{5.39}$$

Note that $F_i(\mathbf{x})$ is the function on the right hand side of Eq. (4.19) corresponding to each x_i; $i=1,2,3,4$. Using Eq. (5.17), substituting for $\mathbf{x}$ gives $\mathrm{B}(\mathbf{x},\mathbf{x})$ as $\mathrm{B}(z\mathbf{q}+\overline{z}\overline{\mathbf{q}}+\mathbf{y},z\mathbf{q}+\overline{z}\overline{\mathbf{q}}+\mathbf{y})$. However, after the Centre Manifold reduction, the equation of motion given by Eq. (5.30) and its *Poincaré normal form* given in Eq. (5.33) are just functions of z and $\overline{z}$. Hence the vector function $\mathrm{B}(\mathbf{x},\mathbf{x})$ is given by [63]:

$$\mathrm{B}(z\mathbf{q}+\overline{z}\overline{\mathbf{q}},z\mathbf{q}+\overline{z}\overline{\mathbf{q}})=z^2\,\mathrm{B}(\mathbf{q},\mathbf{q})+2z\overline{z}\,\mathrm{B}(\mathbf{q},\overline{\mathbf{q}})+\overline{z}^2\,\mathrm{B}(\overline{\mathbf{q}},\overline{\mathbf{q}}), \tag{5.40}$$

where

$$\mathrm{B}_i(\mathbf{q},\mathbf{q})=\sum_{j,k=1}^{4}\frac{\partial F_i(\mathbf{x})}{\partial x_j\partial x_k}\mathbf{q}_j\mathbf{q}_k\ ;\ i=1,2,3,4. \tag{5.41}$$

Likewise, the third derivative term related to g_{21} in Eq. (5.30) can be expressed as:

$$\mathrm{C}_i(\mathbf{q},\mathbf{q},\overline{\mathbf{q}})=\sum_{j,k,l=1}^{4}\frac{\partial^3 F_i(\mathbf{x})}{\partial x_j\partial x_k\partial x_l}\mathbf{q}_j\mathbf{q}_k\overline{\mathbf{q}}_l;\ i=1,2,3,4. \tag{5.42}$$

The third vector in Eq. (5.42) is $\overline{\mathbf{q}}$ because g_{21} is part of the coefficient of $z^2\overline{z}$ term as shown in Eq. (5.30). Now using Eq. (5.21), it is seen that the higher order terms of the equation of motion in z co-ordinate can be expressed as $\langle\mathbf{p}.\mathrm{F}(z\mathbf{q}+\overline{z}\overline{\mathbf{q}})\rangle$. Thus each $\hat{g}$ coefficient of quadratic terms ($k+l=2$) in Eq. (5.30) can be written in this form, such as:

$$\hat{g}_{20}=\langle\mathbf{p},\mathrm{B}(\mathbf{q},\mathbf{q})\rangle;\ \hat{g}_{02}=\langle\mathbf{p},\mathrm{B}(\overline{\mathbf{q}},\overline{\mathbf{q}})\rangle;\ \hat{g}_{11}=\langle\mathbf{p},\mathrm{B}(\mathbf{q},\overline{\mathbf{q}})\rangle. \tag{5.43}$$

Similarly, the standard scalar product of the linear vector coefficients $\langle\mathbf{g_{10}}.\mathbf{y}\rangle$ and $\langle\mathbf{g_{01}}.\mathbf{y}\rangle$ can be expressed as:

$$\langle \mathbf{g_{10}} . \mathbf{y} \rangle = \langle \mathbf{p}, \mathrm{B}(\mathbf{q}, \mathbf{y}) \rangle; \; \langle \mathbf{g}_{01} . \mathbf{y} \rangle = \langle \mathbf{p}, \mathrm{B}(\bar{\mathbf{q}}, \mathbf{y}) \rangle. \tag{5.44}$$

From the expression of $\dot{\mathbf{y}}$ given in Eq. (5.24), it is known that $\mathbf{h_{20}}$, $\mathbf{h_{11}}$ are the coefficients of the quadratic terms related to the higher order function H; based on Eq. (5.22), they are expressed as [63]:

$$\begin{cases} \mathbf{h_{20}} = \mathrm{B}(\mathbf{q}, \mathbf{q}) - \langle \mathbf{p}, \mathrm{B}(\mathbf{q}, \mathbf{q}) \rangle \mathbf{q} - \langle \bar{\mathbf{p}}, \mathrm{B}(\mathbf{q}, \mathbf{q}) \rangle \bar{\mathbf{q}}; \\ \mathbf{h_{11}} = \mathrm{B}(\mathbf{q}, \bar{\mathbf{q}}) - \langle \mathbf{p}, \mathrm{B}(\mathbf{q}, \bar{\mathbf{q}}) \rangle \mathbf{q} - \langle \bar{\mathbf{p}}, \mathrm{B}(\mathbf{q}, \bar{\mathbf{q}}) \rangle \bar{\mathbf{q}}. \end{cases} \tag{5.45}$$

Substituting Eq. (5.43) into Eq. (5.45) gives:

$$\begin{cases} \mathbf{h_{20}} = \mathrm{B}(\mathbf{q}, \mathbf{q}) - \bar{g}_{20} \mathbf{q} - \bar{\hat{g}}_{02} \bar{\mathbf{q}}; \\ \mathbf{h_{11}} = \mathrm{B}(\mathbf{q}, \bar{\mathbf{q}}) - \hat{g}_{11} \mathbf{q} - \bar{\hat{g}}_{11} \bar{\mathbf{q}}. \end{cases} \tag{5.46}$$

With the expressions given in Eqs. (5.43) through (5.46), now the coefficient $\hat{g}_{21}$ can be defined. However, the expression for $\hat{g}_{21}$ given in Eq. (5.30) has terms such as $\mathbf{A}^{-1}\mathbf{h_{11}}$ and $\left(2\Omega_0 \mathbf{I} - \mathbf{A}\right)^{-1} \mathbf{h_{20}}$ in the place of $\mathbf{y}$ in Eq. (5.44). To further simplify this in order to make the computation easy, from Eq. (5.15), a few identities such as:

$$\begin{cases} \mathbf{A}^{-1} \mathbf{q} = \dfrac{1}{j\Omega_0} \mathbf{q}; \quad \mathbf{A}^{-1} \bar{\mathbf{q}} = -\dfrac{1}{j\Omega_0} \mathbf{q}; \\ \left(2j\Omega_0 \mathbf{I} - \mathbf{A}\right)^{-1} \mathbf{q} = \dfrac{1}{j\Omega_0} \mathbf{q}; \; \left(2j\Omega_0 \mathbf{I} - \mathbf{A}\right)^{-1} \bar{\mathbf{q}} = \dfrac{1}{j3\Omega_0} \bar{\mathbf{q}}, \end{cases} \tag{5.47}$$

can be derived [63]. Using Eqs. (5.43), (5.44) along with (5.46), (5.47), the coefficient $\hat{g}_{21}$ given in Eq. (5.30) can be written as:

$$\hat{g}_{21} = \begin{Bmatrix} \left(\langle \mathbf{p}, \mathrm{C}(\mathbf{q}, \mathbf{q}, \bar{\mathbf{q}} \rangle - 2 \langle \mathbf{p}, \mathrm{B}(\mathbf{q}, \mathbf{W}_1) \rangle + \langle \mathbf{p}, \mathrm{B}(\bar{\mathbf{q}}, \mathbf{W}_2) \rangle \right) \\ + \dfrac{1}{j\Omega_0} \hat{g}_{20} \hat{g}_{11} - \dfrac{2}{j\Omega_0} \left| \hat{g}_{11} \right|^2 - \dfrac{1}{3j\Omega_0} \left| \hat{g}_{02} \right|^2 \end{Bmatrix}, \tag{5.48}$$

where: $\mathbf{W}_1 = \left\{ \mathbf{A}^{-1} \mathrm{B}(\mathbf{q},\bar{\mathbf{q}}) \right\}$, $\mathbf{W}_2 = \left\{ \left(2j\Omega_0 \mathbf{I} - \mathbf{A} \right)^{-1} \mathrm{B}(\mathbf{q},\mathbf{q}) \right\}$. Equation (5.48) is a function consisting of only the eigenvectors and the second and third derivatives given in Eqs. (5.41), (5.42). Calculation of the eigenvector $\mathbf{q}$ and the ad-joint eigenvector $\mathbf{p}$ are given in Appendix C. Note that, the last two terms of Eq. (5.48) are purely imaginary. Thus using the coefficients determined from Eqs. (5.43) and (5.48) in Eq. (5.36), c_1 can be calculated.

The *Poincaré normal form* given in Eq. (5.33) can be transformed further by dividing by Ω which gives:

$$\frac{dz}{d\left(\Omega\tau\right)} = \left(\mu + j\right) z + \left(\frac{c_1(\mu)}{\Omega} \right) z\left|z\right|^2, \tag{5.49}$$

where $\Omega\tau$ is the modified time and $\mu\left(\nu\right) = \alpha\left(\nu\right)/\Omega\left(\nu\right)$ is the new parameter because, $\mu(0) = 0; \mu'(0) > 0$ similar to ν. However, $\left(\frac{c_1(\mu)}{\Omega} \right)$ which is the coefficient of $z\left|z\right|^2$ (nonlinear term) is complex. The aim is to get the *first Lyapunov coefficient*, which is a purely real coefficient of $z\left|z\right|^2$. In order to make this real, the imaginary part of this term is added to the modified time $\Omega\tau$ such that the new time is given by [63]:

$$\hat{\tau}\left(\tau,\ \mu\right) = \Omega\tau + \Im\left\{ \frac{c_1(\mu)}{\Omega} \right\} \left|z\right|^2. \tag{5.50}$$

This allows the modified time $\Omega\tau$ to be re-parameterised along the orbits [63], as $\hat{\tau}$ is now a function of μ. Expressing Eq. (5.49) in the new time gives,

$$\frac{dz}{d\hat{\tau}} = \left(\mu \pm j\right) z + l_1(\mu) z\left|z\right|^2, \tag{5.51}$$

where $l_1(\mu) = \Re\left\{ c_1(\mu)/\Omega \right\} - \mu\Im\left\{ c_1(\mu)/\Omega \right\}$ is real and is called the *first Lyapunov coefficient* [63]. From Eq. (5.36), l_1 when $\mu = 0$ is given by:

$$l_1(0) = \frac{\Re\{c_1(0)\}}{\Omega_0} = \frac{1}{2{\Omega_0}^2}\Re\left\{\left(j\hat{g}_{20}\hat{g}_{11} + \Omega_0\hat{g}_{21}\right)\right\}. \tag{5.52}$$

Substituting for $\hat{g}_{20}$, $\hat{g}_{11}$, $\hat{g}_{21}$ using Eqs. (5.43) and (5.48), the *first Lyapunov coefficient* is given by:

$$l_1(0) = \frac{1}{2\Omega_0}\Re\left\{\langle \mathbf{p}, \mathrm{C}(\mathbf{q},\mathbf{q},\bar{\mathbf{q}})\rangle - 2\langle \mathbf{p}, \mathrm{B}(\mathbf{q},\mathbf{W}_1)\rangle + \langle \mathbf{p}, \mathrm{B}(\bar{\mathbf{q}},\mathbf{W}_2)\rangle\right\}. \tag{5.53}$$

Equation (5.51) becomes the normal form of the equation of motion if l_1 can be replaced by its sign, i.e. its signum function. This can be done by multiplying Eq. (5.51) by $\left(\left|l_1(\mu)\right|\right)^{\frac{1}{2}}$; introducing a new complex variable $\hat{u} = z\left(\left|l_1(\mu)\right|\right)^{\frac{1}{2}}$ and supposing $\alpha'(0) \neq 0$, $\Re\{c_1(0)\} \neq 0$; $l_1(\mu) \neq 0$, the normal form is given by:

$$\dot{\hat{u}} = \left(\mu + j\right)\hat{u} + \sigma\,\hat{u}\left|\hat{u}\right|^2. \tag{5.54}$$

The over-dot denotes the derivative with respect to the new time $\hat{\tau}$; $\sigma = sgn\left(\ l_1(0)\ \right) = sgn\ \left(\Re\{c_1(0)\}\right) = \pm 1$. It is just the sign of the *first Lyapunov coefficient* at the bifurcation point $\mu = 0$, *i.e.* $\nu = 0$ that decides the direction of bifurcation. In order to find the amplitude of the resulting periodic journal motion, it is helpful to introduce the polar form of the co-ordinate $\hat{u}$. Letting $\hat{u} = r_p e^{j\theta_p}$, and writing it in the polar form, Eq. (5.54) becomes:

$$\dot{\hat{u}} = \dot{r}_p e^{j\theta_p} + j r_p \dot{\theta}_p e^{j\theta_p} = r e^{j\theta_p}\left(\mu + j + \sigma r^2\right). \tag{5.55}$$

The subscript p indicates the perfectly balanced rotor. By equating the real and the imaginary parts of Eq. (5.55),

$$\dot{r}_p = r_p\left(\mu + \sigma r_p^2\right), \tag{5.56}$$

$$\dot{\theta}_p = 1. \tag{5.57}$$

Since limit cycle is a steady-state solution, by setting $\dot{r}_p = 0$, Eq. (5.56) gives the radius of the limit cycle as:

$$r_p = \sqrt{-\mu/\sigma} = \sqrt{-\alpha(\nu)/\sigma\Omega(\nu)}\,, \tag{5.58}$$

while Eq. (5.57) indicates a constant angular speed. From the radius Eq. (5.56), two types of behaviour can be studied based on the sign of the r^3 term, σ. Figure 5.4 shows the possible steady-state dynamic behaviour of the system depending on the values of σ and ν.

i) When $\sigma = +1$, Figure 5.4(a) shows an asymptotically stable equilibrium (**SE**) state for $\nu < 0$; Figure 5.4(b) shows an unstable equilibrium state (**UE**) at the critical parameter value, $\nu = 0$. Figure 5.4(c) shows an **UE** state for $\nu > 0$. There is an unstable limit cycle (**ULC**) shown in dashed lines, also known as a repelling cycle for $\nu < 0$, which disappears when ν crosses zero from its negative to positive values as shown in Figure 5.4(a). This is sub-critical *Hopf bifurcation* [63].

ii) When $\sigma = -1$, Figure 5.4(d) shows a **SE** state for $\nu < 0$; Figure 5.4(e) shows the system remaining in the neighbourhood of the equilibrium (**NE**). For $\nu > 0$, a stable limit cycle (**SLC**) for of radius $\sqrt{\mu}$ exists as shown in Figure 5.4(f). All the orbits starting outside or inside the cycle except at the origin $\nu = 0$ tend to the cycle as time → ∞. This is super-critical *Hopf bifurcation*. It should be noted that the *Hopf bifurcation* is local bifurcation and is in the neighbourhood of the equilibrium.

In both the cases there is a loss of stability of the equilibrium at $\nu = 0$ under increase of the bifurcation parameter (the speed). In the sub-critical case ($\sigma = +1$), the region of attraction of the equilibrium point is bounded by the unstable cycle, which shrinks as the parameter approaches its critical value and disappears. Thus, the system is "pushed out" from a neighbourhood of the equilibrium, giving a *sharp or catastrophic stability* *loss* [63]. In super-critical bifurcation, the stable equilibrium is replaced by a stable limit cycle with finite amplitude. Therefore, the system remains in the neighbourhood of the equilibrium and we have a *soft or non-catastrophic stability loss* [63]. If the bifurcation parameter ν is made negative again, the system returns to the stable equilibrium in the case of a soft stability loss. On the contrary, if the system loses its stability sharply, resetting to a negative value of the parameter may not return the system back to the stable equilibrium since it may have left its region of attraction. It can be seen that the type of *Hopf bifurcation* is determined by the stability of the equilibrium state at the critical parameter value. The type of bifurcation in the rotor system under investigation will be discussed in detail in Section 5.5.

It is now evident that to determine the regions of sub-critical and super-critical bifurcation for the rotor-bearing system under investigation, it is necessary to compute the *first Lyapunov coefficients* corresponding to each steady-state eccentricity ratio. Table 5.1 lists the sign of the *first Lyapunov coefficient* and the real and imaginary parts of the coefficient c_1 corresponding to the steady-state eccentricity ratios $0.01 \le n_s \le 0.75$ calculated in MATLAB. The signs of these coefficients are also verified by using a similar algebraic formula discussed in the following Section.

5.3.3 POORE'S BIFURCATION FORMULA

This Sub-Section is aimed at verifying the sign change discussed above using the *first Lyapunov coefficient* by an equivalent method known as the *Poore's bifurcation formula*. The way in which this formula is related to that of the *first Lyapunov coefficient* given in Eq. (5.53) is also presented.

A.B. Poore [71] derived an algebraic formula to determine the existence and the stability of the bifurcated periodic orbits in a sufficiently small neighbourhood of $(\mathbf{x}, \nu) = (0,0)$. The formula is given by:

$$\alpha'(0)\delta'(0) \; + \; j\left(\Omega'(0)\delta'(0)+\Omega_0\eta'(0)\right)$$
$$= k_a^2 \begin{Bmatrix} -p_l \dfrac{\partial^3 F_l}{\partial x_j \partial x_k \partial x_p} q_j q_k \bar{q}_p + 2p_l \dfrac{\partial^2 F_l}{\partial x_j \partial x_k \partial x_p} q_j (\mathbf{A}^{-1})_{kr} \dfrac{\partial^2 F_r}{\partial x_p \partial x_q} q_p \bar{q}_q \\ +p_l \dfrac{\partial^2 F_l}{\partial x_j \partial x_k} \bar{q}_j (\mathbf{A} - \left(2i\Omega_0\right)\mathbf{I})^{-1}{}_{kr} \dfrac{\partial^2 F_r}{\partial x_p \partial x_q} q_p q_q \end{Bmatrix}, \qquad (5.59)$$

where the right-hand side is similar to that of the *first Lyapunov coefficient* given in Eq.(5.53); $\mathbf{p} = [p_1, p_2, p_3, p_4]^T$ and $\mathbf{q} = [q_1, q_2, q_3, q_4]^T$ are the eigenvector and the adjoint eigenvector used in the previous section; it is referred as the left and the right eigenvectors respectively in this formula, corresponding to the eigenvalue $+i\Omega_0$ of the Jacobian $\mathbf{A}$, at $\nu = 0$; The over bar denotes the conjugates; vectors $\mathbf{p}$ and $\mathbf{q}$ are normalised by the requirement $\mathbf{p}\,.\,\mathbf{q} = 1$, which is the dot product of the vectors similar to that of the standard scalar product; k_a is an arbitrary constant, and $(\mathbf{A}^{-1})_{kr}$ denotes the k^{th} row r^{th} column of the inverse of the Jacobian $\mathbf{A}$. Repeated indices within each term imply a sum from 1 to n where n is the number of degrees of freedom. Although the right-hand side of Eq. (5.59) can only be evaluated with an arbitrary positive constant k_a^2, this is sufficient to indicate whether the period of these orbits are increasing or decreasing [8]. The left-hand side of the formula is a complex number. It is the sign of the real part which decides the type of the bifurcation [71]. However, $\alpha'(0)$ has already been verified to be positive as the fourth condition of the *Hopf bifurcation* in Section 5.2.1. Hence, the sign of $\delta'(0)$ indicates whether the bifurcation is super-critical ($\delta'(0) > 0$) or sub-critical ($\delta'(0) < 0$), under the condition that the bifurcation can only occur for different signs of the bifurcation parameter, i.e. $\nu > 0$ or $\nu < 0$.

The sign of $\eta'(0)$ informs about the time period of the limit cycle. A positive sign implies an increase in the time period, while a negative sign implies a decrease in the time period [71]. This is further discussed in detail in the following section. The left-hand side is equivalent to the coefficient of the resonant cubic term $c_1(0)$ given in Eq. (5.33)[51]. The relation between c_1 and Poore's formula is discussed in the following Sub-Section.

5.4 AMPLITUDE OF THE LIMIT CYCLE

This Sub-Section describes the calculation of the amplitude of the stable and the unstable limit cycles which are shown to exist in the system around the threshold speed, in the previous Section. The amplitudes depend on the system parameters which can be calculated from Eq. (5.33). It should be noted that the limit cycle of the journal centre corresponding to higher eccentricity ratios becomes elliptical in shape compared to the ones at low eccentricity ratios. This is attributed to the increase in the asymmetry of the bearing properties with an increase in the steady-state eccentricity ratio. Hence, the equation for the approximate limit cycle whose shape is determined by the eigenvector is also presented.

It is convenient to write the *Poincaré normal form* given in Eq. (5.33) in the polar form as:

$$\dot{r}_p = \alpha(0) r_p + \tilde{a} r_p^3 , \tag{5.60}$$

$$\dot{\theta}_p = \Omega(0) + \tilde{b} r_p^2 , \tag{5.61}$$

where: $\hat{s} = \alpha + j\Omega$ and $c_1 = \tilde{a}(\nu) + j\tilde{b}(\nu)$, which are the functions of the bifurcation parameter ν. Since the interest here is in the dynamics near the critical value $\nu = 0$, expanding the coefficients about $\nu = 0$ gives:

$$\dot{r}_p = \alpha'(0)\nu r_p + \tilde{a}(0) r_p^3 + \tilde{a}'(0)\nu r_p^3 , \tag{5.62}$$

$$\dot{\theta}_p = \Omega(0) + \Omega'(0)\nu + \tilde{b} r_p^2 + \tilde{b}'(0)\nu r_p^2 , \tag{5.63}$$

where α' represents the differentiation with respect to ν; $\alpha(0) = 0$ and $\Omega(0) > 0$. For sufficiently small ν, by setting $\dot{r}_p = 0$, the steady-state periodic solution to Eqs. (5.62) and (5.63) are given by [62]:

$$r_p = \sqrt{\frac{-\nu\alpha'}{\tilde{a}}} = \sqrt{\frac{-\left(\varpi - \varpi_0\right)\alpha'}{\Re\{c_1(0)\}}}\,, \tag{5.64}$$

and

$$\theta_p = \left[\Omega(0) + \left(\Omega'(0) - \alpha'(0)\frac{\tilde{b}(0)}{\tilde{a}(0)}\right)\nu\right]t + \theta_0\,, \tag{5.65}$$

where θ_0 is the initial phase. Note that the last terms in Eqs. (5.62) and (5.63) are ignored, since $\nu r^2, \nu r^3$ are relatively too small for sufficiently small ν, since $r < 1$. Allowing for a slow increment of the bifurcation parameter in μ, let $\nu = \nu\left(\mu\right) = \mu\delta\left(\mu\right)$. Using Taylor's expansion of this expression about $\nu = 0$ i.e. $\nu \approx \delta'\left(0\right)\mu^2$, when $\delta(0) = 0$, Eqs. (5.62) , (5.63) become:

$$\dot{r}_p = \alpha'(0)\delta'\left(0\right)\mu^2 r_p + \tilde{a}(0) r_p^3\,, \tag{5.66}$$

$$\dot{\theta}_p = \Omega(0) + \Omega'(0)\delta'\left(0\right)\mu^2 + \tilde{b}(0) r_p^2\,. \tag{5.67}$$

When the amplitude is very small, let $r_p = \mu$ be the non-trivial solution of Eq. (5.66) [51]. Substituting for r_p into Eq. (5.66) gives,

$$\tilde{a} = -\alpha'(0)\delta'\left(0\right). \tag{5.68}$$

Introducing a time period change of the form $T(1+\eta(\nu)\mu)$ [63, 71], where T is the time period corresponding to the frequency $\Omega(0)$ at the threshold speed, i.e.,

$$\Omega(0) = 2\pi/T\,; \tag{5.69}$$

$\eta(\nu)\mu$ is the change in the time period. It can be seen that the time period increases or decreases depending on the sign of $\eta(\nu)$. Using Taylor's expansion about $\nu = 0$,

$\eta(\nu)\mu \approx \eta'(0)\mu^2$, which gives the time period change as $T(1+\eta'(0)\mu^2)$. Thus, the change in whirl frequency corresponding to the time period change is given by:

$$\dot{\theta}_p = 2\pi \big/ \left[T(1+\eta'(0)\mu^2) \right]. \tag{5.70}$$

Using the binomial expansion of Eq. (5.70) and ignoring $O(\mu^3)$ terms, for very small μ, Eq. (5.67) can be written as:

$$\frac{2\pi}{T}(1-\eta'(0)\mu^2) = \Omega(0) + \left[\Omega'(0)\delta'(0) + \tilde{b}(0) \right]\mu^2, \tag{5.71}$$

which by using Eq. (5.69), results in,

$$\tilde{b} = -\left[\Omega'(0)\delta'(0) + \Omega(0)\eta'(0) \right]. \tag{5.72}$$

From Eqs. (5.68) and (5.72), the coefficient $c_1(0)$ in Eq. (5.33) is given as:

$$c_1(0) = \tilde{a} + j\tilde{b} = -\left[\alpha'(0)\delta'(0) + j\left(\Omega'(0)\delta'(0) + \Omega_0\eta'(0) \right) \right]. \tag{5.73}$$

Equation (5.73) relates $c_1(0)$ to the left-hand side of the *Poore's bifurcation formula* given in Eq. (5.59). Increase in the static load increases the static eccentricity which changes the shape of the limit cycle to an ellipse from a circle. Hence, using Eq. (5.68) in Eq. (5.64) and adding the steady-state solution, the limit cycle is better approximated in shape by the form [78, 79]:

$$x_i = x_s + \left(\frac{\varpi - \varpi_0}{\delta'} \right)^{\frac{1}{2}} \Re\left\{ e^{\left(2\pi j\hat{\tau}/T\right)} q_i \right\}, \tag{5.74}$$

where $i = 1, 3$, since $x_1 = X - X_s$, $x_3 = Y - Y_s$ as given in Eq. (4.19) in Chapter 4. Based on the sign of the *first Lyapunov coefficients*, the dynamic behaviour of the rotor system under investigation is discussed along with the findings from the numerical analysis in the following Section. The limit cycle using Eq. (5.74) is compared with that from the numerical analysis.

5.5 DISCUSSION OF THE ANALYTICAL AND THE NUMERICAL RESULTS

In this Section, the nonlinear behaviour of the perfectly balanced rotor system with short-bearing approximation and oscillating π-film under investigation is discussed based on the analytical and the numerical findings discussed in the previous Sub-Sections. Table 5.1 shows two regions from the effect of the static load, based on the steady-state eccentricity ratios of the journal in short journal bearings with oscillating π-film cavitation. The journal dynamics exhibit sub-critical bifurcation for $n_s \leq 0.32$, and super-critical bifurcation for $0.33 \leq n_s \leq 0.75$, which are defined in Section 5.2.

The two regions for the rotor system under investigation corresponding to sub-critical bifurcation and super-critical bifurcation respectively are shown in the parameter plane in Figure 5.5(a). It is determined from the linear analysis in Chapter 4 that the journal centre spirals into a stable equilibrium (**SE**) state below the threshold speed and spirals out to an unstable equilibrium (**UE**) state above the threshold speed. In addition, the nonlinear analysis of the rotor system reveals the existence of a limit cycle other than the equilibrium state, either above or below the threshold speed, according to the *Hopf bifurcation* theorem discussed in Section 5.2.

The dynamic behaviour of the journal in the two regions is discussed below in detail:

Region I - sub-critical bifurcation $\left(l_1(0) > 0, \delta' < 0\right)$:

In this region, below the stability threshold line, along with the **SE** state, there exists an unstable limit cycle (**ULC**) of radius $\sqrt{\mu}$. Figure 5.5(b) shows the sub-critical bifurcation diagram appertaining **Region I**. The amplitude of the **ULC** reduces as the speed approaches the threshold value. At $\bar{\omega}_0$ **ULC** disappears. Above $\bar{\omega}_0$, the journal centre spirals out towards an **UE** state. Dashed lines represent the unstable solution. Figure 5.6(a) shows the plot of the amplitude of the limit cycles in X direction, in the two regions. Figure 5.6(b) shows the plot of the approximate limit cycles calculated using Eq. (5.74) for the rotor system under investigation for increasing steady-state eccentricity ratio. It can be seen that the amplitude of the **ULC** increases with the increase in the steady-state eccentricity ratio, which attains its maximum at the boundary $n_s = 0.32$ between the regions shown in Figure 5.5. It should be noted that the size of the **ULC** is very small for $n_s \approx 0$, which is the case for negligible static load.

The bifurcation in the dynamic behaviour of the rotor system under investigation is also predicted from the numerical analysis by using the Runge-Kutta method. Figure 5.7 marks the corresponding locations on the parametric plane for which the dynamic behaviour of the journal centre are plotted from the numerical solution. Figure 5.8(a) shows the plot of the journal centre orbit corresponding to the steady-state eccentricity ratio $n_s = 0.1$ from **Region I**, for a speed below the threshold speed $\bar{\omega} = \bar{\omega}_0 - 0.1$. The **ULC** given by $r_p = \sqrt{\mu} = 0.21$ is shown to demarcate the two initial eccentricity ratios presented in Figure 5.8. The journal centre spirals inwards when the initial eccentricity ratio n_0, which is the amplitude of the whirl motion, is less than the **ULC** radius ($n_0 = 0.16$). Conversely, the journal centre spirals outwards away from the **SE** state, when n_0 is greater than r_p ($n_0 = 0.26$). Figure 5.8(b) shows the corresponding time series plot of the journal centre showing the variation in the eccentricity ratio n of the journal centre. The figure shows the amplitude of the whirl motion as time increases, when the rotor is spinning at a constant speed which is below the threshold speed.

For the same initial eccentricity ratios (n_0) shown in Figure 5.8(a) and (b), for a speed above the threshold speed $\bar{\omega} = \bar{\omega}_0 + 0.1$, Figure 5.9(a) shows the journal spiralling out towards an **UE** state. Figure 5.9(b) shows the corresponding time series.

Region II - super-critical bifurcation $\left(l_1(0) < 0, \delta' > 0\right)$:

In this region, the journal centre spirals into a stable equilibrium state (**SE**) below the threshold speed. But when the rotor spins at a speed above the threshold speed, the *Hopf bifurcation* leads to the birth of a stable limit cycle (**SLC**) other than the existence of an **UE**. Figure 5.5(c) shows the super-critical bifurcation diagram for **Region II**. As the speed increases, the journal centre reaches a **SE** below $\bar{\omega}_0$. The **SLC** appears above $\bar{\omega}_0$ and starts increasing in size with increasing speed. During the **SLC**, the journal centre keeps whirling at finite amplitude. Any neighbouring state of the journal centre, inside or outside of the **SLC**, attracts the journal centre to the **SLC** as shown in Figure 5.1(b). The amplitude of the **SLC** reduces with the increasing eccentricity ratio after the boundary for $n_s > 0.32$ as shown in Figure 5.6. From the numerical analysis, for $n_s = 0.5$, Figure 5.10(a) shows the orbits approaching a **SLC** of radius $r_p = 0.6$ for both the given initial eccentricity ratios that are inside ($n_0 = 0.59$) and outside the **SLC** ($n_0 = 0.61$) for a speed above the threshold speed $\bar{\omega} = \bar{\omega}_0 + 0.1$. Figure 5.10(b) shows the corresponding time series plot. But, for the same initial eccentricity ratios, Figure 5.11(a) and (b) show the orbit and the time series plots for $\bar{\omega} = \bar{\omega}_0 - 0.1$. The journal centre spirals inwards to a **SE** state for a speed below the threshold speed.

Figure 5.12 shows the plot of the dynamic behaviour of the rotor-system under investigation across the bearing clearance. This gives a summary of the behaviour discussed above. If the steady-state eccentricity of the journal centre is within about 32% of the clearance (**Region I**) with respect to the bearing centre, then the journal centre exhibits sub-critical bifurcation; if the eccentricity of the journal centre is between about 33% and 76% of the clearance (**Region II**), then the journal centre exhibits super-critical bifurcation. Above about 76%, the rotor has a stable equilibrium.

On the basis of the fact that $\eta' > 0$, it is evident that the time period of the limit cycle increases in both the regions as the eccentricity ratio is increased [71]. This suggests that the whirling frequency of the journal centre exhibiting a limit cycle reduces, as the static load is increased. The procedure for determining the boundary from the *first Lyapunov coefficients* was verified by determining the same using the long bearing approximation for the fluid-film forces. This was found to be in agreement with the two boundaries given by Myers and Gardner [23, 43] for a similar system.

The above discussion suggests that a rotor system operating in **Region I** is undesirable, since the journal centre mostly grows in amplitude towards the housing, unless limited by other nonlinearity in the system. Operating in **Region II** is desirable as the journal centre whirls at finite amplitude above the threshold speed. This requires choosing a very low σ_m as shown in Figure 4.3 in Chapter 4, for example, $\sigma_m = 0.1$; this means that the design parameters and the static load combine in such a way that the operating curve lies mostly in **Region II**. For a given set of bearing parameters such as the bearing dimensions and the lubricant viscosity, Eq. (4.18) suggests that the external static load can aid in achieving this. However, the analysis signifies that for the case of a turbocharger, σ_m is very high due to the negligible static load. Figure 5.13 depicts the operating curves corresponding to very high $\sigma_m = 100,\ 500$ in comparison with that of relatively low values, such as, $\sigma_m = 1.2,\ 10$ in **Region I**. It is evident that the operating curves represented by $\sigma_m = 100$ and 500 reach a very low eccentricity ratio close to $n_s \approx 0.001$, at a very low speed and asymptote vertically. It is shown that in **Region I**, the journal centre reaches **SE** or **ULC** below the threshold speed and **UE** above the threshold speed. It can be seen in Figure 5.6(a) that the **ULC** is too small for very small eccentricity ratios. This suggests that for most of the speed range, the journal centre of a turbocharger rotor spirals outwards.

5.6 CONCLUSIONS

In a dynamic system of a perfectly balanced rotor in short-bearings with oscillating π-film cavitation, the onset of oil-whirl was reviewed and related to the *Hopf bifurcation*. The 4-dimensional system was reduced to a 2-dimensional one by applying the Centre Manifold Theorem. Then the system was transformed to a normal form, wherein the nonlinear hydrodynamic oil-film forces were considered upto the third order; the *Hopf bifurcation* was examined. The nature (type) of bifurcation in the parameter plane was determined by calculating the *first Lyapunov coefficients* of the normal form. A boundary was determined between the two identified bifurcation regions for the rotor system, in terms of the steady-state eccentricity ratio. This was verified using the *Poore's bifurcation algebra*. The dynamic behaviour of the rotor system in these regions was presented in the form of orbit plots produced from the numerical analysis.

The dynamic behaviour of the journal bifurcates by experiencing a change in the stability at the threshold speed that separates the stable and the unstable equilibrium states of the journal centre and is characterized also by the disappearance or appearance of a limit cycle. The rotor system exhibits sub-critical bifurcation (disappearance of an unstable limit cycle) if the steady-state eccentricity ratio of the journal under the static load is less than 0.32 and super-critical bifurcation (appearance of a stable limit cycle) if the eccentricity ratio is between 0.33 and 0.76. Operating the rotor system in the super-critical bifurcation region allows the journal centre to assume a stable limit cycle above the threshold speed. The presence of a static load increases the steady-state eccentricity ratio of the rotor, which helps in achieving this.

Since an automotive turbocharger is generally lightly loaded, the journal has a very low steady-state eccentricity ratio in the bearings. Hence, the turbocharger must be operating in the sub-critical bifurcation region. This is undesirable since the journal effectively spiralled outward close to the housing, for most of the speeds. Hence, the presence of a static load seemed to be an option to keep the turbocharger operating in the higher eccentricity range, thereby allowing the existence of a stable limit cycle.

The understanding of the dynamic behaviour of a turbocharger with a perfectly balanced rotor pertaining to very high σ_m (non-dimensional group of bearing parameters), helps in analysing the waterfall plots shown in Chapter 1 to determine the effect of unbalance. This is presented in the next Chapter.

n_s	$\sigma_m = S_m/\omega_0$	ω_0	Ω_0	$\alpha'(0)$	$\delta'(0)$	$\eta'(0)$	$l_1(0)$	$\Re\{c_1(0)\}$	$\Im\{c_1(0)\}$	
0.01	46.07	2.76	0.5	0.01	<0	>0	>0	0.02	-0.001	sub-critical bifurcation
0.05	9.18	2.76	0.50	0.03	<0	>0	>0	0.08	-0.018	
0.10	4.54	2.74	0.50	0.06	<0	>0	>0	0.13	-0.07	
0.2	2.16	2.68	0.51	0.09	<0	>0	>0	0.12	-0.16	
0.3	1.31	2.61	0.52	0.09	<0	>0	>0	0.02	-0.17	
0.32	1.19	2.59	0.52	0.08	<0	>0	>0	0.004	-0.17	
0.33	1.15	2.58	0.52	0.08	>0	>0	<0	-0.006	-0.16	super-critical bifurcation
0.4	0.84	2.54	0.52	0.08	>0	>0	<0	-0.07	-0.12	
0.5	0.52	2.54	0.51	0.06	>0	>0	<0	-0.17	-0.01	
0.6	0.29	2.70	0.47	0.04	>0	>0	<0	-0.39	0.19	
0.7	0.11	3.63	0.34	0.01	>0	>0	<0	-1.49	0.42	
0.75	0.03	9.87	0.13	0.00	>0	>0	<0	-10.6	-5.1	

Table 5.1 Table of the parameters α', δ', η' , the sign of the *first Lyapunov coefficient* l_1 and the non linear coefficient of the cubic term in the normal form c_1 evaluated at the threshold speed $\nu = 0$ for a set of steady-state eccentricity ratios. The corresponding threshold speed $\bar{\omega}_0$ and the whirl frequency Ω_0 are also shown.

FIGURES

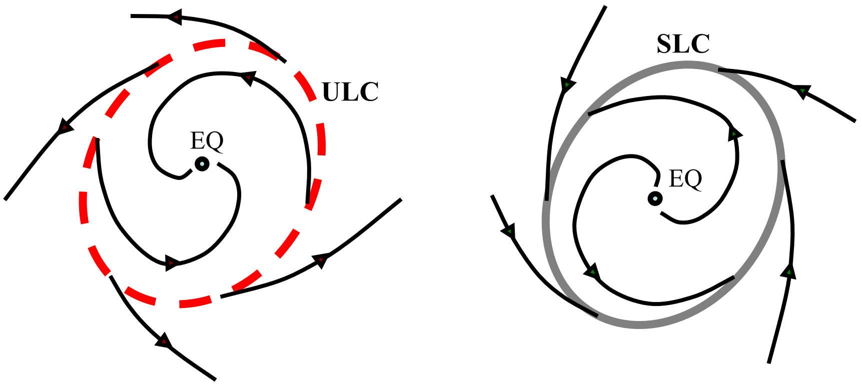

(a) unstable limit cycle (**ULC**) (b) stable limit cycle (**SLC**)

Figure 5.1 Schematic of (a) the unstable and (b) the stable limit cycles showing the repelling and attracting nature respectively towards the neighbouring trajectories. EQ is the equilibrium state of the dynamic system. The dashed line shows the **ULC** and the grey continuous line shows the **SLC**. Based on [23]

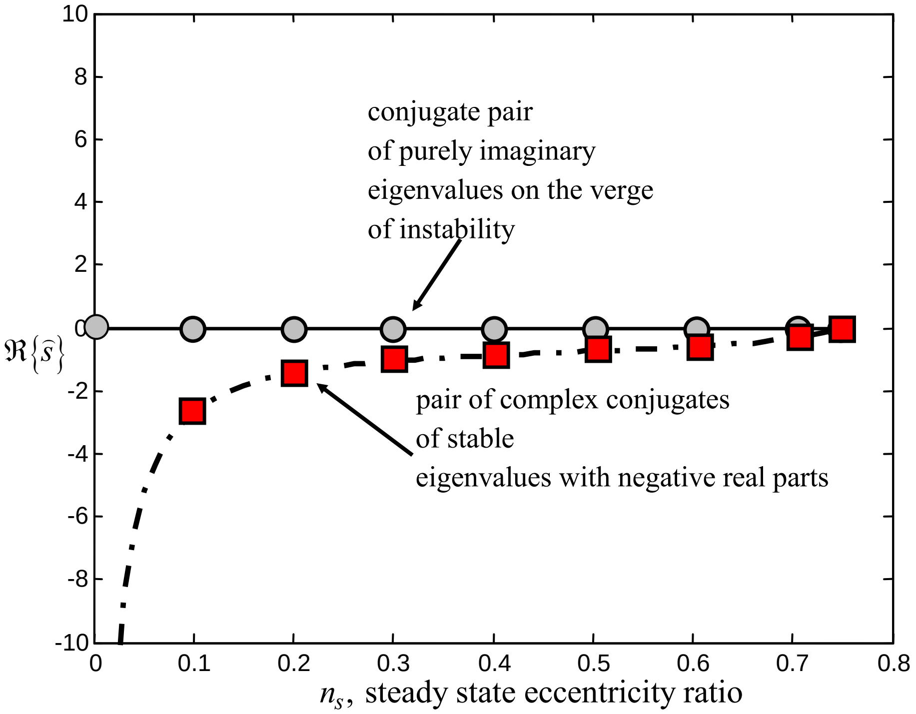

Figure 5.2 Plot of the real part of the eigenvalues ($\hat{s}$) at the threshold speed, varying with the steady-state eccentricity ratio showing a conjugate pair of purely imaginary eigenvalues and a conjugate pair of stable eigenvalues, which satisfies one of the conditions for the occurrence of the *Hopf bifurcation*.

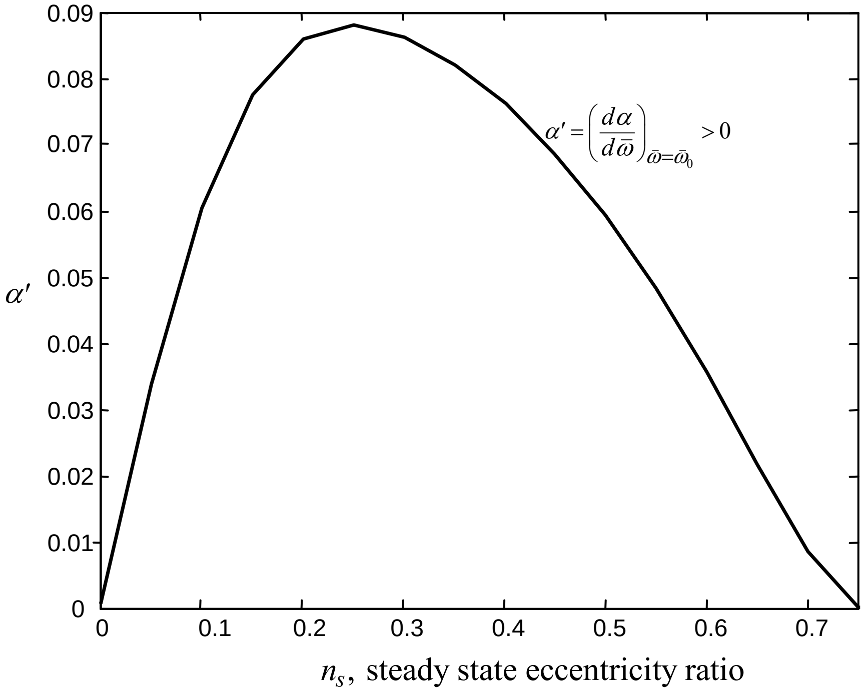

Figure 5.3 Plot of the derivative of the real part of the eigenvalue $\hat{s}$ which is purely imaginary at the threshold speed, with respect to the rotational speed. The derivative is evaluated at the threshold speed to show its continuity at the threshold speed.

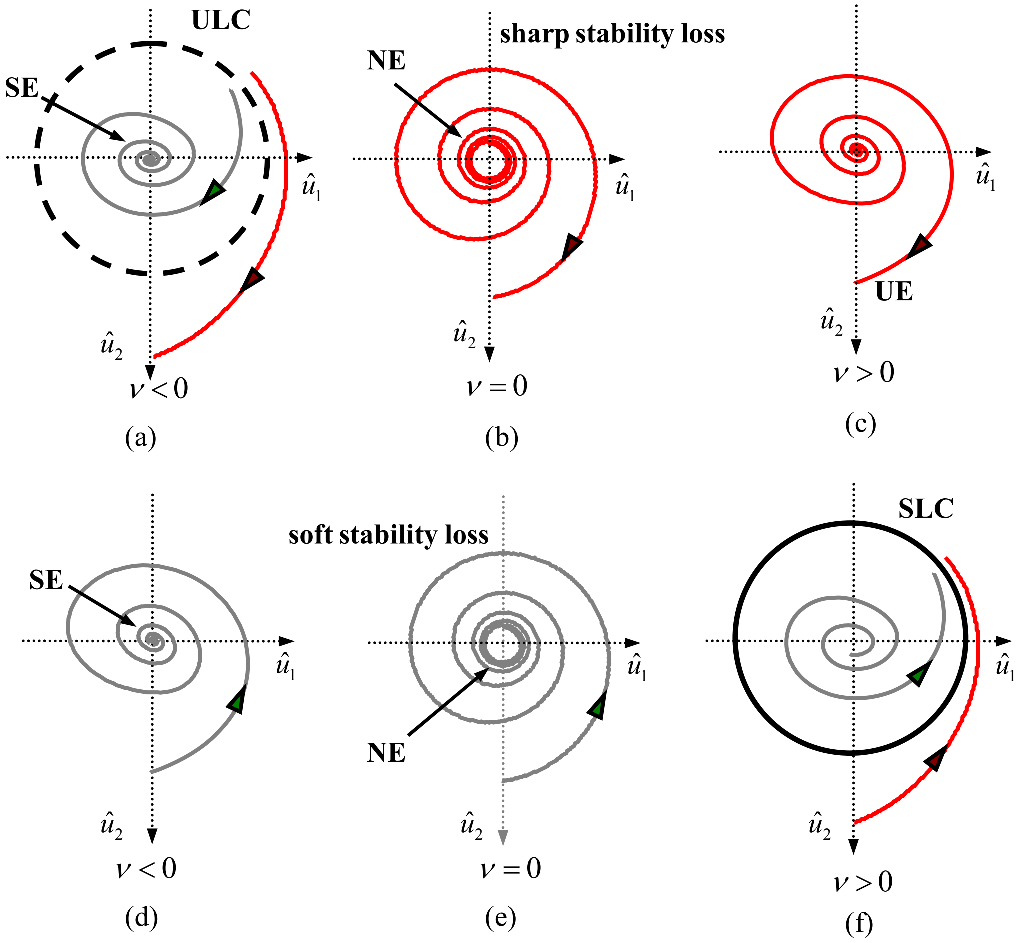

Figure 5.4 Phase portraits (orbits) related to the sub-critical and super-critical bifurcations, which are possible solutions to Eq. (5.54) where $\hat{u} = \hat{u}_1 + j\hat{u}_2$; (a) orbit below the threshold speed (b) at the threshold speed (c) above the threshold speed related to the sub-critical bifurcation (d) orbit below the threshold speed (e) at the threshold speed (f) above the threshold speed related to the super-critical bifurcation. **SE** – stable equilibrium, **UE** – unstable equilibrium, **SLC** – stable limit cycle, **ULC** – unstable limit cycle, **NE** – neighbourhood of equilibrium, $\nu = \varpi - \varpi_0 - \text{bifurcation paramater}$. Reproduced based on the diagram given in [63].

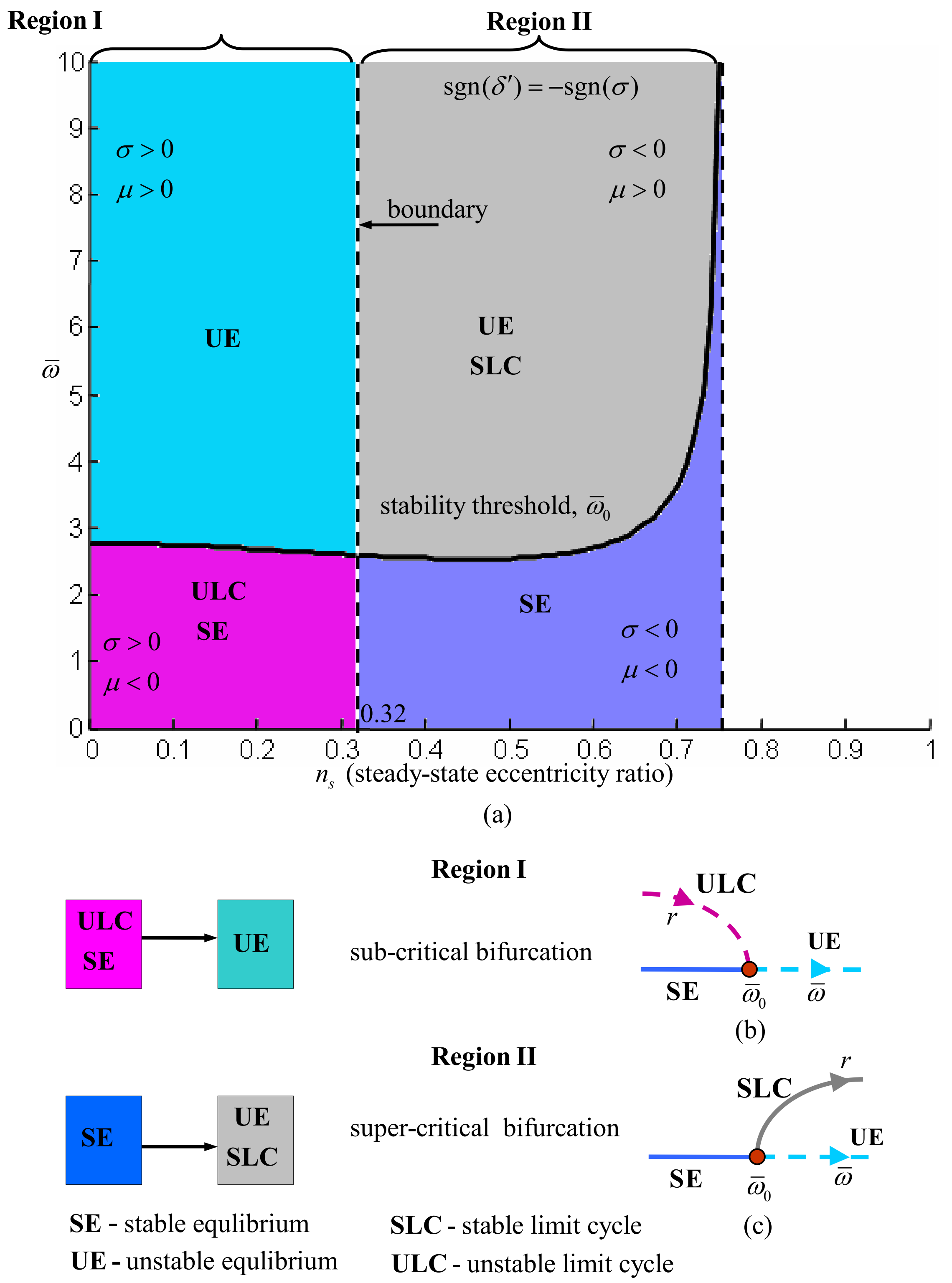

Figure 5.5 (a) Plot showing the regions of sub-critical and super-critical bifurcations in the dynamics of the journal in a short-bearing with an oscillating π-film cavitation under the effect of a static load. σ is the sign of the *first Lyapunov coefficient* $l_1(0)$ and $\mu = \alpha / \Omega$ (b) Schematic illustration of the sub-critical bifurcation with reduction in the **ULC** amplitude below the threshold speed (c) Schematic illustration of the super-critical bifurcation with increase in the **SLC** amplitude above the threshold speed; $\bar{\omega}_0$ is the threshold speed and $\bar{\omega}$ is the rotor speed.

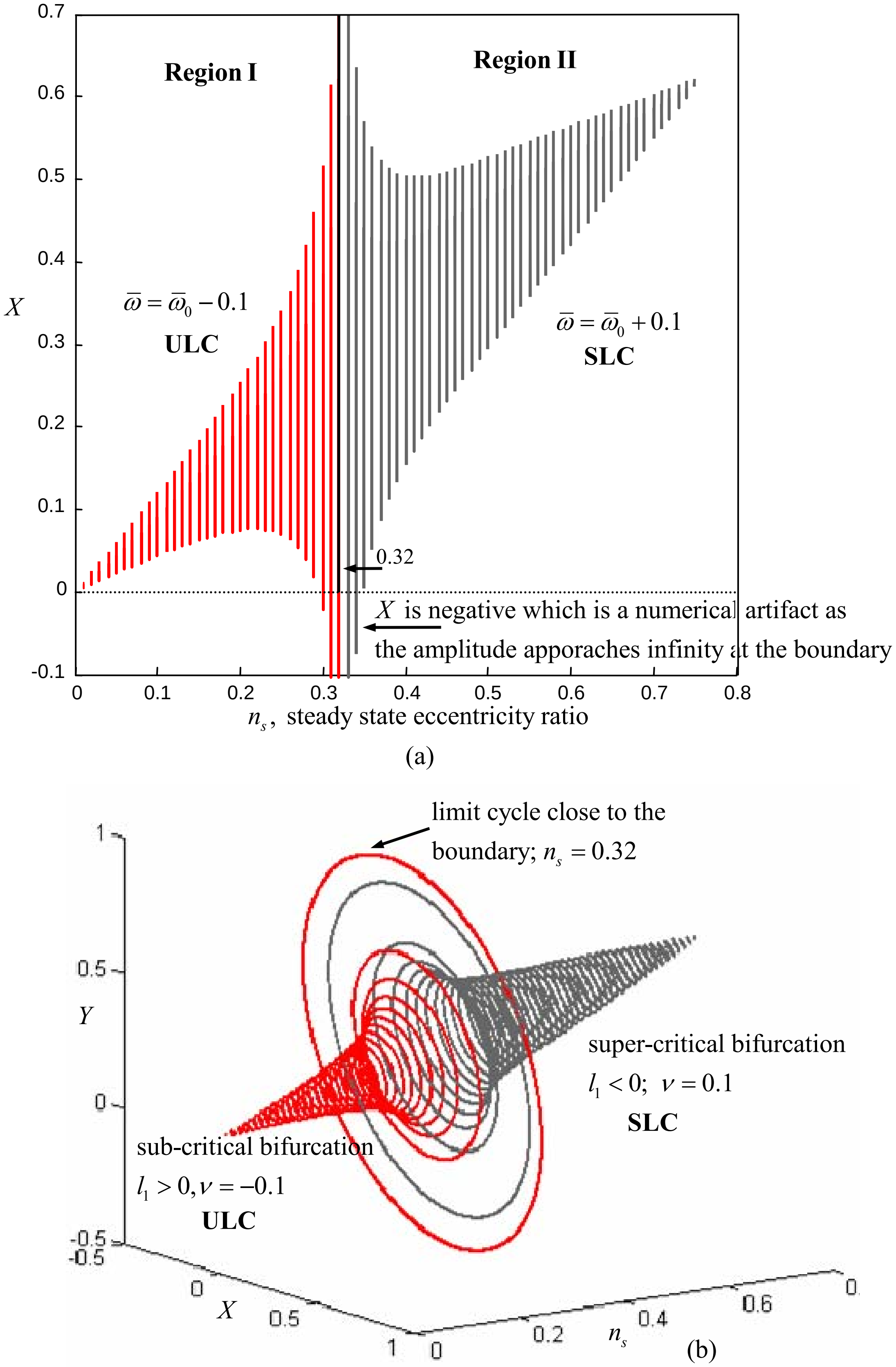

Figure 5.6 (a) Plot showing the limit cycle amplitude along X direction in **Region I** and **II** (b) Plot showing the **ULC** and **SLC** amplitudes varying with n_s; l_1 is the *first Lyapunov coefficient*.

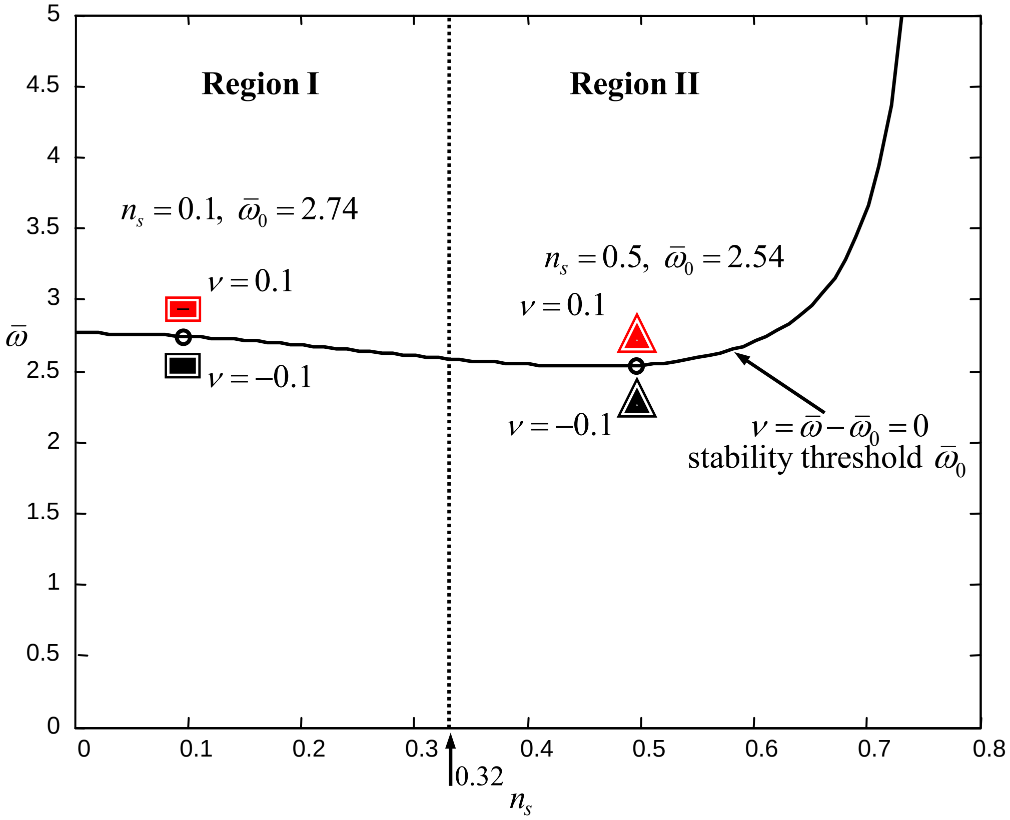

Figure 5.7 Plot showing the regions on the parametric plane with markers signifying the parameters - steady-state eccentricity ratio and the rotational speed, corresponding to the numerical plots presented in the following figures.

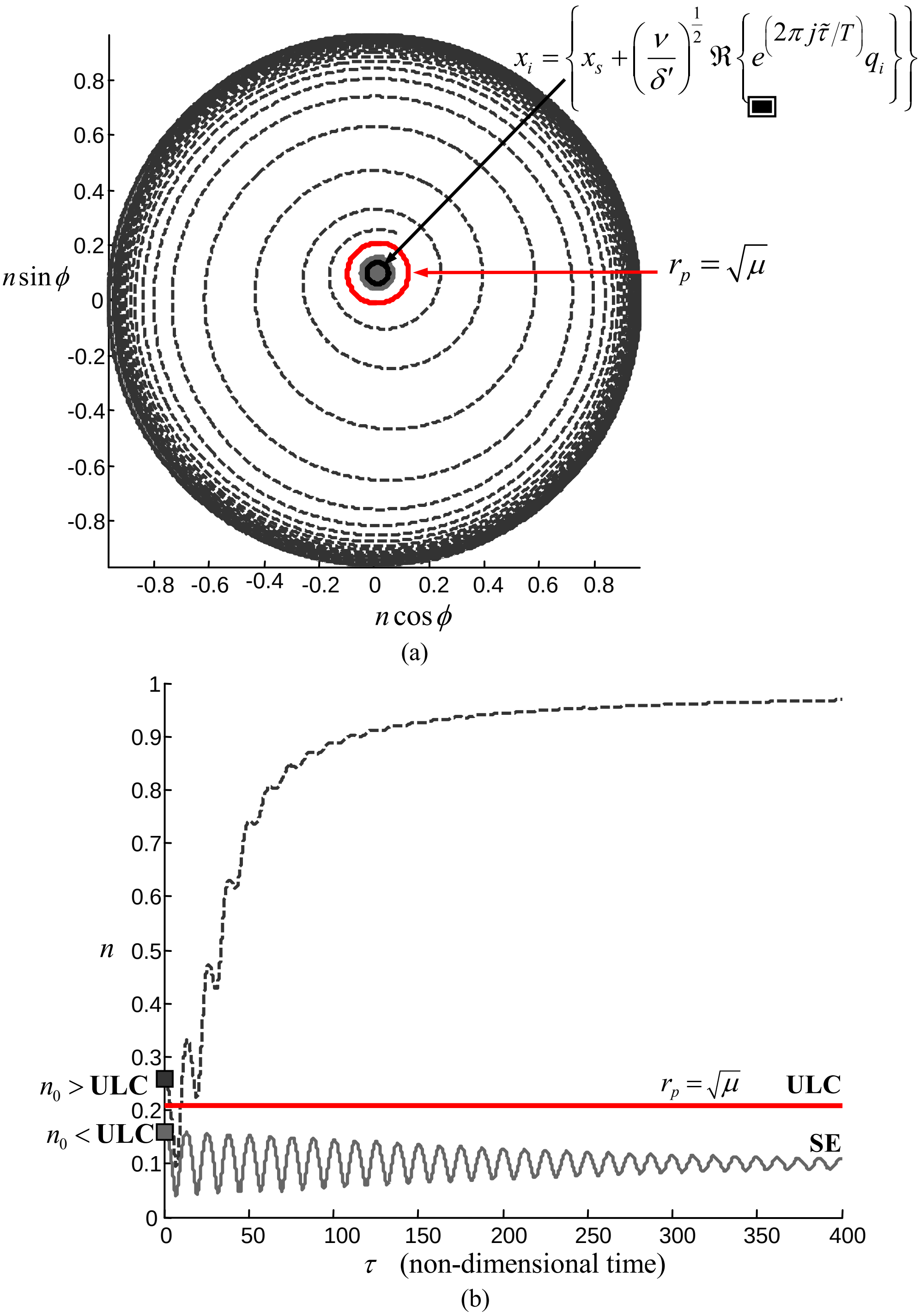

(a)

(b)

Figure 5.8 (a) Plot of the orbits corresponding to $n_s = 0.1$ (**Region I**) related to sub-critical bifurcation, along with the **ULC**, when the rotor spins below the threshold speed $\varpi = \varpi_0 - 0.1$. The journal centre orbits into a **SE** state from an initial eccentricity ratio $n_0 = 0.16$ $(<\textbf{ULC})$ and orbits outwards for the initial eccentricity ratio $n_0 = 0.26$ $(>\textbf{ULC})$, when $\sigma_m = 4.38,\ r_p = 0.21$; the black rectangle indicates the location in Figure 5.7 in the parameter plane. (b) Time series corresponding to the orbits given in (a) showing the variation of the journal centre eccentricity ratio with the non-dimensional time.

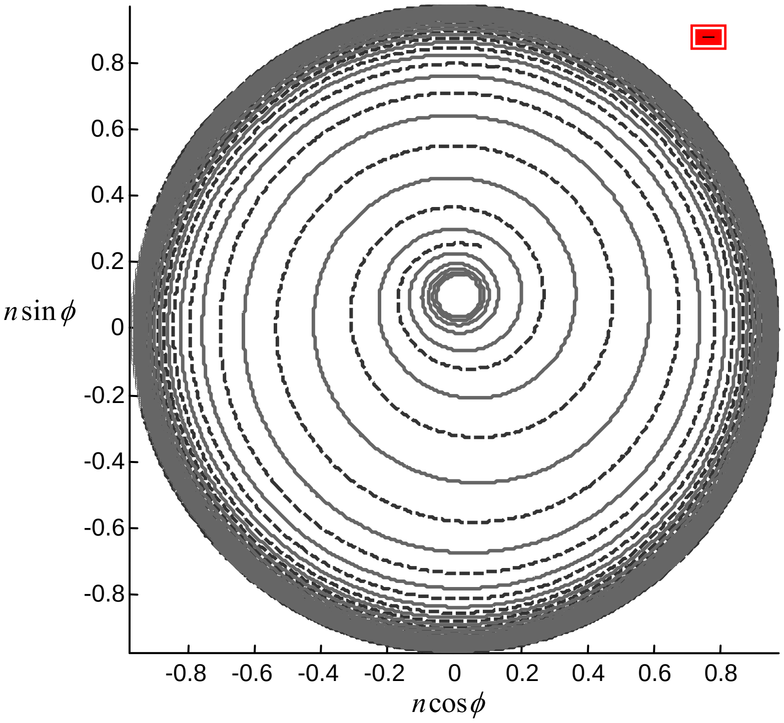

(a)

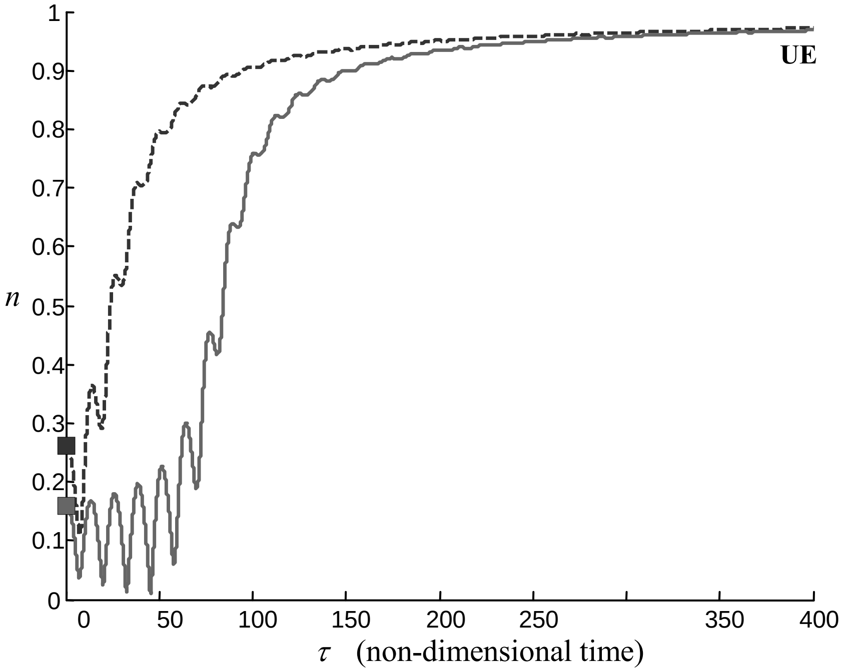

(b)

Figure 5.9 (a) Plot of the orbits corresponding to $n_s = 0.1$ (**Region I)** related to sub-critical bifurcation, when the rotor spins above the threshold speed $\bar{\varpi} = \bar{\varpi}_0 + 0.1$; the journal centre spirals outwards to an **UE** state, for the same initial eccentricity ratios (n_0) given in Figure 5.8, while all the other parameters are maintained the same; the red rectangle indicates the location in Figure 5.7 in the parameter plane. (b) Time series corresponding to the orbits shown in (a), showing the variation of the journal centre eccentricity ratio with the non-dimensional time.

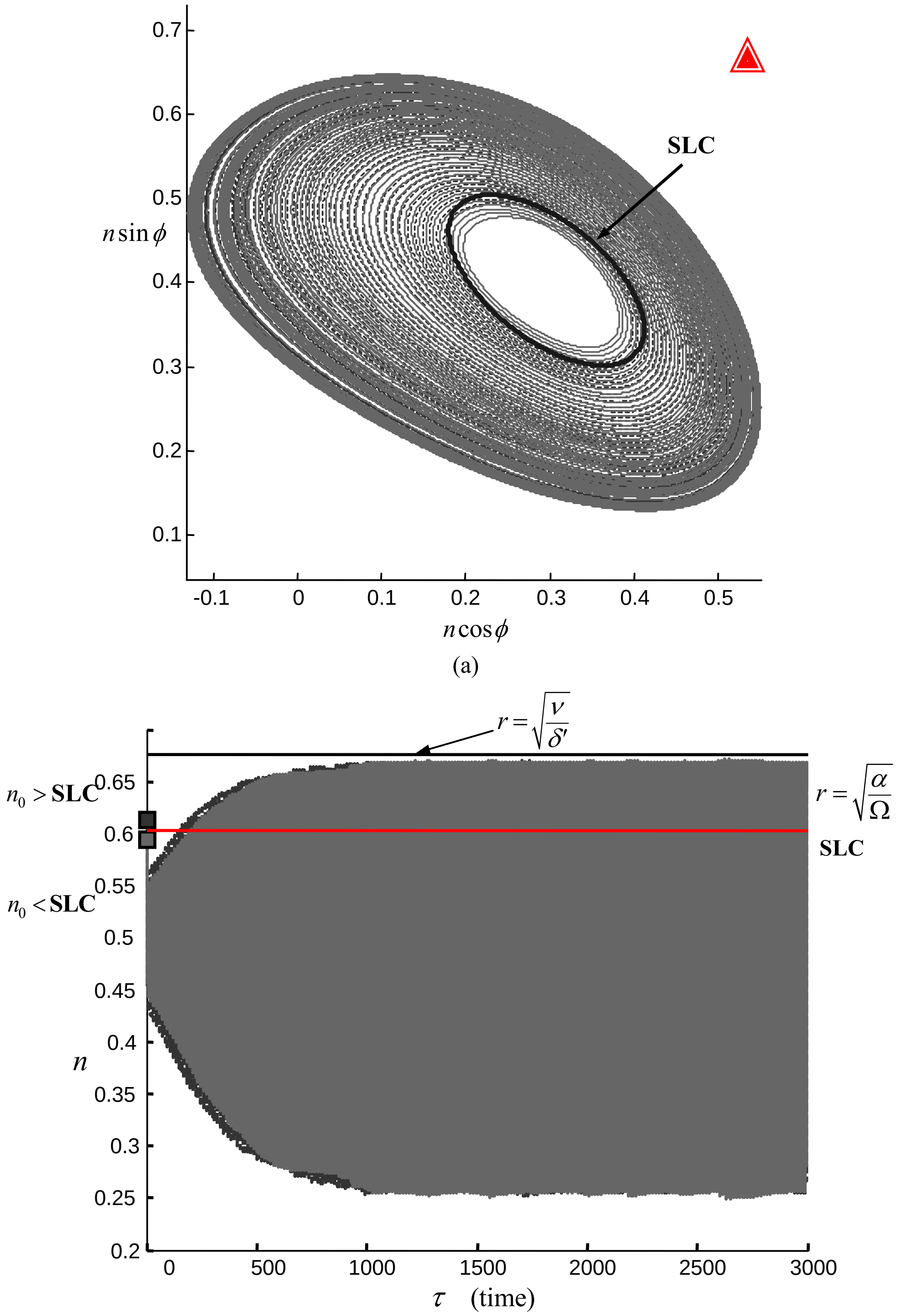

(a)

(b)

Figure 5.10 (a) Plot of the orbits corresponding to $n_s = 0.5$ (**Region II**) showing a stable limit cycle (**SLC**) of radius $r_p = \sqrt{\mu}$ for a speed above the threshold speed $\varpi = \varpi_0 + 0.1$. The journal centre reaches a **SLC** for both the initial eccentricity ratios $n_0 = 0.59$ $(< \textbf{SLC})$ and $n_0 = 0.61$ $(> \textbf{SLC})$, when $\sigma_m = 0.55$, $r_p = 0.60$; the red triangle indicates the location in Figure 5.7 in the parameter plane. (b) Time series corresponding to the orbits given in (a), showing a stable periodic whirl motion as time increases.

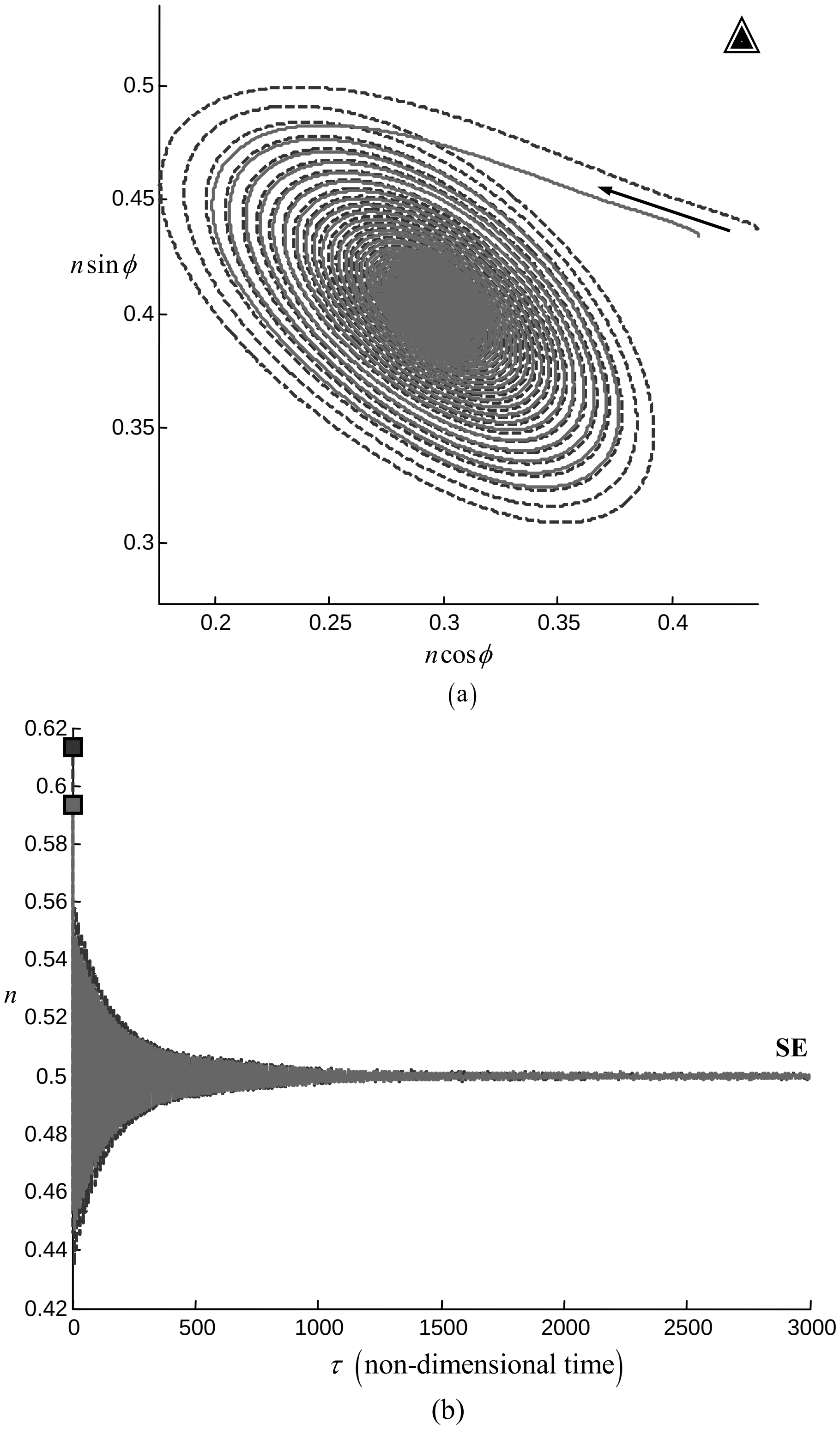

(a)

(b)

Figure 5.11 (a) Plot of the orbits corresponding to $n_s = 0.5$ (**Region II**) showing the journal centre spiralling into a **SE** state from the same initial eccentricity ratios given in Figure 5.10 for a speed below the threshold speed $\bar{\omega} = \bar{\omega} - 0.1$, when $\sigma_m = 0.55,\ r_p = 0.60$; the black triangle indicates the location in Figure 5.7 in the parameter plane. (b) Time series corresponding to the orbits shown in (a).

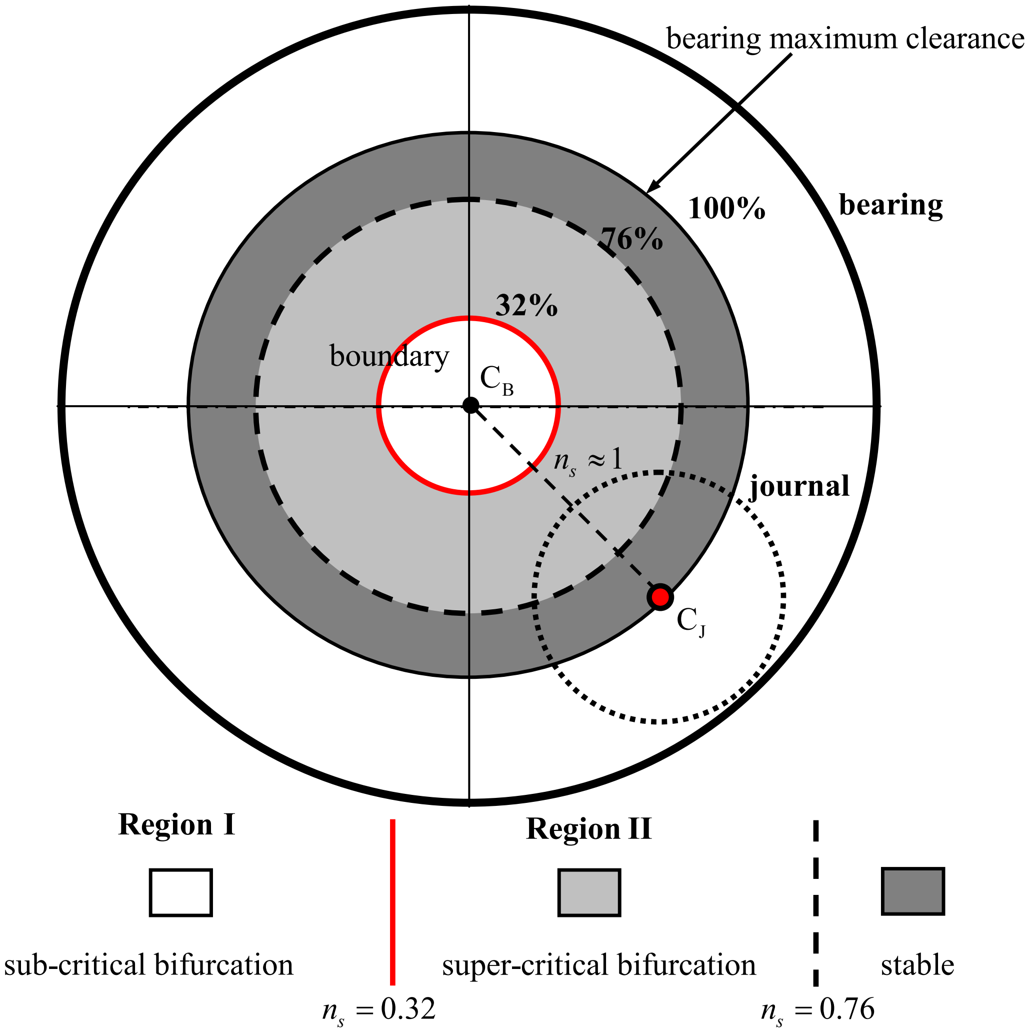

\

Figure 5.12 Plot showing the dynamic behaviour of the rotor-bearing system under investigation, across the clearance of the bearing depending on the journal eccentricity ratio; the system has a rigid rotor supported in short journal bearings having an oscillating π-film cavitation. The clearance is exaggerated for clarification; $\mathrm{C_B}$ is the bearing centre; $\mathrm{C_J}$ is the journal centre. Note that $n_s = 1$ is an impractical case, where there is metal-to-metal contact, which is the reason for marking as $n_s \approx 1$ in the figure.

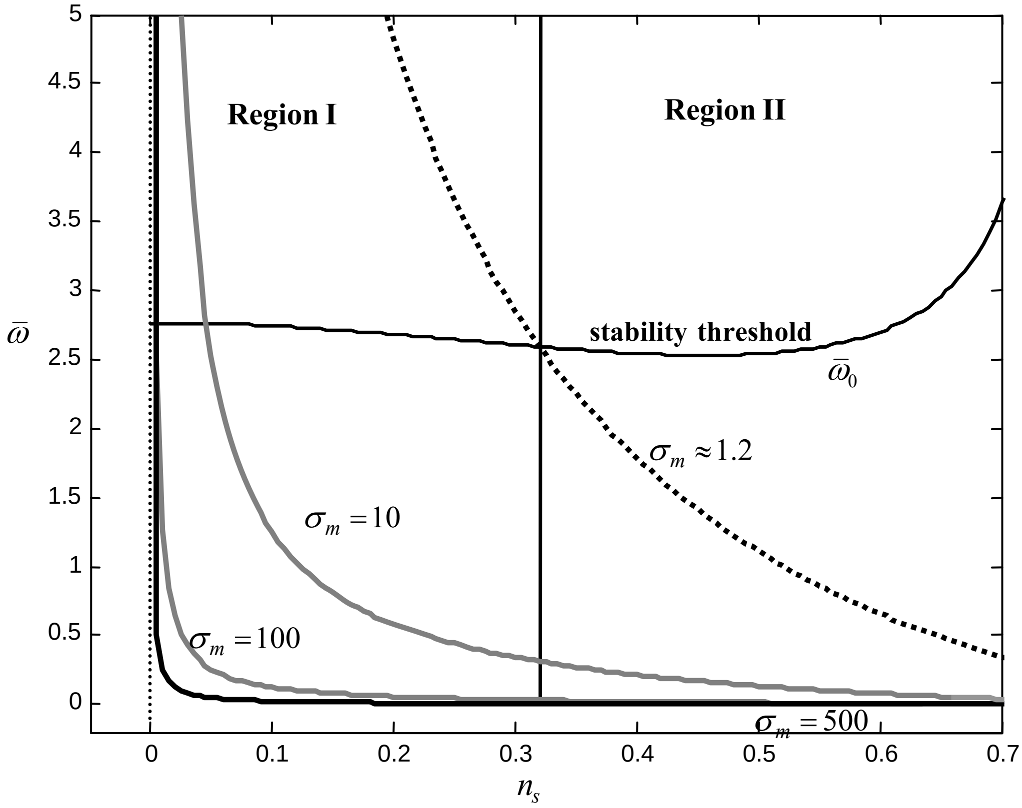

Figure 5.13 Parameter plane showing the regions and the operating curves for very high σ_m values indicating the operating region of a turbocharger due to its light weight; the steady-state eccentricity ratios corresponding to $\sigma_m = 100$ and $\sigma_m = 500$ remain constant for most of the speed range. $\sigma_m \approx 1.2$ is about the minimum value in **Region I**.

CHAPTER 6

THE EFFECT OF UNBALANCE ON OIL-WHIRL INSTABILITY IN A TURBOCHARGER

6.1 INTRODUCTION

In Chapter 4, the effect of a static load was shown to be advantageous in achieving high eccentricity operation in a rotor-bearing system. Added to that, it was concluded in Chapter 5 that a turbocharger due to its light-weight, operates in **Region I** of the parameter plane of the steady-state eccentricity ratio and the speed as shown in Figure 5.5, where there is a sub-critical bifurcation. As discussed in Chapter 1, the unbalance test data of a turbocharger was obtained from *Cummins Turbo-Technologies Ltd.*, Huddersfield, UK, in the form of waterfall plots. These plots illustrate a shift in the system response frequency, from the second whirl frequency to the synchronous frequency for a certain speed range. It was shown in Chapter 2 that the second whirl frequency in a turbocharger corresponds to the in-phase whirl mode. Previous work, for example [39, 80, 81] suggests the suppression of self-excited vibration by means of an excitation. Castro et al.. [82] analysed the effect of unbalance on the rotor dynamic behaviour of a vertical rotor system. They showed that increasing the unbalance increased the stability threshold, thereby increasing the stable region of operation characterised by synchronous vibration. Nayfeh [81] defines the process of increasing the amplitude of the excitation to cause the free-oscillation term to decay as ‘quenching’. In the case of an automotive turbocharger where the speed range of operation is quite high, the test waterfall plot from *Cummins* for the high imbalance case shows a frequency shift in the speed range of 80,000 rpm to 130,000 rpm from sub-synchronous to synchronous order. Hence, this Chapter aims at investigating the effect of rotor unbalance on the in-phase whirl frequency of a turbocharger, in both the transient and the steady-state conditions. Particular emphasis is placed on the speed range of interest based on the test data. The rotor-bearing system with a rigid rotor in rigidly supported journal bearings analysed with a static load in Chapter 4 and 5, is investigated in this Chapter with an added unbalance; this is a periodic load varying with speed. The bearing forces are derived by using the short-bearing approximation and an oscillating π-film cavitation as in Chapter 4 and 5. By numerical analysis, waterfall plots are produced simulating the behaviour presented from the tests. The equations of motion are reduced from a 4-dimensional system to a 2-dimensional system using the Centre Manifold Reduction theorem [63] discussed in Chapter 5. The equations are then simplified into an equivalent system by applying the method of averaging [83] for analysis and comparison with the numerical results.

6.2 EQUATIONS OF MOTION WITH HARMONIC EXCITATION DUE TO UNBALANCE

This Section details the derivation of the equations of motion for the unbalanced rotor system. Similar to the procedure used in Chapter 5, the first order form of the equations of motion which are 4-dimensional are reduced to 2-dimensions by applying the Centre Manifold Reduction theory [63]. Using the method of averaging, the equations are averaged to a mathematically equivalent system that simplifies the analysis.

Figure 6.2 shows the co-ordinate system of the rotor-bearing system with unbalance in the rotor. Compared to the system shown in Figure 4.1 in Chapter 4, this system has the centrifugal force $F_u (= m_u u \omega^2)$ due to the unbalance acting at the mass centre $\mathrm{C_M}$ which is eccentric by u from the geometric centre $\mathrm{C_J}$, of the journal. This force rotates at the rotor speed ω. The system consists of a symmetric rigid rotor of mass $2m_u$ supported in two identical rigidly housed journal bearings where m_u is the rotor mass inclusive of the unbalance mass; n is the eccentricity ratio of the journal centre with respect to the housing centre O; ϕ is the attitude angle; $\bar{F}_r, \bar{F}_t$ are the radial and tangential forces; F is the static load; ω is the spin speed; $\mathrm{C_J}$ is the journal centre and $\mathrm{C_B}$ is the bearing centre. The equations of motion of the journal centre along X and Y are given by:

$$m\frac{d^2X}{dt^2} = F + F_r^p \cos\phi - F_s^p \sin\phi + F_u \cos\omega t = F_X \, , \tag{6.1}$$

$$m\frac{d^2Y}{dt^2} = F_r^p \sin\phi + F_s^p \cos\phi + F_u \sin\omega t \quad = F_Y \, . \tag{6.2}$$

Similar to Chapter 4, dividing by $S_m F$, Eqs. (4.4) and (4.5) can be written in the non-dimensional form as:

$$\ddot{\bar{X}} = \frac{S_m}{\bar{\omega}^2}\left(1 + \bar{F}_r \cos\phi - \bar{F}_s \sin\phi\right) + \rho^2 \cos\tau \, , \tag{6.3}$$

$$\ddot{\bar{Y}} = \frac{S_m}{\bar{\omega}^2}\left(\bar{F}_r \sin\phi + \bar{F}_s \cos\phi\right) + \rho^2 \sin\tau \, , \tag{6.4}$$

where $\rho^2 = \dfrac{u}{C}$ is the unbalance eccentricity ratio which is the mass eccentricity with respect to the geometric centre. Following Shaw and Shaw [47] and Ding [51], the unbalance magnitude is represented as ρ^2 rather than just ρ to emphasise that the ratio is relatively small compared to the dynamic eccentricity ratio governed by the film forces. The equations of motion can be written in simple form as:

$$\bar{X}'' = \frac{S_m}{\bar{\omega}^2}\bar{F}_X(X,Y,X',Y',S_m) \; + \; \rho^2 \cos\tau \, , \tag{6.5}$$

$$\bar{Y}'' = \frac{S_m}{\bar{\omega}^2}\bar{F}_Y(X,Y,X',Y',S_m) \; + \; \rho^2 \sin\tau \, . \tag{6.6}$$

The equations of motion (6.5) and (6.6) are defined in the form of a first order system in terms of the state variables, $x_1 = X - X_s, x_2 = X', x_3 = Y - Y_s, x_4 = Y'$ as:

$$\begin{cases} \dot{x}_1 = x_2, \\ \dot{x}_2 = \dfrac{S_m}{\bar{\omega}^2} \bar{F}_X(x_1, x_2, x_3, x_4, S_m) + \rho^2 \cos\tau, \\ \dot{x}_3 = x_4, \\ \dot{x}_4 = \dfrac{S_m}{\bar{\omega}^2} \bar{F}_Y(x_1, x_2, x_3, x_4, S_m) + \rho^2 \sin\tau. \end{cases} \tag{6.7}$$

In the state variables, $(\cdot)_S$ denotes the steady-state. This equation (6.7) is similar to the system defined in Chapter 4 with a periodic harmonic excitation at frequency equal to the rotor speed ($\tau = \omega t$). Setting ρ^2 as zero in Eq. (6.7), gives the equations of motion for the balanced rotor given in Eq. 4.19. The Cartesian form of the equation of motion is useful for further reduction using the Centre Manifold theorem similar to the procedure given in Chapter 5. However, the polar form which is given in the following Sub-Section is quite convenient for the numerical integration using Runge-Kutta method [84] in MATLAB.

6.2.1 POLAR FORM

The equations of motion for the rotor system shown in Figure 6.2 in the polar form are given by:

$$mC\left(\frac{d^2 n}{dt^2} - n\left(\frac{d\phi}{dt}\right)^2\right) = \bar{F}_r + \bar{F}_u \cos(\omega t - \phi) + F\cos\phi, \tag{6.8}$$

$$mC\left(n\frac{d^2\phi}{dt^2} + 2\frac{dn}{dt}\frac{d\phi}{dt}\right) = \bar{F}_s + \bar{F}_u \sin(\omega t - \phi) - F\sin\phi, \tag{6.9}$$

which have the non-dimensional form given by:

$$\ddot{n} = n\dot{\phi}^2 + \frac{S_m}{\overline{\varpi}^2}\left(\frac{\cos\phi}{S_m} + \overline{F}_r\right) + \rho^2\cos(\tau-\phi), \tag{6.10}$$

$$\ddot{\phi} = -\frac{2\dot{n}\dot{\phi}}{n} + \frac{S_m}{n\overline{\varpi}^2}\left(\overline{F}_t - \frac{\sin\phi}{S_m}\right) + \frac{\rho^2\sin(\tau-\phi)}{n}. \tag{6.11}$$

These equations show that the amount of unbalance ρ^2 that participates in the dynamics is controlled by the harmonic term whose argument depends on the phase difference between the excitation τ and the response ϕ. To make the analysis easier, the Cartesian system is used for reducing the system to 2-dimensions, which is given in the following Section.

6.3 CENTRE MANIFOLD REDUCTION AND THE METHOD OF AVERAGING:

This Section gives the Centre Manifold reduction of the equation of motion given in Eq. (6.7) similar to the procedure applied in Chapter 5. The reduced equations are represented as a standard perturbation problem [83] for the application of the method of averaging. The unbalanced rotor system given by Eq. (6.7) can be written as [46]:

$$\dot{\mathbf{x}} = \mathbf{A}(\nu)\mathbf{x} + \mathrm{F}(\mathbf{x},\nu) + \rho^2\mathbf{\Lambda}(t), \tag{6.12}$$

where, $\mathbf{\Lambda}(t) = [0, \cos\tau, 0, \sin\tau]^T$; τ is 2π peridic, since the period of excitation is one rotation of the rotor. Following the procedure outlined in Chapter 5 - Section 5.3.1, similar to Eq. (5.20), Eq. (6.12) can be written as:

$$\dot{z}\mathbf{q} + \dot{\overline{z}}\overline{\mathbf{q}} + \dot{\mathbf{y}} = \mathbf{A}\left(z\mathbf{q} + \overline{z}\overline{\mathbf{q}} + \mathbf{y}\right) + \mathrm{F}(\left(z\mathbf{q} + \overline{z}\overline{\mathbf{q}} + \mathbf{y}\right), \nu) + \rho^2\mathbf{\Lambda}(t). \tag{6.13}$$

From Eq. (5.20), the $\dot{z}$ and $\dot{\mathbf{y}}$ terms can be separated directly except for the higher order function F. Similar to Chapter 5, using the scalar product of $\mathbf{p}$ on both the sides and separating the $\dot{z}$ terms gives:

$$\dot{z} = \widehat{s}_1 z + \left\langle \mathbf{p}, \mathrm{F}(z\mathbf{q} + \overline{z\mathbf{q}} + \mathbf{y}, \nu) \right\rangle + \rho^2 \left\langle \mathbf{p}, \mathbf{\Lambda}(t) \right\rangle . \tag{6.14}$$

From Eq. (5.20), using Eq. (5.19), $\dot{\mathbf{y}}$ is expressed as:

$$\dot{\mathbf{y}} = \mathbf{A}\mathbf{y} + \begin{pmatrix} \mathrm{F}(z\mathbf{q} + \overline{z\mathbf{q}} + \mathbf{y}, \nu) \\ -\left\langle \mathbf{p}, \mathrm{F}(z\mathbf{q} + \overline{z\mathbf{q}} + \mathbf{y}, \nu) \right\rangle \mathbf{q} \\ -\left\langle \overline{\mathbf{p}}, \mathrm{F}(z\mathbf{q} + \overline{z\mathbf{q}} + \mathbf{y}, \nu) \right\rangle \overline{\mathbf{q}} \end{pmatrix} + \begin{pmatrix} \rho^2 \Lambda(t) \\ -\left\langle \mathbf{p}, \rho^2 \Lambda(t) \right\rangle \mathbf{q} \\ -\left\langle \overline{\mathbf{p}}, \rho^2 \Lambda(t) \right\rangle \overline{\mathbf{q}} \end{pmatrix}, \tag{6.15}$$

which after substituting for $\mathbf{\Lambda}(t)$, $\mathbf{p}, \mathbf{q}$, $\overline{\mathbf{p}}, \overline{\mathbf{q}}$, Eq. (5.22) can be written similar to Eq. (6.14) as:

$$\dot{\mathbf{y}} = \mathbf{A}\mathbf{y} + \begin{pmatrix} \mathrm{F}(z\mathbf{q} + \overline{z\mathbf{q}} + \mathbf{y}, \nu) \\ -\left\langle \mathbf{p}, \mathrm{F}(z\mathbf{q} + \overline{z\mathbf{q}} + \mathbf{y}, \nu) \right\rangle \mathbf{q} \\ -\left\langle \overline{\mathbf{p}}, \mathrm{F}(z\mathbf{q} + \overline{z\mathbf{q}} + \mathbf{y}, \nu) \right\rangle \overline{\mathbf{q}} \end{pmatrix} + \rho^2 \left(\mathbf{h}_\mathrm{c} \cos(\tau) + \mathbf{h}_\mathrm{s} \sin(\tau) \right), \tag{6.16}$$

where $\mathbf{h}_\mathrm{c} = \left\{ \begin{bmatrix} -2\Re\{p_2 q_1\} \\ \left(1 - 2\Re\{p_2 q_2\}\right) \\ -2\Re\{p_2 q_3\} \\ \left(1 - 2\Re\{p_2 q_4\}\right) \end{bmatrix} \right\}$; $\mathbf{h}_\mathrm{s} = \left\{ \begin{bmatrix} -2\Re\{p_4 q_1\} \\ -2\Re\{p_4 q_2\} \\ -2\Re\{p_4 q_3\} \\ -2\Re\{p_4 q_4\} \end{bmatrix} \right\}$.

Now, Eqs. (6.14) and (6.16) can be written in a simplified form as:

$$\dot{z} = \hat{s}_1 z + \mathrm{G}(z, \bar{z}, \mathbf{y}, \nu) + \rho^2 \left(p_2 \cos\tau + p_4 \sin\tau \right), \tag{6.17}$$

$$\dot{\mathbf{y}} = \mathbf{A}\mathbf{y} + \mathrm{H}(z, \bar{z}, \mathbf{y}, \nu) + \rho^2 \left(\mathbf{h}_\mathrm{c} \cos(\tau) + \mathbf{h}_\mathrm{s} \sin(\tau) \right), \tag{6.18}$$

where the expansion of G and H are the same as given in Eq. (5.23) and (5.24) in Chapter 5. According to the Centre Manifold Theorem discussed in Chapter 5, let the Centre Manifold to which the equation of motion given in Eqs. (6.17) and (6.18) are restricted be of the form:

$$\mathbf{y} = \mathrm{V}(z,\bar{z}) + \mathrm{V}(\tau) = \frac{1}{2}\mathbf{w}_{20}z^2 + \mathbf{w}_{11}z\bar{z} + \frac{1}{2}\mathbf{w}_{02}\bar{z}^2 + \rho^2\left(\mathbf{w}_{\mathbf{sn}}\sin(\tau) + \mathbf{w}_{\mathbf{cs}}\cos(\tau)\right), \tag{6.19}$$

where the last term is a function of τ, which is added due to the presence of the excitation term in Eqs. (6.17) and (6.18); V is real as discussed in Chapter 5. In order to express $\mathbf{y}$ in terms of $z, \bar{z}$, it is necessary to calculate $\mathbf{w}$ coefficients in Eq. (6.19). To this end, the derivative of the right hand side of Eq. (6.19) has to be equated to that of Eq. (6.18). Similar to the expression given in Chapter 5 in Eq. (5.26), in order to find the time derivative of Eq. (6.19), $\dot{\mathbf{y}}$ is defined as:

$$\dot{\mathbf{y}} = \frac{\partial \mathrm{V}(z,\bar{z})}{\partial z}\dot{z} + \frac{\partial \mathrm{V}(z,\bar{z})}{\partial \bar{z}}\dot{\bar{z}} + \frac{\partial \mathrm{V}(\tau)}{\partial \tau}. \tag{6.20}$$

Using Eq. (6.20), equating the derivative of the right hand side of Eq. (6.19) to the right hand side of Eq. (6.18) and substituting for $\mathbf{y}$ from Eq. (6.19), gives:

$$\begin{aligned} &\mathbf{w}_{20}z\dot{z} + \mathbf{w}_{11}\left(z\dot{\bar{z}} + \bar{z}\dot{z}\right) + \mathbf{w}_{02}\bar{z}\dot{\bar{z}} + \rho^2\left(\mathbf{w}_{\mathbf{sn}}\cos(\tau) - \mathbf{w}_{\mathbf{cs}}\sin(\tau)\right) \\ &= \mathbf{A}\left(\frac{1}{2}\mathbf{w}_{20}z^2 + \mathbf{w}_{11}z\bar{z} + \frac{1}{2}\mathbf{w}_{02}\bar{z}^2 + \rho^2\left(\mathbf{w}_{\mathbf{sn}}\sin(\tau) + \mathbf{w}_{\mathbf{cs}}\cos(\tau)\right)\right). \\ &+ \frac{1}{2}\mathbf{h}_{\mathbf{20}}z^2 + \mathbf{h}_{\mathbf{11}}z\bar{z} + \frac{1}{2}\mathbf{h}_{\mathbf{02}}\bar{z}^2 + \rho^2\left(\mathbf{h}_{\mathbf{c}}\cos(\tau) + \mathbf{h}_{\mathbf{s}}\sin(\tau)\right) \end{aligned} \tag{6.21}$$

Comparing the coefficients of like-terms in z, $\bar{z}$ on either side of Eq. (6.21) upto quadratic level gives:

$$\begin{cases} z^2: & \left(2\mathbf{I}\Omega_0 - \mathbf{A}\right)\mathbf{w}_{20} = \mathbf{h}_{20}; \\ z\bar{z}: & \left(2\mathbf{I}\Omega_0 - \mathbf{A}\right)\mathbf{w}_{11} = \mathbf{h}_{11}; \\ \bar{z}^2: & \left(-2\mathbf{I}\Omega_0 - \mathbf{A}\right)\mathbf{w}_{02} = \mathbf{h}_{02}; \\ \sin(\tau): & -\mathbf{w_{cs}} = \mathbf{A}\mathbf{w_{sn}} + \mathbf{h_s}; \\ \cos(\tau): & \mathbf{w_{sn}} = \mathbf{h_c} + \mathbf{A}\mathbf{w_{cs}}. \end{cases} \tag{6.22}$$

Using Eq. (5.28), $\mathbf{w_{ij}}$ can be calculated for the Centre Manifold, which are the same as in Chapter 5. However, due to the excitation terms in the original equation of motion given in Eq. (6.7), Eq. (5.28) has two more vector coefficients $\mathbf{w_{cs}}$ and $\mathbf{w_{sn}}$. As discussed in Chapter 5, the function $\mathrm{G}(z,\bar{z},\mathbf{y},\nu)$ in Eq. (6.17) consists of $\mathbf{y}$ which can now be substituted with $z,\bar{z}$ terms using Eq. (6.19), resulting in the reduced equation given by:

$$\begin{gathered} \dot{z} = \hat{s}z + \frac{1}{2}g_{20}z^2 + g_{11}z\bar{z} + \frac{1}{2}g_{02}\bar{z}^2 + g_{21}z^2\bar{z} + \rho^2\left\langle G_{10}.\mathbf{w_{cs}}\cos\tau + \mathbf{w_{sn}}\sin\tau\right\rangle z \\ + \rho^2\left\langle G_{01}.\mathbf{w_{cs}}\cos\tau + \mathbf{w_{sn}}\sin\tau\right\rangle \bar{z} + \rho^2\left(p_2\cos\tau + p_4\sin\tau\right) \end{gathered}, \tag{6.23}$$

where $\mathbf{w_{cs}} = -\left[\mathbf{I} + \mathbf{A}^2\right]^{-1}\left((\mathbf{A}\mathbf{h_c}) + \mathbf{h_s}\right)$; $\mathbf{w_{sn}} = \mathbf{h_c} + \mathbf{A}\mathbf{w_{cs}}$; while the other terms are the same as given in Chapter 5. Letting $\rho^2 = 0$, gives the reduced equation of motion of the balanced system given in Eq. (5.30).

Since the interest is to understand the amplitude and the phase change of the response, it is necessary to convert Eq. (6.23) to the polar form. Letting $z = r_u e^{i\theta_u}$ in Eq. (6.23) gives,

$$e^{i\theta_u}\left(\dot{r}_u + i r_u\dot{\theta}_u\right) = \begin{bmatrix} \left(\alpha + i\Omega\right)r_u e^{i\theta_u} + \frac{1}{2}g_{20}r_u{}^2 e^{i2\theta_u} + g_{11}r_u{}^2 + \frac{1}{2}g_{02}r_u{}^2 e^{-2i\theta_u} + \frac{1}{2}g_{21}r_u^3 e^{i\theta_u} \\ \rho^2\left\langle G_{10}.\left(\mathbf{w_{cs}}\cos\tau + \mathbf{w_{sn}}\sin\tau\right)\right\rangle r_u e^{i\theta_u} \\ +\rho^2\left\langle G_{01}.\left(\mathbf{w_{cs}}\cos\tau + \mathbf{w_{sn}}\sin\tau\right)\right\rangle r_u e^{-i\theta_u} \\ +\rho^2\left(p_2\cos\tau + p_4\sin\tau\right) \end{bmatrix}, \tag{6.24}$$

where the subscript u denotes an unbalanced rotor. Cancelling $e^{i\theta_u}$ on both the sides of Eq. (6.24) and using the expressions $w_1 = G_{10}\mathbf{w_{cs}}$, $w_2 = G_{10}\mathbf{w_{sn}}$, $w_{1c} = G_{01}\mathbf{w_{cs}}$, $w_{2c} = G_{01}\mathbf{w_{sn}}$ for simplification, results in:

$$\left(\dot{r}_u + i r_u \dot{\theta}_u\right) = \begin{bmatrix} (\alpha + i\Omega) r_u + \frac{1}{2}\left(g_{20r} + i g_{20i}\right) r_u^2 e^{i\theta_u} + \left(g_{11r} + i g_{11i}\right) r_u^2 e^{-i\theta_u} \\ + \frac{1}{2}\left(g_{02r} + i g_{02i}\right) r^2 e^{-3i\theta_u} + \frac{1}{2}\left(g_{21r} + g_{21i}\right) r^3 \\ + \rho^2 \left\langle \left(w_{1r} + i w_{1i}\right)\cos\tau + \left(w_{2r} + i w_{2i}\right)\sin\tau \right\rangle r_u \\ + \rho^2 \left\langle \left(w_{1cr} + w_{1ci}\right)\cos\tau + \left(w_{2cr} + w_{2ci}\right)\sin\tau \right\rangle r e^{-2i\theta_u} \\ + \rho^2 \left(p_2 \cos\tau + p_4 \sin\tau\right) e^{-i\theta_u} \\ \end{bmatrix}, \tag{6.25}$$

where the subscripts r, i denote the real and the imaginary parts of the coefficients respectively. Separating the real and the imaginary parts gives:

$$\left(\dot{r}_u\right) = \begin{bmatrix} (\alpha(\nu)) r_u + \frac{1}{2}\left(g_{20r}\cos\theta_u - g_{20i}\sin\theta_u\right) r_u^2 + \left(g_{11r}\cos\theta_u + g_{11i}\sin\theta_u\right) r_u^2 \\ + \frac{1}{2}\left(g_{02r}\cos 3\theta_u + g_{02i}\sin 3\theta_u\right) r_u^2 + \frac{1}{2}\left(g_{21r}\right) r_u^3 \\ + \rho^2 \left\langle \left(w_{1r}\right)\cos\tau + \left(w_{2r}\right)\sin\tau \right\rangle r_u \\ + \rho^2 \left\langle \left(w_{1cr}\cos 2\theta_u + w_{1ci}\sin 2\theta_u\right)\cos\tau + \left(w_{2cr}\cos 2\theta_u + w_{2ci}\sin 2\theta_u\right)\sin\tau \right\rangle r_u \\ + \rho^2 \left(\left(p_{2r}\cos\theta_u + p_{2i}\sin\theta_u\right)\cos\tau + \left(p_{4r}\cos\theta_u + p_{4i}\sin\theta_u\right)\sin\tau\right) \\ \end{bmatrix}, \tag{6.26}$$

$$\left(r_u \dot{\theta}_u\right) = \begin{bmatrix} (\Omega(\nu)) r_u + \frac{1}{2}\left(g_{20i}\cos\theta_u + g_{20r}\sin\theta_u\right) r_u^2 + \left(g_{11i}\cos\theta_u - g_{11r}\sin\theta_u\right) r_u^2 \\ + \frac{1}{2}\left(g_{02i}\cos 3\theta_u - g_{02r}\sin 3\theta_u\right) r_u^2 + \frac{1}{2}\left(g_{21i}\right) r_u^3 \\ + \rho^2 \left\langle \left(w_{1i}\right)\cos\tau + \left(w_{2i}\right)\sin\tau \right\rangle r_u \\ + \rho^2 \left\langle \left(w_{1ci}\cos 2\theta_u - w_{1cr}\sin 2\theta_u\right)\cos\tau + \left(w_{2ci}\cos 2\theta_u - w_{2cr}\sin 2\theta_u\right)\sin\tau \right\rangle r_u \\ + \rho^2 \left(\left(p_{2i}\cos 2\theta_u - p_{2r}\sin 2\theta_u\right)\cos\tau + \left(p_{4i}\cos 2\theta_u - p_{4r}\sin 2\theta_u\right)\sin\tau\right) \\ \end{bmatrix}. \tag{6.27}$$

It was shown in Chapter 4 that the non-dimensional bifurcation frequency Ω_0 at the threshold speed is about 0.5. Given the fact that the excitation frequency is the rotor speed, the interest is to study the effect on in-phase whirl instability during sub-harmonic resonance, i.e., when the rotor whirling frequency is about half the excitation frequency. Hence, it is helpful to introduce a detuning parameter σ_u [51]. This is a small deviation of the whirl frequency from the sub-harmonic bifurcation frequency Ω_0 due to the excitation frequency $\bar{\omega}$, such that:

$$\Omega_0 = \frac{1}{2} + \sigma_u . \tag{6.28}$$

In order to study the nonlinear time variant system defined by Eqs. (6.26) and (6.27), it is easier to study the averaged form of it. To this end, it is necessary to get the system to the standard form for averaging [83]. The standard form of a perturbation problem for the application of averaging is given by [83]:

$$\dot{x} = \varepsilon\, \mathrm{f}(x,t;\varepsilon), \quad x \in \Re^n , \tag{6.29}$$

where, x is the variable, t is the time and ε is a small parameter. Some details of the method of averaging used to obtain the information regarding the approach to the limit cycle is given in Appendix D. Now, to convert the rotor system given in Eqs. (6.26) and (6.27) into the standard form in Eq.(6.29), it is necessary to introduce the small parameter ε to order the terms of the equation. Since the amplitude of the limit cycles born at the *Hopf bifurcation* curve i.e., the stability threshold discussed in Chapter 4 increases with the square root of the bifurcation parameter ν, an appropriate scaling of $r_u = \varepsilon^{\frac{1}{2}} r_1$ is chosen following the work of Namachivaya and Ariaratnam [49] and Ding [51]. This leads to,

$$\rho^2 = \varepsilon \rho_1^{\,2}, \quad \nu = \varepsilon \nu_1, \quad \sigma_u = \varepsilon \sigma_1 . \tag{6.30}$$

Using Eq. (6.30), the coefficients of the linear terms in Eqs. (6.26) and (6.27) take the form,

$$\alpha\left(\nu\right) = \alpha'(0)\nu = \varepsilon\alpha'(0)\nu_1, \tag{6.31}$$

$$\Omega\left(\nu\right) = \Omega(0) + \Omega'(0)\nu = \frac{1}{2} + \varepsilon\left(\sigma_1 + \Omega'(0)\nu_1\right). \tag{6.32}$$

Substituting Eq. (6.30) through Eq. (6.32), Eqs. (6.26) and (6.27) can be represented in the standard form for the application of averaging as:

$$\dot{r}_1 = \varepsilon^{\frac{1}{2}}\left(Q_1^r\left(\theta_u\right)r_1^2 + \rho_1{}^2\,\mathrm{G}^r(\tau)\right) + \varepsilon\left(\alpha'(0)\nu_1 r_1 + \frac{1}{2}\left(g_{21r}\right)r_1^3 + \rho_1{}^2 r_1\,\mathrm{h}^r(\theta_u,\tau)\right), \tag{6.33}$$

$$\dot{\theta}_u = \frac{1}{2} + \varepsilon^{\frac{1}{2}}\left(Q_1^\theta\left(\theta_u\right)r_1 + \frac{\rho_1{}^2}{r_1}\mathrm{G}^\theta(\tau)\right) + \varepsilon\left(\left(\sigma_1 + \Omega'(0)\nu_1\right) + Q_2^\theta\left(\theta_u\right)r_1^2 + \rho_1{}^2\,\mathrm{h}^\theta(\theta_u,\tau)\right), \tag{6.34}$$

where, $Q_1^r(\theta_u)$ and $Q_1^\theta(\theta_u)$ are the quadratic terms of harmonic functions, $Q_2^\theta\left(\theta_u\right)$ is a cubic term of harmonic function, $\mathrm{h}^r(\theta_u,\tau)$ and $\mathrm{h}^\theta(\theta_u,\tau)$ are functions of both the excitation phase τ and the response phase θ_u, $\mathrm{G}^r(\tau)$ and $\mathrm{G}^\theta(\tau)$ are purely harmonic functions in τ. It should be noted that, the standard form given in Eqs. (6.33) and (6.34) have a harmonic excitation term, that is combined with a linear term in r_1 and another purely harmonic excitation term, both ordered differently. Thus, the way of ordering used in Eq. (6.30) allows the r_1^3 term and the excitation terms with function $\mathrm{h}^r, \mathrm{h}^\theta$, to be of the same order in ε. It can be seen that Eqs. (6.33) and (6.34) consist of the functions of θ_u and τ, which are the response and the excitation phase angles respectively. To allow integration with respect to τ while averaging, these can be related using $\theta_u = \frac{\tau}{2} + \varphi_u$, which implies that $\frac{d\theta_u}{d\tau} = \dot{\theta}_u = \frac{1}{2} + \dot{\varphi}_u$. To incorporate the influence of the quadratic terms that disappear in the first order averaging, the equations are averaged upto the second order and the resulting equations are given by:

$$\dot{\overline{r}}_u = \varepsilon\left[\left(\alpha'\nu\right)\overline{r}_u + \tilde{a}\overline{r}_u^{\,3} + \rho^2\overline{r}_u\left(U_1\sin(2\overline{\varphi}_u) + V_1\cos(2\overline{\varphi}_u)\right)\right], \tag{6.35}$$

$$\overline{r}_u\dot{\overline{\theta}}_u = \varepsilon\left[\left(\Omega_0 + \Omega'\nu\right)\overline{r}_u + \tilde{b}\overline{r}_u^{\,3} + \rho^2\overline{r}_u\left(U_1\cos(2\overline{\varphi}_u) - V_1\sin(2\overline{\varphi}_u)\right)\right], \tag{6.36}$$

where: $\overline{(.)}$ denotes the averaged variables.

$$\tilde{a} = \frac{1}{2}\Re\{g_{21}\} - \Im\{g_{20}g_{11}\},$$

$$\tilde{b} = \Re\{g_{20}g_{11}\} - \frac{1}{3}|g_{02}|^2 - 2|g_{11}|^2 + \frac{1}{2}\Im\{g_{21}\},$$

$$U_1 = -\frac{1}{3}\left(\begin{array}{l} 3\Re\{p_4\} - 3\Im\{p_2\}\Im\{g_{11}\} + \left(3\Re\{p_2\} + 3\Im\{p_4\}\right)\Re\{g_{11}\} \\ +\left(\Im\{p_2\} + \Re\{p_4\}\right)\Im\{g_{02}\} + \left(\Re\{p_2\} - \Im\{p_4\}\right)\Re\{g_{02}\} \\ +\frac{3}{2}\left(\Re\{w_{2c}\} - \Im\{w_{1c}\}\right) \end{array}\right),$$

$$V_1 = -\frac{1}{3}\left(\begin{array}{l} \left(-3\Im\{p_4\} - 3\Re\{p_2\}\right)\Im\{g_{11}\} + \left(3\Re\{p_4\} - 3\Im\{p_2\}\right)\Re\{g_{11}\} \\ +\left(-\Re\{p_2\} + \Im\{p_4\}\right)\Im\{g_{02}\} + \left(\Im\{p_2\} + \Re\{p_4\}\right)\Re\{g_{02}\} \\ -\frac{3}{2}\left(\Im\{w_{2c}\} + \Re\{w_{1c}\}\right) \end{array}\right).$$

Note that the expressions related to $\tilde{a}$ and $\tilde{b}$ give $c_1 = \tilde{a} + j\tilde{b}$ as given in Eq. (5.36) in Chapter 5. Using linear transformation [49], the equations of motion further simplifies to:

$$\dot{\overline{r}}_u = \varepsilon\left(\alpha_u\overline{r}_u + \tilde{a}\overline{r}_u^{\,3} + \rho_1^{\,2}\overline{r}_u\hat{U}\sin 2(\overline{\varphi}_u + \zeta)\right), \tag{6.37}$$

$$\dot{\overline{\varphi}}_u = \varepsilon\left(\Omega_u + \tilde{b}\overline{r}_u^{\,2} + \rho_1^{\,2}\hat{U}\cos 2(\overline{\varphi}_u + \zeta)\right), \tag{6.38}$$

where $\hat{U} = \sqrt{U_1^{\,2} + V_1^{\,2}}$, $\tan 2\zeta = U_1/V_1$, $\alpha_u = \alpha'(0)\nu_1$, $\Omega_u = \left(\sigma_1 + \Omega'(0)\nu_1\right)$, $\dot{\overline{\theta}}_u = \frac{1}{2} + \dot{\overline{\varphi}}_u$.

It should be noted that Eqs. (6.37) and (6.38) are the same as the normal form given in Eqs. (5.62) and (5.63) in Chapter 5, if the unbalance magnitude $\rho_1^{\,2}$ is set to zero. Note that $\tilde{a}'$, $\tilde{b}'$ terms are ignored in Eqs. (5.62) and (5.63) subsequently. The harmonic excitation term has the phase as twice as the phase of the response $\overline{\varphi}_u$. This term is a linear function of the response amplitude $\overline{r}_u$, which keeps increasing as the amplitude increases for a given unbalance value ρ_1^2. From the averaged equations, the steady-state amplitude of the journal motion can be determined by setting the time dependent terms to zero. This is done in the following Section and the modified stability threshold is determined.

6.4 MODIFIED STABILITY THRESHOLD

The amplitude equation for a two-dimensional perturbation problem was derived by Namachivaya and Ariaratnam [49] after averaging them. Based on a stability analysis, they arrived at the critical bifurcation parameter, which gives the stability threshold for the excited system. The aim of this Section is to apply the same procedure for the rotor system under investigation to determine the modified stability threshold. However, the stability analysis is presented using the Jacobian determinant following Gross [85]. Under the steady-state conditions, that is, $\dot{\overline{r}}_u = 0$, $\dot{\overline{\varphi}}_u = 0$, Eqs. (6.37) and (6.38) become:

$$\rho_1{}^2\hat{U}\sin 2(\overline{\varphi}_u + \zeta) = -\alpha_u - \tilde{a}\overline{r}_u^2, \tag{6.39}$$

$$\rho_1{}^2\hat{U}\cos 2(\overline{\varphi}_u + \zeta) = -\Omega_u - \tilde{b}\overline{r}_u^2. \tag{6.40}$$

It must be noted that $\dot{\overline{\varphi}}_u$ gives the shift in the phase rate from $1/2$. This stems from the relation $\dot{\overline{\theta}}_u = \dfrac{1}{2} + \dot{\overline{\varphi}}_u$ introduced before averaging. Squaring and adding Eqs. (6.39) and (6.40) gives

$$\left(\rho_1{}^2\hat{U}\right)^2 = \mathrm{f}(\overline{r}_u^2) = \left(\tilde{a}^2 + \tilde{b}^2\right)\left(\overline{r}_u^2\right)^2 + 2\left(\alpha_u\tilde{a} + \Omega_u\tilde{b}\right)\overline{r}_u^2 + \left(\alpha_u^2 + \Omega_u^2\right). \tag{6.41}$$

Re-arranging Eq. (6.41) gives the quadratic equation in $\bar{r}_u^2$ as:

$$\left(\tilde{a}^2+\tilde{b}^2\right)\left(\bar{r}_u^2\right)^2+2\left(\alpha_u\tilde{a}+\Omega_u\tilde{b}\right)\bar{r}_u^2+\left(\alpha_u^2+\Omega_u^2\right)-\left(\rho_1{}^2\hat{U}\right)^2=0, \qquad (6.42)$$

whose roots give the amplitude of the limit cycle, under the effect of unbalance as:

$$\bar{r}_u=\left(\frac{-\left(\alpha_u\tilde{a}+\Omega_u\tilde{b}\right)\pm\sqrt{\left(\tilde{a}^2+\tilde{b}^2\right)\left(\rho_1^2\hat{U}\right)^2-\left(\Omega_u\tilde{a}-\alpha_u\tilde{b}\right)^2}}{\left(\tilde{a}^2+\tilde{b}^2\right)}\right)^{1/2}. \qquad (6.43)$$

Equation (6.43) gives a meaningful solution only if the root is real and positive. A quadratic equation $ax^2+bx+c=0$ has one positive real root if $4ac<0$ and two positive real roots if $b<0,\ 4ac>0$ and the discriminant $b^2-4ac\geq 0$. Eq. (6.43) has one positive real root provided,

$$\alpha_u^2+\Omega_u^2<\left(\rho_1{}^2\hat{U}\right)^2, \qquad (6.44)$$

and two positive real roots if,

$$\alpha_u^2+\Omega_u^2\geq\left(\rho_1{}^2\hat{U}\right)^2,\ \left(\alpha_u\tilde{a}+\Omega_u\tilde{b}\right)<0 \text{ and } \left(\rho_1{}^2\hat{U}\right)^2\geq\frac{\left(\tilde{a}\Omega_u-\tilde{b}\alpha_u\right)^2}{\left(\tilde{a}^2+\tilde{b}^2\right)}. \qquad (6.45)$$

However, the possibility of two real roots suggests two possible whirling amplitudes. In order to ascertain the significance of this case, the stability of the solutions needs to be analysed [49]. This can be determined using the determinant of the Jacobian [85, 86] as:

$$\mathbf{J_t}=\begin{vmatrix}\dfrac{\partial\dot{\bar{r}}_u}{\partial\bar{r}_u} & \dfrac{\partial\dot{\bar{r}}_u}{\partial\bar{\phi}_u}\\[2ex] \dfrac{\partial\dot{\bar{\phi}}_u}{\partial\bar{r}_u} & \dfrac{\partial\dot{\bar{\phi}}_u}{\partial\bar{\phi}_u}\end{vmatrix}=\begin{vmatrix}\alpha_u+3\tilde{a}r_u{}^2+\rho_1{}^2\hat{U}\sin 2(\bar{\varphi}_u+\zeta) & 2r_u\rho_1{}^2\hat{U}\cos 2(\bar{\varphi}_u+\zeta)\\ 2\tilde{b}r_u & -2\rho_1{}^2\hat{U}\sin 2(\bar{\varphi}_u+\zeta)\end{vmatrix}, \qquad (6.46)$$

which after substituting Eqs. (6.39) and (6.40) for the harmonic terms gives:

$$\begin{bmatrix} 2\tilde{a}\bar{r}_u^{\,2} & 2\bar{r}_u(-\Omega_u - \tilde{b}\bar{r}_u^{\,2}) \\ 2\tilde{b}\bar{r}_u & 2\alpha_u + 2\tilde{a}\bar{r}_u^{\,2} \end{bmatrix}, \tag{6.47}$$

which is of the standard form $s_u^2 - \hat{T}s_u + \hat{D} = 0$, where $\hat{T}$ is the trace of the matrix in Eq. (6.47), and $\hat{D}$ is the determinant of the matrix. The eigenvalue of the Jacobian determinant is given by:

$$\hat{s}_u = \alpha_u + 2\tilde{a}\bar{r}_u^{\,2} \pm \sqrt{\alpha_u^2 + \Omega_u^2 - (2\tilde{b}\bar{r}_u^{\,2} + \Omega_u)^2}\ . \tag{6.48}$$

This gives two conditions for stable eigenvalues such as:

i) sum of the diagonal elements, $\hat{T} < 0$, i.e., $2\alpha_u + 4\tilde{a}\bar{r}_u^{\,2} < 0$,

$$\tilde{a}\bar{r}_u^{\,2} < -\frac{1}{2}\alpha_u\,; \tag{6.49}$$

ii) determinant of the matrix, $\hat{D} > 0$, i.e., $4\alpha_u\tilde{a} + 4\Omega_u\tilde{b} + 4\alpha_u^2 + 4\Omega_u^2 > 0$,

$$\bar{r}_u^2 > -\frac{\left(\alpha_u\tilde{a} + \Omega_u\tilde{b}\right)}{\tilde{a}^2 + \tilde{b}^2}\,. \tag{6.50}$$

Condition given in Eq. (6.50) also stems from the derivative of the function given in Eq.(6.41), which is $\mathrm{f}'(\bar{r}_u^2) = 2\left(\tilde{a}^2 + \tilde{b}^2\right)\bar{r}_u^2 + 2\left(\alpha_u\tilde{a} + \Omega_u\tilde{b}\right)$. As discussed in [49], Eq. (6.50) implies that only the one with positive sign of Eq. (6.43) gives a stable eigenvalue, i.e.,

$$\overline{r}_u^2 = \frac{-\left(\alpha_u \tilde{a} + \Omega_u \tilde{b}\right) + \sqrt{\left(\tilde{a}^2 + \tilde{b}^2\right)\left(\rho^2 \hat{U}\right)^2 - \left(\alpha_u \tilde{a} - \Omega_u \tilde{b}\right)^2}}{\left(\tilde{a}^2 + \tilde{b}^2\right)}. \tag{6.51}$$

Equation (6.49) is the stability condition along with the conditions given in Eqs. (6.44) and (6.45), for one and two positive real roots respectively. The condition given in Eq. (6.49) signifies the loss of stability giving the stability threshold as [49]:

$$\nu_c = -\frac{2\tilde{a}\overline{r}_u^2}{\alpha'}. \tag{6.52}$$

Recalling that $\nu = \omega - \omega_0$ for the balanced rotor, ν_c signifies the shift in the stability threshold. The modified stability threshold is given by:

$$\overline{\omega}_{0u} = \overline{\omega}_0 - \frac{2\tilde{a}\overline{r}_u^2}{\alpha'}. \tag{6.53}$$

It was shown in Chapter 5, for the system under investigation $\alpha' > 0$. This signifies that the threshold speed reduces when $\tilde{a}$ is positive, i.e., in **Region I**, when r_u is real as shown in Figure 5.5. It is also evident that the threshold speed increases in **Region II**, where $\tilde{a} < 0$. Figure 6.3 shows the plot of the modified stability threshold, $\overline{\omega}_{0u}$ for $\rho^2 = 0.01$ and 0.03 with $\overline{\omega}_{0u} < \overline{\omega}_0$ in **Region I** and $\overline{\omega}_{0u} > \overline{\omega}_0$ in **Region II**. This effect further increases with increasing unbalance. As $n_s \to 0$, $\overline{r}_u^2$ is relatively very small i.e., the **ULC** radius is very small as shown in Figure 5.6 in Chapter 5; α' is negligible as shown in Figure 5.3. This suggests that the term $\frac{2\tilde{a}\overline{r}_u^2}{\alpha'}$ is too small when compared to $\overline{\omega}_0$ such that $\overline{\omega}_{0u} \approx \overline{\omega}_0$.

It was shown in Chapter 5 that the operating curve of a turbocharger determined by the modified Sommerfeld number σ_m must lie in **Region I**. Based on the dynamic behaviour of the system in **Region I**, a detailed analysis of the steady-state and transient motion is presented in the following Section based on the numerical analysis. The

Section focuses on the speed range of interest given in the test waterfall plots shown in Chapter 1. A related analysis of the averaged equations is also presented.

6.5 DISCUSSION OF THE NUMERICAL AND THE ANALYTICAL RESULTS

The waterfall plots obtained from *Cummins Turbo-Technologies Ltd.* were discussed in Chapter 1. They showed the effect of unbalance over a certain speed range. Figure 1.4 shows the comparative waterfall plots produced from the data collected from the same hardware and conditions for two different imbalance levels. These plots show the response frequency shifting from the in-phase whirl frequency (**IP**) to the synchronous frequency ($\mathbf{1\times}$) for a range of speed. This effect seems to be quite simultaneous in the high unbalance case at about 80,000 rpm, than the low unbalance case, where the synchronous response is seen only at about 120,000 rpm. This Section aims at investigating similar waterfall plots obtained from the numerical analysis of a turbocharger. Further to that, to determine the effect of unbalance in the transient motion, the growth rate of whirl orbit is analysed. This study is also analytically verified using the averaged model.

In Chapter 5, the steady-state dynamic behaviour of a general rotor system in terms of equilibrium states and limit cycles was investigated. Various rotor systems were represented on the parameter plane of steady-state eccentricity ratio and the speed in terms of operating curves determined by the non-dimensional group σ_m. It was also shown that very high σ_m represents the rotor system corresponding to a turbocharger due to the negligible static load. As shown in Figure 5.13 in Chapter 5, $\sigma_m = 500$ represents a rotor system where the operating curve asymptotes at a very low eccentricity ratio $n_s \approx 0.001$. For any value $\sigma_m > 500$, it may not make any significant difference. Hence, it seems reasonable to represent the turbocharger by $\sigma_m = 500$, to demonstrate the effect of unbalance on the in-phase whirl instability. Here onwards, the turbocharger model is represented by the operating curve $\sigma_m = 500$.

Since the operating curve $\sigma_m = 500$ lies in **Region I** of the parameter plane as shown in Figure 5.13, the journal centre theoretically reaches an unstable limit cycle (**ULC**) below the threshold speed. It is also shown in Figure 5.6(a), that this **ULC** is too small for very low eccentricities. Moreover, Figure 6.3 shows the plot of the modified stability threshold under the influence of unbalance excitation, which shows a further reduction in the threshold speed in **Region I**, depending on the unbalance magnitude. Due to very small **ULC**, the journal orbit keeps growing for any perturbation to a position above the **ULC**. This could probably be the reason for the existence of the sub-synchronous whirling frequency right from the starting speed, as seen in Chapter 2. Moreover, the growth rate of the whirl orbit reduces with increasing σ_m. For instance, Figure 6.4 shows the time history of the journal motion for $\sigma_m = 5$, 50 and 500 to show the difference in the growth rate of a balanced rotor. Figure 6.5 shows the plot of the amplitude increasing with time for $\sigma_m = 500$. This implies that a turbocharger takes relatively more time to reach the steady-state than a rotor system with a heavier rotor, at any given speed.

6.5.1 TRANSIENT MOTION

In order to produce the waterfall plots similar to that shown in Figure 1.4, simulations are conducted by the numerical integration of the equations of motion given in Eqs. (6.10) and (6.11) using Runge-Kutta method. The speed is increased slowly in steps of 0.2 from $\bar{\omega} = 0.5$ to 20, where the orbit is allowed to grow at each speed for a non-dimensional time of $\tau = 2000$ (≈ 318 revolutions). Then, at each speed, for a time interval of about 1500, close to the end time, the time series is transformed to the frequency domain using the Fast Fourier Transformation (FFT). These are plotted in waterfall form which shows the information of frequency vs. magnitude varying with speed along the z-axis. It should be noted that this study focuses on the effect of unbalance on the transient behaviour and not the steady-state. However, at high speed such as $\bar{\omega} > 18$, the amplitude is quite high approaching the steady-state.

Figure 6.6 shows the envelope of the time series corresponding to the waterfall plots for $\rho^2 = 0$ and $\rho^2 = 0.003$. It can be seen that the amplitude reduces for the system with unbalance, in the speed range of $\varpi = 8$ to 16, corresponding to a particular speed range. This effect can be seen more clearly in the numerical waterfall plots. Figure 6.7 shows the waterfall plot for the turbocharger without any unbalance $\rho^2 = 0$. It shows the response of the in-phase whirl frequency, which is the sub-synchronous half-frequency whirl. Based on Figure 1.4, the speed range of interest is $50,000$ rpm to $130,000$ rpm. From the non-dimensional form discussed in Chapter 4, $\varpi = \left(mC/F\right)^{\frac{1}{2}}\omega = \left(C/g\right)^{\frac{1}{2}}\omega$, where g is the acceleration due to gravity. For a clearance of 0.02×10^{-3} m, ϖ is $\approx 6691\omega$. Hence a non-dimensional speed range of $10 \le \varpi \ge 20$ is the main focus. Figure 6.8 shows the waterfall plot, when there is an unbalance of $\rho^2 = 0.002$ in the rotor. It can be clearly seen that there is a reduction in the magnitude of the sub-synchronous response corresponding to the in-phase whirl for $\varpi > 15$. Figure 6.9 shows a similar waterfall plot with further increase in the unbalance to $\rho^2 = 0.003$ where there is a reduction in the response for $\varpi > 12$. It is also seen in Figure 6.8 and Figure 6.9 that the synchronous response increases when the sub-synchronous in-phase whirl response reduces. However, Figure 6.10 shows the response for $\rho^2 = 0.005$, in which, there is an increase in the response amplitude for $\varpi > 15$, although the response reduces for the speed range about $10 \le \varpi \ge 15$.

Figure 6.11 shows the plot tracing the maximum amplitude $n_{\max}$ varying with speed for various unbalance values. The figure shows that there is a reduction in the amplitude with increase in the unbalance for only a specific speed range. This range is wider for low unbalances than the higher ones. Beyond a certain value, unbalance has a negative effect by increasing the amplitude. However, this value depends on the range of speed as seen in Figure 6.11. For example, for $\varpi = 12$, $\rho^2 = 0.003$ gives the minimum amplitude, whereas, for $\varpi = 15$, $\rho^2 = 0.002$ is the optimum unbalance. This implies that, as the speed is changed continuously, depending on the rate at which the rotor speed is changed, the response characteristics may differ. That is, the speed range in which the sub-synchronous response is suppressed may vary with the rate of change of speed and the amount of unbalance in the rotor.

These curves show a dip in the amplitude at a certain speed, when the rotor is not balanced. Figure 6.12 shows the corresponding phase plot, i.e., the plot of the attitude angle corresponding to $n_{\max}$. The phase angle becomes constant after the speed about which $n_{\max}$ of the unbalanced rotor crosses that of the balanced rotor as marked in Figure 6.11 by circles. This plot also shows an interesting drop in the phase at speeds corresponding to the dips in Figure 6.11. This suggests that the phase angle (attitude angle) controls the unbalance response. It should be noted that the unbalance term in Eqs. (6.10) and (6.11), has the harmonic terms with the argument which is the phase difference between the excitation phase and the response phase in the harmonic functions. Figure 6.13 and Figure 6.14 demonstrate the way in which the amplitude varies with unbalance when time $\tau = 2000$, at a speed of $\bar{\omega} = 10$ (≈ 66900 rpm) and $\bar{\omega} = 15$ (≈ 100365 rpm) respectively. It is evident that the unbalance has a positive effect till it reaches an optimum value beyond which the whirl amplitude increases. Figure 6.15 shows the plot of the magnitude of only the sub-synchronous component of the whirl motion. This demonstrates a similar behaviour as seen in the time history in Figure 6.11.

6.5.2 STEADY-STATE

As mentioned earlier, the positive effect of unbalance is seen in the transient motion of the rotor. However, at the steady-state, unbalance does not seem to influence the system significantly. For example, Figure 6.16 presents the amplitude of the whirl motion in the transient and the steady-state, for different unbalance values when the rotor spins at about 66900 rpm. Above the stability threshold, the journal orbits outwards as there is an unstable equilibrium (**UE**) in **Region I** as detailed in Chapter 5. For all the unbalance levels, Figure 6.16 shows the plot of the eccentricity ratio, where the whirl motion approaches the same level.

It is known that the present rotor system has the fluid-film forces, static load and the unbalance force in action, at any point of time. To understand the interplay of these forces, Figure 6.17 is a plot of the terms of Eq. (4.7) showing the forces varying with time along the Y direction. This direction is chosen to avoid the static load effect. It is seen that the unbalance force remains constant, while the fluid-film forces increase with time, forcing the whirl orbit to grow in size until the rotor motion reaches the steady-state. It is evident that as the rotor motion reaches the steady-state, the unbalance force becomes relatively insignificant compared with the dynamic fluid forces acting on the rotor and does not influence the dynamic behaviour. Nevertheless, as seen in Figure 6.16, the whirl motion for an unbalanced rotor increases at a slower rate compared to that of a balanced rotor in the transient state, even though they approach the same steady-state. Hence, it may be useful to investigate the unbalance effect on the growth rate of the orbit size.

6.5.3 UNBALANCE EFFECT ON THE GROWTH RATE OF THE WHIRL AMPLITUDE

Now, to investigate the effect of unbalance in the transient motion, where, beyond an optimum value, unbalance shows a negative effect by increasing the amplitude, three cases are analysed for $\rho^2 = 0,\ 0.005,\ \text{and}\ 0.05$. At the same speed $\overline{\omega} = 10\ (\approx 66{,}900\ \text{rpm})$ considered for the steady-state analysis, Figure 6.18 shows the plot of the whirl amplitude for the three cases. These unbalance values are chosen to illustrate the effect on the whirl amplitude. Note that all the analyses have been run upto time $\tau = 3500\ (\approx 518\ \text{revolutions})$. Figure 6.19 shows the corresponding orbit plots with a reduced size (radius) of 0.62 for $\rho^2 = 0.005$, compared to the balanced rotor with an orbit size of 0.8. On the other hand, the orbit increases in size to 0.85 for $\rho^2 = 0.05$. Figure 6.20 shows the corresponding phase angle ϕ variation with the non-dimensional time τ. Interestingly, the ratio $\frac{\phi}{\tau}$ reduces for $\rho^2 = 0.005$ due to a phase lag at the start of whirling with respect to the balanced rotor case. But, the ratio increases for $\rho^2 = 0.05$ when the phase angle experiences a lead at the start. This suggests that the value of $\dot{\phi}$, at the start, may play a significant role in the growth rate of the whirl amplitude. Similar behaviour is also seen in the frequency domain. For example, at a given speed $\overline{\omega} = 10$, Figure 6.21 shows the frequency response plot for various unbalance values; the time history in the range $750 \le \tau \le 1000$ (139 to 159 revolutions) is transformed into the frequency domain to examine its frequency contents. As unbalance is increased to 0.005 and 0.007, the sub-synchronous response reduces, while there is an increase in the synchronous component. For a further increase in the unbalance to 0.15, the sub-synchronous component increases again, with a drop in the synchronous component. Figure 6.22 shows a similar plot for a lower speed $\bar{\omega} = 5$, which is the frequency transformation of the time history in the range $825 \le \tau \le 1000$ (139 to 159 revolutions). This shows a consistent behaviour but the unbalance values are on the higher side. Since the unbalance force is centrifugal and speed dependent, a higher unbalance is required at a lower speed for similar effect. Here an increase to 0.01 and 0.05 has a positive effect. But, further increase of unbalance to 0.09 has a negative effect.

The above discussion clearly suggests that the unbalance effect in the transient motion must be controlled by the initial phase angle and its rate of change. In order to verify this, a simple exercise is performed for $\sigma_m = 50$ at a speed $\bar{\omega} = 3$ ($\approx$20,093 **rpm**). The system is analysed for four unbalance cases, $\rho^2 = 0,\ 0.05,\ 0.1,\ 0.15$ for $\tau = 100$ to investigate the mechanism, at the start of whirling. A relatively low σ_m is chosen for this study to have the benefit of faster orbit growth. Figure 6.23 shows the orbit plots for these four cases. The orbits of the unbalanced rotor, show an internal loop. Gunter and Barrett [37, 87] have shown that, when the rotor motion is started from the bearing centre at zero initial velocity, the shaft spirals outward with a combination of the synchronous and half-frequency whirl. The two vectors in combination produce the characteristic internal loop associated with oil-whirl in an unbalanced journal. These internal loops increase in size with increase in the unbalance magnitude. When $\rho^2 = 0.1$, the internal loop is close to that of the external loop, making the rotor motion almost whirl at the synchronous frequency. When $\rho^2 > 0.1$, the overall orbit size starts growing relatively larger, where the synchronous component reduces over time. This is better seen in Figure 6.24, which shows the corresponding time history with difference in the amplitudes and the internal loop size. Figure 6.25 shows the growth of amplitude in time $\tau = 500$, where the growth rate reduces for $\rho^2 = 0.05$ and 0.1 compared to a balanced rotor, and increases for $\rho^2 = 0.15$. As mentioned earlier, to understand the change in the phase angle due to the presence of the unbalance, Figure 6.26 (a) and (b) are plotted showing the phase change with time for the case under investigation. Figure 6.26 (b) shows a closer view of (a) emphasising the change in the first two cycles. For $\rho^2 = 0,\ 0.05$ and 0.1, $\phi < \pi$ when $\tau = 2\pi$ and for $\rho^2 = 0.15$, $\phi > \pi$. After the second cycle, at the sub-synchronous frequency, $\rho^2 = 0.1$ seem to have an added phase delay, by shifting back to zero. This phase delay during the first and the second cycles causes the rotor response to slow down in the case of the unbalance $\rho^2 = 0.1$. Note that, the number of cycles in which phase reversals occur depends on the unbalance magnitude and the speed. This may depend on the significance of the unbalance force compared to the fluid-film forces in those cycles. However, for $\rho^2 = 0.15$, the response leads that of the balanced rotor, bringing a negative effect. This behaviour can be verified using the argument of the harmonic term in Eq. (6.10), such as,

$$\text{if } \phi < \pi \text{, when } \tau = 2\pi \text{ implies that } (\tau - \phi) > \frac{\tau}{2},$$

$$\text{and, if } \phi > \pi \text{ at } \tau = 2\pi \text{ implies that } (\tau - \phi) < \frac{\tau}{2}.$$

To determine the rate of change of phase, differentiating $(\tau - \phi)$ with respect to τ gives $1 - \frac{d\phi}{d\tau} = 1 - \dot{\phi} > 0.5 \Rightarrow \dot{\phi} < 0.5$, if $\phi < \pi$ and $\dot{\phi} > 0.5$ for $\phi > \pi$. Figure 6.27 shows the rate of change of the phase angle which gives the non-dimensional frequency of the rotor motion, corresponding to the phase angle shown in Figure 6.26. Figure 6.27 shows that at the start of whirling, $\dot{\phi} < 0.5$ for $\rho^2 = 0, 0.05$ and 0.1. But, for $\rho^2 = 0.15$, $\dot{\phi} > 0.5$. This suggests that for any given amplitude of unbalance, if the whirl frequency is less than 0.5, the unbalance force vector reduces the effect of film forces in the transient motion. Figure 6.28 shows the plot of the radial and the tangential force terms in Eq. (4.7) under the effect of the unbalance. Both the forces increase at a slower rate relative to the balanced case, for $\rho^2 = 0, 0.05$ and 0.1. However, the forces increase in the case of $\rho^2 = 0.15$. This coupled nature of amplitude and phase is clearly seen in the averaged Eqs. (6.37) and (6.38). Unlike the equations of motion for the balanced rotor given in Eqs. (5.62) and (5.63) in Chapter 5, these equations have the harmonic terms that couple them through the phase angle. This suggests that depending on the phase angle and its rate of change, the response amplitude rate changes. Figure 6.29 shows the plot of $\dot{\bar{r}}_u$ varying with increasing unbalance. $\bar{\varphi}_u$ is incremented by 0.03 and 0.04 to show the difference in $\dot{\bar{r}}_u$. Eqs. (6.37) and (6.38) reveal that the addition of a harmonic term to the linear and cubic functions of $\bar{r}_u$, forces $\dot{\bar{r}}_u$ to vary harmonically for any given rate of change of phase. To enunciate this behaviour, Figure 6.30 is plotted with all the three terms of Eq. (6.37) separately, against $\bar{r}_u$. Depending on the phase angle $\bar{\varphi}_u$, the unbalance term can either increase or decrease $\dot{\bar{r}}_u$. This is in agreement with the numerical results, where the unbalance force basically reduces the growth rate of the whirl amplitude, by affecting the phase at which the response occurs.

6.6 CONCLUSIONS

The turbocharger with a rigid rotor supported on two identical rigidly supported bearings with π-film cavitation was analysed to study the effect of unbalance. Numerical simulations were done aiming to produce waterfall plots similar to the experimental waterfall plot provided by *Cummins Turbo-Technologies Ltd.* The experimental waterfall plot showed a shift in the response frequency of the rotor-system from the in-phase whirl frequency to the synchronous frequency over a certain speed range. Both the numerical and the analytical methods were used to investigate this behaviour of the turbocharger to determine the influence of unbalance in terms of the whirl amplitude, phase angle and their rate of change.

Turbochargers due to their light weight, operate in **Region I** of the parameter plane of speed and eccentricity ratio with high σ_m. Hence the turbocharger rotor, most of the time has its journal centre tracing an orbit that keeps growing in size. Unbalance seems to slow down the growth of the whirl amplitude in the transient motion, by introducing a phase lag in the unbalance response compared to that of the self-excited response of the balanced rotor. However, above a certain optimum value, unbalance has a negative effect by increasing the growth rate of the amplitude. This happens due to the coupled effect of the phase and the amplitude introduced by the unbalance in the rotor.

Depending on the speed range of interest, the optimum unbalance varies. When the in-phase whirl frequency component reduces, the synchronous component increases.

This suggests that the effect of unbalance could be beneficial during the transient motion, for instance, during the acceleration and the deceleration of the engine. Depending on the time allowed at each speed, the effect of unbalance could be different. For practical reasons, it is almost impossible to have a perfectly balanced rotor. Hence, allowing some unbalance within the optimum level, for controlling the sub-synchronous vibrations seem to be a cost-effective solution worth considering into the rotor dynamic design of an automotive turbocharger.

FIGURES

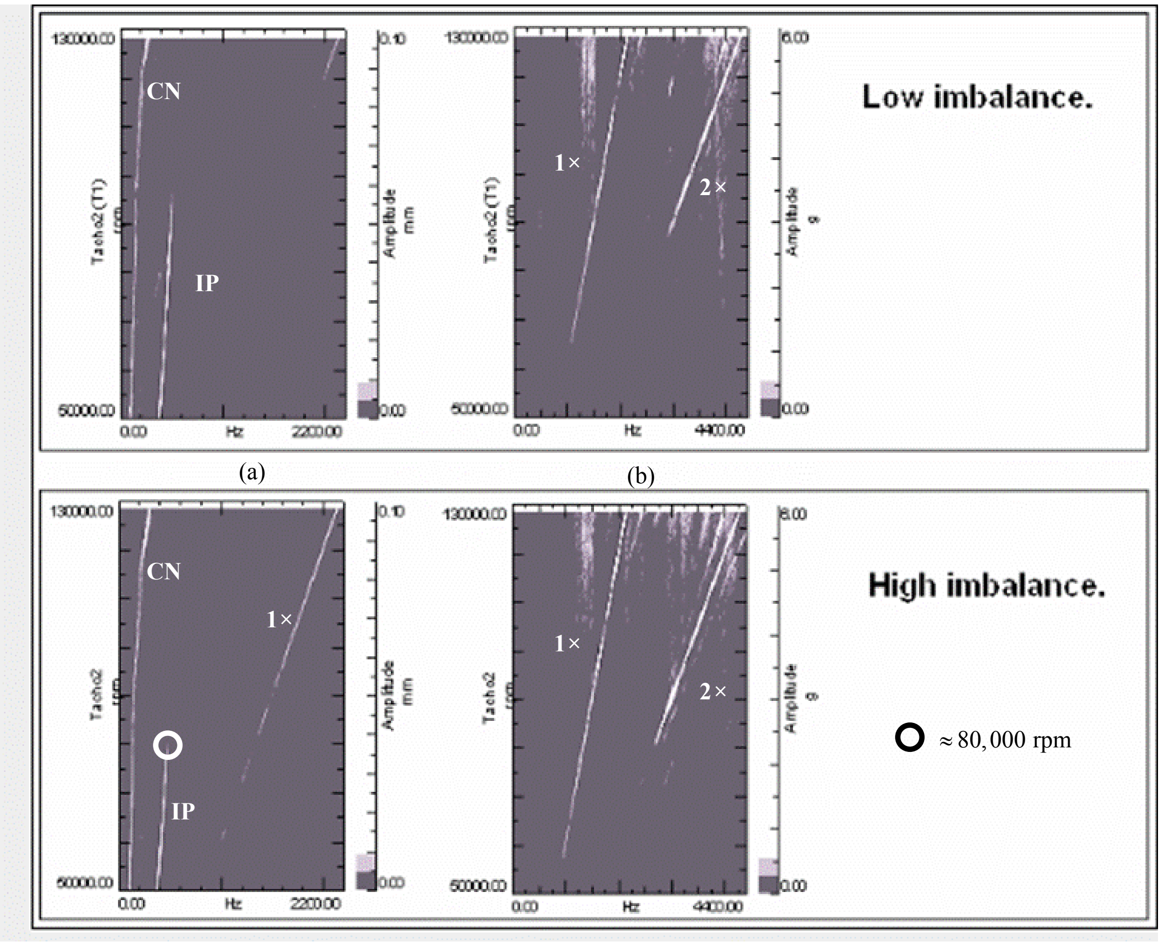

(a) (b)

SHAFT MOTION **ACCELERATION**

(c) (d)

CN - CONICAL WHIRL

IP - IN-PHASE WHIRL

1× - SYNCHRNOUS WHIRL FIRST HARMONIC

2× - SYNCHRNOUS WHIRL SECOND HARMONIC

Figure 6.1 Adapted from the comparative waterfall plots provided by *Cummins Turbo Technologies Ltd.* based on the data was collected from the same hardware/conditions but with different unbalance levels: (a) shaft motion with low unbalance b) acceleration with low unbalance (c) shaft motion with high unbalance (d) acceleration with high unbalance. The speed at which the response frequency shifts from sub-synchronous to synchronous frequency is marked by a circle in (c).

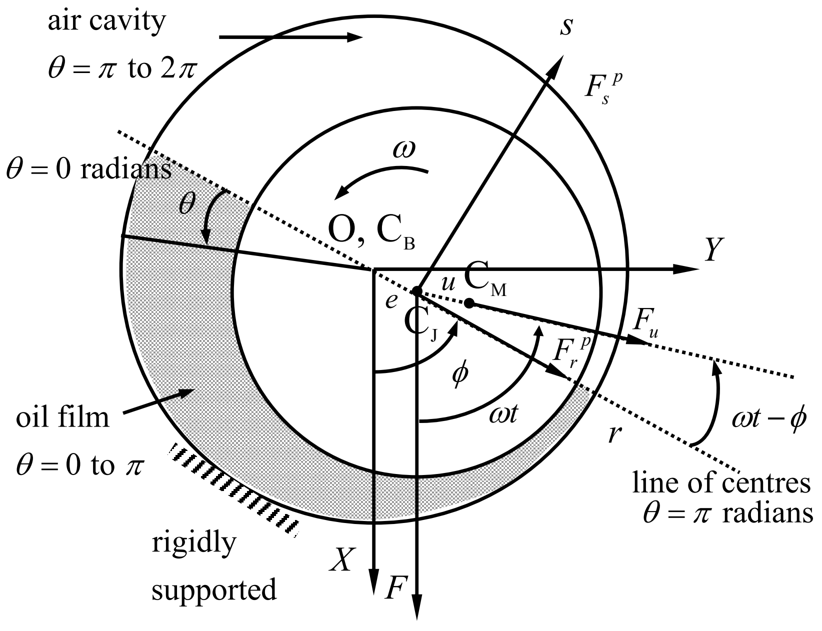

Figure 6.2 Co-ordinate system of a rotor-bearing system with a rigid rotor in rigidly supported bearing with oscillating π-film cavitation; ε is the eccentricity of the journal centre from the bearing centre C_B. The bearing is rigidly supported to the housing making C_B coincide with the housing centre O; $n = e/C$ is the eccentricity ratio where C is the clearance; ϕ is the attitude angle of the line of centres of the journal C_J and the bearing centre C_B; with respect to the vertical axis; F_r^p, F_s^p are the radial and tangential forces acting along r and s respectively; $F_u = m_u u \omega^2$ is the centrifugal force due to the rotor unbalance, whose eccentricity from the geometric centre of the journal C_J is u; m_u is the rotor mass with unbalance; C_M is the centre of the mass centre; F is the static load; ω is the spin speed; X, Y are the co-ordinates of the journal centre along the axes X, Y whose origin is at the housing centre.

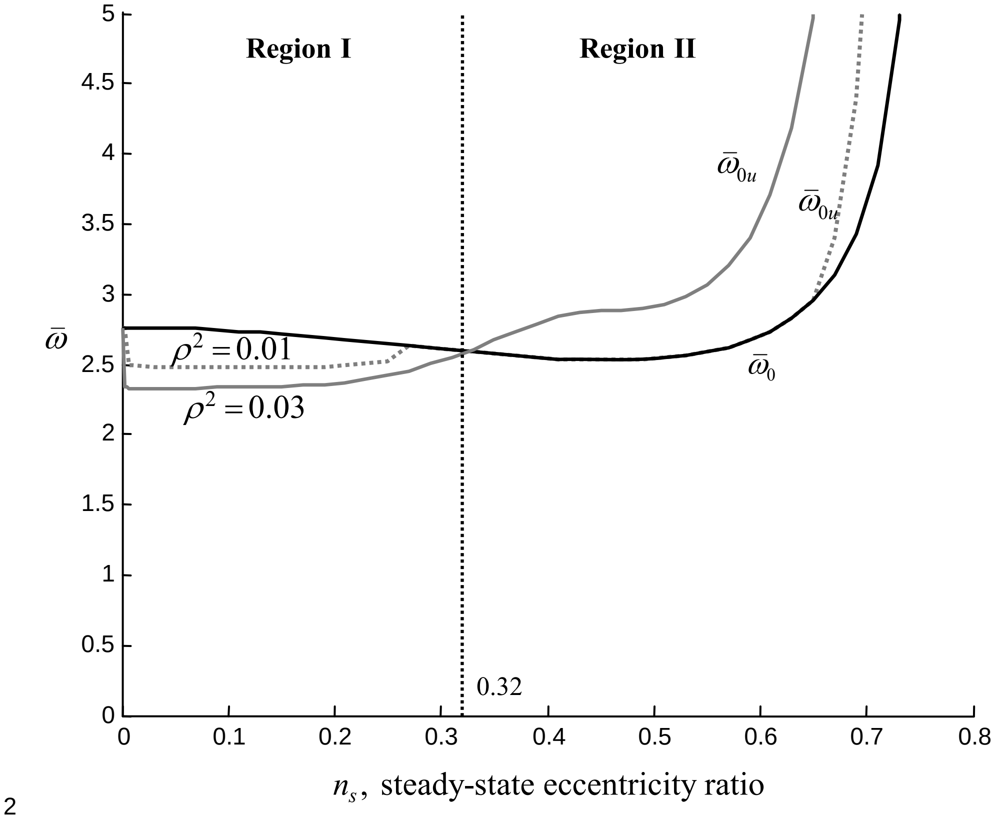

Figure 6.3 Plot of the modified stability threshold from Eq. (6.53) due to the influence of the unbalance, when the tuning parameter $\sigma_1 \approx 0$; $\nu = -0.1$ for $\rho^2 = 0.01$ and 0.03.

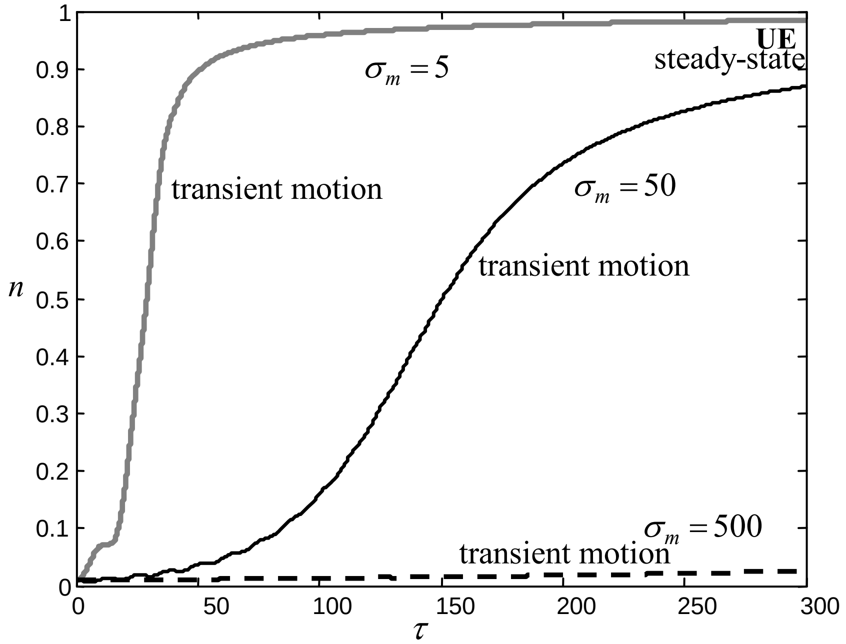

Figure 6.4 Plot of the whirl amplitude n (eccentricity ratio) growing with non-dimensional time τ for various values of σ_m, which means different rotor systems with balanced rotor $(\rho^2 = 0)$. As σ_m increases the growth rate reduces.

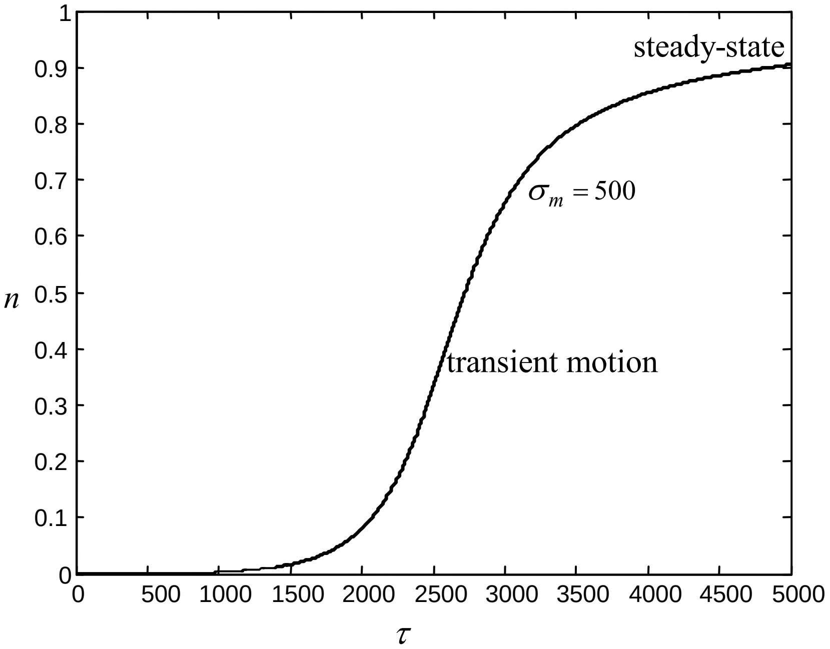

Figure 6.5 Plot of the whirl amplitude n (eccentricity ratio) growing with time τ for $\sigma_m = 500$, which represents a turbocharger rotor system with perfectly balanced rotor for given bearing dimensions and oil viscosity; $\rho^2 = 0$.

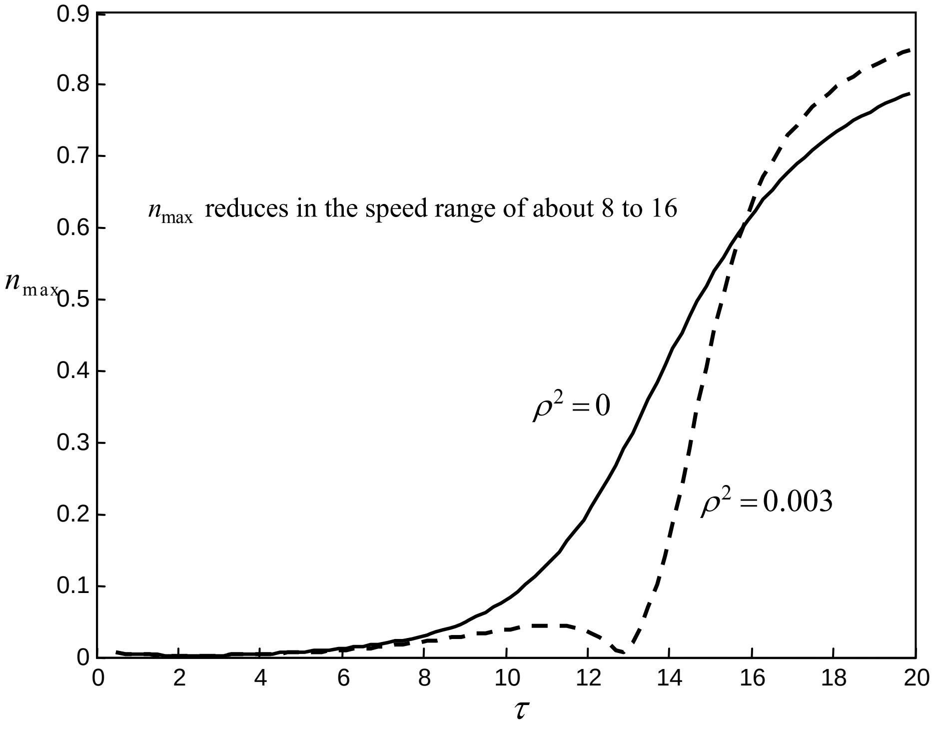

Figure 6.6 Envelope of the time history showing the variation of amplitude as speed is increased slowly from $\bar{\omega} = 0.5$ to 20 for the turbocharger without unbalance $\rho^2 = 0$, and with unbalance $\rho^2 = 0.003$. $n_{\max}$ is the maximum amplitude reached at each speed. Since the orbit mostly grows outwards in the case of a turbocharger, the envelope gives the maximum amplitude, at each speed.

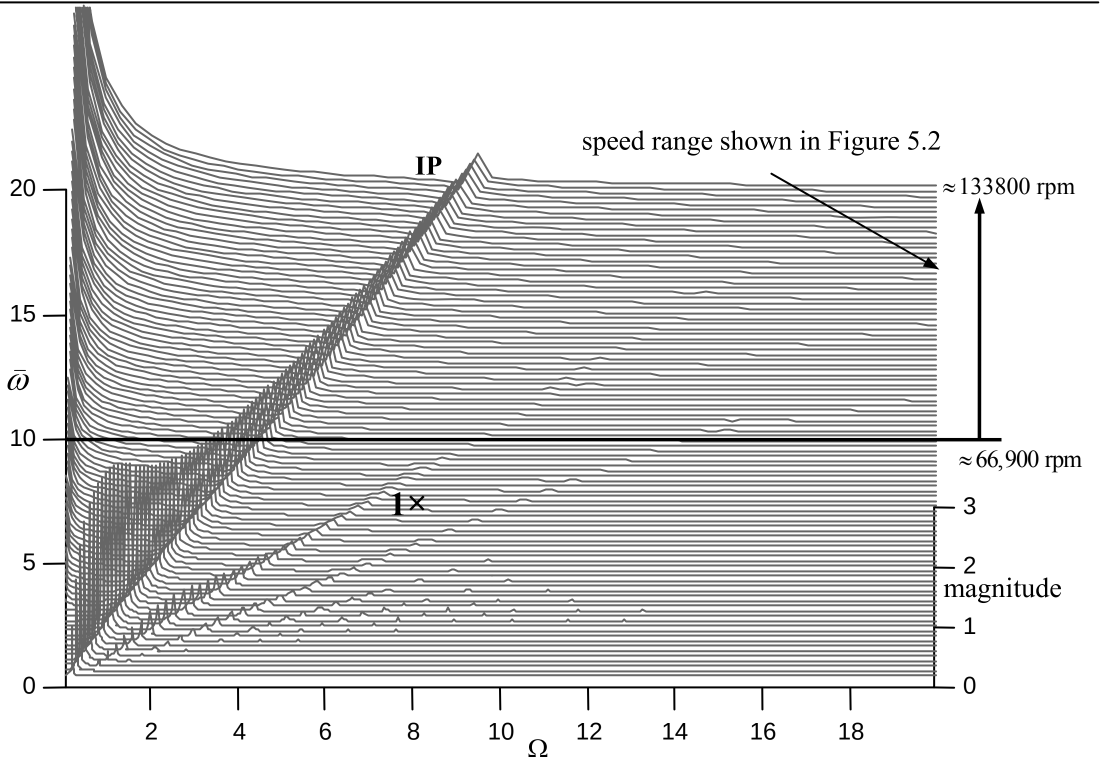

Figure 6.7 Waterfall plot showing the in-phase whirl frequency (**IP**) of the rotor-system with balanced rotor, when $\sigma_m = 500$ and $\rho^2 = 0$.

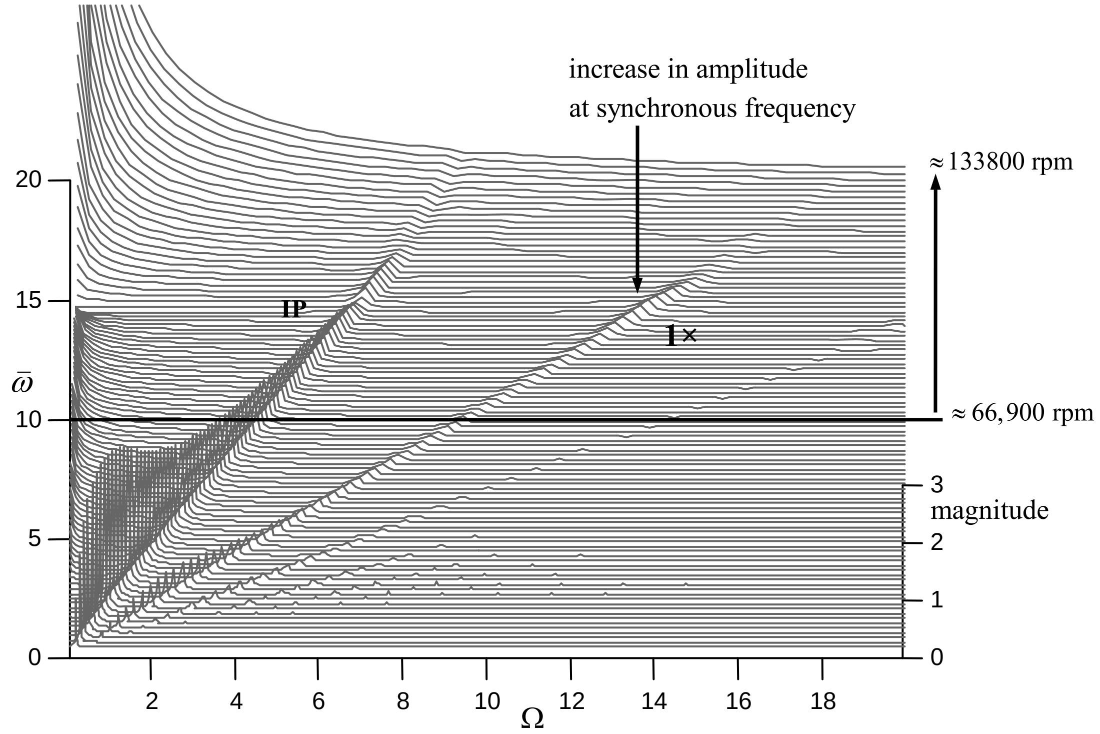

Figure 6.8 Waterfall plot showing reduction in the amplitude at in-phase whirl frequency (**IP**) for speeds above $\bar{\omega} \approx 15$. The amplitude of synchronous frequency increases around that speed for the rotor-system with unbalance, when $\sigma_m = 500$ and $\rho^2 = 0.002$.

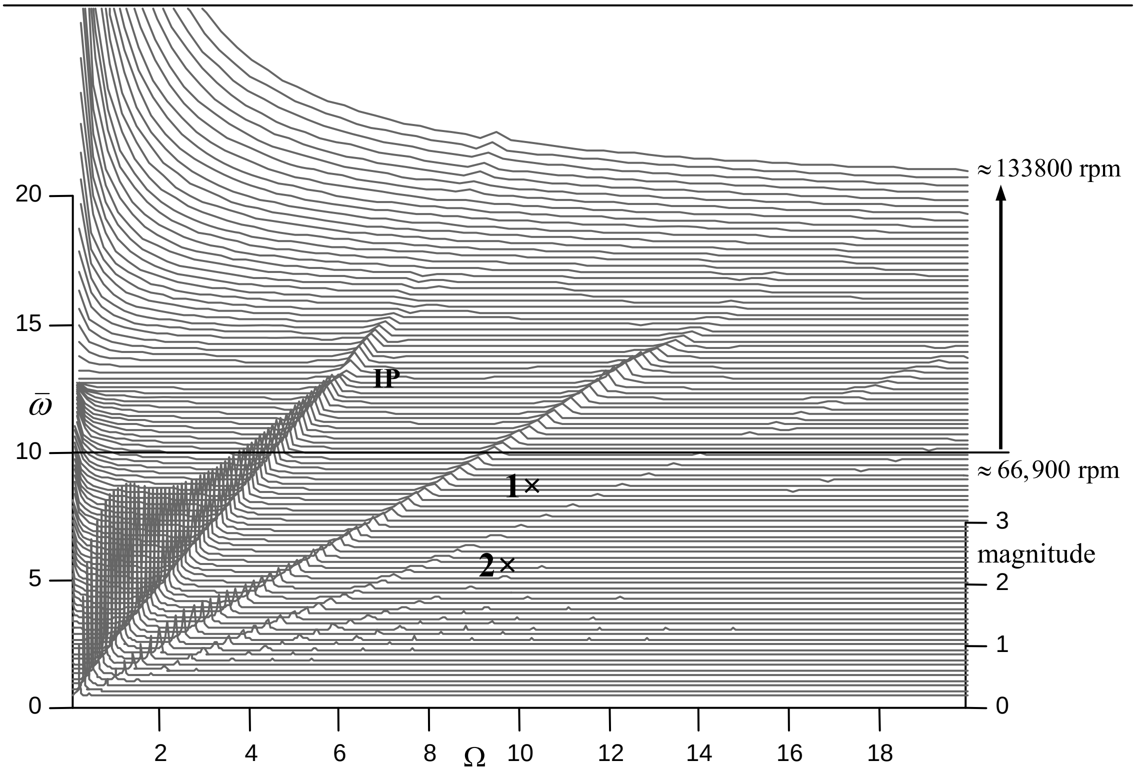

Figure 6.9 Waterfall plot showing reduction in the amplitude at in-phase whirl frequency ($\mathbf{IP}$) for speeds above $\bar{\omega} \approx 12$. The amplitude of synchronous frequency increases around that speed for the rotor-system with unbalance, when $\sigma_m = 500$ and $\rho^2 = 0.003$.

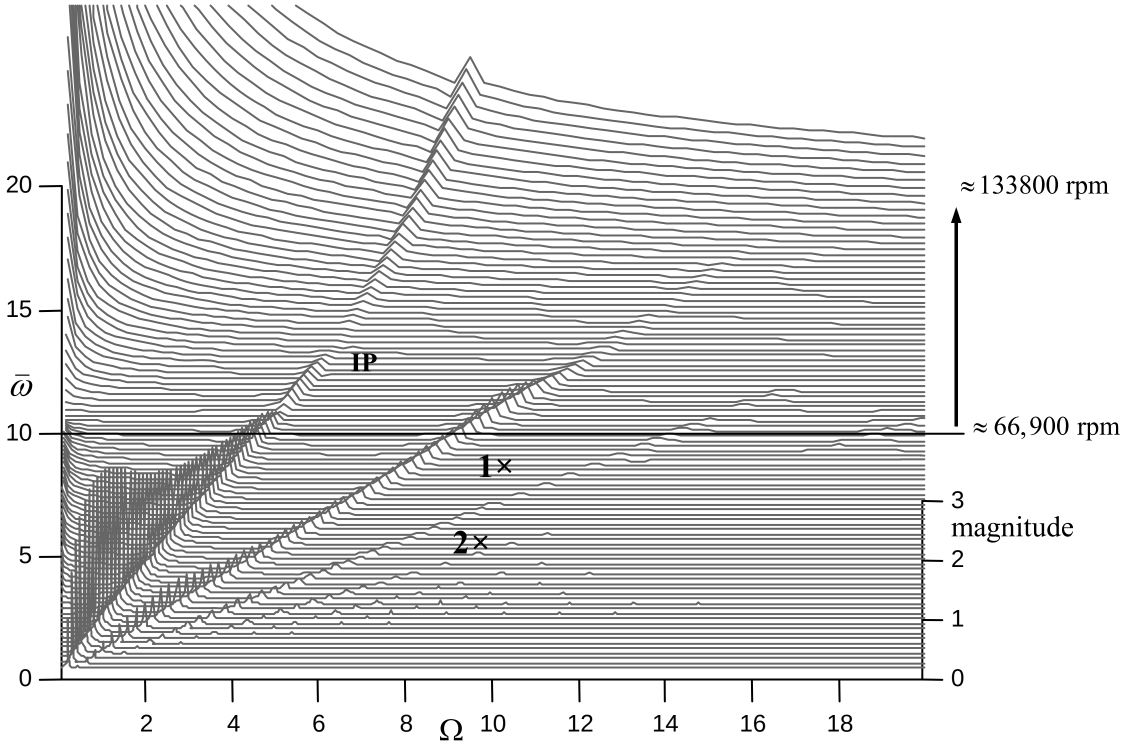

Figure 6.10 Waterfall plot showing increase in the amplitude at the in-phase whirl frequency ($\mathbf{IP}$) for speeds above $\bar{\omega} \approx 15$ and reduction in the amplitude for speeds between $10 \le \bar{\omega} \le 15$ for the rotor-system with unbalance, when $\sigma_m = 500$ and $\rho^2 = 0.005$.

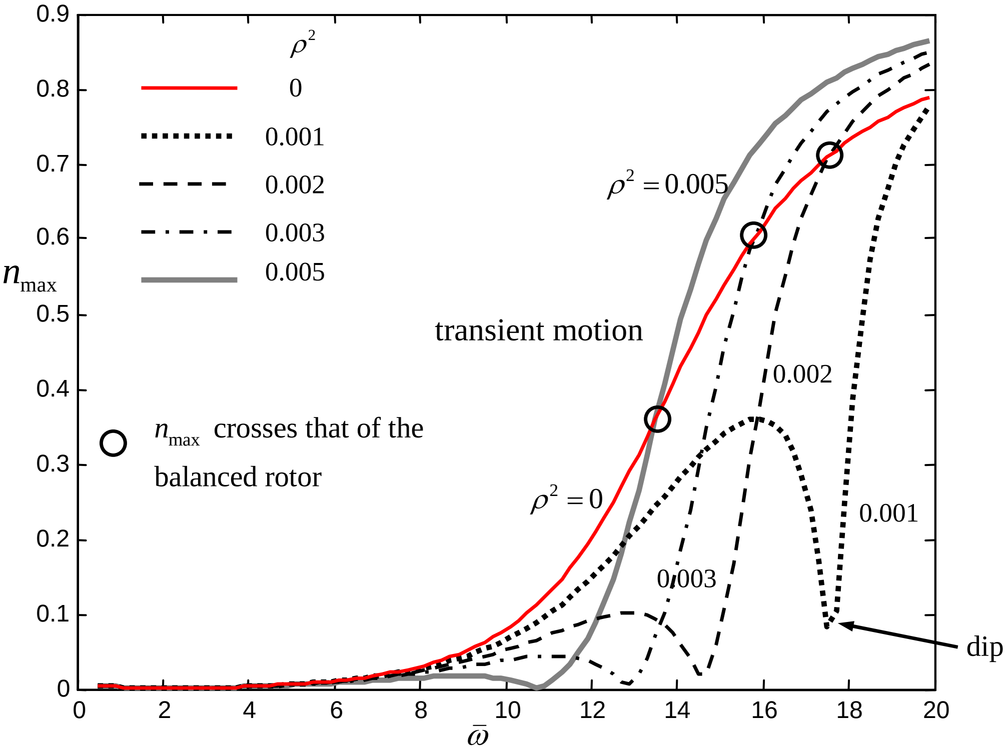

Figure 6.11 Plot of the maximum amplitude (eccentricity ratio) $n_{\max}$ against the rotor speed for various values of unbalance for the rotor system corresponding to $\sigma_m = 500$ in the time domain. The plot shows a reduction in the amplitude with increase in unbalance for a certain speed range. This range reduces with increase in unbalance.

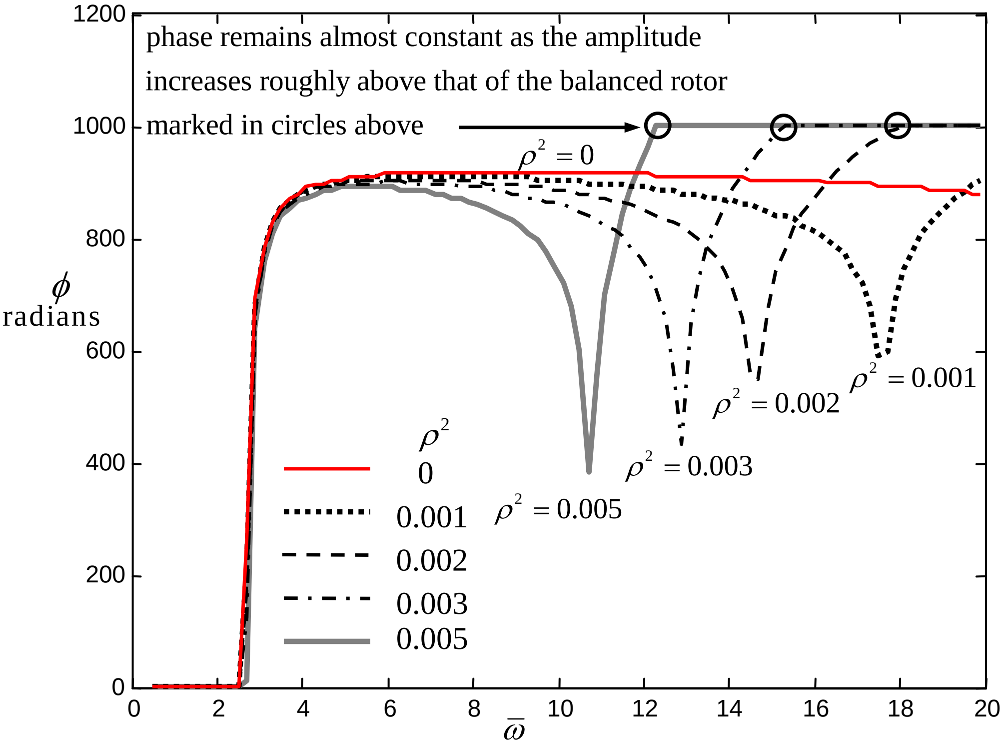

Figure 6.12 Plot of the attitude angle ϕ against the speed corresponding to the amplitudes shown in Figure 6.11. The plot shows a phase drop in the speed range of interest in the case of unbalanced rotor ($\rho^2 > 0$). This corresponds to the dip in the amplitude shown in Figure 6.11.

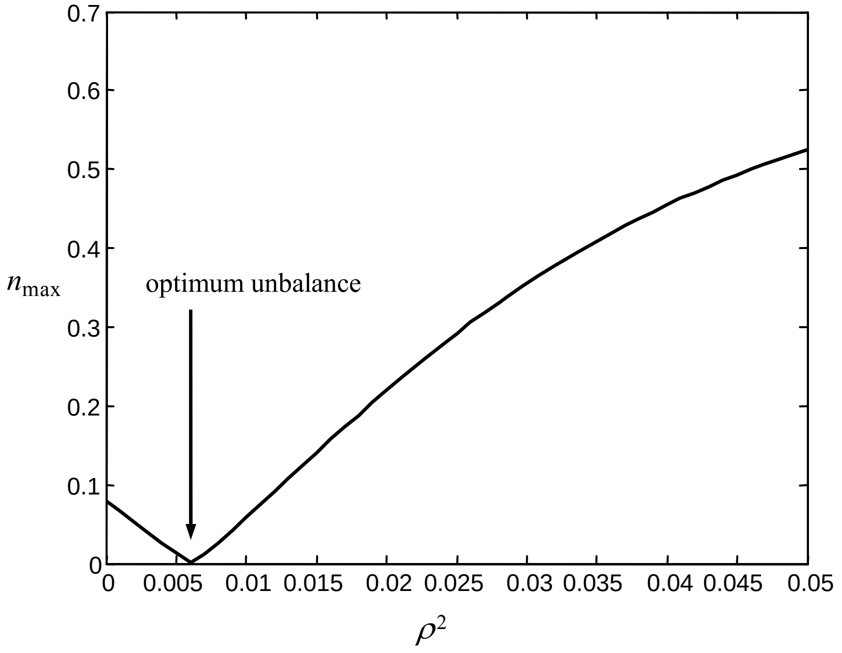

Figure 6.13 Plot of the maximum amplitude $n_{\max}$ against unbalance at a speed of $\bar{\omega} = 10$ (≈ 66900 rpm) run for a time of $\tau = 2000$ (≈ 318 revolutions) for $\sigma_m = 500$.

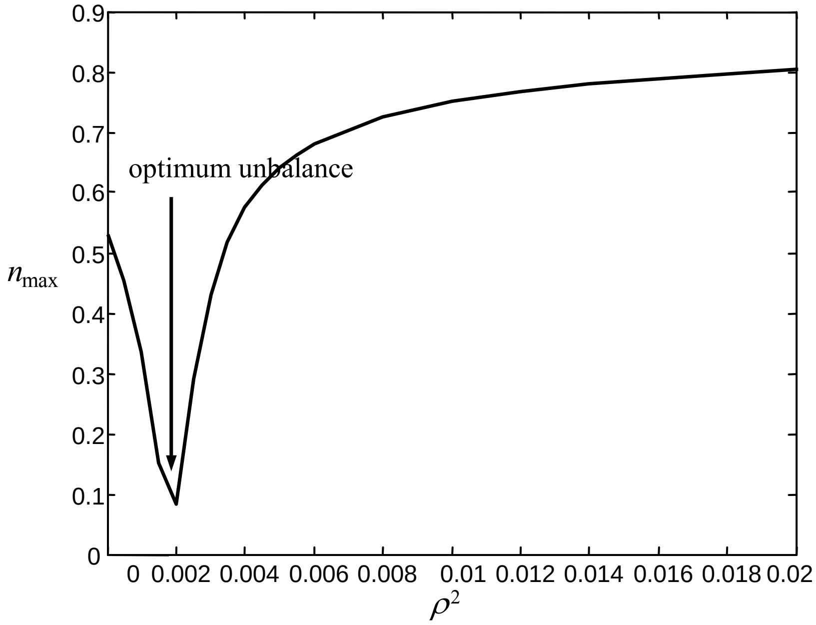

Figure 6.14 Plot of the maximum amplitude $n_{\max}$ against unbalance at a speed of $\bar{\omega} = 15$ (≈ 100365 rpm) run for a time of $\tau = 2000$ (≈ 318 revolutions) for $\sigma_m = 500$.

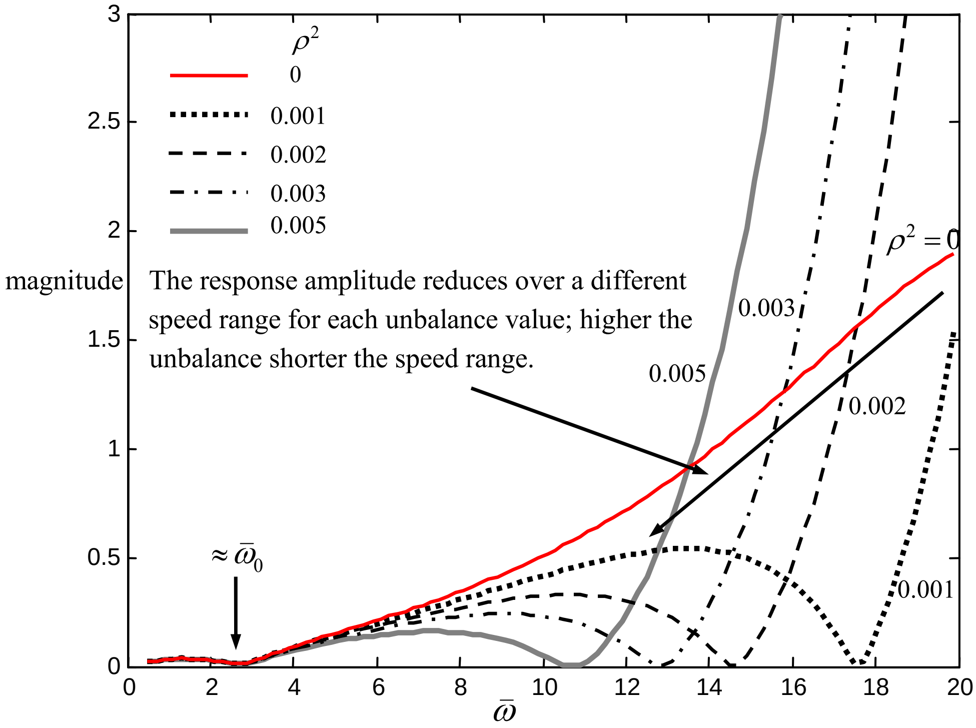

Figure 6.15 Plot of the response magnitude at the sub-synchronous frequency from the frequency domain against unbalance for $\sigma_m = 500$. This plot corresponds to the waterfall plots where the amplitude limit (y-axis) is based on the time series windowed for Fourier transformation.

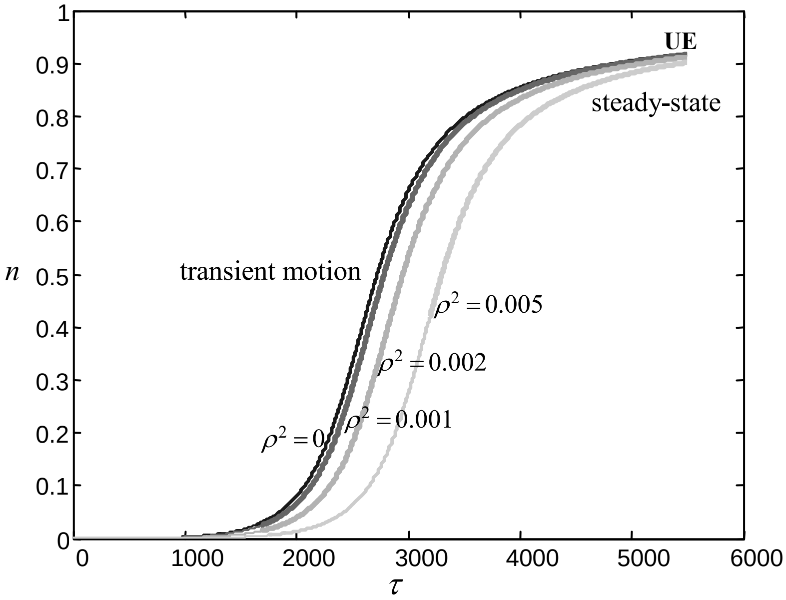

Figure 6.16 Plot of the amplitude n (eccentricity ratio) against non-dimensional time τ, for various unbalance values at a constant speed of $\bar{\omega} = 10$ (66,900 rpm) showing negligible effect in the steady-state. Each unbalance case is solved for a non-dimensional time of 5500 $\approx$ 875 revolutions for $\sigma_m = 500$.

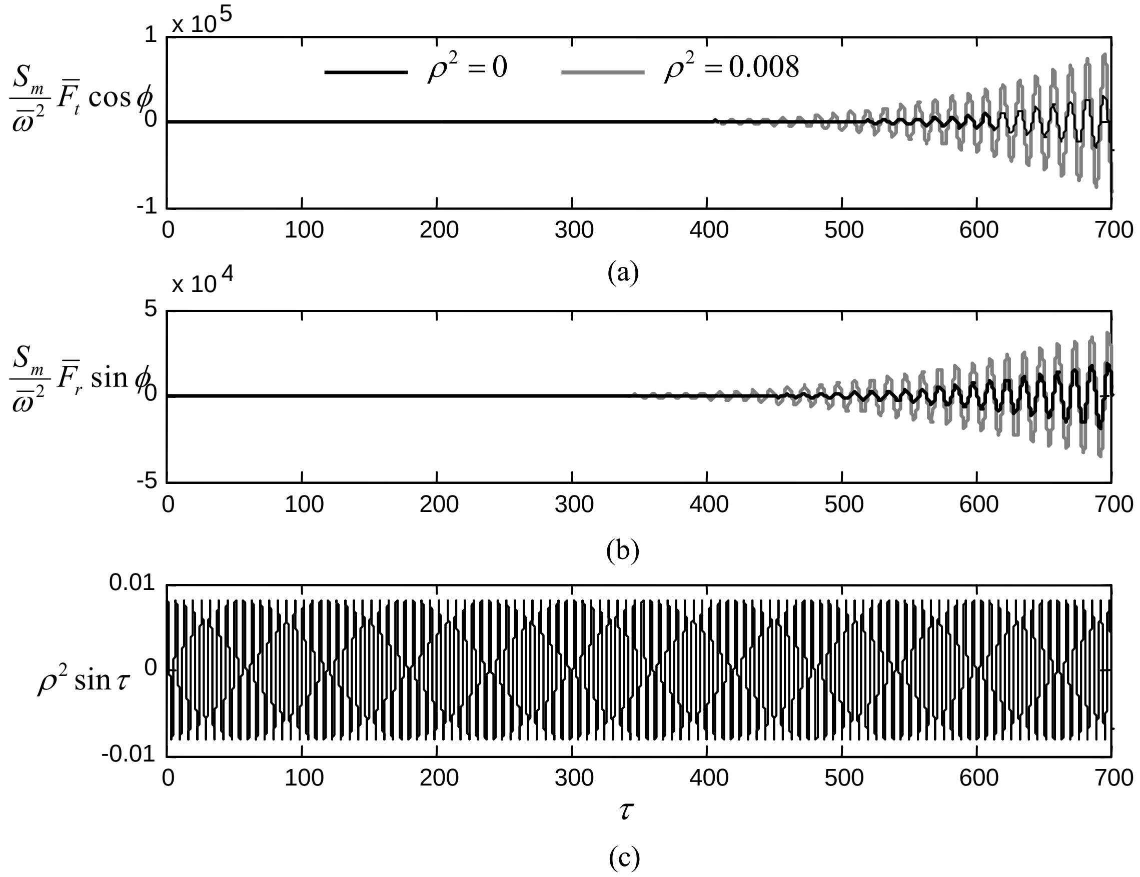

Figure 6.17 Plot of the (a) radial, (b) tangential and (c) unbalance forces acting along Y direction given in Eq. (4.7) varying with time when the rotor spins at a constant speed of $\overline{\varpi}=10$ and $\rho^2=0$ and 0.008. Plot shows the increase in the fluid forces with time, which leads to their high values in the steady-state compared to the unbalance force.

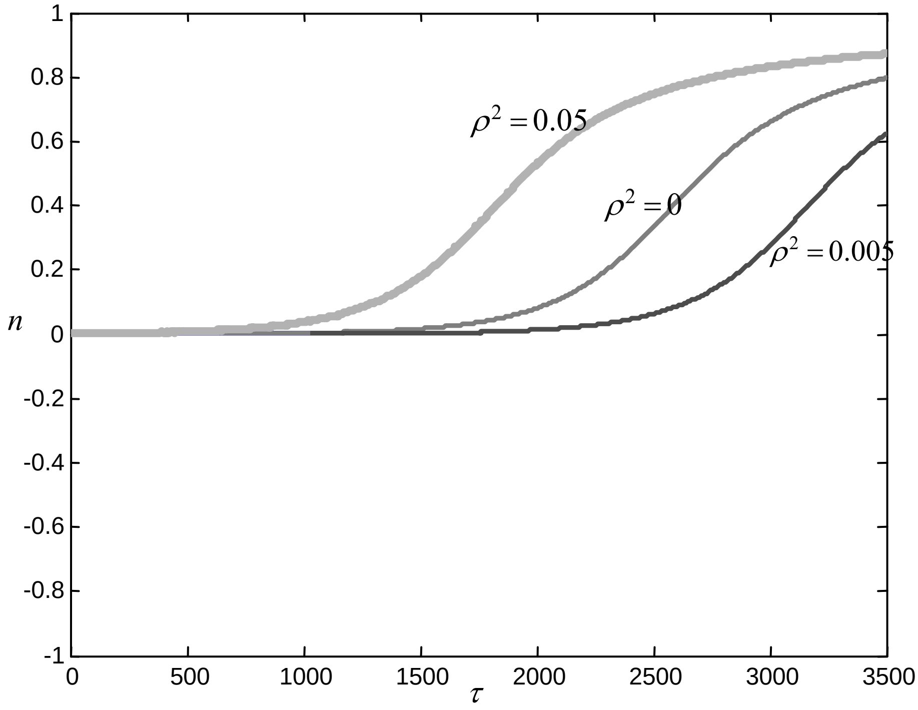

Figure 6.18 Plot of the eccentricity ratio n (amplitude), for various unbalance values, showing variation in the size of the orbits in transient motion at a constant speed of $\bar{\varpi} = 10$ (66,900 rpm); each unbalance case is solved for a non-dimensional time of 3500 $\approx$ 518 revolutions for the rotor system $\sigma_m = 500$

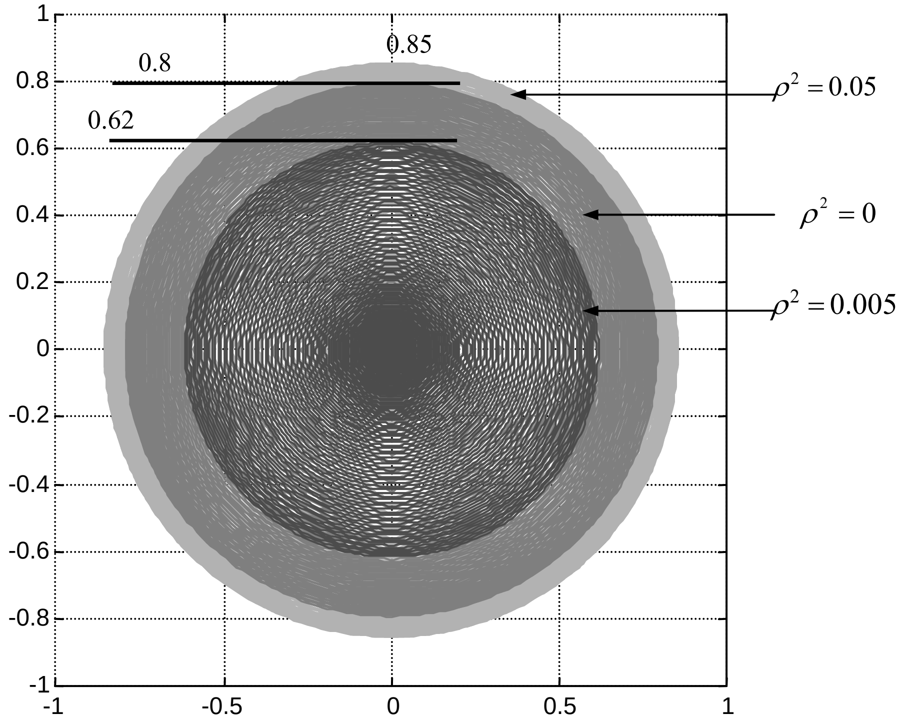

Figure 6.19 Orbit plot corresponding to the x amplitudes in Figure 6.18 showing decrease in the orbit size for $\rho^2 = 0.005$ and increase in the orbit size for $\rho^2 = 0.05$. Value of 0.05 is chosen purposely to bring it larger than the size corresponding to the balanced rotor at this speed.

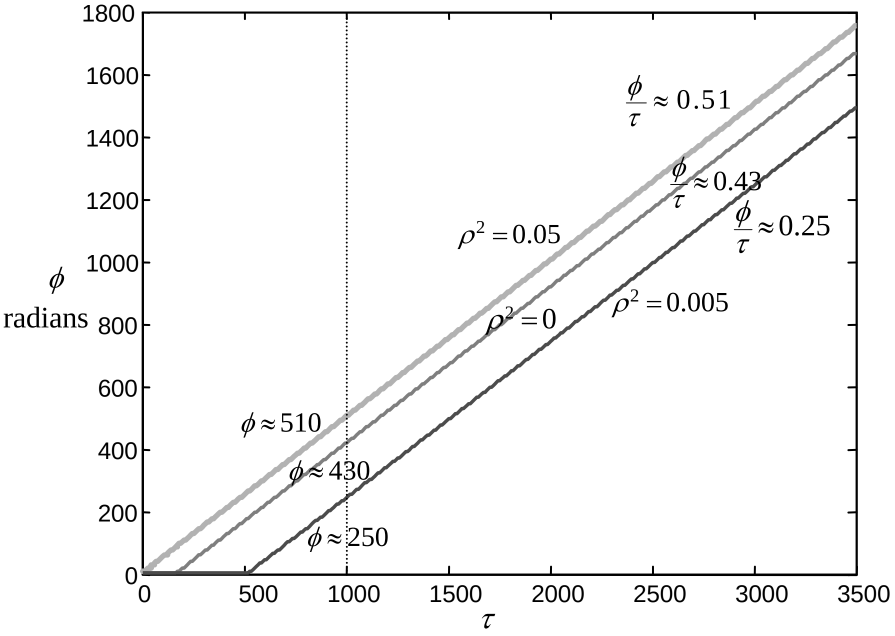

Figure 6.20 Plot of the attitude angle (phase) against time, i.e., response phase against excitation phase corresponding to the amplitudes shown in Figure 6.16. Reduction in phase ratio implies positive effect of unbalance. For $\phi = 430$, $(\tau - \phi) = \tau(1 - \phi/\tau) \approx 0.57\tau$.

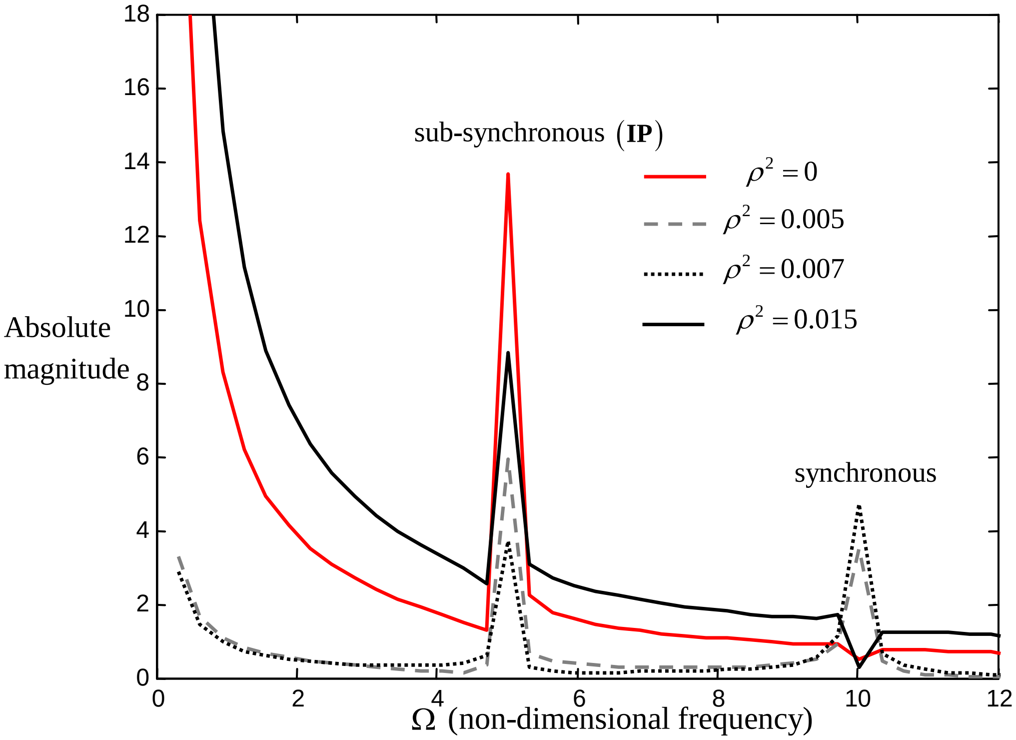

Figure 6.21 Frequency response plot at a speed of $\bar{\omega} = 10$ (66,900 rpm) for various unbalance values showing increase in the synchronous response; $\sigma_m = 500$; time history for $\tau = 750$ to 1000 (≈ 119 to 159 revolutions) is transformed to the frequency domain; The high amplitude at very low frequency is an artifact of the zero frequency component.

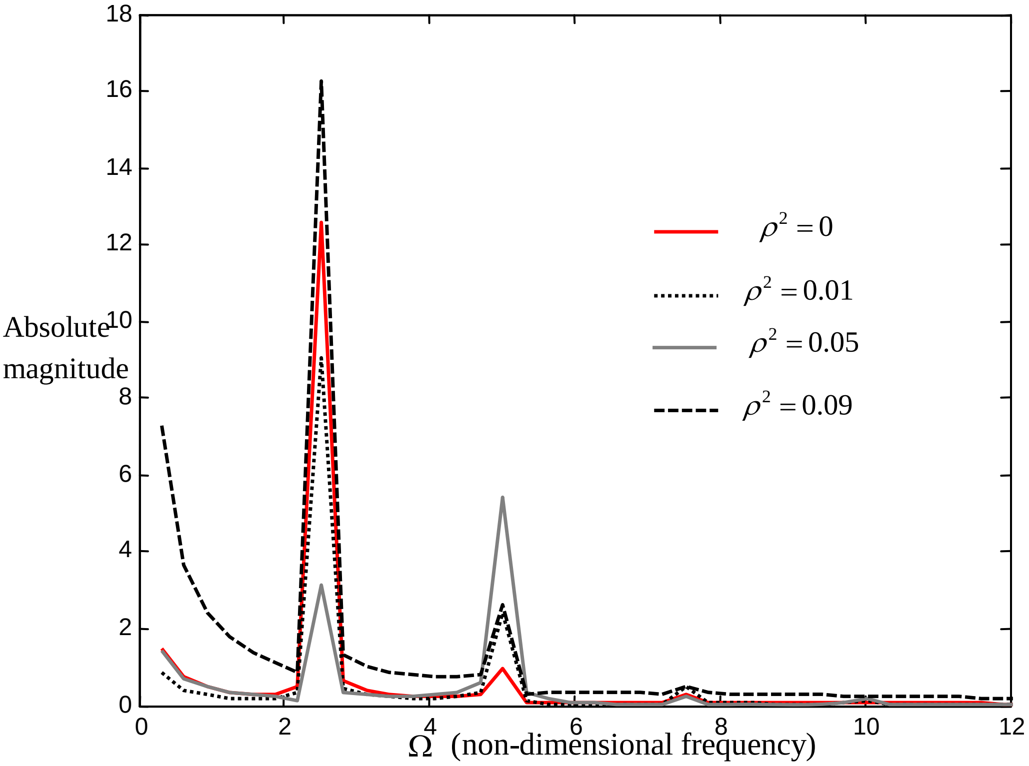

Figure 6.22 Frequency response plot at a speed of $\bar{\omega} = 5$ (33,455 rpm) for various unbalance values showing increase in the synchronous response; $\sigma_m = 500$; time history for $\tau = 875$ to 1000 ($\approx$139 to 159 revolutions) is transformed to the frequency domain; Note that unbalance values are higher than that shown in Figure 6.21 since the speed is less.

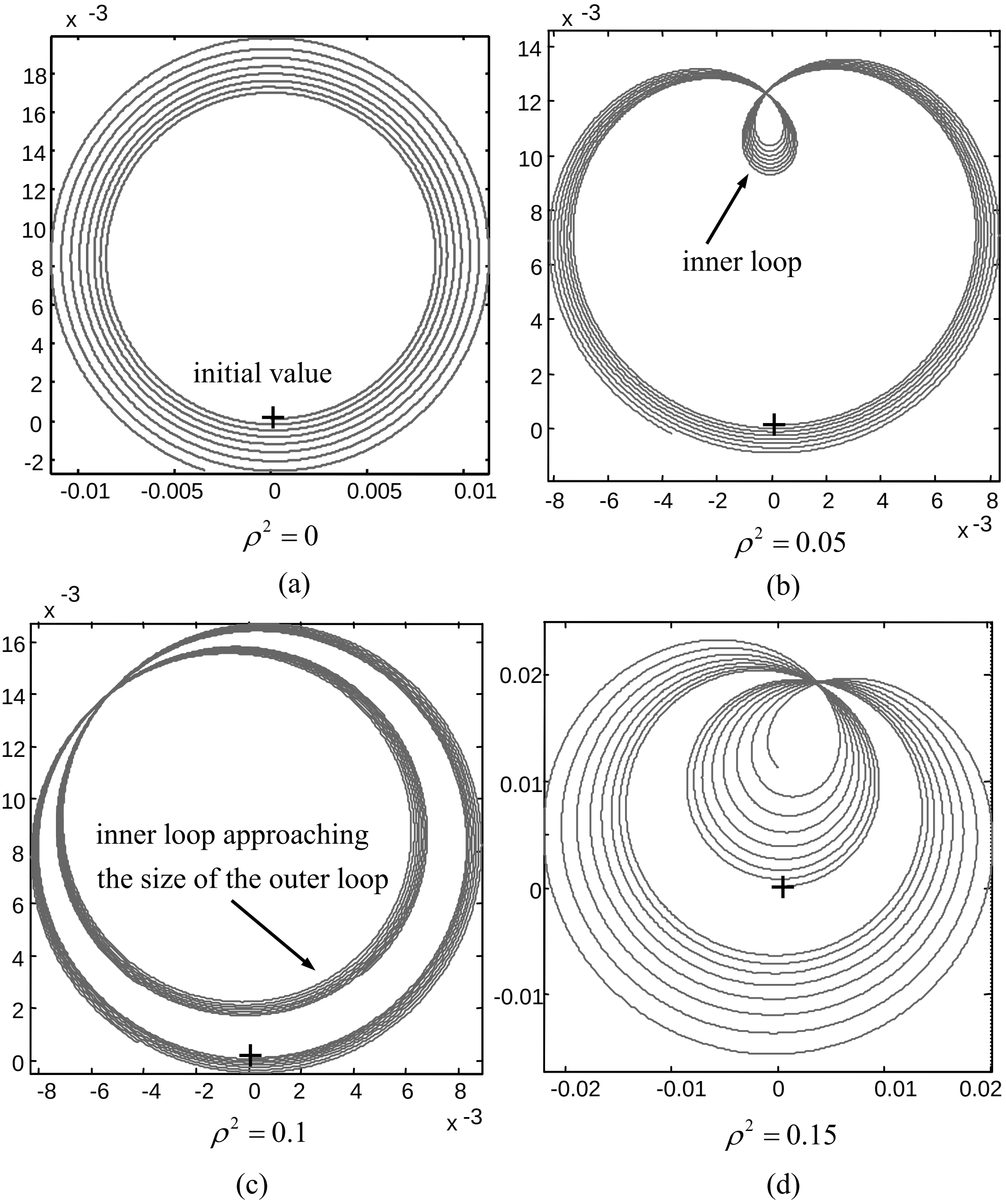

$\rho^2 = 0$

(a)

$\rho^2 = 0.05$

(b)

$\rho^2 = 0.1$

(c)

$\rho^2 = 0.15$

(d)

Figure 6.23 Orbit plots showing the journal motion under the influence of the unbalance at the start, for a speed of $\bar{\omega} = 3$ ($\approx 20{,}093$ rpm), when $\sigma_m = 50$; (a) for a balanced rotor (b) for $\rho^2 = 0.05$ (c) for $\rho^2 = 0.1$ (d) for $\rho^2 = 0.15$. $\sigma_m = 50$ is chosen for convenience in the demonstration of the change in the inner loop size as well as to show the growth of amplitude in the following figure, in a short time duration.

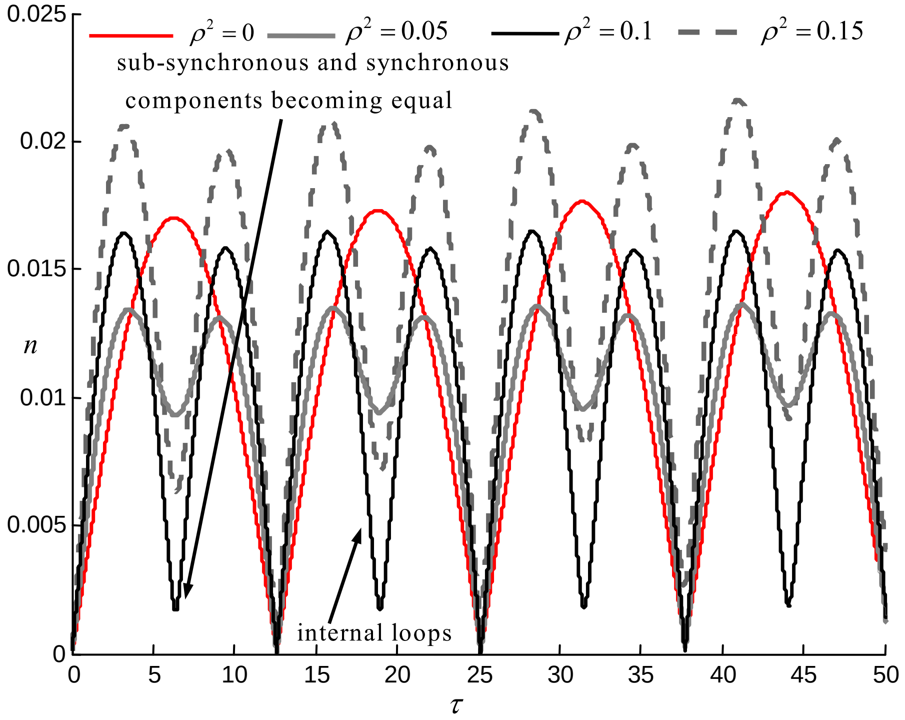

Figure 6.24 Time history corresponding to the orbit plots given in Figure 6.23 showing the journal motion under the influence of the unbalance at the start at a speed of $\bar{\varpi}=3$ (≈20,093 rpm) for $\sigma_m=50$.

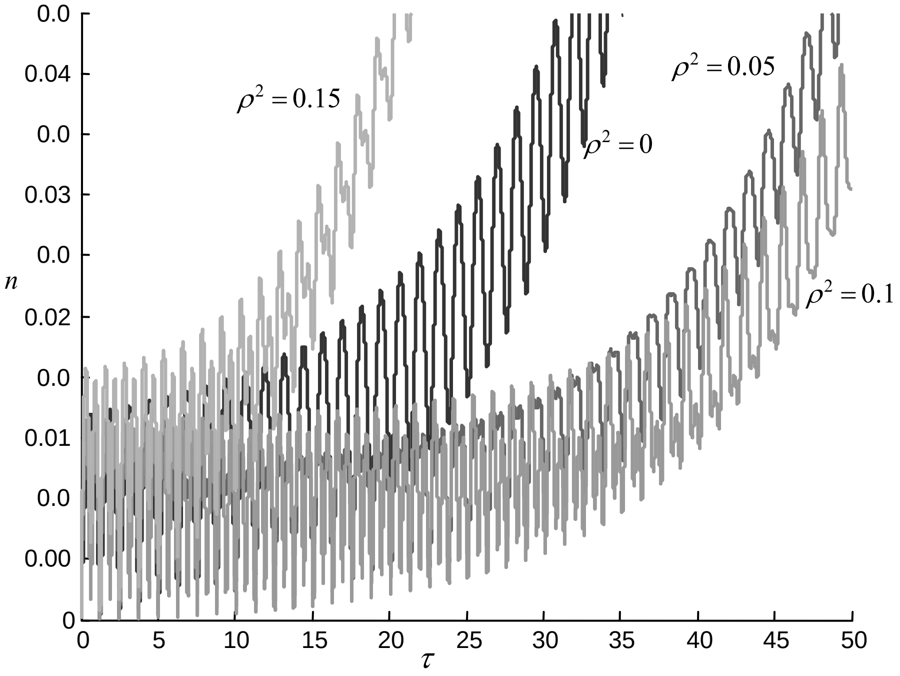

Figure 6.25 Time history corresponding to the orbit plots given in Figure 6.23 showing the growth of the whirl amplitude with time at a speed of $\bar{\varpi}=3$ (≈20,093 rpm) for $\sigma_m=50$. The rate of growth is reduces upto $\rho^2=0.1$, beyond which the growth rate increases.

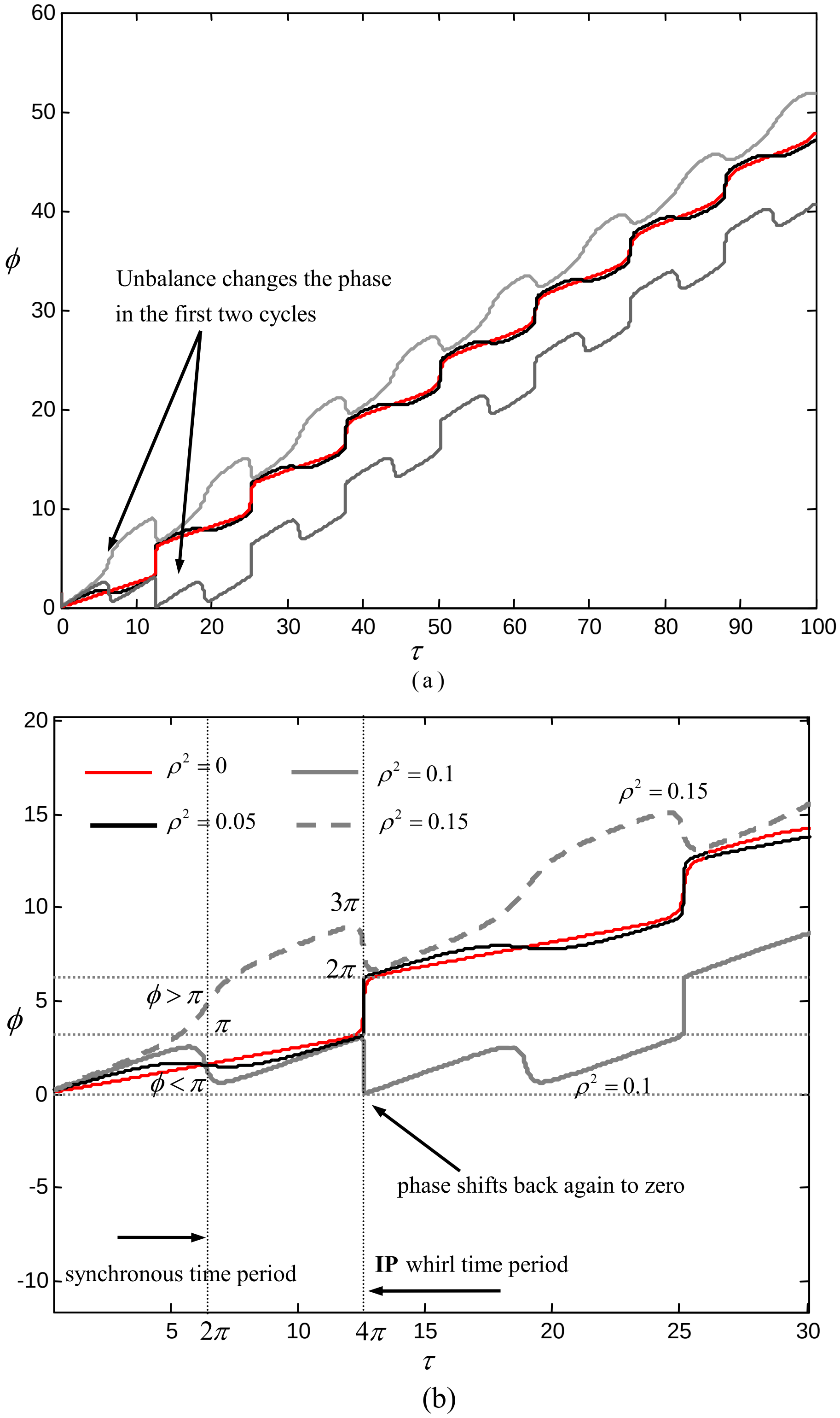

Figure 6.26 (a) Plot of the attitude angle (phase) against time, i.e., the response phase against the excitation phase corresponding to the orbits shown in Figure 6.23. The phase angle shifts at the start and continues at that rate. (b) Closer view of (a) showing the change in the phase, at the start of the rotor motion in the bearing. Phase angle is greater than π for $\rho^2 = 0.15$ and less than π for $\rho^2 = 0,\ 0.05,\ 0.1$ after one cycle. The phase angle further goes down to zero for $\rho^2 = 0.1$, after two cycles. ($\bar{\omega} = 3$ ($\approx$20,093 rpm); $\sigma_m = 50$)

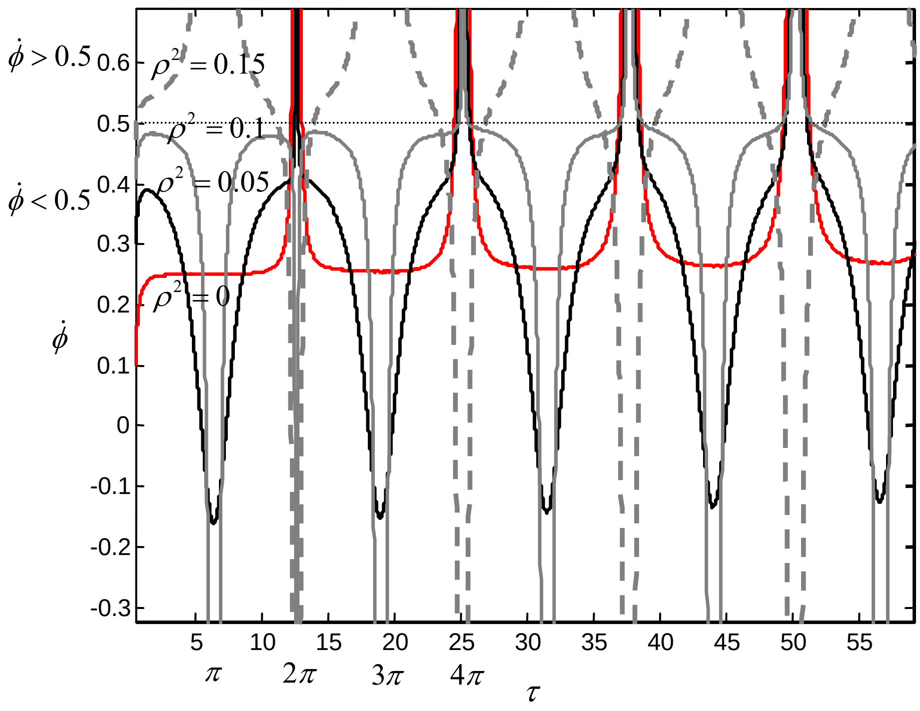

Figure 6.27 Plot of the rate of change of phase corresponding to the phase angle shown in Figure 6.26 where $\dot{\phi} < 0.5$ for $\rho^2 < 0, 0.05$ and 0.1 and $\dot{\phi} > 0.5$ for $\rho^2 > 0.15$.

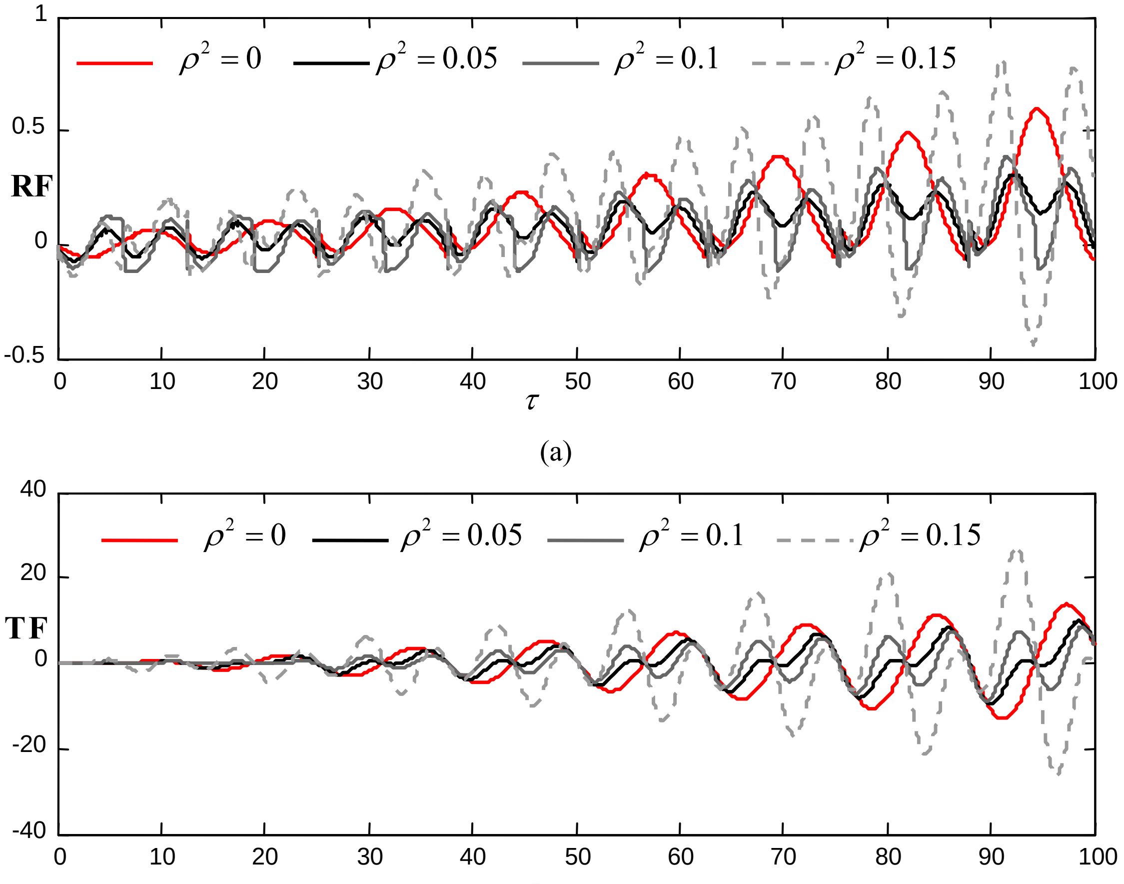

(a)

$$\mathbf{RF} = \frac{S_m}{\varpi^2}\bar{F}_r \cos\phi \quad \mathbf{TF} = \frac{S_m}{\varpi^2}\bar{F}_t \sin\phi$$

(b)

Figure 6.28 (a) Plot of the radial force term in Eq.(4.7) along Y direction, perpendicular to the direction of the static load. (b) Plot of the tangential force term. Both the film forces reduce in amplitude relative to the forces in the bearing with a balanced journal for $\rho^2 = 0.05,\ 0.1$. The film forces increase for $\rho^2 = 0.15$.

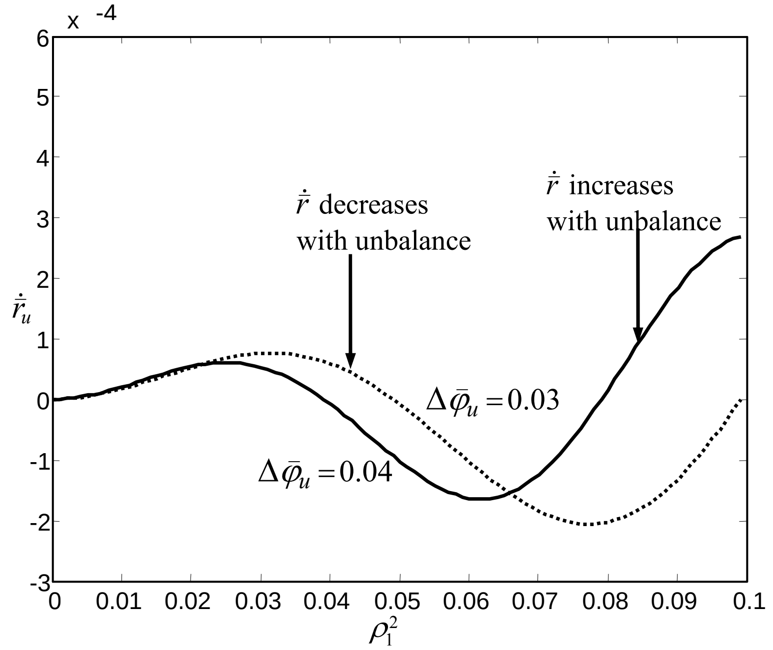

Figure 6.29 Plot of $\dot{\bar{r}}_u$ from the averaged equation of motion given in Eq. (6.37) varying with ρ_1^2, and $\bar{\varphi}_u$ for a given value of $\bar{r}_u = 0.1$, when $\nu = 0.01,\ n_s = 0.01,\ \sigma_1 \approx 0$.

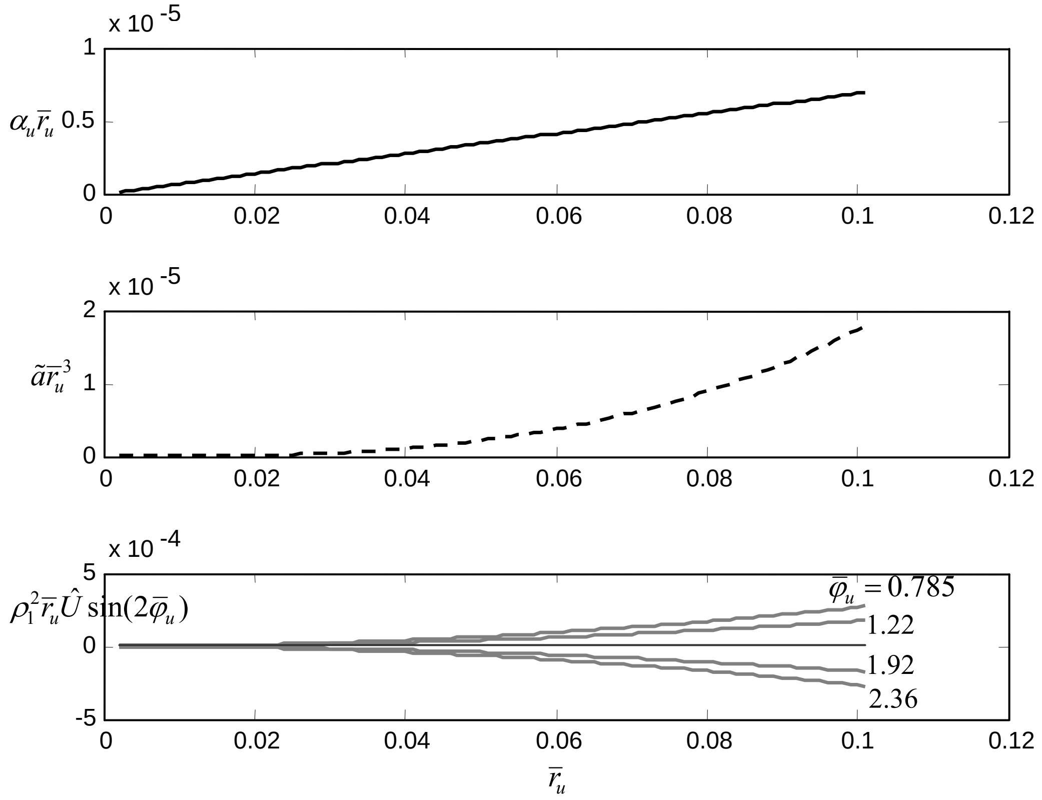

Figure 6.30 Plot of the terms in Eq. (6.37) varying with $\bar{r}_u$ for various values of $\bar{\varphi}_u$ when $\nu = 0.01,\ n_s = 0.01,\ \sigma_1 \approx 0$.

CHAPTER 7

CONCLUSIONS

7.1 INTRODUCTION

At the end of each Chapter, conclusions are presented related to the objective of the respective Chapters. This Chapter summarises the major conclusions drawn in this thesis. A summary of the research carried out in the thesis is also given and some recommendations are made for the future work.

7.2 BRIEF OVERVIEW OF THE THESIS

This thesis investigated the nonlinear dynamic behaviour of a turbocharger. The research work included classical analytical techniques and numerical simulations. Two unbalance test waterfall plots obtained from *Cummins Turbo-Technologies* were utilised to stimulate the investigation. These were produced under two different unbalance levels from the same hardware and conditions. A brief overview of the thesis is given below.

Turbochargers operate at very high speeds and use oil-film bearings due to their cheap cost. These units exhibit instability due to oil-whirl in the form of a conical mode and an in-phase whirl mode. Oil-whirl instabilities occur at sub-synchronous frequencies, which are usually a little less than 50% of the rotor speeds. These instabilities are sensitive to various factors such as the support conditions, bearing cavitation, film pressure, bearing geometry and so on. Oil-whirl instability is a potentially damaging operating condition that must be avoided. Despite such instabilities, turbochargers operate successfully. It has been reported in the literature that the turbocharger rotor exhibits limit cycle behaviour due to the nonlinearity of the oil-film. The test waterfall plots introduced in Chapter 1, revealed a shift in the response frequency from the sub-synchronous in-phase whirl frequency to the synchronous frequency, over a certain speed range, particularly for the high unbalance case. To investigate this specific behaviour of the turbocharger under the influence of some unbalance in the rotor, firstly a clear understanding of the nonlinear dynamic behaviour of the system with a perfectly balanced rotor is inevitable. Hence this thesis investigated the nonlinear behaviour that results in the limit cycle. To avoid over-complicated mathematical modelling, certain assumptions were essential in the investigation. To validate two such assumptions: the effect of gyroscopic moments and the rotor flexibility were investigated using a linear analysis in Chapter 2 and Chapter 3 respectively.

A review of previous work by Holmes [3] was done to evaluate the dynamic performance of three types of bearing supports in a turbocharger. A rigid support, an external damper support and a flexible support were analysed to investigate the influence of plain journal bearing, floating ring journal bearing and a press-fit bearing respectively. A simple method was implemented to analyse the effect of gyroscopic moments on the conical whirl instability of a turbocharger with symmetric rotor and rigidly supported bearings. Bearings with 360^0 oil-film (a full oil-film) were used. A gyroscopic coefficient was introduced as the ratio of the polar moment of inertia to the transverse moment of inertia of the rotor. A threshold value for the gyroscopic coefficient of $1/2$ was calculated for the stability of the conical whirl. It was found that, any rotor with a gyroscopic coefficient above $1/2$, the conical whirl instability was suppressed for any speed. This value was also verified for floating ring bearings by using an external damper to support the bearings. Since the turbocharger has a heavier turbine wheel compared to the compressor wheel, an asymmetric rotor was analysed with floating ring bearings. It was shown that the threshold value of the gyroscopic coefficient remained unaffected by the external damper and the asymmetry of the rotor, As the gyroscopic effect is governed by the tilt motion it affects only the conical whirl.

Hence it was neglected for the nonlinear analysis of the in-phase whirl. However, the assumption of a rigid rotor used in Chapter 2, needed investigating before proceeding to the nonlinear analysis. Hence, the rotor flexibility effect was analysed in Chapter 3. The flexible deflection of the rotor determined under static conditions was superimposed onto the rigid dynamic equations of motion of the rotor. This was done by calculating the influence coefficients of the rotor using a simple finite element model of one-dimensional beams. It was shown that the rotor started bending after a speed of about 100,000 rpm. Hence, the assumption of a rigid rotor seemed to be reasonable

Hitherto, due to the light-weight of the turbocharger rotor, the static displacement compared to the dynamic displacement neglected. However, to help understand the nonlinear behaviour of the turbocharger with a perfectly balanced rotor, it was necessary to investigate a more general rotor-bearing system. Hence, in Chapter 4, the effect of static load was considered to determine the dynamic characteristics of the rotor-bearing system in the parameter plane of steady-state eccentricity ratio and rotor speed. The linearised system of equations was analysed to determine the stability threshold separating the stable and the unstable equilibrium states of the journal centre, in the parameter plane. An analysis of the case when the eccentricity ratio tends to zero was presented to investigate the role of the fluid-film forces in relation to the static load. The static load was found to counteract the radial restoring force, in the higher eccentricity region, leading to a stable system above an eccentricity ratio of 0.76. In Chapter 5, the onset of oil-whirl at the stability threshold, where the rotor behaviour destabilises, was found to be the *Hopf bifurcation.* In order to perform the nonlinear analysis, the system was analytically reduced to a simple system of equations by applying the Centre Manifold reduction and normal form theory. From the normal form, *first Lyapunov coefficients* were calculated to determine the appearance and the disappearance of the limit cycle close to the stability threshold. The appearance of a stable limit cycle (**SLC**) was super-critical bifurcation and the disappearance of an unstable limit cycle (**ULC**) was sub-critical bifurcation. The same was verified using Poore’s bifurcation algebra. Apart from the equilibrium states (steady-states) obtained from the linear analysis, the rotor system was found to have these limit cycles as a nonlinear characteristic of the system, attributed to the oil-film in the bearings. The parameter plane was shown to have two regions: **Region I** with sub-critical bifurcation and **Region II** with super-critical bifurcation as shown in Figure 5.5. For the rotor-bearing system with a rigid symmetric perfectly balanced rotor mounted in two identical journal bearings with oscillating π-film cavitation, the boundary between **Region I** and **Region II** in terms of the steady-state eccentricity ratio was determined to be 0.32. It was shown that in **Region I**, there existed an unstable limit cycle along with the stable equilibrium (**SE**) state below the stability threshold, and the unstable equilibrium (**UE**) state above the stability threshold. In **Region II** there existed a **SLC** along with the **UE** state above the stability threshold and the **SE** state below the stability threshold. These steady-states were demonstrated using the numerical analysis, where, in **Region I** below the threshold speed, the journal centre spirals inwards to the **SE** state, for any initial perturbation within the **ULC** and spirals outwards for any perturbation to a state outside of the **ULC** as shown in Figure 5.8. Above the threshold speed, the journal centre always spiralled outwards to reach **UE**, which was close to the housing as shown in Figure 5.9. In **Region II** the journal reached a **SLC** above the threshold speed, irrespective of the initial perturbation as shown in Figure 5.10. However, below the threshold speed, the journal always spiralled into the **SE** state as shown in Figure 5.11. Approximate sizes of the limit cycles corresponding to the eccentricity ratios were calculated. Based on the operating curve determined by the non-dimensional group σ_m, which depended on the bearing parameters such as geometry, oil viscosity and the clearance, the turbocharger was shown to operate in **Region I** for most of the speed and with very small **ULC**.

Having characterised the nonlinear steady-state behaviour of the general rotor-bearing system, the focus was back on the turbocharger in Chapter 6 to investigate the unbalance test data shown in Chapter 1. Choosing an operating curve of $\sigma_m = 500$ for the turbocharger, the waterfall plots similar to the test plots from *Cummins Turbo-Technologies*, were simulated using numerical integration of the equations of motion by the Runge-Kutta method. These plots showed a reduction in the sub-synchronous whirl amplitude in the transient state, where the unbalance had a positive effect as shown in Figures 6.7 to 6.10. Beyond a certain optimum value, unbalance had a negative effect by increasing the amplitude. A plot of the maximum amplitude as a function of speed, demonstrated a dip at some speed for each unbalance value, corresponding to a dip in the respective phase plot as shown in Figure 6.11 and Figure 6.12. This suggested the dependence of the amplitude on the phase of the response. The equations of motion were averaged to simplifying the analysis. The averaged equations clearly showed the coupling of the amplitude and the phase equations through the relationship between the excitation and the response phase angles. As a result, the numerical analysis showed the reduction in the growth rate of the response in the transient motion, while the steady-state response did not have any significant change due to the unbalance. However, the threshold speed reduced due to the effect of unbalance in the turbocharger as shown in Figure 6.3. Since a constant unbalance force was found to be insignificant in the steady-state compared to the higher hydrodynamic bearing forces that increase with time, the effect of the unbalance seemed to be significant at the start of whirling. A simple numerical analysis was performed to analyse the behaviour of the journal motion during the first few cycles of motion, in terms of the response characteristics. This was carried out at a constant speed and σ_m was chosen to be 50, to allow the orbit to grow, quickly facilitating a lower run time and consequent length of data. The synchronous and the sub-synchronous response vectors together formed an internal loop in the orbit. The size of this internal loop grew in size with the increase in the unbalance level. As the inner loop size approached that of the outer loop, the unbalance started showing a negative effect. The response of the unbalanced rotor suffered a phase lag behind that of the balanced rotor, when the unbalance level was below the optimum value. Beyond that, the response phase was ahead of the balanced rotor. This characteristic behaviour aided in slowing the growth rate of the whirl amplitude. The amount of unbalance that introduced a phase difference between the excitation phase (τ) and the response phase (ϕ) greater than $\tau/2$, i.e. $\tau - \phi > \tau/2$, was found to reduce the response in the transient motion. The corresponding rate of change of the phase angle was less than 0.5 rad/sec. Thus, the effect of unbalance up to a certain level was found to be advantageous in the transient journal motion. The major conclusions from the thesis are listed in the next section.

7.3 MAJOR CONCLUSIONS FROM THE THESIS

This section lists the major conclusions drawn from the research work carried out in this thesis:

- The conical whirl instability of the turbocharger with a symmetric rotor in rigidly supported full-film bearings is controlled by the *gyroscopic coefficient* β; This coefficient is given by the ratio of the polar to the transverse moment of inertia of the rotor.

- The threshold value of β for a stable conical whirl is found to be $1/2$. The conical whirl instability is completely suppressed for $\beta > 1/2$. The threshold ratio does not seem to be affected by adding an external damper to the bearing and by the asymmetry of the rotor.

- The conical mode is dominant in the low speed range, while the in-phase whirl mode is dominant in the high speed range. The gyroscopic moment seems to reduce the rotor speed at which the switch in the dominant mode occurs.

- The analysis of rotor flexibility effect suggests that, the assumption of a rigid rotor is reasonable up to a speed of 100,000 rpm, for the turbocharger under investigation.

- In the system of a perfectly balanced rotor mounted in short-bearings with oscillating π-film cavitation, the onset of oil-whirl is related to the *Hopf bifurcation*.

- The dynamic behaviour of the journal bifurcates by experiencing a change in the stability at the threshold speed that separates the stable and the unstable equilibrium states of the journal centre and is characterized also by the disappearance or appearance of a limit cycle.

- The rotor system under investigation exhibits sub-critical bifurcation (disappearance of an unstable limit cycle) if the journal centre eccentricity is within about 32% of the bearing clearance from the bearing centre, under the effect of the static load as shown in Figure 5.12; the system exhibits super-critical bifurcation (appearance of a stable limit cycle) if the journal centre eccentricity is between about 33% and 76% of the clearance.

- If the journal centre eccentricity is above about 76% of the clearance, the system under investigation is completely stable since oil-whirl is completely suppressed. This behaviour seems to be governed by the balancing of the static load by the increased radial restoring force attributed to the air cavity in the bearing.

- The amplitude of the limit cycle can be calculated from the bifurcation parameter ν, the rate of change of the real part of the eigenvalue with speed α', and the real part of c_1; the critical eigenvector gives the approximate shape of the limit cycle as shown in Figure 5.6.

- Automotive turbochargers, due to their light weight, operate in **Region I** of the parameter plane of rotor speed and eccentricity ratio with high σ_m. Hence for the turbocharger rotor, its journal centre traces an orbit that keeps growing in size unless limited by other nonlinearity in the system.

- Due to the very small size of the **ULC**, even below the threshold speed, the journal effectively spirals outward far away from the **SE** state. Above the threshold speed the journal spirals outwards close to the bearing, unless restricted by some other nonlinearity.

- The presence of a static load seems to be an option to keep the turbocharger operating in the higher eccentricity range, thereby allowing the existence of a **SLC**, above the threshold speed.

- Unbalance seems to slow down the growth of the whirl amplitude in the transient motion, by introducing a phase lag in the unbalance response relative to that of the self-excited response of the balanced rotor.

- The advantageous effect of unbalance prevails only up to a certain level (optimum value). Above that value, rotor unbalance seems to have a negative effect by increasing the growth rate of the amplitude.

- This behaviour is likely to be governed by the coupled nature of the amplitude and the phase of the journal response in a turbocharger with an unbalanced rotor. Depending on the speed range of interest, the optimum level of unbalance varies.

- The effect of unbalance appears to be beneficial during the transient motion, for instance, during the acceleration and the deceleration of the engine. Depending on the time allowed at each speed, the effect of unbalance could be different.

- For practical reasons, it is almost impossible to have a perfectly balanced rotor. Hence, allowing some unbalance within the optimum level, for controlling the sub-synchronous vibrations seem to be a cost-effective solution worth considering into the rotor dynamic design of a turbocharger.

1.4 SUGGESTIONS FOR FUTURE WORK

The effect of unbalance in the transient journal motion of the automotive turbocharger leaves the following question:
When the speed rate is varied for the same unbalance, will the shift in the response characteristics from the in-phase whirl frequency to the synchronous frequency occur over a different speed range, when all the other run conditions are maintained?

To answer this question, it is recommended that experimental verification is conducted of the variation in the speed range in which the unbalance is effective. The rate at which the speed is changed needs to be varied significantly and the resulting waterfall plots may be compared to determine the sensitivity of unbalance to the speed change.

The investigation with unbalance may be extended with damped supports with an external damper in series to the bearing to simulate the floating ring bearings and with a flexible support for the press-fit bearings.

In terms of the bearing support, based on the observations made in Chapter 2, a nonlinear investigation of the flexible support with variable stiffness and unbalanced rotor could be interesting in a turbocharger.

APPENDIX A OIL-FILM FORCES

A.1 SHORT-BEARING APPROXIMATION

In this Appendix, the derivation of the oil-film forces from the Reynolds equation [25] using the short-bearing approximation is presented. In this thesis, a full-film bearing model is used in Chapters 2 and 3 and an oscillating π-film cavitation model is used in Chapters 4, 5 and 6. Hence, in this Appendix, the forces are derived for two types of film extents: full-film and oscillating π-film. Since oil-whirl is a vibration problem characterised by frequency and amplitude, the stiffness and damping coefficients are derived from the Reynolds equation that governs the pressure distribution in a thin film, for constant viscosity [20]. The Reynolds equation for a dynamically loaded journal for a constant viscosity oil-film in polar co-ordinates is of the following form:

$$\underbrace{\frac{1}{R}\frac{\partial}{\partial\theta}\left(\frac{h^3}{R}\frac{\partial P}{\partial\theta}\right)}_{\substack{\text{Pressure term}\\ \text{(gradient in the}\\ \text{circumferential}\\ \text{direction } \theta)}} + \underbrace{\frac{\partial}{\partial\theta}\left(h^3\frac{\partial P}{\partial Z}\right)}_{\substack{\text{Pressure term}\\ \text{(gradient in}\\ \text{the axial direction Z)}}} = \underbrace{6\eta_B(\omega-2\dot{\phi})\left(\frac{\partial h}{\partial\theta}\right)}_{\substack{\text{Wedge term}\\ \text{(results from the}\\ \text{relative tangential velocity)}}} + \underbrace{12\eta_B C\frac{dn}{dt}\cos\theta}_{\substack{\text{Squeeze term}\\ \text{(results from the}\\ \text{relative radial velocity)}}} \quad , \tag{A.1}$$

where θ is the circumferential (angular) position on the bearing; R_b is the radius of the journal bearing; Z is the axial coordinate along the length of the bearing; P is the pressure in the lubricant at the point (θ , Z); η_b is the lubricant viscosity; ω is the journal angular velocity (speed); C is the clearance; n is the eccentricity ratio and ϕ is the attitude angle. Since Reynolds equation is insoluble in the closed form and is two dimensional, it is often reduced to a one dimensional problem by using the short-bearing approximation [18] or the long bearing assumption [26]. Then they are applied for a very short-bearing and very long bearing respectively based on their length to diameter ratio l_b/D. As the floating ring bearings in turbochargers have a very low l_b/D ratio, the short-bearing approximation should be applicable. According to the short-bearing approximation [18], for very short journal bearings, pressure gradients in the circumferential direction are much smaller than those in the axial direction, so that the first term on the left-hand side of Eq. (A.1) is negligible and the Reynolds equation simplifies into [18]:

$$\frac{\partial}{\partial \theta}\left(h^3 \frac{\partial P}{\partial Z} \right) = 6\eta_B(\omega - 2\dot{\phi})\left(\frac{\partial h}{\partial \theta} \right) + 12\eta_B C \frac{dn}{dt}\cos\theta \,. \tag{A.2}$$

The solution which follows will therefore include that part of the circumferential flow proportional to the journal surface velocity and varying film thickness but will neglect the effect of the circumferential pressure gradient on this flow. Any change in the circumferential flow will directly influence the axial flow and the axial pressure gradient. In addition, the relationship between the oil-film thickness h and the angular position θ is given by:

$$h = C(1 + n\cos\theta)\,, \tag{A.3}$$

where, C is the radial clearance of the bearing and n is the eccentricity ratio (n/C - ratio of eccentricity to clearance). In the standard short-bearing approximation [18], it is assumed that the lubricant is Newtonian, so that the viscosity is constant. Integrating Eq. (A.2) twice with respect to Z and applying the boundary conditions, pressure $P = 0$ at $Z = 0$ and at $Z = L_B$ is given by:

$$P = Z(Z - l)\frac{12\eta_B C\dot{n}\cos\theta - 6\eta_B(\omega - 2\dot{\phi})Cn\sin\theta}{2C^3(1 + n\cos\theta)^3}\,. \tag{A.4}$$

Figure A1 shows the co-ordinate system of a journal bearing with the oil-film forces. Resolving in directions 1, 2, the oil-film forces F_1 and F_2 become:

$$F_1 = R_B \int_0^{L_B} \int_{\theta_1}^{\theta_2} P \cos\theta d\theta dZ\,, \tag{A.5}$$

$$F_2 = R_B \int_0^{L_B} \int_{\theta_1}^{\theta_2} P \sin\theta d\theta dZ\,, \tag{A.6}$$

where, θ_1 and θ_2 mark the boundaries of the oil-film and are usually determined by the external supply pressure and are important in the determination of the oil-whirl onset characteristics. If the film is full without any cavitation due to rupture, then $\theta_1 = 0$ and $\theta_2 = 2\pi$. Holmes [20] derived the forces using this boundary condition. This assumption is used in Chapter 2 and Chapter 3 in this thesis for the linear analysis. When the oil pressure drops below the atmospheric pressure, the film ruptures leading to cavitation in the bearing. If $\theta_1 = 0$ and $\theta_2 = \pi$, it is an oscillating π-film model. This is based on the assumption of half-film (180° extent) that rotates with the rotor [23]. This model is used in Chapters 4 and 5 for the nonlinear analysis. The following Sub-Sections of this Appendix present the derivation of film forces for the full-film and the oscillating π-film bearing models.

A.1.1 OIL-FILM FORCES IN FULL-FILM BEARINGS

This Sub-Section presents the derivation of the oil-film forces in bearings with full oil-film. As the oil-film rotates after the whirl initiation, the operating parameters at the incipient whirl frequencies will be different from that of the fully developed whirl frequencies. However, if there is 360° film, θ_1 and θ_2 are 0 and 2π i.e. no cavitation, then the operating parameters remain valid for all the whirl frequencies and the whirl frequencies are modified by the system nonlinearities only [20]. This condition is achieved by adequate supply pressure. In a turbocharger, due to its light weight, the dynamic load is much greater than the gravity load on the bearings. So, it can be assumed that the oil-film remains unruptured and is of full 360° extent. Integrating Eqs. (A.5) and (A.6), forces F_1 and F_2 become:

$$F_1 = -\frac{R_B L_B^3}{C^3} \mu_B C \dot{n} \frac{\pi(1+2n^2)}{(1-n^2)^{\frac{5}{2}}}, \tag{A.7}$$

$$F_2 = -\frac{R_B L_B^3 \eta_B \pi C n(\omega - 2\dot{\phi})}{2C^3(1-n^2)^{\frac{3}{2}}}. \tag{A.8}$$

Under the steady-state condition, the journal centre moves to $\mathrm{C_{JS}}$ i.e., when $n = n_0$, $\phi = \phi_0$, $\dot{n} = 0$, $\dot{\phi} = 0$, the fluid forces become:

$$F_1 = 0, \tag{A.9}$$

$$F_2 = \frac{R_B L_B^3 \eta_B \pi C n_0 \omega}{2C^3(1-n_0{}^2)^{\frac{3}{2}}}. \tag{A.10}$$

From (A.10), it is clear that under the static loading, $F_2 = F$ and $\phi_0 = \frac{\pi}{2}$. Thus, the fluid-film forces F_1 and F_2, in terms of the static eccentricity ratio n_0 and the static load F become,

$$F_1 = \frac{-2F(1-n_0{}^2)^{\frac{3}{2}}(1+2n^2)\dot{n}}{\omega n_0 (1-n^2)^{\frac{5}{2}}}, \tag{A.11}$$

$$F_2 = \frac{F(\omega - 2\dot{\phi})(1-n_0{}^2)^{\frac{3}{2}} n}{\omega n_0 (1-n^2)^{\frac{3}{2}}}. \tag{A.12}$$

Considering a small oscillation of the journal with its centre to be $\mathrm{C_{JD}}$, and $\mathrm{C_{JS}}$ being the corresponding steady-state under the action of the static load F as shown in Figure A2, the components of F_1 and F_2 along r and s axes are given by:

$$F_r = F_1 \cos\alpha_0 - F_2 \sin\alpha_0 \,, \tag{A.13}$$

$$F_s = F_1 \sin\alpha_0 + F_2 \cos\alpha_0 \,, \tag{A.14}$$

where $\sin\alpha_0 = \dfrac{s}{Cn}$ and $\cos\alpha_0 = \dfrac{Cn_0 + r}{Cn}$. Using the trigonometric identities, the rate of change of the attitude angle is given by:

$$\dot{\phi} = \frac{\dot{s}\left(Cn_0 + r\right) - \dot{r}s}{\left(Cn\right)^2} \,. \tag{A.15}$$

Thus F_r and F_s are nonlinear functions of r and s. For very small oscillations, when $\alpha_0 \approx 0$; $\cos\alpha_0 \approx 1$, Eqs.(A.13) and (A.14) can be written as:

$$F_r = F_1 - F_2 \frac{s}{Cn} \,, \tag{A.16}$$

$$F_s = F_1 \frac{s}{Cn} + F_2 \,. \tag{A.17}$$

After linearising [20], the radial and the tangential forces on the journal are defined as:

$$F_r = -b_{rr}\dot{r} - a_{rs}s \,, \tag{A.18}$$

$$F_s = a_{sr}r - b_{ss}\dot{s} + \frac{\omega \pi n_0 \eta_B l^3 R_B}{2(1 - n_0{}^2)^{\frac{3}{2}} C^2} \,, \tag{A.19}$$

where the stiffness coefficients a_{rs} and a_{sr} are given by:

$$a_{rs} = \frac{\eta_B L_B^3 R_B \pi\omega}{2C^3(1-n_0^2)^{\frac{3}{2}}} = \frac{F}{Cn_0}, \tag{A.20}$$

$$a_{sr} = \frac{R_B L_B^3 \eta_B \pi\omega(1+2n_0^2)}{2C^3(1-n_0^2)^{\frac{5}{2}}} = \frac{F(1+2n_0^2)}{Cn_0(1-n_0^2)}, \tag{A.21}$$

and the damping coefficients, b_{rr} and b_{ss} are given by :

$$b_{rr} = \frac{2}{\omega}a_{sr}, \quad b_{ss} = \frac{2}{\omega}a_{rs}. \tag{A.22}$$

Since in the steady-state, $F_r = 0$, $F_t = F$. There are only 4 coefficients, direct damping coefficients, b_{rr}, b_{ss} and cross-coupled stiffness coefficients, a_{rs}, a_{sr} for a full-film whilst for a π-film, they would raise to 8 including the direct stiffness and cross-coupled damping terms [88]. The following Section shows the derivation of forces for a π-film.

A.1.2 OIL-FILM FORCES IN BEARINGS WITH OSCILLATING π-FILM CAVITATION

This Sub-Section presents the derivation of the oil-film forces in bearings with an oscillating π-film. By integrating Eqs. (A.5) and (A.6) for the boundary conditions $\theta_1 = 0,\ \theta_2 = \pi$, the film forces in the bearing with an oscillating π-film are given by [23]:

$$F_r = -S_m\left\{-\frac{1}{2}n(1-2\dot{\phi})I_1 + \dot{n}I_2\right\}, \tag{A.23}$$

$$F_s = S_m\left\{\frac{1}{2}n(1-2\dot{\phi})I_3 - \dot{n}I_1\right\}, \tag{A.24}$$

where:

$$S_m = \left(\frac{L_B}{R_B}\right)^2 S = \frac{L_B^3 R_B \omega \eta_B}{FC^2}, \tag{A.25}$$

where S_m is the modified Sommerfeld number for the short-bearing approximation. and S is the Sommerfeld number for the long bearing approximation. $I_1 = \int_0^{\pi} \frac{\cos^2\theta}{(1+n\cos\theta)^3}d\theta$, $I_2 = \int_0^{\pi} \frac{\cos\theta\sin\theta}{(1+n\cos\theta)^3}d\theta$, $I_3 = \int_{\theta_1}^{\pi+\theta_1} \frac{\sin^2\theta}{(1+n\cos\theta)^3}d\theta$ are the integrals. Using Sommerfeld substitution [88], let

$$1+n\cos\theta = \frac{1-n^2}{1-n\cos\psi}, \tag{A.26}$$

$$\cos\theta = \frac{(\cos\psi - n)}{(1-n\cos\psi)};\ \sin\theta = \frac{\sqrt{(1-n^2)}\sin\psi}{(1-n\cos\psi)};\ d\theta = \frac{\sqrt{1-n^2}}{(1-n\cos\psi)}d\psi, \tag{A.27}$$

$$I_1 = \frac{1}{(1-n^2)^{5/2}}\left[\frac{1}{2}(\pi) + n^2\pi\right], \tag{A.28}$$

$$I_2 = -\frac{2n}{(1-n^2)^2}, \tag{A.29}$$

$$I_3 = \frac{\pi}{2(1-n^2)^{\frac{3}{2}}}. \tag{A.30}$$

Using Eqs. (A.28),(A.29) and, (A.30), the non-dimensional force components in Eqs. (A.23) and (A.24) are given by:

$$F_r = -S_m \left\{ \left(\frac{n^2(1-2\dot{\phi})}{\left(1-n^2\right)^2} + \frac{\pi \dot{n}\left(1+2n^2\right)}{2\left(1-n^2\right)^{5/2}} \right) \right\}, \tag{A.31}$$

$$F_s = S_m \left\{ \left(\frac{\pi n(1-2\dot{\phi})}{4\left(1-n^2\right)^{\frac{3}{2}}} + \frac{2n\dot{n}}{\left(1-n^2\right)^2} \right) \right\}, \tag{A.32}$$

$$S_m = \left(\frac{L_B}{R_B} \right)^2 S = \frac{L_B^3 R_B \omega \eta_B}{FC^2} = \frac{4(1-{n_s}^2)^2}{n_s \left\{ \pi^2 \left(1-{n_s}^2\right) + 16{n_s}^2 \right\}^{\frac{1}{2}}}, \tag{A.33}$$

where n_s is the steady-state eccentricity ratio.

FIGURES

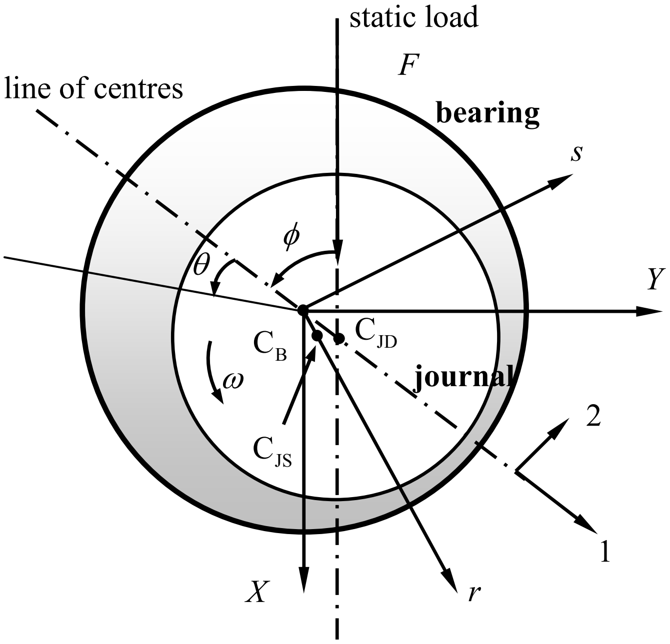

Figure A1 Co-ordinate system of a journal bearing; C_B is the bearing centre; C_{JS} is the static journal centre due to a static load; C_{JD} is the dynamic journal centre; ω is the spin speed; ϕ is the attitude angle of the journal centre with respect to X axis. θ is the angular co-ordinate in the bearing with reference to the line of centres. [20]

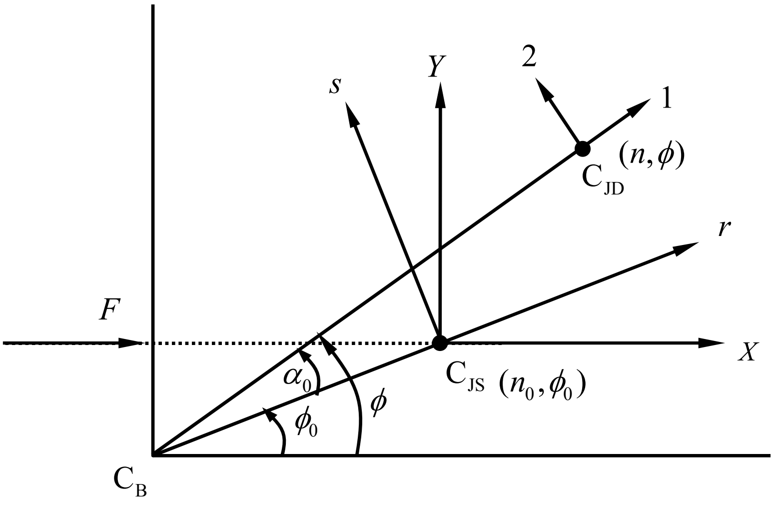

Figure A2 Oil-film forces shown in Figure A2 with reference to the bearing centre C_B in a journal bearing; C_{JS} is the static journal centre; C_{JD} is the dynamic journal centre; C is the radial clearance in the bearing; n is the eccentricity ratio. n_0, ϕ_0 are the eccentricity ratio and attitude angle (phase) corresponding to the static journal centre.

APPENDIX B FINITE ELEMENT MODEL

B.1 ONE-DIMENSIONAL BEAM MODEL

In Chapter 3, the flexibility of the rotor is included in the mathematical model in terms of the influence coefficients. These coefficients are determined by using a simple finite element beam model. This Appendix details the modelling of a one-dimensional beam model with two degrees of freedom at each node and its assemblage for a multi-degree of freedom system.

Figure B1 shows a one-dimensional beam with one translation and one rotation at each node according to Euler-Bernoulli theory [69, 89]. This is a simplification of the linear theory of elasticity which provides a means of calculating the load-carrying and deflection characteristics of beams. It covers the case for small deflections of a beam which is subjected to lateral loads only. Using cubic displacement function for the element [69], the stiffness matrix of a beam is given by [69]:

$$\mathbf{K} = \frac{EI}{L^3}\begin{bmatrix} 12 & 6L & -12 & 6L \\ 6L & 4L^2 & -6L & 2L^2 \\ -12 & -6L & 12 & -6L \\ 6L & 2L^2 & -6L & 4L^2 \end{bmatrix}, \tag{B.1}$$

where $\mathbf{K}$ is the stiffness matrix of the element, E is the Young's modulus of the material, I is the transverse moment of inertia of the beam and L is the length of the beam. Under static conditions, the lateral and angular deflections are given by:

$$\begin{Bmatrix} \hat{F} \\ \hat{M} \end{Bmatrix} = \mathbf{K} \begin{Bmatrix} \hat{d} \\ \hat{\phi} \end{Bmatrix}, \tag{B.2}$$

where $\hat{F}$ and $\hat{M}$ are the force and the moment, $\hat{d}$ and $\hat{\phi}$ are the lateral and angular displacements respectively. Substituting for $\mathbf{K}$ from Eqs. (A.1) and (B.2) becomes:

$$\begin{Bmatrix} \hat{F}_1 \\ \hat{M}_1 \\ \hat{F}_2 \\ \hat{M}_2 \end{Bmatrix} = \frac{EI}{L^3} \begin{bmatrix} 12 & 6L & -12 & 6L \\ 6L & 4L^2 & -6L & 2L^2 \\ -12 & -6L & 12 & -6L \\ 6L & 2L^2 & -6L & 4L^2 \end{bmatrix} \begin{Bmatrix} \hat{d}_1 \\ \hat{\phi}_1 \\ \hat{d}_2 \\ \hat{\phi}_2 \end{Bmatrix}, \tag{B.3}$$

where $(.)_{1,2}$ denote the node numbers. Since the rotor is represented by an assembly of beams connected at the nodes, the stiffness matrices of the beams are assembled to get the global stiffness matrix. Figure B2 shows a simple assemblage of two beams. The corresponding two stiffness matrices are assembled as follows [69]:

$$\begin{Bmatrix} \hat{F}_1 \\ \hat{M}_1 \\ \hat{F}_2 \\ \hat{M}_2 \\ \hat{F}_3 \\ \hat{M}_3 \end{Bmatrix} = \frac{EI}{L^3} \begin{bmatrix} 12 & 6L & -12 & 6L & 0 & 0 \\ 6L & 4L^2 & -6L & 2L^2 & 0 & 0 \\ -12 & -6L & 12+12 & -6L+6L & -12 & 6L \\ 6L & 2L^2 & -6L+6L & 4L^2+4L^2 & -6L & 2L^2 \\ 0 & 0 & -12 & -6L & 12 & -6L \\ 0 & 0 & 6L & 2L^2 & -6L & 4L^2 \end{bmatrix} \begin{Bmatrix} \hat{d}_1 \\ \hat{\phi}_1 \\ \hat{d}_2 \\ \hat{\phi}_2 \\ \hat{d}_3 \\ \hat{\phi}_3 \end{Bmatrix}. \tag{B.4}$$

Figure B3(a) shows the schematic of the finite element model of a turbocharger. The rotor is pinned at the bearings locations by arresting the lateral displacements of nodes 2 and 3, allowing only rotation at these nodes. It is shown in Chapter 2, how the influence coefficients are determined from the finite element model. The natural bending frequency of the rotor can be determined by adding a mass matrix, which is given in the following Section.

B.2 NATURAL FREQUENCY

Figure B3(b) shows the finite element model of the turbocharger with lumped masses at the nodes 1 and 6. The equation of motion of a finite element beam under no external forces according to Newton's second law of motion is given by:

$$\mathbf{M}\underline{\mathbf{x}} + \mathbf{K}\underline{\mathbf{x}} = 0\,, \tag{B.5}$$

where $\mathbf{M}$ is the mass matrix and $\underline{\mathbf{x}}$ is the displacement vector. The mass matrix of the beam element with a translation and a rotation shown in Figure B1 is given by [69]:

$$\mathbf{M} = \frac{\rho AL}{420}\begin{bmatrix} 156 & 22L & 54 & -13L \\ 22L & 4L^2 & 13L & -3L^2 \\ 54 & 13L & 156 & -22L \\ -13L & -3L^2 & -22L & 4L^2 \end{bmatrix}, \tag{B.6}$$

where L is the beam length. Similar to the method in Eq. (B.4), mass matrices are also assembled as:

$$\mathbf{M_1} + \mathbf{M_2} = \frac{\rho AL}{420}\begin{bmatrix} 156 & 22L & 54 & -13L & 0 & 0 \\ 22L & 4L^2 & 13L & -3L^2 & 0 & 0 \\ 54 & 13L & 156+156 & -22L+22L & 54 & -13L \\ -13L & -3L^2 & -22L+22L & 4L^2+4L^2 & 13L & -3L^2 \\ 0 & 0 & 54 & 13L & 156 & -22L \\ 0 & 0 & -13L & -3L^2 & -22L & 4L^2 \end{bmatrix}, \tag{B.7}$$

where $\mathbf{M_1}$, $\mathbf{M_2}$ are the mass matrices of the elements e_1, e_2 respectively. The compressor and the turbine masses are lumped at node 1 and node 6 by adding them to the corresponding diagonal element. Inertia effect associated with the rotational degrees of freedom is assumed to be zero. Now assuming time-harmonic motion, and assuming a solution of the form $\underline{x} = \underline{X}e^{j\omega_n t}$ to Eq. (B.5) and re-arranging gives:

$$\left[\mathbf{K} - \omega_n{}^2\mathbf{M}\right]\underline{\mathbf{x}} = 0\,, \tag{B.8}$$

where ω_n is the natural frequency of the system and $\underline{X}$ is the amplitude. The eigenvalues of the determinant $\left[\mathbf{K}-\omega_n{}^2\mathbf{M}\right]$ and the corresponding eigenvectors for the pin-pin condition are calculated in MATLAB using steel properties i.e., $E = 2e11$ N/m^2 and $\rho = 7850$ Kg/m^3. The pin-pin constraints are applied by arresting the translation for nodes 3 and 4, while the rotations are allowed. These degrees of freedom are removed by deleting the corresponding rows and columns from the stiffness and mass matrices.

FIGURES

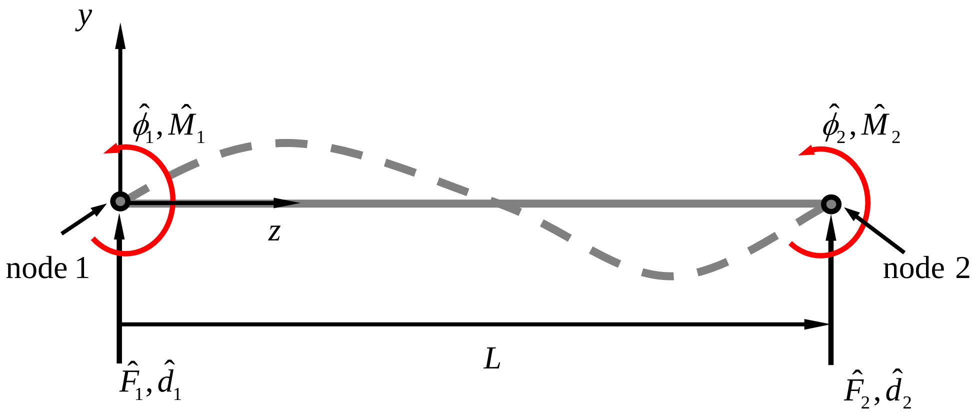

Figure B1 One-dimensional uniform beam element of length L with one translation $\hat{d}_i$ and one rotation $\hat{\phi}_i$ at each node i; $\hat{F}_i$ and $\hat{M}_i$ are the forces and moments at these nodes where $i = 1, 2$ are the node numbers. The cubic displacement function [69] is shown in dotted line.

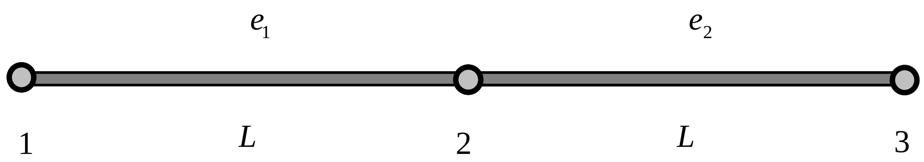

Figure B2 Two beam elements of equal length L, connected at node 2. e_1, e_2 are the element numbers.

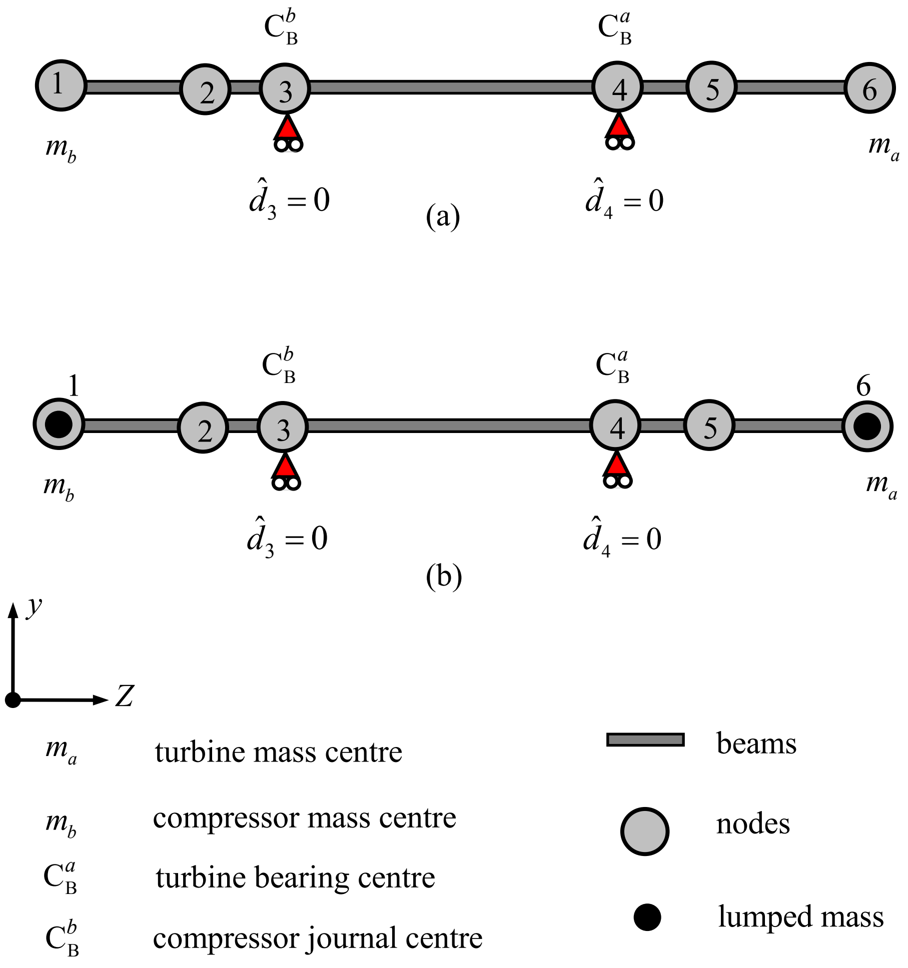

Figure B3 (a) Schematic of the finite element model with flexible mass-less beams representing the turbocharger rotor to determine the influence coefficients. Nodes 3 and 4 are fixed along y ; $\hat{d}_i$=0 , where i is the node number and allowed to rotate. (b) Schematic of the finite element model for calculating the eigenvalues; the compressor and turbine masses are lumped at node 1 and 6 respectively.

APPENDIX C EIGENVECTOR AND AD-JOINT EIGENVECTOR

In Chapter 4, the determination of the *first Lyapunov coefficients* and the application of *Poore's bifurcation algebra* required the calculation of the eigenvectors of the Jacobian determinant $\mathbf{A}$. In this Appendix, details are given about the calculation of the eigenvectors, following the procedure given by Myers [21]. The eigenvector $\mathbf{q}$ of Jacobian $\mathbf{A}$ corresponding to the eigenvalue $\hat{s} = i\Omega_0$ is given by:

$$\left|\mathbf{A} - i\Omega_0\mathbf{I}\right|\mathbf{q} = 0, \tag{C.1}$$

where $\mathbf{q} = \{q_1, q_2, q_3, q_4\}^T$ matrix and $\mathbf{I}$ is eigenvector. Eq. (C.1) gives three equations as below, while the fourth one is redundant:

$$-\hat{s}q_1 + q_2 = 0, \tag{C.2}$$

$$\left(-\frac{k_{xx}}{\overline{\omega}^2}\right)q_1 + \left(-\frac{b_{xx}}{\overline{\omega}^2} - \hat{s}\right)q_2 + \left(-\frac{k_{xy}}{\overline{\omega}^2}\right)q_3 + \left(-\frac{b_{xy}}{\overline{\omega}^2}\right)q_4 = 0, \tag{C.3}$$

$$-\hat{s}q_3 + q_4 = 0. \tag{C.4}$$

Assuming $q_1 = q_{1i} + iq_{1r}$, for the eigenvalue $\hat{s} = i\Omega_0$, the elements of eigenvector are given as follows:

$$q_2 = i\Omega_0 q_1, \tag{C.5}$$

$$q_3 = q_1 \frac{\left[\varpi^2 {\Omega_0}^2 - i\Omega_0 b_{xx} - k_{xx}\right]}{\left[k_{xy} + i\Omega_0 b_{xy}\right]} \equiv q_1 \mathrm{T}_1, \tag{C.6}$$

$$q_4 = i\Omega_0 q_3 = \left[i\Omega_0 q_1 \frac{\left[\varpi^2 {\Omega_0}^2 - i\Omega_0 b_{xx} - k_{xx}\right]}{\left[k_{xy} + i\Omega_0 b_{xy}\right]} \right] \equiv i\Omega_0 q_1 \mathrm{T}_1 . \tag{C.7}$$

Similarly, the ad-joint vector $\mathbf{p}$ from the transpose of the Jacobian matrix is given by:

$$\left| \mathbf{A}^T + i\Omega_0 \mathbf{I} \right| \mathbf{p} = 0 , \tag{C.8}$$

where $\mathbf{p} = \{p_1, p_2, p_3, p_4\}^T$. Determinant in Eq. (C.8) is given by:

$$\begin{vmatrix} i\Omega_0 & -\frac{k_{xx}}{\varpi^2} & 0 & -\frac{k_{yx}}{\varpi^2} \\ 1 & -\frac{b_{xx}}{\varpi^2} + i\Omega_0 & 0 & -\frac{b_{yx}}{\varpi^2} \\ 0 & -\frac{k_{xy}}{\varpi^2} & i\Omega_0 & -\frac{k_{yy}}{\varpi^2} \\ 0 & -\frac{b_{xy}}{\varpi^2} & 1 & -\frac{b_{yy}}{\varpi^2} + i\Omega_0 \end{vmatrix} \begin{Bmatrix} p_1 \\ p_2 \\ p_3 \\ p_4 \end{Bmatrix} = 0 , \tag{C.9}$$

which results in the following equations:

$$i\Omega_0 p_1 - \frac{k_{xx}}{\varpi^2} p_2 - \frac{k_{yx}}{\varpi^2} p_4 = 0 , \tag{C.10}$$

$$p_1 + \left(-\frac{b_{xx}}{\varpi^2} + i\Omega_0 \right) p_2 - \frac{b_{yx}}{\varpi^2} p_4 = 0 , \tag{C.11}$$

$$-\frac{k_{xy}}{\varpi^2} p_2 + i\Omega_0 p_3 - \frac{k_{yy}}{\varpi^2} p_4 = 0 . \tag{C.12}$$

Letting $p_4 = 1$, eliminating p_1 from the Eqs. (C.10) and (C.11) results in :

$$p_2 = \frac{i\Omega_0 b_{yx} - k_{yx}}{\left[k_{xx} - b_{xx} i\Omega_0 - \Omega_0{}^2 \bar{\omega}^2\right]}, \tag{C.13}$$

$$p_1 = \frac{b_{yx}}{\bar{\omega}^2} + \left(\frac{b_{xx}}{\bar{\omega}^2} - i\Omega_0\right) p_2, \tag{C.14}$$

$$p_3 = \frac{1}{i\Omega_0 \bar{\omega}^2}\left(k_{yy} + k_{xy} p_2\right), \tag{C.15}$$

where q_1 is determined from the normalisation requirement $\langle p, q \rangle = \sum_{j=1}^{4} \bar{p}_j q_j = 1$ which gives:

$$q_1 = \frac{1}{\left\{\bar{p}_1 + \bar{p}_2 i\Omega_0 + \bar{p}_3 \mathrm{T}_1 + i\Omega_0 \mathrm{T}_1\right\}}. \tag{C.16}$$

APPENDIX D THE METHOD OF AVERAGING

In Chapter 6, the method of averaging is applied to the equations of motion of the rotor-system with unbalance, for simplifying the analysis. In this Appendix, the theory behind the method of averaging is given in brief, based on the procedure given in [83] and [90].

The standard form of a perturbation problem for the application of averaging is given by [83]:

$$\dot{x} = \varepsilon\,\mathrm{f}(x,t;\varepsilon),\quad x \in \Re^{n}\,, \tag{D.1}$$

where, x is an n-dimensional real variable, t is the time and ε is a small parameter. Expanding Eq. (D.1) as a power series in ε gives,

$$\dot{x} = \varepsilon\left(\mathrm{f}_1(x,t) + \varepsilon\,\mathrm{f}_2(x,t) + ...\right). \tag{D.2}$$

Using a near identity transformation up to the quadratic term [90],

$$x = \xi + \varepsilon W_1(\xi,t) + \varepsilon^2 W_2(\xi,t)\,, \tag{D.3}$$

where, $W_{1,2}$ are called generating functions to be chosen so that, the transformed equations on ξ is as simple as possible. Substituting Eq. (D.3) into Eq. (D.2) gives,

$$\dot{x} = \varepsilon\,\mathrm{f}_1(\xi + \varepsilon W_1 + \varepsilon^2 W_2, t) + \varepsilon^2\,\mathrm{f}_2(\xi + \varepsilon W_1 + \varepsilon^2 W_2, t) + \dots. \tag{D.4}$$

Equation. (D.4) expands as [91]:

$$\dot{x}=\varepsilon\left(\mathrm{f}_1(\xi,t)+\varepsilon\frac{\partial\,\mathrm{f}_1}{\partial\xi}W_1+\varepsilon^2\frac{\partial\,\mathrm{f}_1}{\partial\xi}W_2\right)+\varepsilon^2\left(\mathrm{f}_2(\xi,t)+\varepsilon\frac{\partial\,\mathrm{f}_2}{\partial\xi}W_1+\varepsilon^2\frac{\partial\,\mathrm{f}_2}{\partial\xi}W_2\right)+\ldots, \tag{D.5}$$

which up to second order term in ε^2 is given by:

$$\dot{x}=\varepsilon\,\mathrm{f}_1(\xi,t)+\varepsilon^2\left[\frac{\partial\,\mathrm{f}_1}{\partial\xi}W_1+\mathrm{f}_2(\xi,t)\right]. \tag{D.6}$$

The first derivative of Eq. (D.3) is given by:

$$\dot{x}=\dot{\xi}+\varepsilon\left[\frac{\partial W_1}{\partial\xi}\dot{\xi}+\frac{\partial W_1}{\partial t}\right]+\varepsilon^2\left[\frac{\partial W_2}{\partial\xi}\dot{\xi}+\frac{\partial W_2}{\partial t}\right]. \tag{D.7}$$

Equation. (D.7) re-arranges into [83]

$$\dot{\xi}=\dot{x}-\varepsilon\left[\frac{\partial W_1}{\partial\xi}\dot{\xi}+\frac{\partial W_1}{\partial t}\right]-\varepsilon^2\left[\frac{\partial W_2}{\partial\xi}\dot{\xi}+\frac{\partial W_2}{\partial t}\right]. \tag{D.8}$$

Substituting Eq. (D.6) into Eq. (D.8) and considering up to second order in ε gives,

$$\dot{\xi}=\varepsilon\left[\mathrm{f}_1(\xi,t)-\frac{\partial W_1}{\partial\xi}\dot{\xi}-\frac{\partial W_1}{\partial t}\right]+\varepsilon^2\left[\frac{\partial\,\mathrm{f}_1}{\partial\xi}W_1+\mathrm{f}_2(\xi,t)-\frac{\partial W_2}{\partial\xi}\dot{\xi}-\frac{\partial W_2}{\partial t}\right]. \tag{D.9}$$

Let the averaged form of Eq. (D.2) be:

$$\dot{\xi}=\varepsilon\,\overline{\mathrm{f}}_1(\xi)+\varepsilon^2\,\overline{\mathrm{f}}_2(\xi). \tag{D.10}$$

Equating Eqs. (D.9) and (D.10) leads to,

$$\varepsilon\,\overline{\mathrm{f}}_1(\xi)+\varepsilon^2\,\overline{\mathrm{f}}_2(\xi)=\varepsilon\left[\mathrm{f}_1(\xi,t)-\frac{\partial W_1}{\partial t}\right]+\varepsilon^2\left[\mathrm{f}_2(\xi,t)+\frac{\partial \mathrm{f}_1}{\partial \xi}W_1-\frac{\partial W_1}{\partial \xi}\overline{\mathrm{f}}_1(\xi)-\frac{\partial W_2}{\partial t}\right].\text{(D.11)}$$

Now, equating the first order terms in Eq. (D.11) gives:

Order ε:

$$\overline{\mathrm{f}}_1(\xi)=\mathrm{f}_1(\xi,t)-\frac{\partial W_1}{\partial t}, \tag{D.12}$$

where, W_1 is chosen in such a way that all the $O(\varepsilon)$ terms on the right hand side disappear except their average value [90]. This result in,

$$\overline{\mathrm{f}}_1(\xi)=\frac{1}{\mathrm{T}}\int_0^{\mathrm{T}}\mathrm{f}_1(\xi,t)dt, \tag{D.13}$$

where, T is the period of excitation in the case of non-autonomous systems with periodic forcing, Eqs. (D.12),(D.13) imply that:

$$\frac{\partial W_1}{\partial t}=\mathrm{f}_1(\xi,t)-\frac{1}{\mathrm{T}}\int_0^{\mathrm{T}}\mathrm{f}_1(\xi,t)dt. \tag{D.14}$$

Like-wise, equating the second order terms in Eq. (D.11) gives:

Order ε^2:

$$\overline{\mathrm{f}}_2(\xi)=\mathrm{f}_2(\xi,t)+\frac{\partial \mathrm{f}_1}{\partial \xi}W_1-\frac{\partial W_1}{\partial \xi}\overline{\mathrm{f}}_1(\xi)-\frac{\partial W_2}{\partial t}. \tag{D.15}$$

Here again W_2 is chosen in such a way that only the average value of $O(\varepsilon^2)$ exists. This result in,

$$\bar{\mathrm{f}}_2(\xi) = \frac{1}{\mathrm{T}}\int_0^{\mathrm{T}} \left(\mathrm{f}_2(\xi,t) + \frac{\partial \mathrm{f}_1}{\partial \xi} W_1 - \frac{\partial W_1}{\partial \xi}\bar{\mathrm{f}}_1(\xi) \right) dt. \tag{D.16}$$

Thus, the second order averaged form given in Eq. (D.10) is evaluated from Eqs. (D.13) and (D.16) such as:

$$\dot{\xi} = \varepsilon \left[\frac{1}{\mathrm{T}}\int_0^{\mathrm{T}} \mathrm{f}_1(\xi,t)dt \right] + \varepsilon^2 \left[\frac{1}{\mathrm{T}}\int_0^{\mathrm{T}} \left(\mathrm{f}_2(\xi,t) + \frac{\partial \mathrm{f}_1}{\partial \xi} W_1 - \frac{\partial W_1}{\partial \xi}\bar{\mathrm{f}}_1(\xi) \right) dt \right], \tag{D.17}$$

where $W_1 = \int_0^t [\mathrm{f}_1(\xi,t)dt] - \frac{1}{\mathrm{T}}\int_0^{\mathrm{T}}\int_0^s \mathrm{f}_1(\xi,t)dtds$ and $\bar{\mathrm{f}}_1(\xi) = \frac{1}{\mathrm{T}}\int_0^{\mathrm{T}} \mathrm{f}_1(\xi,t)dt$. $\mathrm{f}_{1,2}$ are the first and second order coefficients respectively, of the original function given in Eq. (D.2) that is averaged. If the first order term degenerates to zero, then Eq. (D.17) simplifies to [85],

$$\dot{\xi} = \varepsilon^2 \frac{1}{\mathrm{T}} \left(\int_0^{\mathrm{T}} \left(\mathrm{f}_2(\xi,t) + \frac{\partial \mathrm{f}_1}{\partial \xi} W_1 \right) dt \right). \tag{D.18}$$

In Chapter 6, the functions $\mathrm{f}_1, \mathrm{f}_2$ in Eqs. (6.33) and (6.34) are functions of two variables r_u, ϕ_u. Hence, the standard form for averaging in Eqs. (6.33) and (6.34) are of the form:

$$\dot{r}_u = \varepsilon\left(\mathrm{f}_{1r}\left(r_u,\phi_u,t\right) + \varepsilon\, \mathrm{f}_{2r}\left(r_u,\phi_u,t\right) \right), \tag{D.19}$$

$$\dot{\phi}_u = \varepsilon\left(\mathrm{f}_{1\phi}\left(r_u,\phi_u,t\right) + \varepsilon\, \mathrm{f}_{2\phi}\left(r_u,\phi_u,t\right) \right), \tag{D.20}$$

where:

$W_{1r} = \int_0^t [\mathrm{f}_{1r}(\bar{r},\bar{\varphi},t)dt] - \frac{1}{\mathrm{T}}\int_0^{\mathrm{T}} \left(\int_0^s \mathrm{f}_{1r}(\bar{r},\bar{\varphi},t)\; dt \right) ds$; $\bar{\mathrm{f}}_{1r}(\bar{r},\bar{\varphi}) = \frac{1}{\mathrm{T}}\int_0^{\mathrm{T}} \mathrm{f}_{1r}(\bar{r},\bar{\varphi},t)\; dt$;

$W_{1\phi} = \int_0^t \left[\mathrm{f}_{1\phi}(\bar{r},\bar{\varphi},t)dt\right] - \frac{1}{\mathrm{T}}\int_0^{\mathrm{T}} \left(\int_0^s \mathrm{f}_{1\phi}(\bar{r},\bar{\varphi},t)\; dt \right) ds$; $\bar{\mathrm{f}}_{1\phi}(\bar{r},\bar{\varphi}) = \frac{1}{\mathrm{T}}\int_0^{\mathrm{T}} \mathrm{f}_{1\phi}(\bar{r},\bar{\varphi},t)\; dt$.

Applying the averaged form in Eq. (D.17) to both the Eqs. (D.19) and (D.20) gives [92]:

$$\dot{\bar{r}}_u = \varepsilon\left[\frac{1}{\mathrm{T}}\int_0^{\mathrm{T}} \mathrm{f}_{1r}(\bar{r}_1,\bar{\varphi}_1,t)dt\right] + \varepsilon^2\left[\frac{1}{\mathrm{T}}\int_0^{\mathrm{T}}\left(\begin{array}{l} \mathrm{f}_{2r}(\bar{r}_1,\bar{\varphi},t)+\left(\dfrac{\partial\,\mathrm{f}_{1r}}{\partial\bar{r}}W_{1r}+\dfrac{\partial\,\mathrm{f}_{1r}}{\partial\bar{\varphi}}W_{1\varphi}\right) \\ -\left(\dfrac{\partial W_{1r}}{\partial\bar{r}}\bar{\mathrm{f}}_{1r}(\bar{r},\bar{\varphi})+\dfrac{\partial W_{1r}}{\partial\bar{\varphi}}\bar{\mathrm{f}}_{1\varphi}(\bar{r},\bar{\varphi})\right) \end{array}\right)dt\right], \quad \text{(D.21)}$$

$$\dot{\bar{\varphi}}_u = \varepsilon\left[\frac{1}{\mathrm{T}}\int_0^{\mathrm{T}} \mathrm{f}_{1\phi}(\bar{r}_1,\bar{\varphi}_1,t)dt\right] + \varepsilon^2\left[\frac{1}{\mathrm{T}}\int_0^{\mathrm{T}}\left(\begin{array}{l} \mathrm{f}_{2\phi}(\bar{r}_1,\bar{\varphi},t)+\left(\dfrac{\partial\,\mathrm{f}_{1\phi}}{\partial\bar{r}}W_{1r}+\dfrac{\partial\,\mathrm{f}_{1\phi}}{\partial\bar{\varphi}}W_{1\phi}\right) \\ -\left(\dfrac{\partial W_{1\phi}}{\partial\bar{r}}\bar{\mathrm{f}}_{1r}(\bar{r},\bar{\varphi})+\dfrac{\partial W_{1\phi}}{\partial\bar{\varphi}}\bar{\mathrm{f}}_{1\phi}(\bar{r},\bar{\varphi})\right) \end{array}\right)dt\right], \quad \text{(D.22)}$$

where $\bar{r},\bar{\phi}$ are the averaged variables. Note that if a function f is not periodic in T, then the averaging is done over infinitely long time as in $\lim_{\mathrm{T}\to\infty}\frac{1}{\mathrm{T}}\int_0^{\mathrm{T}}\mathrm{f}\,\mathrm{dt}$ [93].

LIST OF REFERENCES

[1] P. Kamesh, M.J. Brennan and R. Holmes, 2008, "An Investigation into the Gyroscopic Effects on the Dynamic Behaviour of a Turbocharger", *Proceedings of the Ninth International Conference in Vibrations in Rotating Machinery (VIRM 9)*, Exeter, UK, September 8-10, 685-696.

[2] E.J. Gunter and W.J. Chen, 2005, "Dynamic Analysis of a Turbocharger in Floating Bush Bearings", *Proceedings of the Third International Symposium on Stability Control of Rotating Machinery (ISCORMA-3), Cleveland, Ohio*, September 19-23.

[3] R. Holmes, 2002, "Turbocharger Vibration - a Case Study", *Seventh International Conference on Turbochargers and Turbocharging*, Savoy Palace, London, UK, May 14-15, 91-100.

[4] L. San Andrés, J.C. Rivadeneira, K. Gjika, C. Groves and G. LaRue, 2007, "Rotordynamics of Small Turbochargers Supported on Floating Ring Bearings-Highlights in Bearing Analysis and Experimental Validation", *Journal of tribology*, 129, 391-397.

[5] P. Freeman, 1962, "Lubrication and Friction", Sir Isaac Pitman & Sons LTD.

[6] M.N. Sahinkaya and C.R. Burrows, 2002, "Stabilisation of High-Speed Flexible Rotors Supported by Oil-Film Bearings", *International Federation for the Promotion of Mechanism and Machine Science (IFToMM), Sixth International Conference on Rotor Dynamics*, Sydney, Australia, September 30, 412-419.

[7] L. San Andrés and J. Kerth, 2004, "Thermal Effects on the Performance of Floating Ring Bearings for Turbochargers", *Proceedings of the Institution of Mechanical Engineers, Part J: J. Engineering Tribology*, 218, 437-450.

[8] M.T. Gardner, 1983, "The Dynamic Behaviour of Oil Lubricated Journal Bearings", PhD thesis, Department of Applied Mathematical Studies, University of Leeds.

[9] "The Death of Whirl and Whip - Use of Externally Pressurized Bearings and Seals for Control of Whirl and Whip Instability", *ORBIT*, Fourth Quarter 2001.

[10] G. Capone, M. Russo and R. Russo, 1992, "The Influence of Oil Supply Pressure on the Behaviour of a Rigid Symmetrical Balanced Rotor in Journal Bearings with Circumferential Feeding", *ASME Journal of Tribology*, 114, 812-817.

[11] Z. Guo and R.G. Kirk, 20-24, August 2001, "Analysis of Externally Pressurized Fluid-Film Bearings for High-Speed Rotating Machinery", *Proceedings from the 1st International Symposium on Stability Control of Rotating Machinery (ISCORMA-1)*, South Lake Tahoe, California USA,

[12] L. San Andrés and D.W. Childs, 1997, "Angled Injection-Hydrostatic Bearings, Analysis and Comparison to Test Results", *ASME Journal of Tribology*, 121 (4), 886-891.

[13] W.J. Chen, 1996, "Instability Threshold and Stability Boundaries of Rotor-Bearing Systems", *ASME Journal of Engineering for Gas Turbines and Power*, 118, 115-121.

[14] P. Fayolle and D.W. Childs, 1999, "Rotor-Dynamic Evaluation of Roughened-Land Hybrid Bearing", *ASME Journal of Tribology*, 121 (1), 133-138.

[15] L. San Andrés, 2001, "A Hybrid Radial Bearing with Improved Rotordynamic Stability", *Proceedings from the First International Symposium on Stability Control of Rotating Machinery (ISCORMA-1)*, South Lake Tahoe, California, USA, August 20-24.

[16] A.H. Nayfeh and D.T. Mook, 1995, "Nonlinear Oscillations", Wiley-VCH, Virginia.

[17] A. El-Shafei, S.H. Tawfick, M.S. Raafat and G.M. Aziz, 2007, "Some Experiments on Oil Whirl and Oil Whip", *Journal of Engineering for Gas Turbines and Power*, 129 (1), 144-153.

[18] F.W. Ocvirk, 1952, "Short Bearing Approximation for Full Journal Bearings", National Advisory Committee for Aeronautics - Technical Note, NACA TN 2808.

[19] Y. Hori, 2005, "Hydrodynamic Lubrication", Springer-Verlag, Tokyo.

[20] R. Holmes, 1963, "Oil-Whirl Characteristics of a Rigid Rotor in 360° Journal Bearings", *Proceedings of the Institution of Mechanical Engineers*, 177 (11), 291-299.

[21] C.J. Myers, 1981, "Linear and Nonlinear Vibrational Characteristics of Oil Lubricated Journal Bearings", PhD thesis, Department of Applied Mathematics, University of Leeds.

[22] H. Poritsky, 1953, "Contribution to the Theory of Oil Whip", *Transactions of the ASME*, 1153-1161.

[23] M.T. Gardner, C.J. Myers, M. Savage and C. Taylor, 1985, "Analysis of Limit-Cycle Response in Fluid-Film Journal Bearings Using the Method of Multiple Scales", *Quarterly Journal of Mechanics and Applied Mathematics*, 38 (1), 27-45.

[24] B. Tower, 1888, "Experiments on the Friction of a Collar Bearing", *Proceedings of the Institution of Mechanical Engineers*, 1, 173-205.

[25] O. Reynolds, 1886, "On the Theory of Lubrication and Its Application to Mr. Beauchamp Tower's Experiments, Including an Experimental Determination of the Viscosity of Olive Oil", *Philosophical Transactions of the Royal Society of London*, 177, 157-234.

[26] A. Sommerfeld, 1904, "The Hydrodynamic Theory of Lubrication Friction", *Zeitschrift für Mathematik und Physik (Journal of Mathematics and Physics, German Edition)*, 50 (1 and 2), 97-155.

[27] G.B. Dubois and F.W. Ocvirk, 1952, "Analytical Derivation and Experimental Evaluation of Short Bearing Approximation for Full Journal Bearings", National

Advisory Committee for Aeronautics - Technical Report -1157, NACA TN 2808, 1199-1230.

[28] J.R. Mitchell, R. Holmes and J. Byrne, 1965-66, "Oil Whirl Characteristics of a Rigid Rotor in 360° Journal Bearings: Further Characteristics", *Proceedings of the Institution of Mechanical Engineers*, 180 (1), 593-610.

[29] F.E. Cardullo, 1930, "Some Practical Deductions from Theory of Lubrication of Short Cylindrical Bearings", *Transactions of the ASME*, 52 (NSP-72-12), 143-153.

[30] R.I. Taylor, 1999, "The Inclusion of Lubricant Shear Thinning in the Short Bearing Approximation", *Proceedings of the Institution of Mechanical Engineers Part J: Journal of Engineering Tribology*, 213, 35-46.

[31] R.I. Taylor, 2004, "Simplifications to the Short Bearing Approximation", *Proceedings of the Institution of Mechanical Engineers, Part J: Journal of Engineering Tribology*, 218, 569-573.

[32] B.L. Newkirk and H.D. Taylor, 1925, "Shaft Whipping Due to Oil Action in Journal Bearings", *General Electric Review*, 28 (8), 559-568.

[33] A. Tondl, 1962, "Experimental Investigation of Self-Excited Vibrations of Rotors Due to the Action of Lubricating Oil Film in Journal Bearings", *Wear*, 5, 136-147.

[34] J. Dworski, 1964, "High-Speed Rotor Suspension Formed by Fully Floating Hydrodynamic Radial and Thrust Bearings", *ASME Journal of Engineering for Power*, 86, 149-160.

[35] M. Tanaka and Y. Hori, 1972, "Stability Characteristics of Floating Bush Bearings", *Transactions of ASME, Journal of Lubrication technology*, 94, 248-259.

[36] D. Robertson, 1934, "The Whirling of Shafts", *Engineer, London*, 158, 216-228.

[37] L.E. Barrett, A. Akers and E.J. Gunter, 1976, "Effect of Unbalance on a Journal Bearing Undergoing Oil Whirl", *Proceedings of the Institution of Mechanical Engineers*, 190, 31/76, 535-544.

[38] R. Holmes, 1974, "Vibration and Its Control in Rotating Systems", *International Union of Theoretical and Applied Mechanics (IUTAM)-Symposium on Dynamics of Rotors*, Lyngby, Denmark, August 12-16, 156-181.

[39] A. Tondl, 1974, "Some Problems of Self-Excited Vibration of Rotors", Monographs and memoranda of the National Research institute for machine design, No. 17, Bechovice, Czech Republic.

[40] H. Li and Y. Shin, C, 2004, "Integrated Dynamic Thermo-Mechanical Modeling of High Speed Spindles, Part 1: Model Development", *Transactions of the ASME*, 126, 148-158.

[41] A. Angantyr, 2004, "Constrained Optimization of Rotor-Bearing Systems by Evolutionary Algorithms", Licentiate thesis, Department of Applied physics and Mechanical Engineering, Lulea University of Technology.

[42] A.C. Hagg and P.C. Warner, 1953, "Oil Whip of Flexible Rotors", *Transactions of the ASME*, 75, 1339–1344.

[43] C.J. Myers, 1984, "Bifurcation Theory Applied to Oil-Whirl in Plain Cylindrical Journal Bearings", *Transactions of the ASME*, 51, 244-250.

[44] A. Boyaci, H. Hetzler, W. Seemann, C. Proppe and J. Wauer, 2008, "Analytical Bifurcation Analysis of a Rotor Supported by Floating Ring Bearings", *Nonlinear Dynamics*, 57 (4), 497-507.

[45] R.G. Kirk and E.J. Gunter, Jr., 1970, "Transient Journal Bearing Analysis", National Aeronautics and Space Administration - Contractor Report, NASA-CR-1549, 197.

[46] J.M. Gambaudo, 1985, "Perturbation of a Hopf Bifurcation by an External Time-Periodic Forcing ", *Journal of Differential Equations*, 57, 172-199.

[47] J. Shaw and S.W. Shaw, 1990, "The Effects of Unbalance on Oil Whirl", *Nonlinear Dynamics*, 1, 293-311.

[48] R.D. Brown, G. Drummond and P.S. Addison, 2000, "Chaotic Response of a Short Journal Bearing", *Proceedings of the Institution of Mechanical Engineers*, 214 (Part J), 387-400.

[49] N.S. Namachivaya and S.T. Ariaratnam, 1987, "Periodically Perturbed Hopf Bifurcation", *SIAM Journal of Applied Mathematics*, 47 (1), 15-39.

[50] Y. Chen and Q. Ding, 2001, "C-L Method and Its Application to Engineering Nonlinear Dynamical Problems", *Applied Mathematics and Mechanics*, 22 (2), 144-153.

[51] Q. Ding, J.E. Cooper and A.Y.T. Leung, 2002, "Hopf Bifurcation Analysis of a Rotor/Seal System", *Journal of Sound and Vibration*, 252 (5), 817-833.

[52] S. Li, Q. Xu, F. Wan and X. Zhang, 2003, "Stability and Bifurcation of Unbalance Rotor/Labyrinth Seal System", *Applied Mathematics and Mechanics*, 24 (11), 1290-1301.

[53] J.A. Calvo, V. Diaz and J.L.S. Roman, 2006, "Controlling the Turbocharger Whistling Noise in Diesel Engines", *International Journal of Vehicle Noise and Vibration*, 2 (1), 17-28.

[54] R. Holmes, M.J. Brennan and B. Gottrand, 2004, "Vibration of an Automotive Turbocharger-a Case Study", *Proceedings of the Eighth International Conference on Vibrations in Rotating Machinery (VIRM-8)*, Swansea, UK, September 7-9, 445-450.

[55] A.A. Alsaeed, 2005, "Dynamic Stability Evaluation of an Automotive Turbocharger Rotor-Bearing System", M.S. dissertation, Mechanical Engineering, Virginia Polytechnic Institute and State University.

[56] E.J. Gunter and W.J. Chen, 2003, "Dynamics of Rotor-Bearing Systems", DyRoBeS Users' Manual, RODYN Vibration Analysis, Inc., Charlottesville, VA.

[57] Y. Guangchi, M. Guang and J. Jianping, 2008, "Turbocharger Rotor Dynamics with Foundation Excitation ", *Archive of Applied Mechanics*, 79 (4), 287-299.

[58] R.G. Kirk, A. Alsaeed, J. Liptrap, C. Lindsey, D. Sutherland, B. Dillon, E. Saunders, M. Chappell, S. Nawshin, E. Christian, A. Ellis, B. Mondschein, J. Oliver and J. Sterling,

2008, "Experimental Test Results for Vibration of a High Speed Diesel Engine Turbocharger ", *Tribology Transactions*, 51 (4), 422 - 427

[59] J. Sterling, 2009, "Influence of Induced Unbalance on Subsynchronous Vibrations of an Automotive Turbocharger", M.S dissertation, Mechanical Engineering, Virginia Polytechnic Institute and State University.

[60] B. Schweizer, 2009, "Total Instability of Turbocharger Rotors-Physical Explanation of the Dynamic Failure of Rotors with Full-Floating Ring Bearings", *Journal of Sound and Vibration*, 328 (1-2), 156-190.

[61] K. Gjika, L. San Andrés and G.D. Larue, 2010, "Nonlinear Dynamic Behavior of Turbocharger Rotor-Bearing Systems with Hydrodynamic Oil Film and Squeeze Film Damper in Series: Prediction and Experiment", *Journal of Computational and Nonlinear Dynamics*, 5 (4), 41006-41013.

[62] S. Wiggins, 1990, "Introduction to Applied Nonlinear Dynamical Systems and Chaos", Springer-Verlag, New York.

[63] Y.A. Kuznetsov, 1998, "Elements of Applied Bifurcation Theory", Springer-Verlag, New York.

[64] 2008, "Basics of Lubrication", *Society of Tribologists and Lubrication Engineers*, http://www.stle.org/resources/lubelearn/lubrication/default.aspx.

[65] K. Hatakenaka, M. Tanaka and K. Suzuki, 2002, "Theoretical Analysis of Floating Bush Journal Bearing with Axial Oil Film Rupture Being Considered", *Transactions of the ASME*, 124, 494-505.

[66] H. Mcallion, 1973, "Vibration of Linear Mechanical Systems", Longman, London.

[67] J.P. DenHartog, 1956, "Mechanical Vibrations", Fourth Edition, McGraw-Hill, New York.

[68] "Dynamic Stiffness in Whirl and Whip", *ORBIT*, First Quarter 1998.

[69] S.S. Rao, 2004, "Mechanical Vibrations", Pearson Education Inc., New Delhi.

[70] J. Wang, 2005, "On the Stability of Rotor Bearing Systems Based on the Hopf Bifurcation Theory", PhD thesis, Department of Mechanical Engineering, Louisiana State University and Agricultural and Mechanical College.

[71] A.B. Poore, 1976, "On the Theory of an Application of the Hopf Bifurcation Theory." *Archives for Rational Mechanics and Analysis*, 60, 371-392.

[72] J.W. Lund, 1966, "Self-Excited, Stationary Whirl Orbits of a Journal in a Sleeve Bearing", PhD thesis, Rensselaer Polytechnic Institute.

[73] L. Hawkins, A, B. Murphy, T and J. Kajs, May 8-11, 2000, "Analysis and Testing of a Magnetic Bearing Energy Storage Flywheel with Gain-Scheduled, Mi-Mo Control", *Proceedings of ASME TURBOEXPO*, Munich, Germany,

[74] J. Guckenheimer and P. Holmes, 1983, "Nonlinear Oscillations, Dynamical Systems, and Bifurcations of Vector Fields", Springer-Verlag, New York.

[75] A. Shoshitaishvili, 1972, "Bifurcations of Topological Type of a Vector Field near a Singular Point of Parameterised Vector Fields", *Translated from the Russian journal Funktsional'Nyi Analiz i Ego Prilozheniya (Functional analysis and its applications)*, 6 (2), 97-98.

[76] J. Murdock, 2006, "Normal Forms", *Scholarpedia*, 1(10):1902.

[77] P.B. Kahn and Y. Zarmi, 1998, "Nonlinear Dynamics: Exploration through Normal Forms", Wiley, New York.

[78] J. Lin and C. Hwang, 2002, "Hopf Bifurcation to a Short Porous Journal-Bearing System Using the Brinkman Model: Weakly Nonlinear Stability", *Tribology International*, 35, 75-84.

[79] P. Hollis and D.L. Taylor, 1986, "Hopf Bifurcation to Limit Cycles in Fluid Film Bearings", *Transactions of the ASME*, 108, 184-189.

[80] A. Tondl and H. Ecker, 2003, "On the Problem of Self-Excited Vibration Quenching by Means of Parametric Excitation", *Archives of Applied Mechanics*, 72, 923-932.

[81] A.H. Nayfeh and D.T. Mook, 2004, "Nonlinear Oscillations", Wiley-VCH Verlag GmbH &Co. KGaA, Weinheim.

[82] H.F. de Castro, K.L. Cavalca and R. Nordmann, 2008, "Whirl and Whip Instabilities in Rotor-Bearing System Considering a Nonlinear Force Model", *Journal of Sound and Vibration*, 317, 273–293.

[83] R.H. Rand and D. Armbruster, 1987, "Perturbation Methods, Bifurcation Theory and Computer Algebra", Springer-Verlag, New York.

[84] J.R. Dormand and P.J. Prince, 1980, "A Family of Embedded Runge-Kutta Formulae", *Journal of Computational and Applied Mathematics*, 6, 19-26.

[85] P. Gross, 1993, "On Harmonic Response in Forced Nonlinear Oscillators Exhibiting a Hopf Bifurcation", *IMA (Institute of Mathematics and its Applications) Journal of Applied Mathematics*, 50, 1-12.

[86] P. Gross, 1994, "On Oscillation Types in Forced Oscillators Close to Harmonic Resonance", *IMA (Institute of Mathematics and its Applications) Journal of Applied Mathematics*, 53, 27-43.

[87] E.J. Gunter, 1966, "Dynamic Stability of Rotor-Bearing Systems", National Aeronautics and Space Administration - Special Publication, NASA-SP-113.

[88] A.Z. Szeri, 1998, "Fluid Film Lubrication: Theory and Design", Cambridge University Press.

[89] S.M. Han, H. Benaroya and T. Wei, 1999, "Dynamics of Transversely Vibrating Beams Using Four Engineering Theories", *Journal of Sound and Vibration*, 225 (5), 935-988.

[90] R.H. Rand, 2005, "Lecture Notes on Nonlinear Vibrations".

[91] N.M. Kryolov and N.N. Bogolibov, "Kryolov-Bogolibov Method of Averaging", Springer Encyclopaedia of Mathematics.

[92] J.A. Sanders and F. Verhulst, 1985, "Averaging Methods in Nonlinear Dynamical Systems", Springer-Verlag, New York.

[93] P. Wahi and A. Chatterjee, 2004, "Averaging Oscillations with Small Fractional Damping and Delayed Terms", *Nonlinear Dynamics*, 38, 3-22.